University of Malta
Faculty of Engineering
Department of Electronic Systems Engineering

CERN - The European Organisation for Nuclear Research
Accelerator Technology Division
Magnets Tests and Measurements Group
Analysis and Studies Section

The Field Description for The Large Hadron Collider

by
Nicholas J. Sammut

under the supervision of
Prof. Ing. Joseph Micallef (UoM)
Dr. Luca Bottura (CERN)

July 2006

A dissertation submitted to the University of Malta
for the degree of Doctor of Philosophy in the Faculty of Engineering

No portion of the work referred to in the thesis has been submitted in support of an application for another degree or qualification of this or any other university or other institute of learning.

Nicholas Sammut

English

Abstract

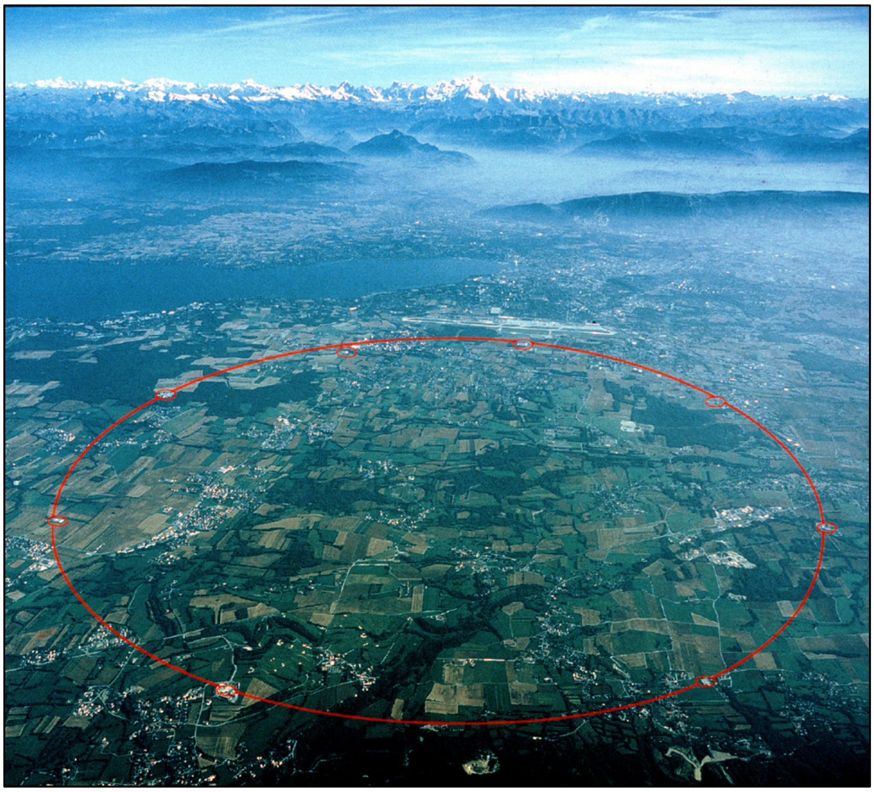

Aerial view of the LHC with the Alps in the background.

The most important product of all knowledge is that it allows us to
pose questions that could not have been posed before.
- David Gross

The Large Hadron Collider (LHC), currently under construction at CERN, is a 27 km particle accelerator and has 1232 superconducting dipole magnets and 392 superconducting quadrupole magnets to respectively bend and focus the particle beams along their circular trajectory. Two counter rotating beams collide in four experimental insertions at a nominal centre of mass energy of 14 TeV.

The LHC requires a powerful control system to correct the field variations that result from inherent properties of the superconducting magnets. If these field changes are not corrected with high speed and precision, they may jeopardize the machine performance significantly. Unfortunately, a feed-back control system that only relies on beam measurements has limited capabilities and is not sufficient to solely provide the error compensation that is needed. A system based on feed-forward control is therefore required to reduce the burden on the beam based feed-back by forecasting what the field variations will be to within a residual error comparable to beam control requirements.

This thesis deals with the formulation of a static and dynamic field model as well as a set of scaling laws that together form the core of the feed-forward control system. This work also includes numerous magnetic measurements on the superconducting magnets in cryogenic conditions which enable the extraction of the parameters used in the model.

The static field model is based on the reproducible magnetic effects that are dependent on the magnet excitation current. The dynamic field model is an extension of the static field model and mostly describes the behavior of the LHC during particle injection. The dynamic effects are dependent on both current and time and are not reproducible from cycle to cycle since they are dependent on the magnet powering history. Scaling laws are also formulated to provide a recalibration mechanism for the model and to extend its validity to a wider scope for the entire magnet population.

The static and dynamic models as well as the scaling laws are applied on an LHC sector for the dipole magnets. The model is also tested on a sample of the main quadrupole magnets, a sample of the insertion region wide aperture magnets and on one long trim quadrupole corrector. The error obtained is within the desired tolerances and this hence demonstrates that the field model formulated is robust and adaptable to a wide range of magnet types.

This dissertation also presents the development of a data acquisition system for a Hall plate based instrument that measures the fast magnetic field variations of the most important harmonics at the beginning of the particle acceleration. This new fully digitized acquisition system is shown to have a better performance than the preceding analogue system and hence provides a better foundation on which to base the scaling law for this crucial part of the LHC excitation cycle.

The work presented in this thesis has been adopted by CERN as an integral part of the LHC feed-forward control system and will be used once the machine becomes operational in 2007.

Malti

Sommarju

L’LHC (bl-aħmar) superimpost fuq il-gżejjer Maltin biex tintwera l-iskala tal-proġett.

Il-mistoqsija oħt il-għerf.
- Qawl Malti

Il-Large Hadron Collider (LHC), li bħalissa qed jinbena f'CERN, huwa aċċeleratur ta' partiċelli, 27 km twil, li jikkonsisti minn 1232 kalamiti dipolari superkonduttivi u minn 392 kalamiti quadrupolari superkonduttivi li, rispettivament, jagħwġu u jiffokaw il-faxxex tal-partiċelli sabiex iżommuhom fuq traġitt ċirkolari ġewwa l-magna. Żewġ faxex li jduru kontra xulxin jitħabbtu f'erba' inserzjonijiet esperimentali f'ċentru tal-massa enerġetika nominali ta' 14 TeV.

L'LHC tirrikjedi sistema ta' kontroll sofistikata biex tikkoreġi il-varjazzjonijiet manjetiċi li jirriżultaw mill-proprjetajiet tal-kalamiti superkonduttivi. Jekk dawn il-varjazzjonijiet manjetiċi m'humiex korretti bi preċiżjoni u b'ritmu mgħaġġel biżżejjed, dawn jistgħu jikkompromettu l-operazzjoni tal-magna b'manjiera sinjifikanti. Sfortunatament, sistema ta' kontroll *feed-back* li togħqod biss fuq il-kejl tal-faxx tal-partiċelli, mhix biżżejjed biex waħeda tipprovdi il-kompensazzjoni li hija meħtieġa. B'hekk, sistema ibbażata fuq kontroll *feed-forward* hija meħtieġa biex tnaqqas il-piż fuq is-sistema ta' kontroll *feed-back* billi tipprevedi x'ser ikunu il-varjazzjonijiet manjetiċi fl-ispeċifikazzjonijiet komparabbli ma dawk tal-faxx ta' partiċelli.

Din it-teżi tirrigwarda l-formulazzjoni ta' mudell statiku u mudell dinamiku kif ukoll sett ta' liġijiet ta' skala li flimkien jiffurmaw il-qalb tas-sistema ta' kontroll *feed-forward*. Dan ix-xogħol jinkludi wkoll numru sostanzjali ta' kejl manjetiċi fuq il-kalamiti superkonduttivi f'kundizzjonijiet krioġeniċi li jippermettu l-estrazzjoni tal-parametri użati fil-mudell.

Il-mudell statiku huwa bbażat fuq effetti manjetiċi riproduċibbli li jiddependu fuq il-kurrent tal-kalamita. Il-mudell dinamiku huwa estensjoni tal-mudell statiku u prinċipalment jifformula l-imġieba tal-magna waqt l-injezzjoni tal-partiċelli. L-effetti manjetiċi dinamiċi jiddependu mhux biss fuq il-kurrent iżda wkoll fuq il-ħin. Dawn m'humiex riproduċċibbli minn ċiklu għall-ieħor, u jiddependu fuq kif il-magna kienet eċitata qabel. Il-liġijiet ta' skala huma fformulati sabiex jipprovdu mekkaniżmu ta' rikalibrazzjoni għall-mudell u biex jestendu il-validità tiegħu għal skop akbar u għall-kalamiti kollha.

Il-mudell statiku u dinamiku, kif ukoll il-liġijiet ta' skala, huma applikati fuq settur ta' l-LHC għall-kalamiti dipolari. Il-mudell huwa ppruvat fuq kampjun tal-kalamiti quadrupolari prinċipali, kampjun tal-kalamiti ta' inserzjoni ta' apertura wiesa u wkoll fuq korrettur quadrupolari twil *trim*. Id-devjazzjoni tal-mudell ikkomparat mal-kejl jinsab fl-ambitu ta' tolleranza desiderata u b'hekk dan juri li l-mudell ifformulat hu robust u adattabbli għall-bosta kalamiti differenti.

Dan l-istudju jippreżenta wkoll l-iżvilupp ta' sistema ta' akkwiżizzjoni ta' dati għal strument ibbażat fuq sensuri *Hall* li jkejjlu l-varjazzjonijiet manjetiċi mgħaġġlin ta' l-iktar *harmonics* importanti fil-bidu ta' l-aċċelerazzjoni tal-partiċelli. Din is-sistema diġitali ġdida għandha andatura aħjar mis-sistema analoġika preċedenti u b'hekk tipprovdi bażi aħjar fuqiex wieħed jista' jibbaża il-liġi ta' skala għal din il-parti kruċjali taċ-ċiklu ta' operazzjoni tal-magna.

Ix-xogħol ippreżentat f'din it-teżi ġie adottat minn CERN bħala parti integrali tas-sistema ta' kontroll *feed-forward* ta' l-LHC u ser jintuża meta il-magna tibda topera fis-sena 2007.

Français

Résumé

Un aimant LHC est transporte vers le banc du test a froid.

Le doute est l’ennemi des grandes enterprises.
- Napoléon Bonaparte

Le Large Hadron Collider (LHC), actuellement en construction au CERN, est un accélérateur de 27 km, ayant 1232 aimants dipolaires supraconducteurs et 392 aimants quadripolaires supraconducteurs, utilisés respectivement pour guider et focaliser les faisceaux de particules sur la trajectoire circulaire. Deux faisceaux de sens opposé entreront en collision en quatre lieux d'expérience avec une énergie de centre de masse de 14 TeV.

Le bon fonctionnement du LHC nécessite un système de contrôle rapide et efficace pour corriger les variations de champ magnétique résultant des propriétés intrinsèques des aimants supraconducteurs. Si ces variations ne sont pas rapidement et précisément compensées, elles peuvent détériorer significativement la performance de la machine. Un système de contrôle de réaction négative n'est malheureusement pas suffisant pour compenser ces imperfections. L'utilisation d'un système de contrôle de réaction positive a été alors pensé pour rétablir les écarts de champ magnétique dans un intervalle de tolérance comparable aux exigences de contrôle du faisceau.

Cette thèse a pour objet la formulation et la description d'un modèle magnétique statique et dynamique ainsi qu'un ensemble de lois de normalisation qui forment le cœur du système de contrôle de réaction positive. Ce travail comprend aussi de nombreuses mesures magnétiques sur les aimants supraconducteurs en conditions cryogéniques, qui permettent d'extraire les paramètres utilisés dans le modèle.

Le modèle statique est basé sur des effets reproductibles qui dépendent du courant d'excitation. Le modèle dynamique est une extension du modèle statique et décrit essentiellement le comportement du LHC à l'injection des particules. Les effets magnétiques dynamiques sont dépendants du courant et du temps mais ne sont pas reproductibles d'un cycle à l'autre car ils sont dépendants des cycles précédents. Des lois de normalisation sont alors établies pour fournir un mécanisme de recalibration pour le modèle et pour en étendre sa validité à l'ensemble des aimants.

Les modèles statiques et dynamiques ainsi que les lois de normalisation sont appliqués aux aimants dipolaires dans un secteur du LHC. Le modèle est testé aussi sur un échantillon d'aimants quadripolaires principaux, un échantillon d'aimants d'insertion à ouverture large et sur un long "trim" correcteur quadripolaire. L'erreur obtenue est dans les tolérances et démontre donc que le modèle de champ formulé est robuste et adaptable à une large portée de types d'aimants.

Ce rapport présente aussi le développement d'un système d'acquisition de données, d'un détecteur basé sur des sondes à effet Hall. Celui-ci a permis de mesurer les variations temporelles des harmoniques les plus importantes du champ magnétique au début de l'accélération des particules. Ce nouveau système digital est plus performant que le précèdent système analogique et fournit une meilleure base pour construire les lois de normalisation pour cette partie du cycle d'excitation de la machine.

Le travail de cette thèse a été adopté par le CERN comme partie essentielle du système de contrôle de réaction positive et sera utilisé quand la machine sera opérationnelle en 2007.

Italiano

Riassunto

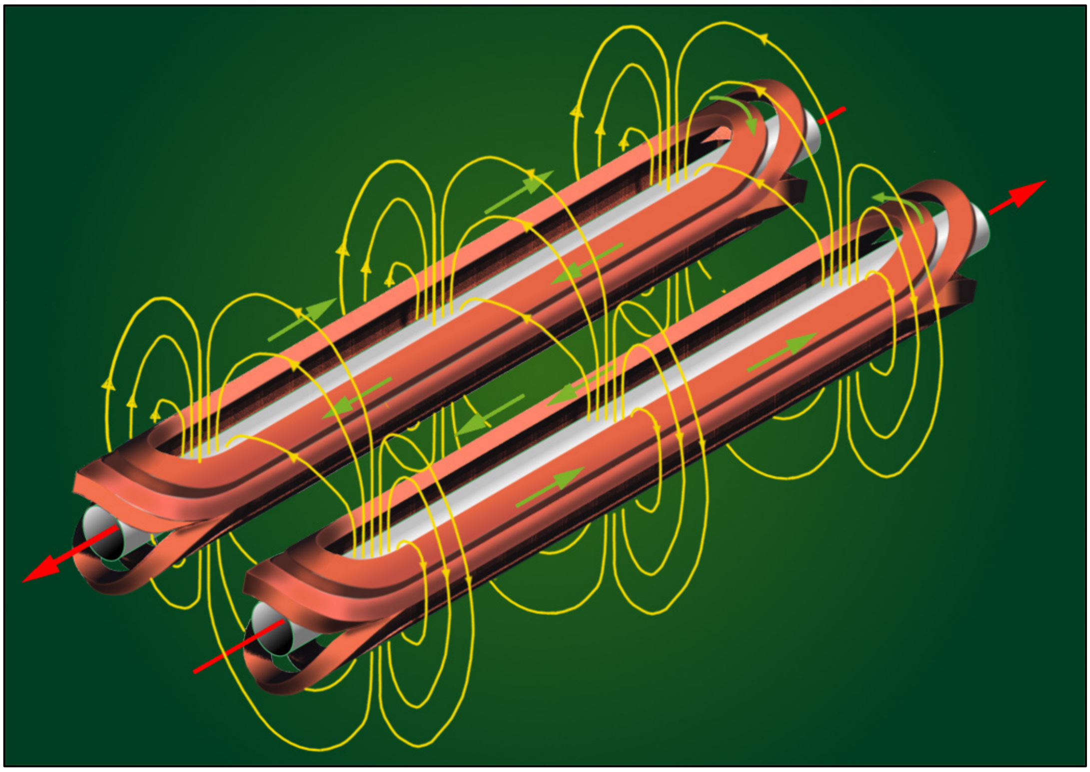

Il campo magnetico dei dipoli superconduttivi dell'LHC.

Ed elli a me: "Questo misero mondo
tegnon l'anime triste di coloro
che visser sanza 'nfamia e senza lodo."
- Dante Alighieri in *La Divina Commedia - Inferno*

Il Large Hadron Collider (LHC), attualmente in construzione al CERN, è un collisionatore di 27 km dotato di 1232 magneti dipolari superconduttivi e 392 magneti quadrupolari superconduttivi che, rispettivamente, deviano e focalizzano due fasci di protoni lungo una traiettoria circolare. I fasci circolano in direzioni opposte e collidono in quattro inserzioni sperimentali con un baricentro nominale di 14 TeV di energia.

L'LHC richiede un potente sistema di controllo per correggere le variazioni di campo che risultano dalle proprietà dei magneti superconduttivi. Se le variazioni di campo non vengono corrette con sufficiente precisione e velocità, queste potrebbero compromettere significativamente le prestazioni della macchina. Purtroppo un sistema di controllo feed-back che dipenda unicamente dalle misure del fascio ha dei limiti intrinseci e non basta per compensare gli errori come richiesto. Un sistema di controllo feed-forward é dunque necessario per prevedere le variazioni di campo con un errore paragonabile a quello delle specifiche del controllo del fascio e, così facendo, minimizzare il campo di azione del sistema di controllo feed-back.

Questa tesi tratta sia la formalizzazione di un modello di campo statico e dinamico che la raccolta di leggi di normalizzazione, che insieme formano il cuore del sistema di controllo feed-forward. Questo lavoro include numerose misure di campo magnetico all'interno dei magneti superconduttivi in condizioni criogeniche tali da permettere di ricavare i parametri usati nel modello.

Il modello statico di campo è basato sugli effetti magnetici riproducibili che dipendono dalla corrente di eccitazione. Il modello dinamico è un'estensione del modello statico di campo e descrive principalmente il comportamento della macchina durante l'iniezione delle particelle. Gli effetti magnetici dinamici dipendono dal tempo e dalla corrente e non sono riproducibili da un ciclo all'altro perché il loro comportamento risente del modo in cui i magneti sono stati alimentati nei cicli precedenti. Le leggi di normalizzazione sono formulate per fornire un meccanismo di recalibrazione del modello e per estendere la sua validità all'intera popolazione dei magneti.

Sia i modelli statici e dinamici che le leggi di normalizzazione sono applicati ad un settore dell'LHC per i magneti dipolari. Il modello è testato su un campione dei quadrupoli principali, un campione dei magneti di inserzione ad aperture larga e su un correttore lungo quadrupolare "trim". L'errore stimato rientra nei limiti di tolleranza e questo dimostra che il modello di campo è solido e adattabile a una grande varietà di magneti.

Questa tesi tratta anche lo sviluppo di un sistema di acquisizione di dati per uno strumento basato sulle sonde Hall che misura la variazione delle armoniche fondamentali di un campo magnetico veloce nella prima fase dell'accelerazione delle particelle. Questo innovativo sistema digitale di acquisizione di dati ha prestazioni superiori a quelle del precedente sistema anlogico e quindi rappresenta uno strumento piú affidabile su cui basare le leggi di normalizzazioni in questa fase cruciale del ciclo di operazione della macchina.

Il lavoro presentato in questa tesi é stato adottato dal CERN come parte integrante del sistema di controllo feed-forward dell' LHC e sarà usato quando la macchina diventerà operativa nel 2007.

Acknowledgements

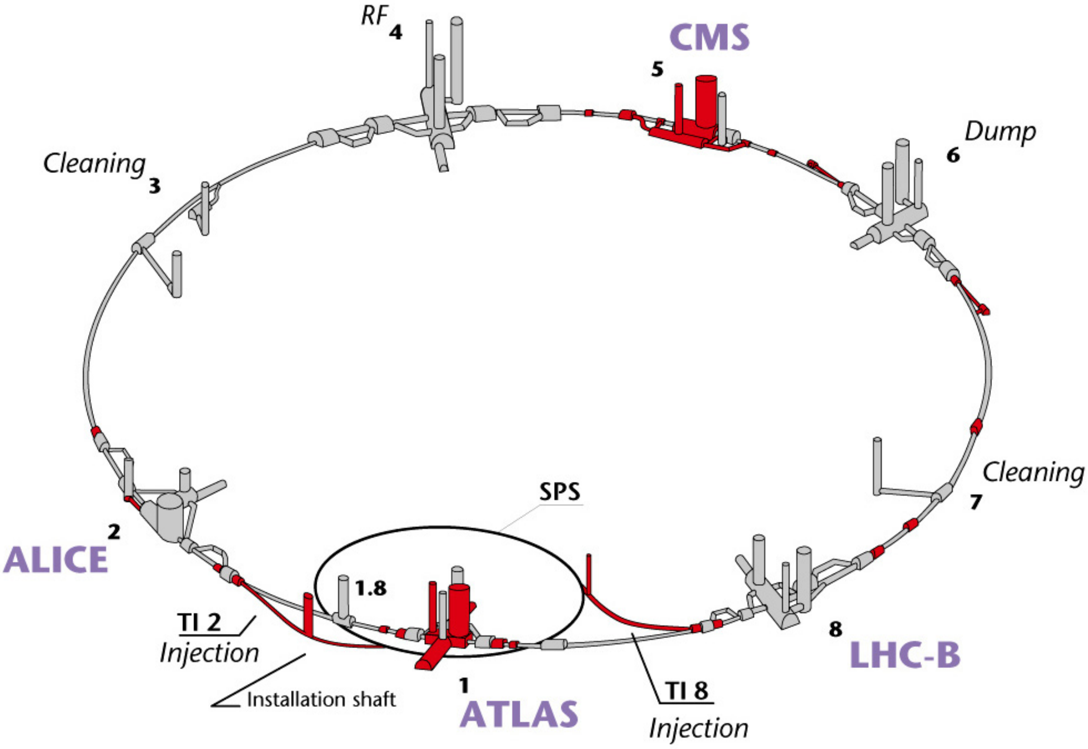

The LHC underground infrastructure.

It does not matter where the wind blows.
What matters is the position in which you put your sail.
-Vera Peiffer

One of the greatest pleasures of writing a thesis is thanking those who most notably helped in its realization.

First and foremost, I would like to thank the one man who was particularly instrumental in the setting up of the collaboration and who guided the activities of the venture throughout. My profound gratitude to Luca Bottura, my CERN supervisor, for his faith in me and for his constant and unfailing support.

I would also like to express my gratitude towards Joseph Micallef, my supervisor at the University of Malta, for his guidance and invaluable comments and suggestions particularly in the structuring of this dissertation.

Special thanks to Stephane Sanfilippo, Alessandro Masi and Nikolay Smirnov for their precious help throughout my training. Thanks also to my CERN colleagues who were a real pleasure to work with as well as all my friends who made this stay an enjoyable one.

Most of all I would heartily like to thank my family, in particular my parents to whom this work is dedicated, for their untiring encouragement, dedication and backing.

List of Publications


The CMS detector being assembled.

Every man is guilty of all the good he didn’t do.
- François-MarieVoltaire

The following publications are the result of the work of this thesis:

1. **N. Sammut**, L. Bottura, J. Micallef, “The LHC Magnetic Field Model”, in *Proceedings of the Particle Accelerator Conference*, pp. 2648-2650, Knoxville, Tennessee, USA, May 2005.

2. P. Bauer, G. Annala, L. Bottura, M. A. Martens, **N. Sammut**, G. Velev, V. Shiltsev, “Advances in the Understanding and Operations of Superconducting Colliders”, in *Proceedings of the Particle Accelerator Conference*, pp. 54-58, Knoxville, Tennessee, USA, May 2005.

3. **N. Sammut**, L. Bottura, J. Micallef, “A Mathematical Formulation to Predict the Harmonics of the Superconducting LHC Magnets”, *Physical Reviews Special Topics: Accelerators and Beams*, vol 9, 012402, January 2006.

4. **N. Sammut**, E. Benedico Mora, L. Bottura, P. Galbraith, D. Giloteaux, G. Greco, M. Haverkamp, M. Marchesotti, A. Masi, J. Micallef, T. Pieloni, N. Smirnov, A. Tikhov, “A Hall Plate Based Instrument to Measure the Snapback in the Large Hadron Collider Superconducting Dipole Magnets”, in *Proceedings of the IEEE Instrumentation and Measurement Technology Conference*, Sorrento, Italy, April 2006.

5. **N. Sammut**, L. Bottura, S. Sanfilippo, J. Micallef, “The Field Description Model for the LHC Quadrupole Superconducting Magnets”, in *Proceedings of the European Particle Accelerator Conference*, pp. 2619-2621, Edinburgh, UK, June 2006.

6. **N. Sammut**, L. Bottura, S. Sanfilippo, J. Micallef, “The Dependence of the Field Decay on the Powering History of the LHC Superconducting Dipole Magnets”, in *Proceedings of the European Particle Accelerator Conference*, pp. 2622-2624, Edinburgh, UK, June 2006.

7. W. Venturini Delsolaro, L. Bottura, Y. Chaudhari, M. Karppinen, **N. Sammut**, “Measurement and Modeling of Magnetic Hysteresis in the LHC Superconducting Correctors”, in *Proceedings of the European Particle Accelerator Conference*, pp. 2026-2028, Edinburgh, UK, June 2006.

8. **N. Sammut**, L. Bottura, P. Bauer, T. Pieloni, J. Micallef, “Three Scaling Laws to Predict the Dynamic Field Changes of the Superconducting LHC Dipole Magnets”, *Physical Reviews Special Topics: Accelerators and Beams* - To be published.

9. L. Bottura, N. Brooks, A. Devred, V. Granata, S. Le Naour, **N. Sammut**, S. Sanfilippo, W. Venturini Delsolaro, R. Wolf, “Persistent Currents in Accelerator Magnets”, in *Proceedings of the Applied Superconductivity Conference*, Seattle August 2006 - To be published.

Table of Contents

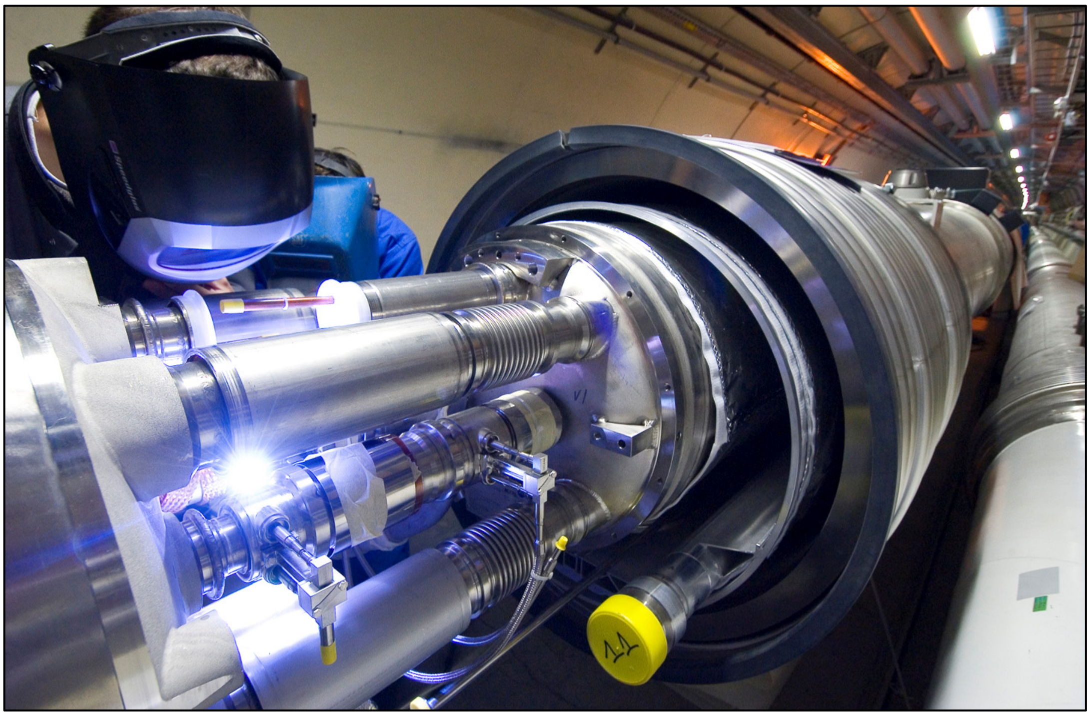

Welcome interconnections in the LHC tunnel.

When I could find voice, I shrieked aloud in agony:
"Either this is madness or this is hell".
"It is neither", cried the voice of the sphere, "It is knowledge".
- Edwin Abbott; *a square in "Flatland; A Romance of Many Dimensions*"

CONTENTS

CONTENTS
(detailed)

4.4 - Parameter Computation

Chapter 9 - Conclusion 226

List of Figures


The assembly of the Short Straight Sections.

If you desire peace of soul and happiness, then believe.
But if you would be a disciple of the truth, then enquire.
- Friedrich Nietzsche

Chapter 1

Chapter 2

Chapter 3

Chapter 4

Chapter 5

Chapter 6

Chapter 7

Chapter 8

Chapter 9

- none -

Appendix

- none -

List of Tables

LHC magnets ready for installation.

Tell me and I'll forget.
Show me and I may not remember.
Involve me and I'll understand.
- Confucius

Chapter 1

Chapter 2

Chapter 3

Chapter 4

Chapter 5

Chapter 6

Chapter 7

Chapter 8

Chapter 9

- none -

Appendix

List of Acronyms

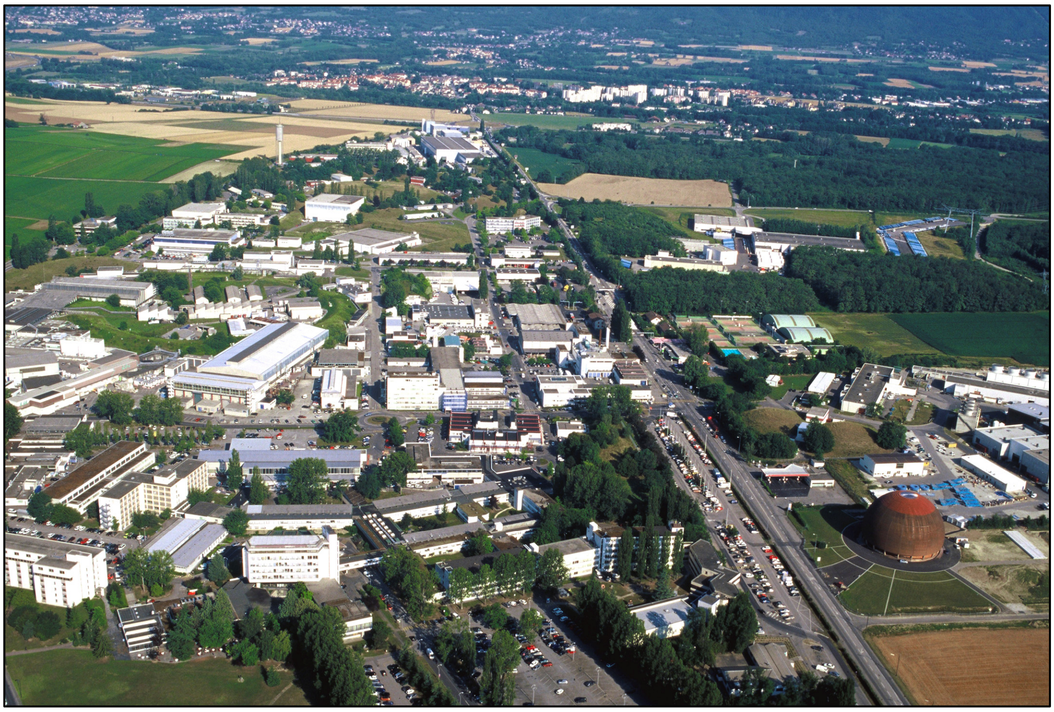

CERN campus (Meyrin site).

Why, sir, there is every possibility
that you will soon be able to tax it!
- Michael Faraday to PM William Gladstone on the usefulness of electricity.

AD - Antiproton Decelerator

ADC - Analogue to Digital Converter

ALICE - A Large Ion Collider Experiment

AT - Accelerator Technology Division

ATLAS - A Toroidal LHC Apparatus

BNL - Brookhaven National Laboratory

CERN - The European Organisation for Nuclear Research

CMS - Compact Muon Solenoid

CNGS - CERN Neutrino to Gran Sasso

DAQ - Data Acquisition

d.c. - Direct Current

DESY - Deutsches Elektronen-Synchrotron

DSP - Digital Signal Processor

FIDEL - Field Description for the LHC

FNAL - Fermi National Accelerator Laboratory

HERA - Hadron Electron Ring Accelerator Facility

ISOLDE - Isotope Separator Online Device

LEIR - Low Energy Ion Ring

LEP - Large Electron Positron Collider

LHC - Large Hadron Collider

LHCb - Large Hadron Collider Beauty Experiment

LINAC - Linear accelerator

MAD-X - Methodical Accelerator Design

MAS - Magnets and Superconductors Group

MBA	- Main Bend Magnets type A
MBB	- Main Bend Magnets type B (main dipole magnets)
MCDO	- Nested Decapole-Octupole Multipole Corrector
MCS	- Sextupole Multipole Corrector
MEB	- Magnet Evaluation Board
ML	- Magnetic length
MO	- Octupole Lattice Corrector
MQ	- Main Quadrupole Magnets
MQM	- Insertion Region Quadrupole
MQS	- Skew Quadrupole Lattice Corrector
MQT	- Tuning Quadrupole Corrector
MQTL	- Long Trim Quadrupole Corrector
MQY	- Insertion region wide Aperture Quadrupole (3.4 m)
MSCB	- Sextupole-Dipole Corrector
MTM	- Magnet Tests and Measurement Group
NMR	- Nuclear Magnetic Resonance
ppm	- parts per million
PCI	- Peripheral Component Interconnect
PELP	- Parabolic Exponential Linear Parabolic
PFP	- Periodic Field Pattern
PGA	- Programmable Gain Amplifier
PS	- Proton Synchrotron
PSB	- Proton Synchrotron Booster
PXI	- PCI Extensions for Integration

SAR	- Successive Approximation Register
SPS	- Super Proton Synchrotron
SSS	- Short Straight Section
RF	- Radio Frequency
RHIC	- Relativistic Heavy Ion Collider
RT	- Real Time
TF	- Transfer Function

Glossary of Symbols

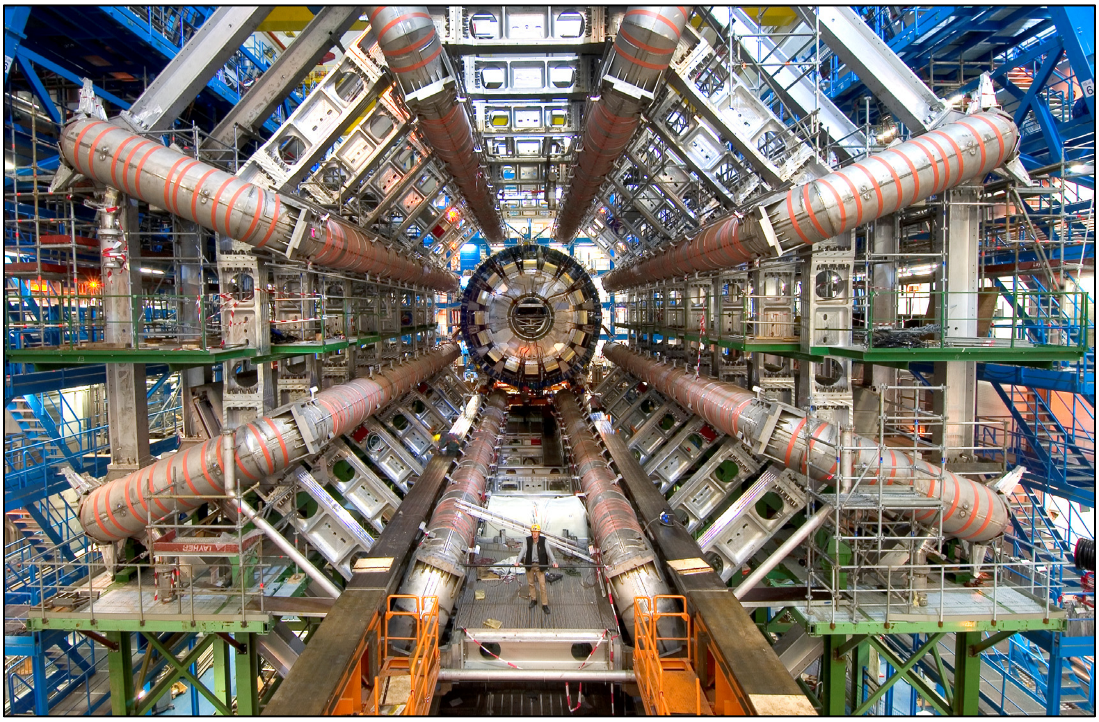

The ATLAS detector being assembled.

> We are at the very beginning of time for the human race. It is not unreasonable that we grapple with problems. But here are tens of thousands of years in the future. Our responsibility is to do what we can, learn what we can, improve the solutions, and pass them on.
>
> \- Richard Feynman

Chapter 1

Q - tune

Q' - first order chromaticity

Q'' - second order chromaticity

Q''' - third order chromaticity

σ - the ratio between the initial amplitude and the beam size

Chapter 2

- none-

Chapter 3

I_0 - current

ϕ - the azimuthal angle

m - order of the main field

n - harmonic order

k - 1,2,3….

r, θ, z - polar coordinates

R_{ref} - the reference radius

b_n - the normalized normal multipole coefficients

a_n - the normalized skew multipole coefficients

B_{ref} - magnitude of the main field at the reference radius

B_n - the non-normalized normal multipole coefficients

A_n - the non-normalized skew multipole coefficients

C_n - the generic non-normalized complex harmonic of order n

$l_{a,n}$ - the effective length of the two dimensional nth order component with amplitude a_n

$l_{b,n}$ - the effective length of the two dimensional nth order component with amplitude b_n

$E_{a,n}$ - the fringe field contribution for the ends for a_n

$E_{b,n}$ - the fringe field contribution for the ends for b_n

g_n^{wc} - warm-cold correlation gradient

Δ_n^{wc} - warm-cold correlation offset

σ - standard deviation

x, y - Cartesian coordinates

Chapter 4

$C_n^{geometric}$ - geometric contribution

C_n^{MDC} - d.c. magnetisation contribution

$C_n^{saturation}$ - saturation contribution

$C_n^{deformation}$ - displacement contribution

$C_n^{residual}$ - residual magnetisation contribution

$\hat{\mathrm{c}}_n$ - the components as stored in the magnet reference database

$I_{geometric}$ - the current value at 5000 A

$\hat{c}_n^{geometric}$ - the geometric component as defined in the magnet reference database

I_{inj} - the current at injection (760 A)

$\hat{c}_n^{DC}$ - the d.c. magnetisation component as defined in the magnet reference database

$\hat{c}_n^{hyst}$ - the hysteresis component as defined in the magnet reference database

$\hat{c}_n^{sat}$ - the saturation contribution as defined in the magnet reference database

C_n^{DC} - the static component

$B_m^{geometric}$ - the geometric contribution to the main field

γ - the geometric coefficient

I - the instantaneous magnet excitation current

$TF^{geometric}$ - the geometric contribution to the transfer function

$c_n^{geometric}$ - the geometric contribution to the normalized harmonics n

g^{wc} - warm-cold correlation gradient

Δ^{wc} - warm-cold correlation offset

ϕ - azimuthal angle

J_c - the critical current density

B - background magnetic field

B_p - the penetration field

M - the magnetisation

M_p - the saturation magnetisation

D_{fil} - the filament diameter

b - the reduced field

t - the reduced temperature

B_c - the upper critical field

B_{co} - the maximum upper critical field

T_{co} - the critical temperature

p,q,h - the pinning exponents

B_m^{MDC} - the d.c. magnetisation contribution to the main field

I_{inj} - magnet excitation current at injection energy

T_{meas} - the measurement temperature

μ_m - the d.c. magnetisation coefficient

I_c - critical current

N - the number of step functions used to model the saturation

σ - iron saturation strength

I_0 - iron saturation current

S - iron saturation current range

I_{nom} - magnet excitation current at nominal energy

ρ - residual magnetisation strength

r - residual magnetisation exponent

I_{high} - the highest measurement current

Q - the number of measurements performed

D_{up} - the number of plateaus performed when the current increases

D_{down} - the number of plateaus performed when the current decreases

$c_n^{beamscreen}$ - the contribution due to the beam-screen

$\bar{c}_n^{av}$ - the average harmonic value along the hysteresis curve

Chapter 5

C_n^{decay} - decay contribution

$C_n^{snapback}$ - snapback contribution

C_n^{MAC} - coupling current contribution

C_n^{AC} - the dynamic component

C_n^{DC} - the static component

I_{inj} - magnet excitation current at injection energy

t_{inj} - the time when injection starts

t - instantaneous time

I - instantaneous magnet excitation current

$\Delta\left(t, t_{inj}, \tau, d\right)$ - the normalised decay

d - the normalized weight of the fast mode of the decay

τ - the time constant

δ - the decay amplitude

t_{inj}^{std} - the time when injection starts

I_{FT} - pre-cycle flat-top current

t_{FT} - pre-cycle flat-top duration

$t_{preparation}$ - preparation plateau duration time

τ_E^n - time constant for flat-top current

τ_T^n - time constant for flat-top duration

τ_P^n - time constant for preparation time

E_0^n E_1^n T_0^n, T_1^n, P_0^n P_1^n - fitting parameters of powering history dependence

$B_m^{decay}(t_{ramp})$ - the change of the main field during the decay evaluated at the time of the beginning of the ramp

$TF^{decay}(t_{ramp})$ - the change of the transfer function during the decay evaluated at the time of the beginning of the ramp

$c_n^{decay}(t_{ramp})$ - the change of the normalized harmonics during the decay evaluated at the time of the beginning of the ramp

ΔI - the current change

θ - the coupling current coefficient.

Chapter 6

f_n^{decay} - the scaling factor

$\Delta_n(t, t_{inj}, \tau, d)$ - the normalised decay

δ - the decay amplitude

I_{FT} - pre-cycle flat-top current

t_{FT} - pre-cycle flat-top duration

$t_{preparation}$ - preparation plateau duration time

τ_E^n - time constant for flat-top current

τ_T^n - time constant for flat-top duration

τ_P^n - time constant for preparation time

E_0^n E_1^n T_0^n, T_1^n, P_0^n P_1^n - fitting parameters of powering history dependence

δ_{std} - the decay amplitude of the standard cycle

$c_n^{decay}(t_{ramp})$ - the change of the normalized harmonics during the decay evaluated at the time of the beginning of the ramp

ΔI - the current change

g_n^{SB} - the linear snapback correlation coefficient

Chapter 7

$\Delta_n(t, t_{inj}, \tau, d)$ - the normalised decay

t_{inj} - the time when injection starts

t - instantaneous time

τ - the time constant

d - the normalized weight of the fast mode of the decay

Δ^{wc} - warm-cold correlation offset

γ - the geometric coefficient

μ_m - the d.c. magnetisation coefficient

p,q,h - the pinning exponents

σ - iron saturation strength

I_0 - iron saturation current

S - iron saturation current range

ρ - residual magnetisation strength

r - residual magnetisation exponent

d - the normalized weight of the fast mode of the decay

τ - the time constant

δ - the decay amplitude

Chapter 8

S_n - total signal of Hall plates

r, θ, z - polar coordinates

V_j^H - the Hall voltage for Hall plate *j*

I_{cs} - the supply current

γ_j - the Hall plate sensitivity

$\vec{p}_j$ - a unit vector orthogonal to the plane of the ideally placed Hall plate

$\delta\alpha$ - pitch angle error

$\delta\beta$ - roll angle error

Δr_j - displacement of Hall plate from the ideal radial position

$\Delta\theta$ - displacement in the θ coordinate

m - number of Hall plates in one ring

Δz_j - displacement of the Hall plate *j* along the z-axis of the magnet

A_{pp} - the periodic field pattern amplitude

t - instantaneous time

L_{pp} - the twist pitch of the cable of the magnet

k - the ring number

R - the number of rings

V_k^H - the total signal including the geometrical error for one ring

V_{probe}^H - the total multipole signal from the Hall probe

$P_{Lpp-Lhp}^H$ - the relative voltage error due to the difference between the period of the periodic field pattern and the period covered by the Hall probe

L_{hp} - the length covered by the Hall probe

$P_{k\Delta z}^H$ - the relative voltage error due to the misalignment of the plane of the ring Δz_k

$\Delta\gamma_j$ - Hall plate j sensitivity error

ΔI_{cs} - the error of the ideal direct current supplied to the Hall plates

V_{offset}^H - the Hall voltage due to the Hall generator offset

V_{offset}^{PXI} - the voltage offset of the PXI data acquisition analogue to digital converter

$V_{ADdrift}^{PXI}$ - the voltage due to the ADC drift

$V_{ADsettling}^{PXI}$ - the voltage due to the ADC settling time

V_{noise} - the voltage due to noise from the whole system

V_n - the average voltage signal from the ring sensors,

V_{offset} - the electronic offset from the amplifiers

K_n - the calibration factor for the voltage of the *n-th* plate sensor read-out

$K_{bucking}$ - the dipole voltage bucking ratio

$K_{non\text{-}linear}$ - a second order correction for the Hall probes non linear sensitivity

Chapter 9

- none -

To my Parents

Chapter 1

Introduction

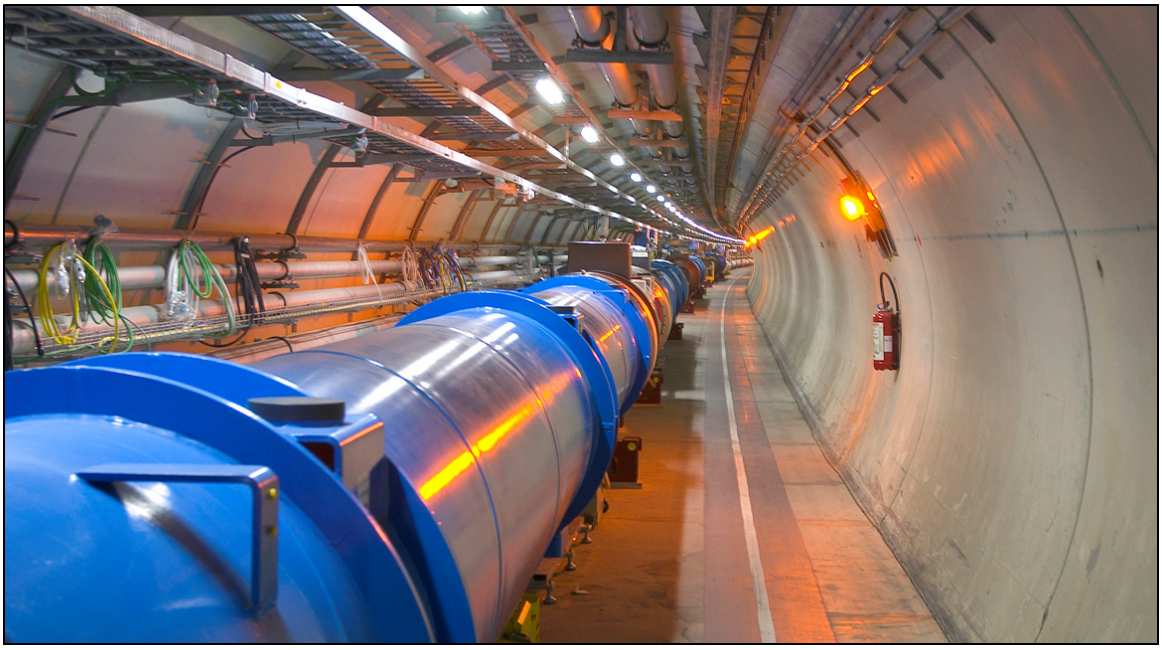

The LHC tunnel.

> We must belong to those who believe, invincibly,
> that science will triumph over ignorance and war.
> - Marie Curie

Chapter 1

Introduction

Currently funded by 20 European member states, the European Organisation for Nuclear Research (CERN) brings together about 7000 scientists from 300 universities of over 80 countries and has consequently become a shining example of international collaboration. CERN's purpose is non-military fundamental research and aims to understand better the laws of nature particularly the composition of matter and the forces that act on it. CERN's flagship project, the Large Hadron Collider (LHC), is currently being assembled and is the largest and most powerful scientific instrument ever to be constructed by mankind.

The LHC is a circular superconducting particle collider and needs a sophisticated control system based on feed-back and feed-forward techniques to satisfy its beam stability requirements. This thesis deals with the core design of the feed-forward control system that will be employed during machine operation. This includes the formulation of a static and dynamic field model, the execution of many magnetic measurements on superconducting magnets which enable the parameter extraction of these models and the implementation of the data acquisition system of an instrument that performs magnetic measurements at the beginning of the magnet ramp-up.

This chapter presents a concise introduction to the LHC and the main components of the machine and recalls the effects of the magnetic field errors on the particle beam. It also highlights the scope of the thesis and illustrates the sequential build-up of the concepts discussed and results obtained in the subsequent chapters.

1.1 - The Large Hadron Collider

The LHC [1], currently under construction at CERN, is a circular particle accelerator crossing the Franco-Swiss border on the outskirts of Geneva. It has a circumference of 26.7 km and is being installed in the underground tunnel that housed the Large Electron-Positron Collider (LEP) up to November 2000. An aerial view of CERN and the surrounding region is shown in Figure 1.1.

The purpose of the machine is to conduct non-military fundamental research to better understand the laws of nature particularly the composition of matter and the forces that act on it. Emphasis is currently given to the search of the Higgs boson and to supersymmetry which are important building blocks in the theory of fundamental particles.

Figure 1.1: Aerial view of CERN and the surrounding region. 3 rings are drawn to show the position of the accelerator complex situated underground. The small ring shows the position of the Proton Synchrotron with a circumference of 600 m, the middle ring is the Super Proton Synchrotron with a circumference of 7 km and the largest ring is the LHC. The Geneva Lake and the Geneva airport can be seen on the right whilst the Jura Mountains can be seen on the left.

The LHC will collide two counter rotating proton beams travelling in a vacuum chamber at a nominal luminosity[1] of 10^{34} cm^{-2}s^{-1} and at a nominal centre of mass energy of 14 TeV. In addition to protons, heavy ions will also be brought into collision. Experiments with Pb nuclei (Z = 82) will reach luminosities of up to 10^{27} cm^{-2}s^{-1} with collision energies of up to 1150 TeV.

The basic layout of the machine is shown in Figure 1.2. It consists of eight straight sections each approximately 528 m long available for experimental insertions and utilities.

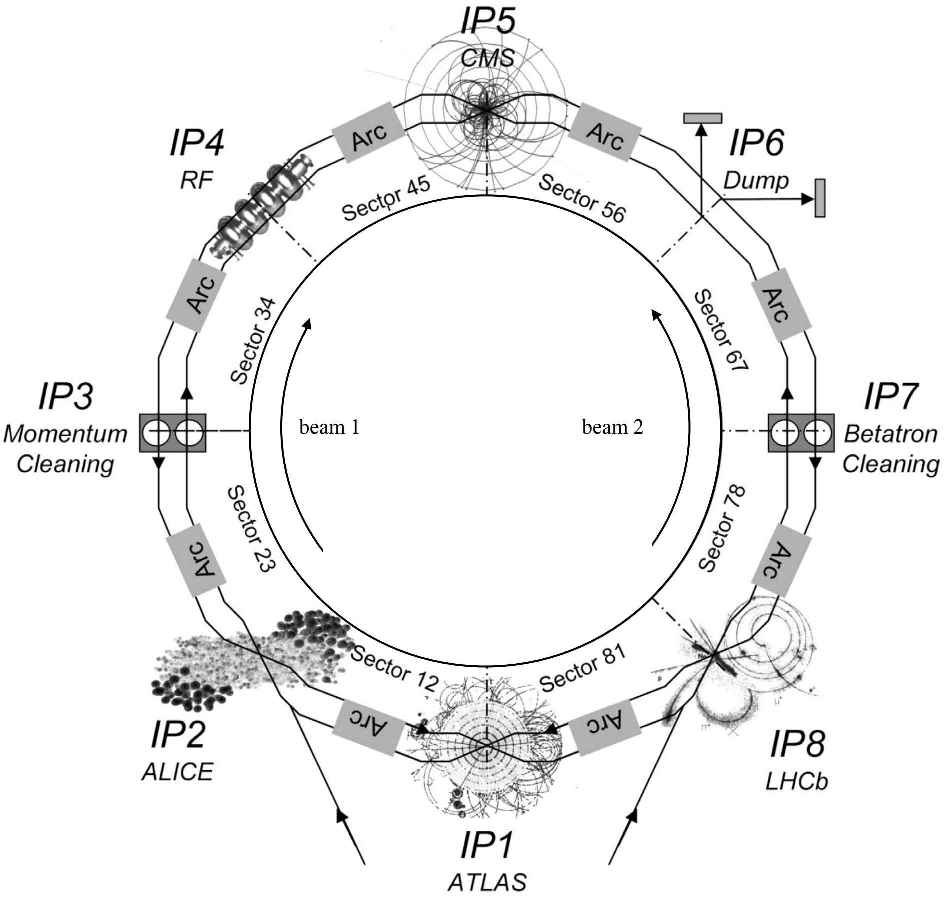

Figure 1.2: The layout of the LHC.

---

[1] The luminosity is a measure of the potential number of particle interactions for a colliding beam. When two bunches collide, the luminosity is defined as: L = $(N^2 f_b)/A$ where N is the number of particles per bunch, f_b is the bunch frequency and A is the transverse beam area crossing. Beam control aims at maximising the luminosity.

A Toroidal LHC ApparatuS (ATLAS) [2] and the Compact Muon Solenoid (CMS) [3] are the larger experiments located at point 1 and point 5, respectively. The Large Hadron Collider Beauty experiment (LHCb) [4] and A Large Ion Collider Experiment (ALICE) [5] are other experiments located at point 8 and point 2, respectively. The latter straight sections also contain the injection systems. The beams cross from one ring to the other only at these four locations. The remaining four straight sections do not have beam crossings. Insertion regions 3 and 7 contain the two beam collimation systems [6]. The RF acceleration systems [7] are placed at point 4. The straight section at point 6 contains the beam dump insertion.

The accelerator operation is divided into three phases:

a. *injection:* during which the beam is prepared by the various pre-accelerators (known as the *injector chain*) and injected into the LHC at a low energy.
b. *acceleration:* during which the beam is accelerated to nominal energy.
c. *storage:* during which the beam is circulated at nominal energy for as long as possible and is made available for physics experiments.

As shown in Figure 1.3, the injector chain [8] of the LHC is formed by the existing CERN infrastructure of accelerators i.e. the LINear ACcelerator (LINAC), the Proton Synchrotron Booster (PSB), the Proton Synchrotron (PS) and the Super Proton Synchrotron (SPS). This imposes an injection energy of 450 GeV thus requiring a large dynamic range in the LHC energy.

The acceleration of the bunched particles to the LHC nominal energy is performed in one insertion of the ring using superconducting Radio Frequency (RF) cavities [7]. The principle of acceleration by these resonating structures is based on an alternating electrical potential which acts on the particles as an accelerating field. The radio frequency is an integer multiple of the particle revolution frequency around the machine and changes in proportion to the varying revolution frequency.

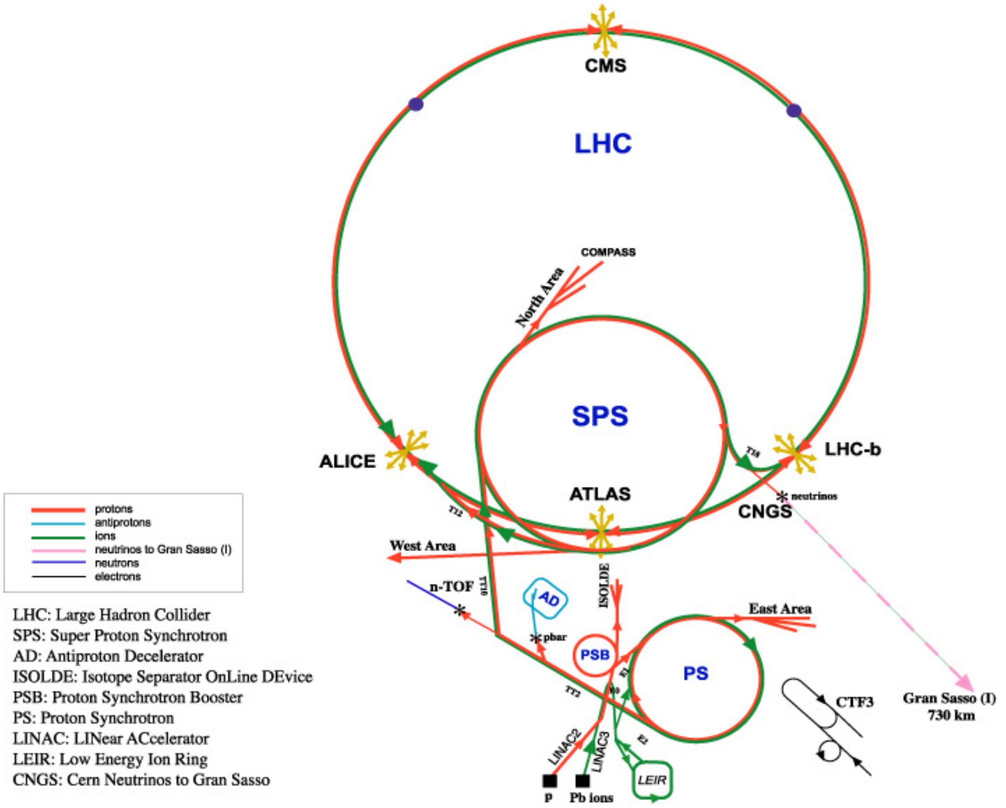

Figure 1.3: The CERN accelerator complex.

1232 superconducting dipole magnets [6] bend the particle beam along the accelerator trajectory by using strong magnetic fields. For hadron accelerators, the maximum particle energy is limited by the strength of the magnetic field keeping the particles in their orbit. The use of superconducting magnets instead of resistive magnets has unique advantages in this respect since the vanishing electrical resistance of superconducting coils opens the way to higher currents and higher magnetic fields. The equivalent operating cost is also reduced significantly.

In addition to the curving of the beam with the dipole magnets, 392 superconducting quadrupole magnets [6] focus it to keep the particles from diverging from the centre of the beam pipe. The field shape of a quadrupole magnet is such that it is zero on the axis of the device but rises linearly with distance from the axis. If a quadrupole magnet focuses the beam along the horizontal plane, it defocuses it along the vertical plane. However, if the quadrupole magnet polarity is inverted (or if the magnet is rotated by 90°), it defocuses the beam along the horizontal plane and focuses it along the vertical plane. Focusing and defocusing quadrupoles are therefore alternated in the accelerator.

Many other small high order magnets are placed along the ring to correct for the magnetic field errors of the larger main magnets. The LHC machine is equipped with corrector magnet circuits that include [9]:

a. horizontal and vertical orbit correctors.

b. trim and skew quadrupole correctors.

c. normal and skew sextupole correctors.

d. normal and skew octupole correctors.

e. normal decapole correctors.

As was seen in Figure 1.2, the magnets will be installed with an 8-fold symmetry in the arc sectors composed mostly of regular cells (23 per sector), dispersion suppressor and matching sections and straight sections before the experiments [6]. The regular arc cells are composed of six dipole magnets, two alternating (focusing/defocusing) quadrupole magnets and many corrector magnets as shown in Figure 1.4.

Figure 1.5 shows the LHC dipole magnet with a structure based on a cost-saving 'two-in-one' design, where two beam channels with separate coil systems are incorporated within the same magnet. The stability of the coils is provided by a support structure of laminated collars which fixes them to a precisely defined geometry. The collared coils are integrated inside an iron yoke which also increases the field by about 19 per cent.

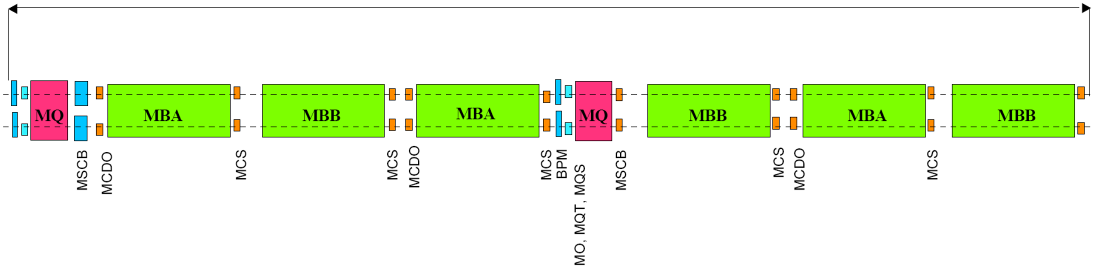

Figure 1.4: Schematic layout of one regular LHC arc cell. MBB and MBA are the main dipole magnets while MQ are the main quadrupole magnets. MQT is a trim quadrupole corrector, MQS is a skew trim quadrupole, MO is a lattice octupole, MSCB is a sextupole and an orbit corrector. MCS are sextupole spool pieces and MCDO are octupole and decapole spool pieces.

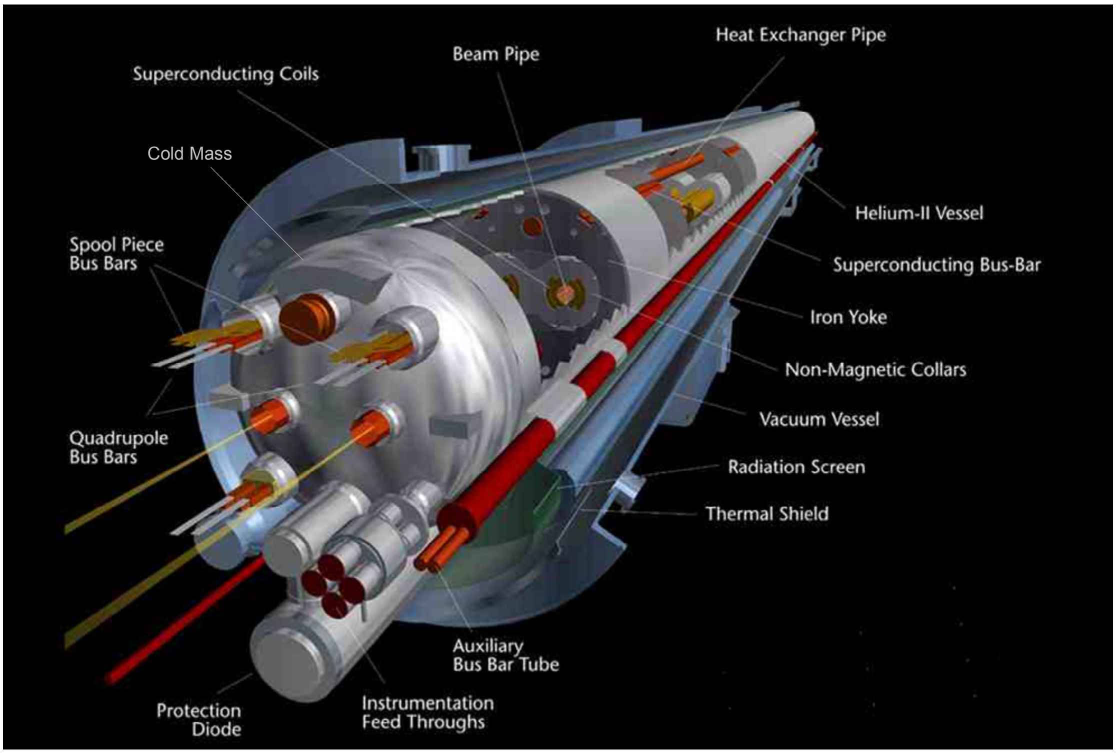

Figure 1.5: The 15 m long LHC twin-aperture dipole.

The iron yoke also shields the field so that no magnetic field leaves the magnet. Located in grooves in the iron yoke, bus bars accommodate the cables to power the magnets of the arcs which are connected in series. The so-called ‘cold-mass’ is immersed in a bath of superfluid liquid helium that acts as a heat sink. The helium is at atmospheric pressure and is cooled to 1.9 K by means of a heat exchanger tube. The cold mass is delimited by the inner wall of the beam pipes on the beam side and by a cylinder on the outside. The iron yoke, the collars and the cylinder compress the coil. All three withstand the Lorentz forces during excitation limiting coil deformations and avoiding conductor displacements. The cylinder improves the structural rigidity and longitudinal support and contains the superfluid helium. The magnetic length at 1.9 K and at nominal field is around 14.3 m. The inner coil diameter at 293 K is 56 mm.

During acceleration, the energy gain of all the particles is matched with the rising magnetic field. To do this, the RF cavities and the superconducting magnets all work in synchronisation to ensure that the beam orbit remains the same throughout the injection, the acceleration and the storage phases. Accelerators that function in this way are hence classified as *synchrotrons*.

1.2 - Beam Dynamics

Beam stability requirements impose stringent tolerances on the field quality of the LHC magnets [10]. They consider constraints on the energy and orbit, tune, coupling, second and third order chromaticity as well as the available corrector strength and considerations of dynamic aperture.

1.2.1 - Energy and Orbit

The particles enter the machine with a trajectory spread with respect to the ideal orbit. Unless restored back to the reference trajectory by the focusing and defocusing quadrupoles, the transverse displacements of the beam will result in particles hitting the beam pipe. As a result of the focusing and defocusing quadrupole fields, every particle oscillates around the ideal orbit in the so called *betatron oscillating motion* [11]. The envelope of these oscillations follows the betatron function $\beta(s)$, where s is the longitudinal coordinate along the designed orbit of the machine.

Particles also deviate from their orbit as a result of field errors in the magnets. The beam size is defined as the width σ of the Gaussian that approximates the profile of the beam density. The peak orbit excursion which is related to the random error in the main field of the dipoles should be inferior to 0.4 σ in the arc and 0.25 σ (dynamic change) in the cleaning sections. The orbit excursion has to be smaller than 4 mm to preserve the mechanical acceptance of the ring at the injection level.

Particles also enter the machine with a momentum spread. In dipole magnetic fields, particles with a different momentum exhibit a different orbit curvature with respect to the nominal trajectory. The energy variation $\Delta E/E$ is related to the momentum spread Δp about the nominal value p_0 and is affected by the systematic error of the main dipole field.

1.2.2 - Tune

The tune is defined as the number of betatron oscillations executed by particles travelling one revolution around the ring. The focusing and defocusing periodic quadrupole fields determine the betatron function as well as the tune [12].

1.2.3 - Coupling Resonances

Betatron motion in a circular accelerator occurs in both the horizontal and vertical plane featuring two tune values Q_x and Q_y. The influence of a tune change in one plane with respect to the other is known as the tune coupling [12] and to a first approximation is caused by a skew quadrupole field.

1.2.4 - Chromaticity

The charged particles have a momentum dispersion around the design momentum, which causes a shift of the equilibrium orbit and changes the optic parameters. In accelerator terminology chromaticity defines the changes of the tune with respect to the beam energy. There is a distinction between the natural chromaticity of the ring and the chromaticity arising from the persistent-current sextupole in the superconducting dipole magnets. The natural chromaticity is derived from the energy dependence of the quadrupole focusing i.e. the chromaticity the ring would have without sextupole magnets [12].

The total chromaticity in a superconducting ring is expressed by the third order Taylor expansion of the machine tune in terms of the particle momentum error:

$$Q = Q_0 + Q' \cdot \left(\frac{\delta p}{p_0} \right) + \frac{1}{2} \cdot Q'' \cdot \left(\frac{\delta p}{p_0} \right)^2 + \frac{1}{6} \cdot Q''' \cdot \left(\frac{\delta p}{p_0} \right)^3 \qquad (1.1)$$

Q_0 is the natural chromaticity of the ring and is related to the relative variation of the main dipole field. In superconducting proton rings, the natural chromaticity is small compared to the one arising from the field component errors.

1.2.3.1 - First Order Chromaticity

The first order chromaticity can be defined as the ratio of the tune deviation from the reference and the momentum spread in the particle beam:

$$Q' \approx \frac{\Delta Q}{\Delta p / p_0} \tag{1.2}$$

The total chromaticity increases proportionally with the sextupole field error in the main magnets.

1.2.3.2 - Chromatic Coupling

A skew sextupole component leads to a momentum dependent coupling between the horizontal and vertical tunes, or the so called *chromatic coupling* [12].

1.2.3.3 - Second Order Chromaticity

The second order chromaticity is defined as the coefficient of the parabolic term in the tune spread caused by the energy dispersion generated by an octupole field over one arc of the LHC. In the absence of linear chromaticity:

$$Q'' \approx 2 \frac{\Delta Q}{\left(\Delta p / p_0 \right)^2} \tag{1.3}$$

This term is generated by the octupole multipole average over one arc of the LHC.

1.2.3.4 - Third Order Chromaticity

At injection field, the systematic decapole error causes a third order chromaticity. In the absence of first and second order chromaticity the third order chromaticity can be written as:

$$Q'' \approx 6 \frac{\Delta Q}{\left(\Delta p / p_0 \right)^3} \tag{1.4}$$

1.2.5 - Dynamic Aperture

The dynamic aperture is the maximum initial oscillation amplitude that guarantees stable particle motion in the presence of field nonlinearities over a given number of turns. The dynamic aperture is expressed as the ratio between the initial amplitude and the beam size σ. 12 σ is considered to be safe for the LHC. Multipoles of order 3 and higher affect the size of the dynamic aperture.

1.2.6 - Beam Requirements

The beam requirements are shown in Table 1.1 [13-14]. In the beginning during machine commissioning, the requirements will be moderate [15]. However, the requirements will become more stringent as the machine approaches nominal operation with nominal beam intensity.

Table 1.1: The beam dynamics requirements for commissioning and nominal operation with a nominal intensity beam.

	commissioning	nominal operation
RMS orbit excursion	4 mm	4 mm
Energy variation	0.0002	0.0001
Tune change (ΔQ)	0.03	0.001
Coupling	0.1	0.001
Chromaticity	Q’>–15 (units)	Q’= 2; ΔQ’= ±1 (units)

1.3 - Scope of the Thesis

From the history of accelerator operation and from measurements that were performed on LHC prototypes and first pre-series LHC main dipoles before the start of this work [16], it was concluded that active control of the machine is required to compensate for the field changes during the proton beam injection and acceleration. The stability requirements during machine operation impose very stringent constraints on the magnetic field quality of the magnets. The field perturbations which vary both with current and time must be controlled to a very high precision. This type of control needs a feed-forward mechanism to accurately forecast the magnetic field in the accelerator.

The research work carried out and presented in this thesis primarily deals with the *FIeld DEscription for the Large Hadron Collider (FIDEL)*. It involves the development, testing and adaptation of models of a physical basis or empirical nature to describe the behaviour of the LHC superconducting magnets during its operation. The feed-forward control system heavily relies on these formulations and they therefore must provide good modelling of the LHC superconducting magnets. The model parameters are mostly based on magnetic measurements which are performed in cryogenic conditions and which are also part of this work. Emphasis is put on the main dipole magnets since measurements on these were more abundant and the effects of their harmonic variations significantly perturb the beam. However, the models are also applied to the quadrupole magnets and to one family of correctors so as to demonstrate the model robustness and adaptability.

The research work also includes the implementation of a fast but precise data acquisition system for a Hall plate based instrument targeted at performing magnetic measurements at the beginning of the ramp-up. The data obtained from these measurements are extensively used to establish the model of the main dipole harmonic variation in this part of the machine cycle.

The thesis is presented as a sequential build-up of the magnetic models and finally also describes the work performed on the data acquisition of the Hall plate based instrument.

In chapter 2 the scope of FIDEL is outlined, followed by a description of the evolution of the concepts it employs. This is done by recalling the different solutions adopted in the other major superconducting machines and then describing the methodology that will be used for the LHC.

Chapter 3 recalls the representation of the magnetic field in a magnet aperture. A description of the magnetic measurements performed in cryogenic conditions on which the magnetic models are mostly based is also presented. This is followed by the establishment of a warm-cold correlation that extrapolates measurements at warm to cold conditions. The desired prediction capability of FIDEL is also presented.

Chapter 4 provides a detailed description of the different magnetic field components that are solely dependent on the magnet excitation current. It provides a mathematical description of the effects based either on a physical understanding or on empirical formulae when the effects are too complex to be described analytically. At the beginning of this work, some crude models and procedures of adopting them had already started being developed by Bottura [17] but these needed to be modified, improved upon and implemented on LHC series magnets. Hence the current dependent modelling results of one sector of the machine are presented at the end of the chapter.

Chapter 5 is dedicated to a detailed description and mathematical formulation of the magnetic field components that are dependent both on current and on time. The dependence of the variation of the magnetic field on the magnet powering history is also included in the model, hence providing a solution for the non reproducibility of the magnetic state from cycle to cycle.

Since the machine magnetic state as predicted by the models is expected to deviate from what is actually found in the machine, the models need to be flexible enough to adapt to these changes. The mechanisms that provide this flexibility are referred to as scaling laws and these are described in detail in chapter 6.

At the beginning of this study, preliminary measurements and modelling by Bottura [18] were already in progress and proved to be a good base for the snapback model which is explained and presented in part of chapters 5 and 6. However, being a critical part of the model, more measurements were required with a better accuracy and with a greater reliability. Additional measurements performed as part of this thesis were only possible thanks to the work presented in chapter 8 which will be highlighted in turn.

Several other aspects that should be considered in the LHC magnetic field model are presented in chapter 7. These include discussions on ways of grouping the magnets in the machine to reduce the random error of the magnetic field. This is important since it indicates whether different models should be considered for different parts of the LHC. Other aspects such as the effect of magnet aging and the effect of the Lorentz forces on the field quality after many excitation cycles are also discussed. The field model is also tested on other magnet types to demonstrate its adaptability and robustness.

The data acquisition system developed for the Hall plate based instrument that measures the fast variations of the sextupole and decapole field harmonics at the beginning of ramp-up is discussed in chapter 8. The instrument's principle of operation, its mechanical arrangement and its uncertainty sources are described. The new digital compensation system is compared to the previous analogue compensation system used by Masi [19] followed by a description of the data analysis procedure and the results obtained in dedicated cryogenic magnetic measurements.

Finally a short discussion and evaluation of the thesis results is presented as a conclusion in Chapter 9. The thesis structure and logic of arguments is illustrated in Figure 1.6.

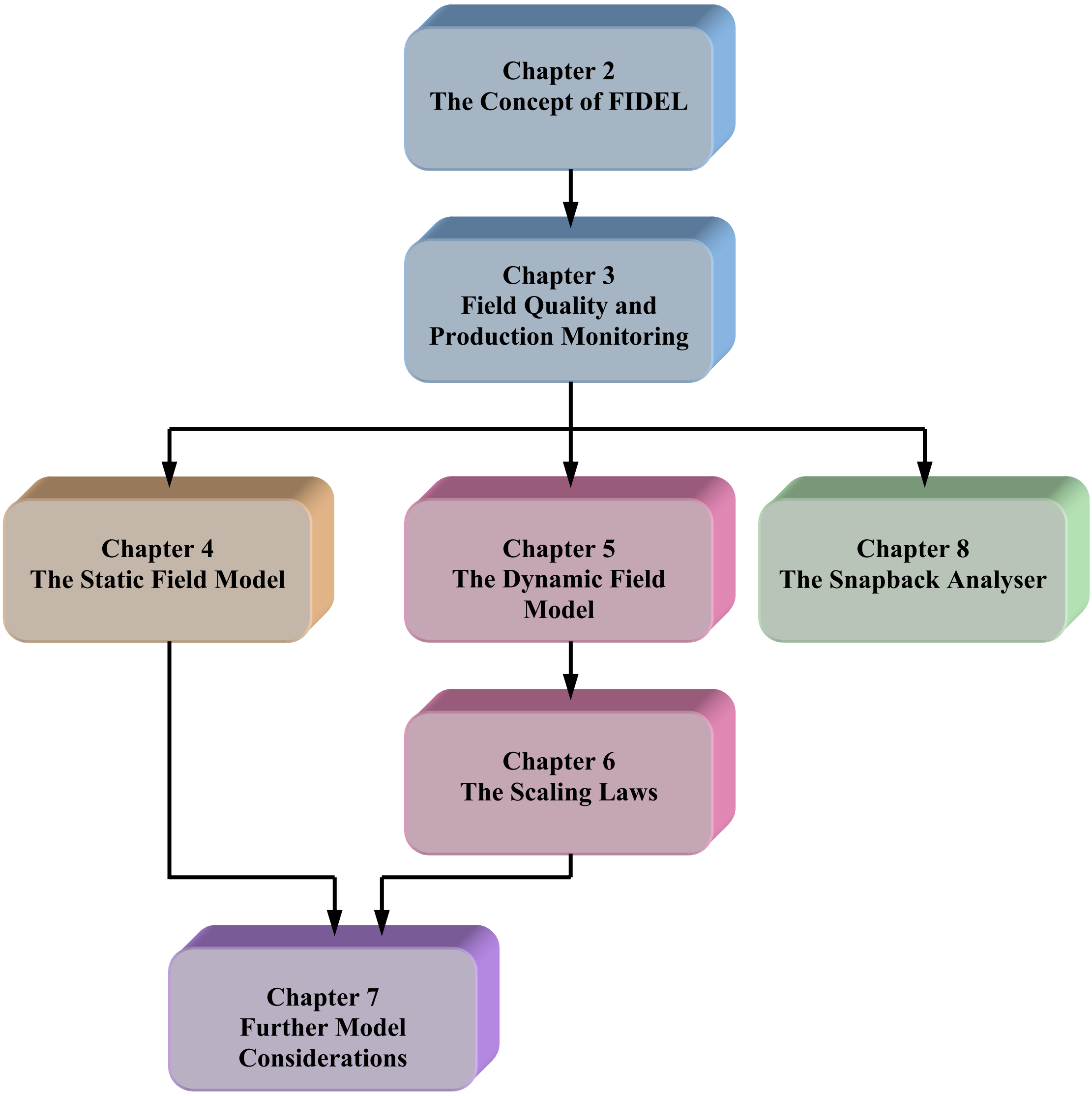

Figure 1.6: Schematic of the thesis structure.

Chapter 2

The Concept of FIDEL

CERN control centre.

> To see a World in a Grain of Sand
> And a Heaven in a Wild Flower,
> Hold Infinity in the palm of your hand
> And Eternity in an hour.
> - William Blake in "*Auguries of Innocence*"

Chapter 2

The Concept of FIDEL

Superconducting colliders require powerful control systems to correct for field variations that result from the inherent properties of the superconducting magnets. If not corrected with high speed and precision, these field changes affect the particle beam considerably and therefore reduce the performance of the machine.

Unfortunately, a feed-back control system based on beam measurements has limited capabilities and is not good enough to solely provide the required error compensation. A system based on feed-forward control is therefore required to reduce the burden on the feed-back system by forecasting what the field variations will be during particle injection, acceleration and collision within a residual error comparable to beam control requirements.

FIDEL is the main part of the feed-forward mechanism consisting of a static and a dynamic magnetic field model. These models are based on the knowledge gained from magnetic measurements on the main superconducting magnets during the machine construction. If required, they will be backed by ad hoc measurements on off-line magnets that will widen the parametric space of the model when needed.

This chapter highlights the motivation of the FIDEL project and describes the evolution of the concepts it employs by identifying the different solutions adopted in the other major superconducting machines. These paradigms, including their scope and implementation method, are outlined.

2.1 - Motivation

In a particle accelerator, particle injection and acceleration to collision energy should be performed with the least particle loss possible and with minimal beam perturbations. This notwithstanding the various non-linearities, the different response times and the distinctive transfer functions of the myriad of equipment.

In superconducting particle accelerators, these problems represent a harder challenge particularly due to field quality issues caused by specific properties of the superconducting cables. These sources of errors can be categorized into two classes:

a. Static multipole variations which are reproducible and which are solely current dependent.
b. Dynamic multipole variations which, to a certain extent, are not reproducible and are dependent on both current and time. These arise particularly from an inhomogeneous current distribution in the superconducting cable and are particularly important in the sextupole harmonic which causes a change in the linear chromaticity of the beam.

Furthermore, particle losses can interrupt machine operation if they exceed the quench level of the superconducting magnets.

For a control system to function effectively, it is clear that the field imperfections in the system must be known with the desired accuracy. A standard control scheme would require direct diagnostics on the beam to employ negative feed-back and hence power the corrector circuits accordingly. However, a correction scheme solely based on beam feed-back is far from ideal in particle accelerators particularly because [20]:

a. some beam based measurements can be destructive since they perturb the beam dynamics and cause undesirable emittance growth [21].
b. some of the beam dynamics parameters are not easily determined from beam measurements. This is particularly the case for the dynamic aperture that may be affected by high order multipoles such as the normal decapole in the main bending dipoles [22].

c. the direct beam diagnostic bandwidth may not be wide enough for the multipole magnitude variation even for optimized ramps [23]. For example in the case of the LHC, the sextupole change in the main dipoles during snapback may require a chromaticity measurement that is an order of magnitude faster than the present instrumentation capabilities.

Therefore, due to the limitations in the beam instrumentation, the LHC requires a complementary system that reduces the burden on the beam based feed-back [24].

2.2 - Experience from Running Machines

The three major operating superconductor accelerators, namely, the Tevatron, the Hadron Electron Ring Accelerator Facility (HERA) and the Relativistic Heavy Ion Collider (RHIC) use different mechanisms to obtain the information needed to implement correction. These systems are based on the same principle but are employed with different levels of complexity according to the magnitude of the errors inherent in the machine and the respective beam requirements.

2.2.1 - RHIC

The simplest case can be found at RHIC at Brookhaven National Laboratory (BNL) located on Long Island in New York, USA, where the variation of the sextupole harmonic at injection produces a linear chromaticity variation of 2 to 3 units [25]. Since the requirements for the beam dynamics are of the same order, the correction system can rely mainly on beam-based measurements. The RHIC team also maintains a magnetic field quality database based on warm (i.e. at room temperature) and cold (i.e. in cryogenic conditions) tests which was primarily created for production monitoring. This database forms the base of the static field model [26] that is embedded within a structured description of the accelerator lattices and is consequently used in tracking studies off-line. However, this static model was also interfaced to the RHIC on-line control system as a feed-forward ramp generator for the corrector circuits [27-29].

2.2.2 - Tevatron

The Tevatron at Fermi National Accelerator Laboratory (FNAL) located in Batavia in Illinois, USA, experiences a change of 45 units of linear chromaticity on the injection plateau [30] due to variations in the sextupole harmonic. As is done in RHIC, apart from beam based feed-back, the control system is equipped with an on-line feed-forward field model. This model, however, not only predicts the static multipoles variation during the current ramp but also predicts their dynamic variation in time during the injection plateau [31-32]. Some simple corrections were also considered to account for the difference in the multipole variation due to the magnet powering history [30]. In addition to this, the infrastructure at the Tevatron provides the possibility of upgrading the model by measuring magnets off-line and studying their behaviour under special conditions. Together, the feedback and feedforward control system provide a chromaticity correction to within ± 2 units.

2.2.3 - HERA

HERA at the Deutsches Elektronen-SYnchrotron (DESY) located in Hamburg, Germany, has the most sophisticated mechanism to correct for the errors due to the persistent currents [33] in the superconducting dipole magnets. In this machine, the change of the linear chromaticity because of sextupole drift in the dipole magnets is in the order of 30 units [34]. This variation is controlled by using two on-line reference magnets (one for each manufacturing line) which track the machine since they are electrically connected in series to the superconducting ring [35]. These magnets are equipped with:

a. Morgan coils to measure the sextupole variation at 5Hz.
b. a Nuclear Magnetic Resonance (NMR) probe that measures the dipole field on the current plateau.
c. stationary pick-up coils which measure the dipole field during the ramps.

Real-time measurements on these magnets using these instruments provide closed loop feed-back to the corrector circuits of the machine. However, since this procedure involves many active components, HERA is also equipped with look-up tables that serve the same purpose of the feed-forward field model in the Tevatron. The look-up tables also have stored increments of the sextupole field during the injection plateau which are tweaked according to the plateau's duration. This system provides a chromaticity correction to within ± 6 units [36].

Table 2.1 shows the operation parameters of the three main superconducting accelerators in operation together with the foreseen operation parameters of the LHC [37]. It should be noted that the ratio between the chromaticity control requirement and the expected chromaticity drift at injection is much tighter for the LHC.

Table 2.1: The main operation parameters for the three major superconducting accelerators, and the foreseen operation parameters for the LHC.

	RHIC	Tevatron	HERA	LHC
Injection field (T)	0.4	0.6	0.22	0.537
Chromaticity drift during injection plateau (units)	2 to3	45	30	90
Control requirement on first allowed harmonic (sextupole in units)	0.5	0.1	0.2	0.02

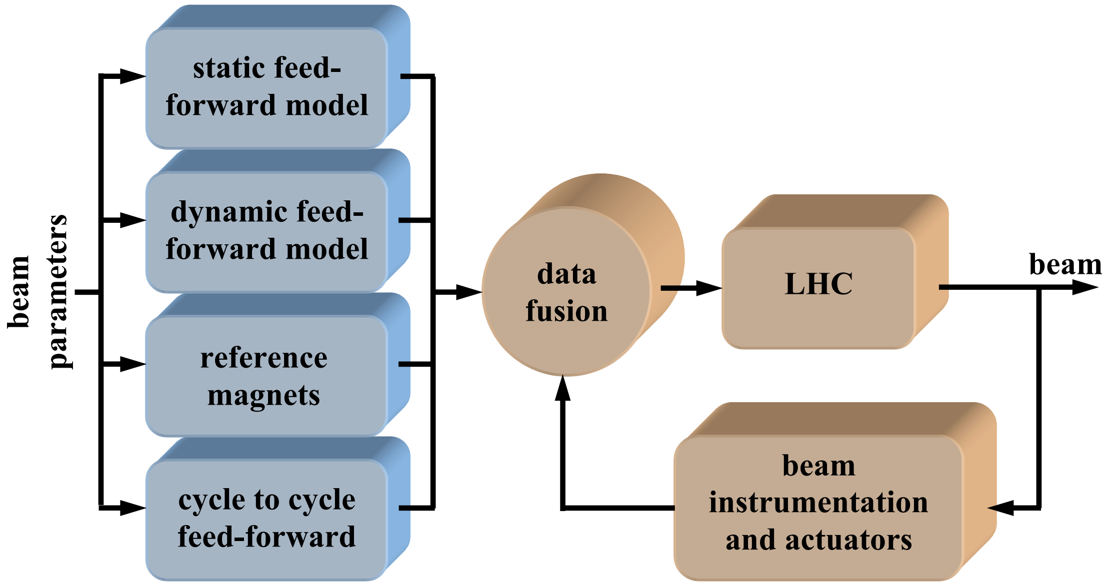

Figure 2.1: The paradigms for an LHC hybrid control system. The reference magnets can be off-line or on-line or both.

2.3 - Control Paradigms Considered for the LHC

The orders of magnitude presented above, point to the fact that a control system solely based on one control mechanism may be too demanding especially for the stringent requirements of the LHC. Hence the idea is to adopt a hybrid control system based both on feed-forward and feed-back control. The available paradigms for such a system are shown in Figure 2.1 and can be summarised as follows:

a. ***Feed-Forward control***:

i. *Static Feed-Forward Model*: this is the field model that is closest to the RHIC paradigm and is based on cold and extrapolated warm data from magnetic measurements primarily intended for production monitoring. This model solely compensates for the reproducible current dependent multipole variation. It is a purely computational system with pre-programmed ramp settings and is rather limited in prediction capability particularly when it comes to predicting dynamic effects and off-nominal conditions. The hardware requirements for this paradigm are minimal merely requiring a processor or microcontroller to store and supply the ramp settings on demand.

ii. *Dynamic Feed-Forward Model*: this is the field model that is closest to the Tevatron paradigm. It is an add-on to i above and uses the magnetic measurements at cold to predict the dynamic time dependent multipole variations. This model also takes into consideration the dependence of the multipole variation due to the magnet powering history and the injection duration. It hence adapts to changes in the machine operation scenario but does not map the complete space of operation variants. This system is purely computational but is much more powerful than i above. The hardware requirements for this paradigm are also negligible merely requiring a processor or microcontroller to store and supply the ramp settings on demand.

iii. *Off-line reference magnets*: this is a solution still within the Tevatron paradigm and is very similar to ii above with the difference that some magnets and the related infrastructure are available to perform cold magnetic measurements when needed. This system has the capability of exploring specific operation scenarios that were not considered prior to machine commissioning and hence can increase the space of operation variants of the dynamic field model. The latter is possible provided the reference magnets are representative of the entire magnet population. This system is also computational but is also experimental to some degree. It is a versatile system but requires the infrastructure of the test installation.

iv. *On-line reference magnets*: this solution is closest to the HERA paradigm and is similar to iii above with the difference that the reference magnets are always running and are tracking the machine current excitation. The on-line reference magnets are continuously measured in real-time and provide information for the field model updates immediately, with no delay. This allows the model to be much more flexible and adaptable on-line to diverse machine operation scenarios. This system represents the best possible feed-forward scenario. However, such a system would not only require the testing infrastructure but would also require a robust instrumentation system that is capable of running for a long period of time without servicing as well as supplying measurements in real-time. As in iii above, the dynamics of the reference magnets must be representative of the entire magnet population within the required precision.

v. *Cycle to Cycle Feed-Forward*: this paradigm uses the information obtained from the beam instrumentation in one cycle and applies this information for correction in the next cycle.

b. ***Feed-Back control***: Once the feed-forward control system meets the requirements to put the machine in a status suitable for beam injection, the feed-back control system can take over. This type of closed-loop control uses the beam-based measurements to determine the errors on the beam and hence corrects them in real-time [38].

2.4 - The LHC Feed-Forward Control System

The static and dynamic feed-forward paradigms, which together are commonly known as the *field model*, are applied in the case where the expected perturbations and machine responses are well known for a given machine operation cycle. This is foreseen to be the case for the great majority of the runs since the machine will have very strict cycling and ramping policies. The two cycles used during the *series* cold magnetic measurements namely the *loadline* and the *standard LHC cycle* (also known as the *standard machine cycle*), had their parameters fixed to maximize the knowledge of the magnetic response and the multipole variations of the magnets within a fixed domain. As highlighted previously, the dynamic feed-forward paradigm is also designed to adapt (within specific bounds) to different machine cycles based on an extended cold magnetic measurement programme. However, it should be pointed out that apart from being limited to the domain explored in magnetic measurements, the field model is also limited by:

a. the absolute uncertainty and sensitivity of the magnetic measurements on which it is based.
b. the confidence interval obtained from the limited sample of magnetic measurements performed during production.
c. the error between the model and the magnetic measurements.
d. the reproducibility of the magnet field in the magnets.

In the case of the off-line and on-line reference magnet paradigms, it is particularly crucial to use reference magnets that represent the behaviour of the entire magnet population well. It is also important to reproduce the exact conditions of the domain that is being studied. The latter includes the temperature of the magnet population, the instantaneous current excitation and the powering history.

Of course, the best hybrid control system is the one that includes all of the paradigms and that intelligently fuses all the information together to extrapolate it with the required frequency and with the required precision. This allows the limitations of one paradigm to be compensated by the strengths of the others. Initially, all the feed-forward paradigms were planned to be included in the LHC control system and were the basis of what was commonly known as the *multipoles factory* [39].

However, the decision was taken to adopt all the control paradigms mentioned above except for the on-line reference magnets paradigm. This decision was taken because:

a. the resources that need to be employed to run an on-line reference magnet system are significant [40].
b. the guarantee that on-line reference magnets can be representative of the entire magnet population might be limited [34].
c. the understanding of the static and dynamic responses of the superconducting magnets has increased substantially over the last few years. This is the result of the group effort of several researchers most notably at FNAL, DESY, BNL and CERN (including this work) and several other laboratories worldwide.

The off-line reference magnets paradigm has been approved provisionally and its necessity will be revised after the LHC commissioning.

Therefore, conceptually, the multipoles factory has now evolved into an open-loop system that heavily relies on a static and dynamic field model, supported by off-line reference magnets, and that complements the beam instrumentation. This open-loop system is now known as *FIDEL*.

Once the field imperfections in the main superconducting magnets (dipoles, main quadrupoles and insertion region quadrupoles) are determined, the control system will excite different families of high-order corrector magnets to compensate them.

2.5 - Conceptual Details of FIDEL

From the discussion above, the aim of FIDEL is to:

a. use the modelled transfer function to generate the current ramps and load them into the power supplies for the main dipole, the main quadrupole and the insertion region quadrupole magnets.

b. forecast the field imperfections (i.e. multipole harmonics) of the main dipoles, the main quadrupoles and the insertion region quadrupoles with a target accuracy comparable to beam control requirements. (The residual error will be defined in more detail in chapter 3).

c. supply the corrector circuits transfer functions to the control system. The control system will hence transform the forecasted field imperfections into the equivalent current ramps that must be forwarded to the corrector circuits.

A schematic of the use of FIDEL in LHC control is shown in Figure 2.2.

To do this, FIDEL must satisfy a number of requirements. It should:

a. implement the field imperfection forecast in the current (static) and time (dynamic) domain for the standard LHC cycle.

b. extend the forecast to other pre-defined accelerator cycles.

c. extend the understanding obtained from the sampled measured magnets to the magnets on a sector by sector basis.

d. be continuous in its domain of validity and not be susceptible to discontinuities.

e. be versatile enough to allow adjustment of the model parameters from beam-based measurements.

The inputs supplied by the LHC control operation are the instantaneous time from the global positioning system clocks, the operating current, the parameters of the powering history and the average temperature of the magnet population. The predicted magnetic field properties are returned in terms of current, time and the complex magnetic field harmonics.

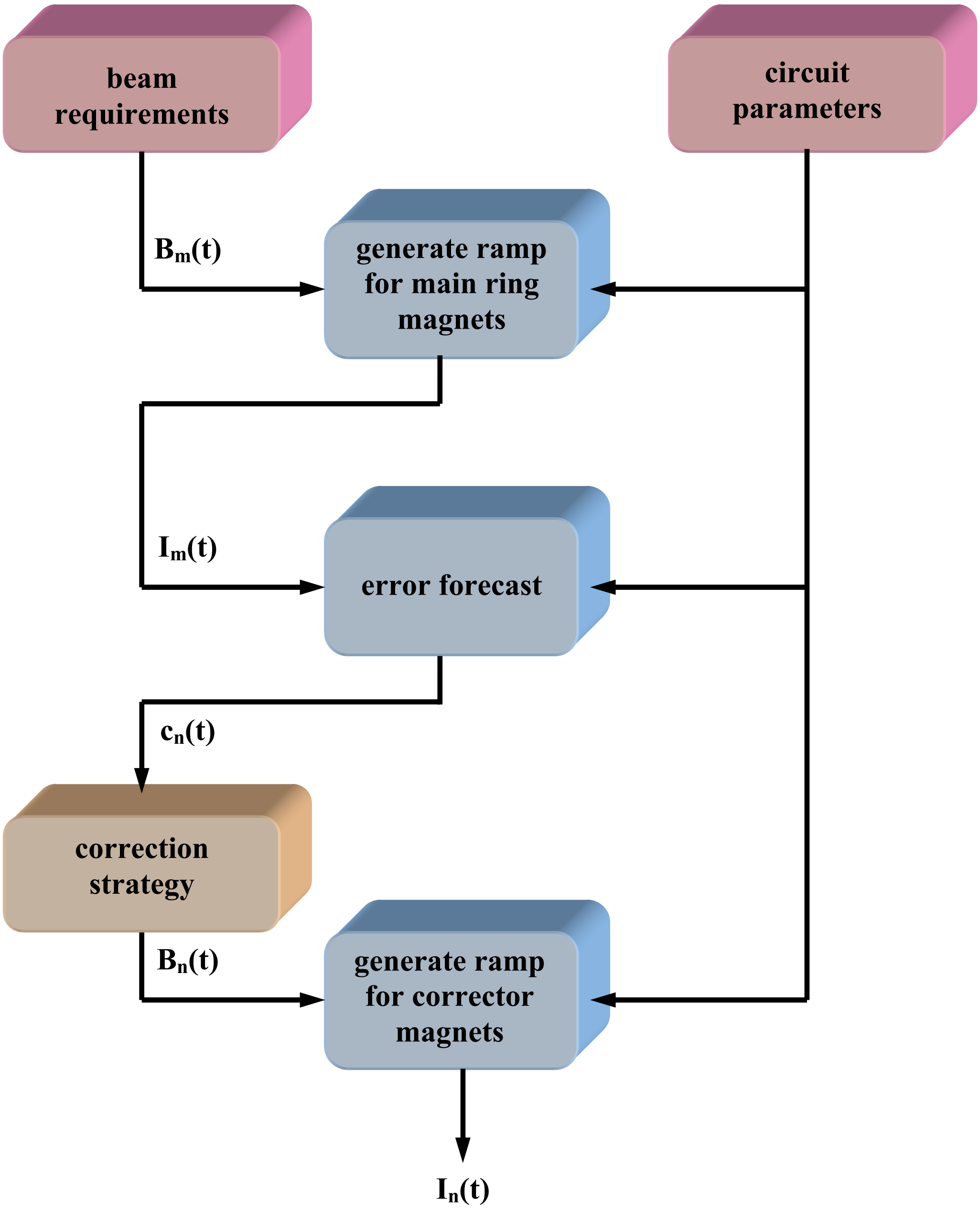

Figure 2.2: The use of FIDEL in LHC control.

In order to reach its aims and fulfil its requirements, FIDEL is composed of four elements:

a. The magnet reference database.

b. The magnet topology database.

c. The field model.

d. The off-line reference magnet system.

2.5.1 - The Magnet Reference Database

The series magnetic measurements were performed both at warm (room temperature) by the manufacturers in industry [41] and at cold (1.89K) at CERN and collaborating laboratories. These measurements were performed on series cryodipoles [42], main quadrupoles [43], insertion region quadrupoles and other corrector magnets [44] with various measuring instruments [45-47] and were stored in the magnet reference database [48]. The number of measurement entries during these series tests is estimated to reach 5,000,000 raw entries. The entries were analysed systematically using an infrastructure of automatic software tools and were all verified and corrected manually. This process filtered the raw data converting them into reference tables on which the field model is based to determine the model parameters. Due to limited resources, the following constraints were imposed on the series measurements [49]:

a. magnetic measurements are performed at warm in industry on 100 per cent of the main dipoles, main quadrupoles, insertion region quadrupoles and correctors.
b. series magnetic measurements, which are part of this work, are performed at cold on 18 per cent of the dipole magnets, 7 per cent of the main quadrupoles, 25 per cent of the insertion region quadrupoles and between 2 to 5 per cent of the overall correctors.
c. extended magnetic measurements, which are part of this work, are performed on 3 per cent of the main dipoles at cold to study dynamic effects further and investigate the response of the magnets in different machine operation domains. These tests included snapback tests, powering history tests, ramp rate effect studies (eddy currents), and the impact of the powering and storage on the field quality.

Due to the above constraints, the measurements at warm were primarily used to monitor and steer the magnet production whilst the cold magnetic measurements were used to:

a. establish a warm-cold correlation.
b. monitor the field quality at cold.
c. establish whether the magnets can be grouped up into families to reduce the random error.
d. establish the static and dynamic parameters of the field model.

2.5.2 - The Magnet Topology Database

The magnet topology database is where the information of the location of each individual magnet inside the machine is stored. It is used to compute the field model parameters on a sector by sector basis.

The slot allocation is the responsibility of the Magnet Evaluation Board (MEB) and is mainly based on the suitability of each magnet in terms of quench performance, geometry and field quality to optimize the machine installation [50].

2.5.3 - The Field Model

The field model is the heart of FIDEL and consists of a mathematical description of the empirical and physical knowledge obtained from series and extended measurements on the LHC magnet population. It is based on the static feed-forward and dynamic feed-forward paradigms highlighted earlier and is the main discussion of this dissertation.

2.5.4 - The Off-line Reference Magnet System

The off-line reference magnets and their related measuring instruments represent the hardware part of FIDEL. Having the test stations readily available after the magnet production is complete, it is planned to have two magnets on the benches available on demand [51]. The scope of these extended measurements is to:

a. monitor the stability and reproducibility of the magnet harmonics and implement corrections to the field model parameters if needed.
b. perform measurements targeted at refining the existing dynamic models. This will be done by widening the exploration of the relevant parameter space particularly for scenarios with new machine operation modes.
c. perform precision transfer function measurements.
d. carry out special investigations considered to be of 2^{nd} order and left out during series tests, e.g. changes in coil geometry due to thermal contractions or Lorentz forces [52], non-linear cross-talk between adjacent magnets and fringe field effects.
e. perform measurements targeted at investigating unforeseen phenomena.

For the time being, it is foreseen to use the standard series instrumentation for FIDEL related measurements on the off-line reference magnets. This instrumentation particularly includes the twin rotating coils [45] and the snapback analyser which will be discussed in detail in chapter 8.

However, as part of the standard magnetic measurement research and development programme at CERN, a new fast measurement system is currently being developed [53]. This is a fast rotating coils system consisting of 15 m long shafts which are divided into 12 sectors. The instrument will deliver precise measurements of the main field and the field harmonics integrated over the whole magnet length at a frequency of 3 Hz [19]. The fast rotating coils will rotate continuously in one direction to generate the signals. The signals will be passed through slip rings and will be processed by state-of-the-art Digital Signal Processor (DSP) integrators [54] and advanced analysis algorithms optimised for fast harmonic measurements in changing fields.

The reference magnets are planned to be off-line and will therefore supply information to FIDEL asynchronously i.e. upon demand. However, the fast measurement infrastructure is being designed such that it will be possible to upgrade it to an on-line system if the need arises. In this way, it will be technically possible to revert to the original intended multipoles factory design similar to the HERA paradigm where the reference magnets provide synchronous information to the machine.

Figure 2.3 shows the paradigms employed in FIDEL and the various elements within its infrastructure. The dashed lines represent the calibration data of the field model.

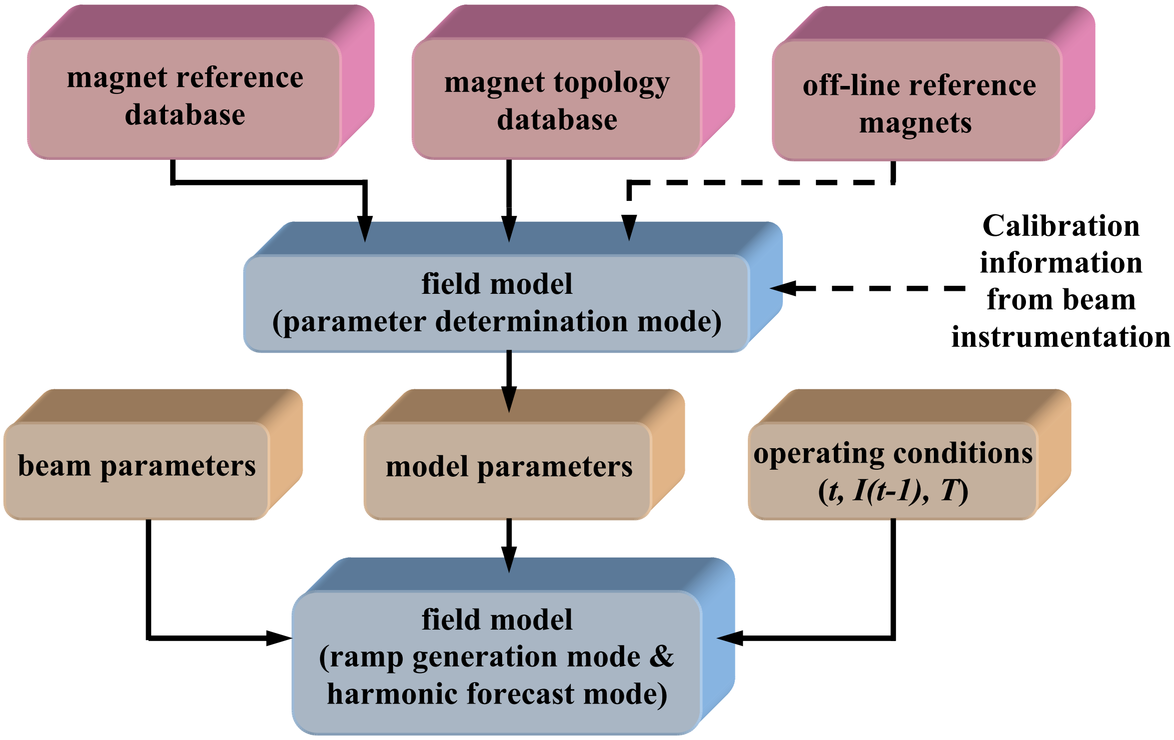

Figure 2.3: A block diagram of the FIDEL concept. The continuous lines represent data flow whilst dotted lines represent calibration data.

2.6 - The Use of FIDEL for Tracking Studies

The application of FIDEL is not only limited to the control of the machine but can also be extended to build a virtual LHC that can be used for simulation. Therefore, it can be integrated within the *Methodical Accelerator Design* software tool (MAD-X). The field model combined with the magnet reference database and the magnet topology database can be used to characterise each and every single magnet measured at cold. Hence, the model parameters of these magnets can be used for particle tracking simulations, amongst other things [55].

2.7 - Conclusion

Being a superconducting collider, the LHC needs a robust control system to compensate for the static and dynamic field variations in the superconducting magnets. These variations affect the beam stability substantially and result in particle loss if not compensated adequately. Unfortunately, a system solely based on beam feed-back may be too complex for precision compensation with the bandwidth required. The experience gained from the three major operating superconductor colliders shows that a hybrid control mechanism is the best way to compensate for the magnetic field variations.

The LHC hybrid system consists of 4 feed-forward paradigms (static feed-forward model, dynamic feed-forward model, off-line reference magnets and cycle to cycle feed-forward) which complement the feed-back system.

Conceptually, FIDEL is the main part of the feed-forward control system and encompasses the static and dynamic field model based on the magnet reference database and the magnet topology database, as well as the off-line reference magnet system. FIDEL generates the current ramps of the main superconducting magnets, forecasts their field imperfections and hence calculates the current ramps of the corrector circuits.

Therefore, by using the knowledge gained from the series and extended magnetic measurements performed during production, FIDEL will be able to provide information that can be used to compensate for the magnetic field variations that would otherwise cause beam perturbations.

Chapter 3

Field Quality

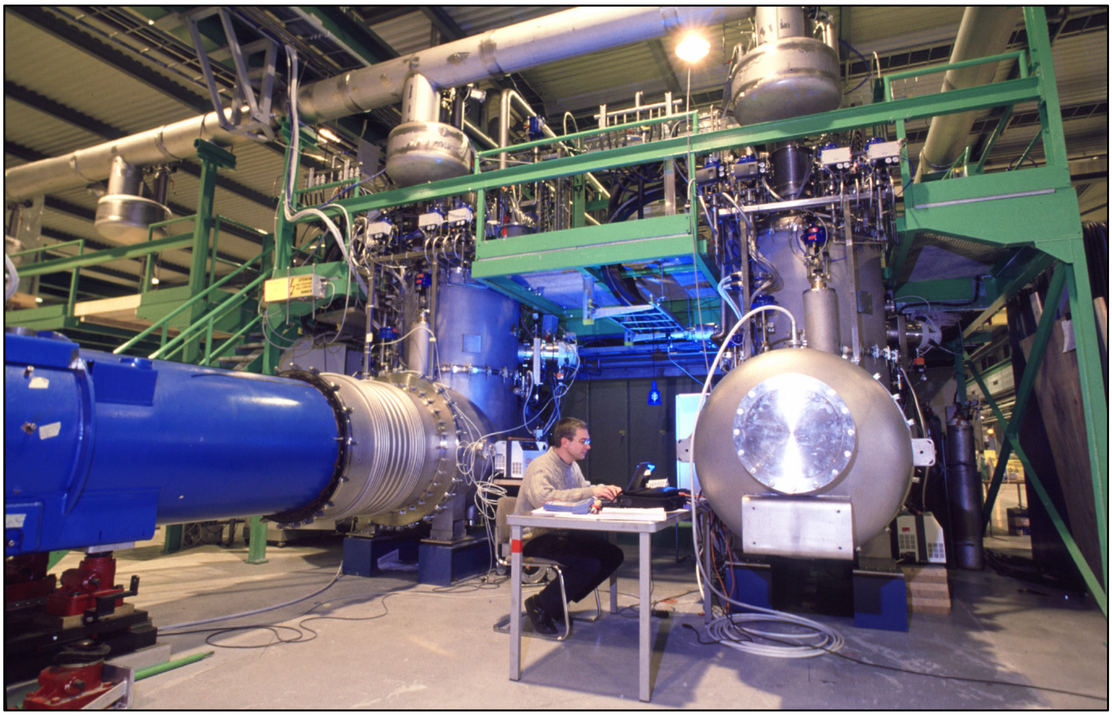

Part of the superconducting magnet test station.

> Quality is not an act, it is a habit.
> - Aristotle

Chapter 3

Field Quality

Imperfections in the magnetic field of the superconducting magnets cause beam instabilities and may lead to particle loss. Being superconducting, the magnetic field of the LHC magnets is determined by the coil geometry. To a first approximation, a two-dimensional mathematical formulation can be used to describe the main field and its inherent harmonics.

The field quality of the magnets is measured at warm in industry to steer the production. Field quality measurements at cold are performed at CERN to monitor the production and to establish a warm-cold correlation. The cold measurements form the base on which the static field model and the dynamic field model are based.

This chapter recalls how the magnetic field of a magnet is represented and also describes the procedure used during cold magnetic measurements to measure the field quality of the magnets. The results of the warm and cold magnetic measurements are used to compute the warm-cold correlations that extrapolate warm data to cryogenic conditions. Finally, the desired feed-forward prediction accuracy to be reached by FIDEL is discussed.

3.1 - Multipole Fields

The design of the main LHC superconducting dipoles [56] and quadrupoles [57] is optimized so as to obtain the highest possible beam bending strength and beam focusing strength, respectively, whilst remaining within the specified technological, economical and logistical constraints [6].

In warm electromagnets, the strength and field quality is determined by the iron yoke. Therefore, as was done in LEP, it is important to control and shim the iron laminations to obtain the best field quality possible [58]. However, in the case of superconducting magnets, the dominant contribution to the field comes from the current flowing in the cables. Therefore the coil geometry is the starting point in the optimization of the system design [59].

Theoretically, a pure multipole field inside a cylinder, containing just the single order m desired, can be obtained if the current is concentrated on an infinitely thin cylindrical boundary with a distribution given by [60]:

$$I(\phi) = I_0 \cos(m\phi) \tag{3.1}$$

where I_0 is the current (in ampere) and ϕ is the azimuthal angle.

However, it is very difficult to manufacture and lay cables that generate the perfect current distribution of Eq. 3.1. In practice, an approximation of a pure normal dipole field as required to bend the beam along its trajectory can be obtained with a current shell, the simplest of which is shown in Figure 3.1 (left) [60]. Similarly, an approximation of a pure normal quadrupole field can be obtained with a current shell of the type shown in Figure 3.1 (right).

An approximation of the pure skew multipole field is obtained by rotating the arrangements by an angle of $-\pi/(2m)$ to obtain a $\sin(m\phi)$ distribution.

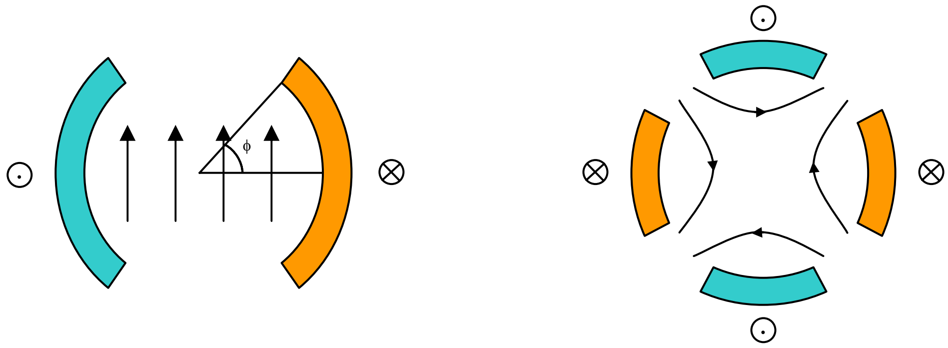

Figure 3.1: Current shell models. The generation of: **(left)** a normal dipole field; **(right)** a quadrupole field.

Since these current shells are only approximations of the ideal current distribution of Eq. 3.1, higher order harmonics which are allowed by the symmetry are present in the magnet aperture. As shown in Figure 3.2, in a perfect dipole shell magnet, only the odd normal multipoles are allowed by the symmetry [61] and their amplitudes strongly decrease in magnitude with increasing harmonic order. Optimisation of the current distribution by limiting the angle ϕ of the shells and dividing the shells into blocks may result in the vanishing of these allowed harmonics [60].

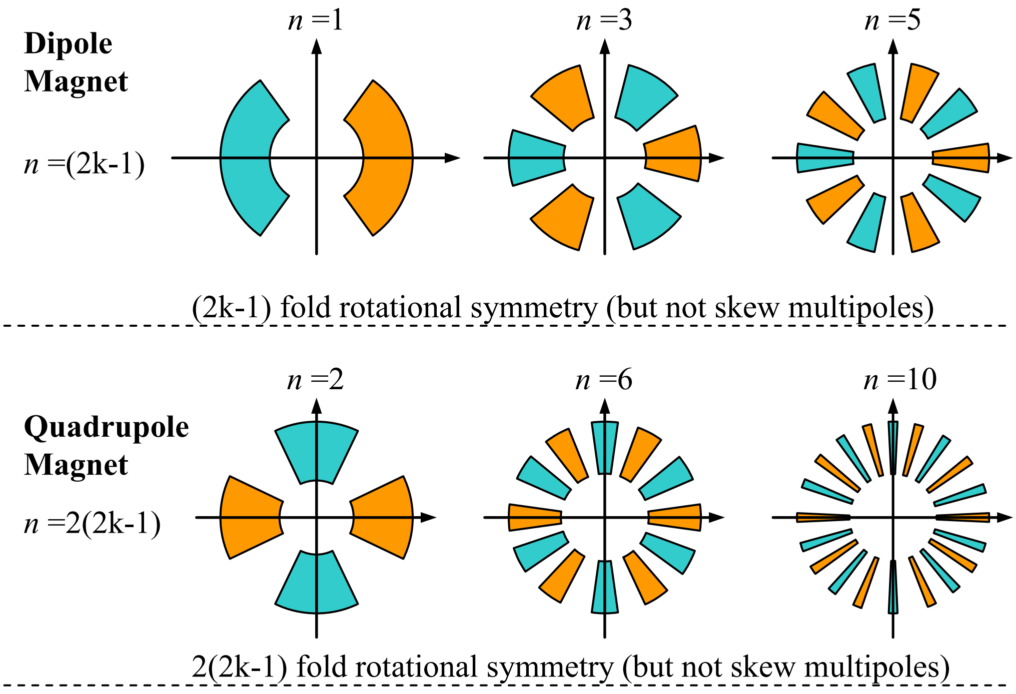

Figure 3.2: A schematic of the allowed multipoles in dipole and quadrupole magnets. n is the multipole order and k = 1,2,3…

However, due to the limitations in the precision of the manufacturing process, it is impossible to obtain a coil geometry which generates an exact symmetrical current shell distribution. These limitations result in some non-allowed harmonics being present in the magnet aperture [62]. In the case of the dipole magnet, the even normal harmonics and all the skew harmonics are non-allowed harmonics.

As shown in Figure 3.3, the coils are made from strands containing several thousand thin superconducting Nb-Ti filaments embedded in a copper matrix [60]. The strands are formed into a two layer flat arrangement into what is commonly called the *Rutherford-type* cable. The cos($m\phi$) shaped current distribution is approximated by discretizing the homogenous current shells into blocks of several layers of flat, key-stoned Rutherford cable.

To a first approximation, the magnetic field in the main LHC magnets can be represented by a purely two-dimensional field since their length (14.3 m) is much larger compared to their aperture (56 mm). In the local cylindrical polar coordinate system (r, θ, z) of the magnet, the magnetic field can be expanded in the following series:

$$B_r(r,\theta) = B_{ref} \sum_{n=1}^{\infty} \left(\frac{r}{R_{ref}} \right)^{n-1} \left(b_n \sin(n\theta) + a_n \cos(n\theta) \right) \tag{3.2}$$

$$B_\theta(r,\theta) = B_{ref} \sum_{n=1}^{\infty} \left(\frac{r}{R_{ref}} \right)^{n-1} \left(b_n \cos(n\theta) - a_n \sin(n\theta) \right) \tag{3.3}$$

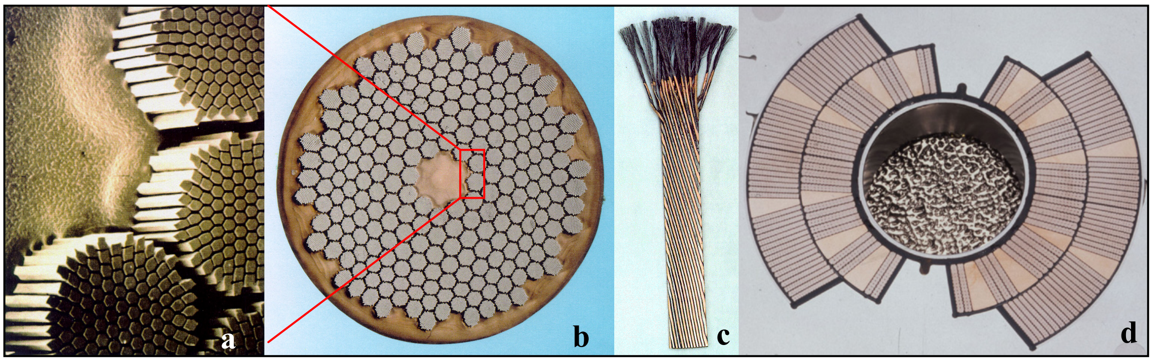

Figure 3.3: **(a)** A cross-section of the NbTi filaments, **(b)** a cross-section of a multi-filament strand, **(c)** the Rutherford cable, **(d)** LHC dipole cross-section.

where n is the multipole order and R_{ref} is the reference radius which should be in the same order as the maximum deviation of the protons from the centre axis of the magnet. For the LHC, R_{ref} is 17mm. b_n and a_n are, respectively, the normalized normal and skew multipole coefficients expressed in "units", also referred to as the field harmonics. B_{ref} is the amplitude of the main field of the magnet. The coefficients a_n and b_n are very small, typically in the range $|a_n|, |b_n| < 1\times10^{-4}$.

For a Cartesian coordinate system, the complex magnetic field can be expanded in the multipole series:

$$\begin{aligned} B(x,y) &= B_y + iB_x \\ &= \sum_{n=1}^{\infty}(B_n + iA_n)\left(\frac{x+iy}{R_{ref}}\right)^{n-1} \\ &= \sum_{n=1}^{\infty} C_n\left(\frac{z}{R_{ref}}\right)^{n-1} \end{aligned} \tag{3.4}$$

where B_n and A_n are the non-normalized normal and skew multipole coefficients, respectively, and C_n indicates the generic non-normalized complex harmonic of order n given in the reference frame aligned with the main field direction. For convenience, the normalized harmonic coefficients, indicated as c_n can be defined as:

$$c_n = b_n + ia_n = 10^4 \frac{C_n}{B_m} \tag{3.5}$$

expressed in "units". In practice the above normalization is mainly used for the harmonics of order higher than the main field, i.e. for

$$n \geq m+1 \tag{3.6}$$

where the index m stands for the order of the main field (with $m = 1$ for dipole and m = 2 for quadrupole). Finally, the local main field transfer function (TF) is defined as the ratio of field generated and operating current:

$$TF = \frac{B_m}{I} \tag{3.7}$$

which is expressed in T/A @R_{ref}. If integrated over the whole magnetic length (ML);

$$TF = \int_0^{ML} \frac{B_m(z)}{I} dz \tag{3.8}$$

which for the dipole is expressed in Tm/A.

To be more precise, one should also consider the end-fields of the magnet which are not two-dimensional. Luckily, the LHC magnets are short compared to the wavelength of the betatron oscillations in the machine so the field integral and the effective field length of a magnet is all that is necessary to know and to correct for the end effect. Elmore and Garrett in [63] show that the magnetic field including the end-field essentially behaves as a two-dimensional field provided the integration is carried out over a region that is long enough so that the field drops to zero.

3.2 - Standard Cold Magnetic Measurements

Because of the fast reaction needed, production steering must be driven by warm magnetic measurements that are performed at the magnet manufacturer [41]. Cold magnetic measurements have been performed extensively in the beginning of the production to establish the warm-cold correlation. The standard magnetic measurement programme at cold is presently performed on the main dipole and on the main quadrupole magnets and consists of two consecutive cycles: the standard LHC cycle and the loadline.

The loadline cycle is shown in Figure 3.4. This cycle is particularly targeted to study the static current dependent multipole variations i.e. the harmonic hysteresis curves. It consists of taking two measurements on current plateaus which range from the injection current to the nominal current. The measurements obtained from this cycle are the basis of discussion of chapter 4.

The loadline is preceded by a pre-cycle which consists of a quick cycle to a nominal current plateau of 1000 s. Its acceleration ramp is linear except for a parabolic part when changing to and from the nominal current plateau. The pre-cycle linear acceleration ramp rate is of 50 A/s (ramp-down rate is –50 A/s). The pre-cycle is solely used in tests to induce persistent currents inside the coils and to put the magnet in a known magnetic state. During machine operation, the pre-cycle will only be used in the case the machine magnetic state runs the risk of not being reproducible e.g. after a magnet quench [64] in one of the sectors or after a thermal cycle.

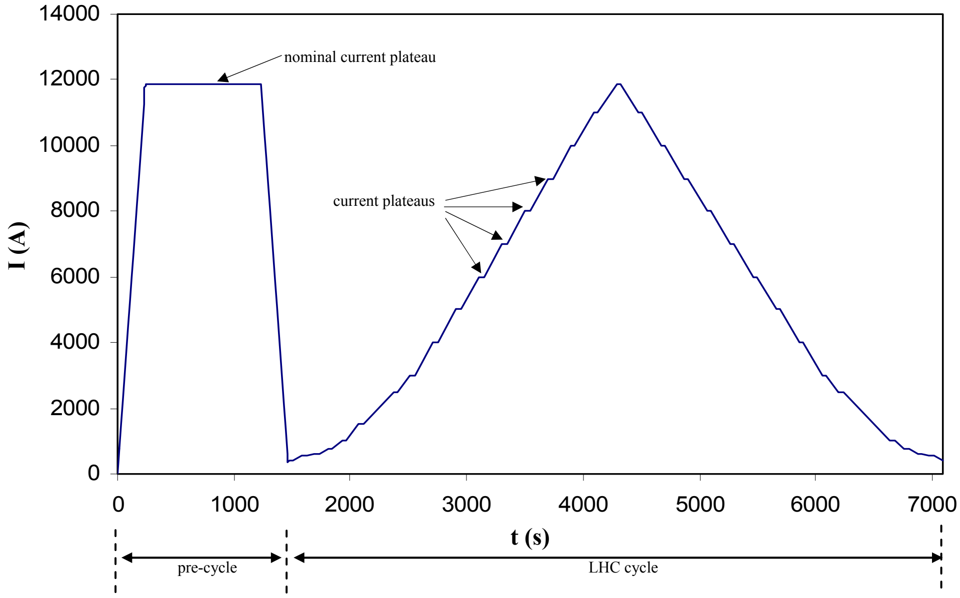

Figure 3.4: The loadline cycle.

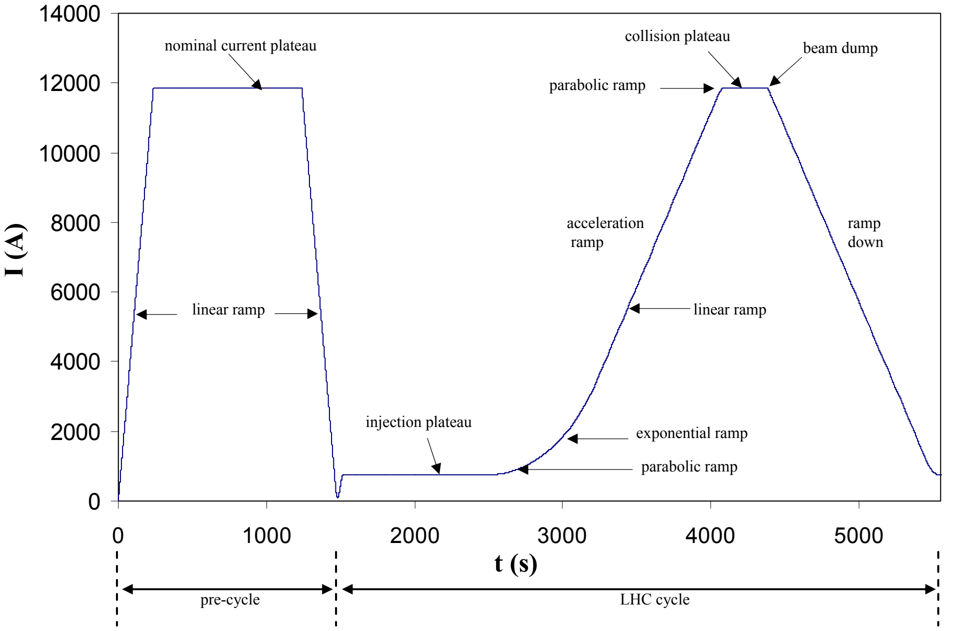

Figure 3.5: The standard reference LHC cycle.

As shown in Figure 3.5, the standard LHC cycle used in measurements consists of a simulation of a real cycle in the machine. The particle injection occurs at a current of 760 A and has a duration of 1000 s in the LHC. The particles are then accelerated with the R.F. cavities [7] and the magnets are ramped up to the nominal current of 11850 A achieving a nominal dipole field of 8.33 T. This ramp follows a Parabolic-Exponential-Linear-Parabolic (PELP) acceleration cycle that is optimized to [65]:

a. remain within the maximum voltage that the power converters can deliver.
b. reduce the effects of inter strand coupling currents in the Rutherford cable.
c. minimize the control bandwidth requirements during particle acceleration.
d. avoid current overshoots once the magnets reach nominal current.

The linear acceleration is of 10 A/s. The collision plateau occurs at an excitation current of 11850 A. The beam is dumped at the end of the collision plateau and the magnets are consequently ramped down.

The purpose of the LHC cycle is to study the dynamic time dependent multipole variations. During series cold magnetic measurements, this cycle is always preceded by a magnet quench and a pre-cycle so as to put the magnet in a known magnetic state. Therefore, the LHC cycle always precedes the loadline in series cold tests. In normal operation, the time spent on the collision plateau may vary. This affects the reproducibility of the machine magnetic state and so has to be modelled and taken into account. As will be seen in chapter 5, this modelling is performed by varying the parameters of the pre-cycle in extended magnetic measurements.

The standard cold magnetic measurements are performed with the twin rotating coil measurement system that is shown in Figure 3.6 [45]. The uncertainty and repeatability of the rotating coil measurements performed on dipoles and quadrupoles are shown in Table 3.1 [66] and Table 3.2 [67], respectively. It should be noted that these values include uncertainty sources originating from equipment other than just the rotating coils (e.g. current supplies).

The measurement analysis is a semi-automatic procedure of data cleaning, data validating and data formatting of the raw measurements. The problems associated with the raw data can be of four types:
a. Mechanical: e.g. broken shaft, damaged ribbon cable of the twin rotating unit.
b. Electronic: amplifier drift.
c. Software: configuration: error in coil calibration factor, error amplifier gain setting.
d. Operation: error in cycle settings, error in data entry.

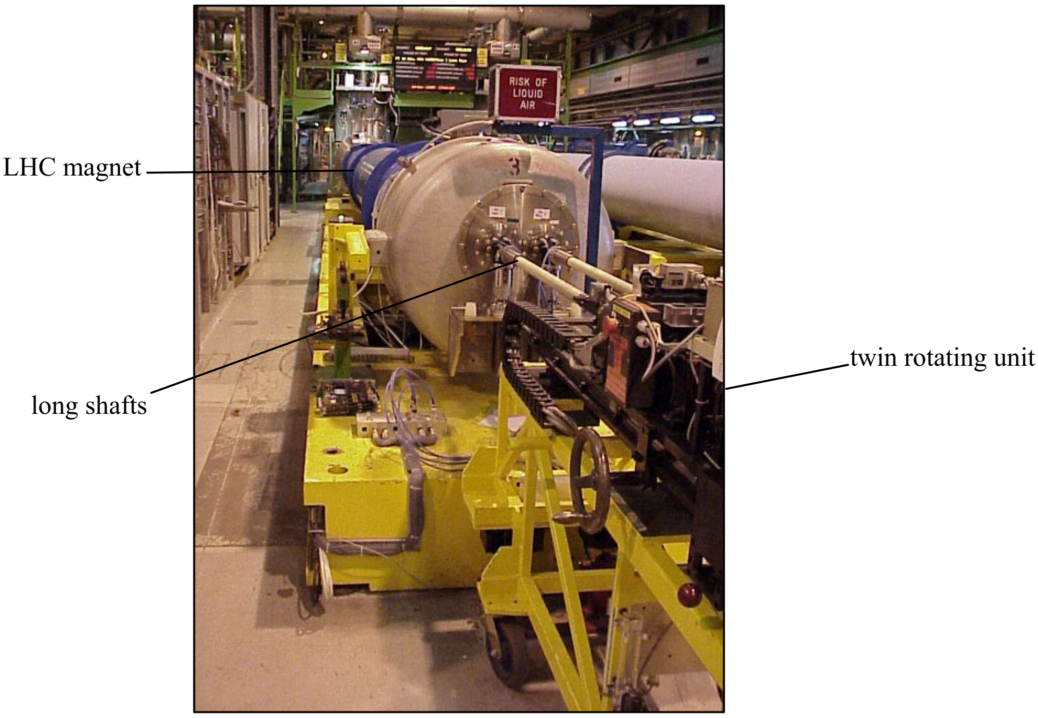

Figure 3.6: The measurement set-up for standard cold measurements on the magnet test station.

Table 3.1: The uncertainty and repeatability of the dipole rotating coil measurements (all values are in units).

	main field b_1	harmonics
uncertainty	3	0.1
repeatability	0.5	0.01

Table 3.2: The uncertainty and repeatability of the quadrupole rotating coil measurements (all values are in units).

	main field b_2	harmonics
uncertainty	5	0.1
repeatability	0.5	0.05

These measurement errors are therefore corrected and the results are entered into the magnet reference database. The typical harmonic values obtained from such a measurement are depicted in Figure 3.7. It should be noted that the magnitude of the allowed harmonics (normal odd multipoles) is significantly larger than that of the non-allowed harmonics.

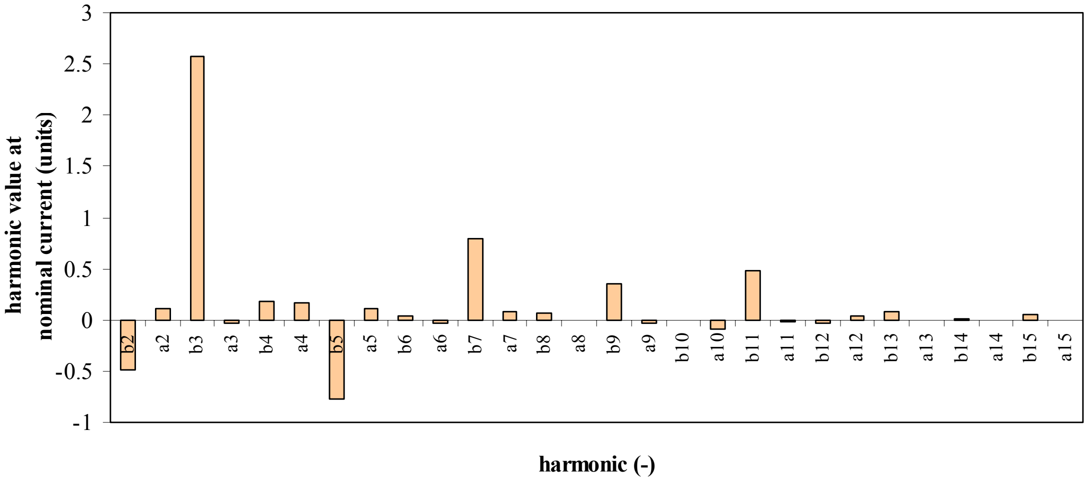

Figure 3.7: The field harmonics integrated along an LHC dipole magnet at nominal current.

Provided the magnet is already at 1.89 K, a typical standard measurement takes around 5 hours including the installation of the rotating coils. Cooling down a dipole magnet from room temperature to 1.89 K requires approximately 12 hours depending on the cryogenic priority on the test bench.

3.3 - Warm-Cold Correlations

Since all the magnets are measured at room temperature but only a small sample of them is measured at cryogenic temperatures, a warm-cold correlation allows the measurements at warm to be extrapolated to cold conditions.

As at June 2006, 1150 cold masses were measured at room temperature and analysed by the Magnets and Superconductors (MAS) group at CERN [68] and 190 dipole magnets were measured in cryogenic conditions by the Magnet Tests and Measurements (MTM) group (a great proportion of which as part of this thesis). From the cold test reviews of January 2005 [69], it was decided to select the magnets for the field quality measurements at cold according to their inner and outer cable type so as to take a sample of all the magnets with different cable type combinations.

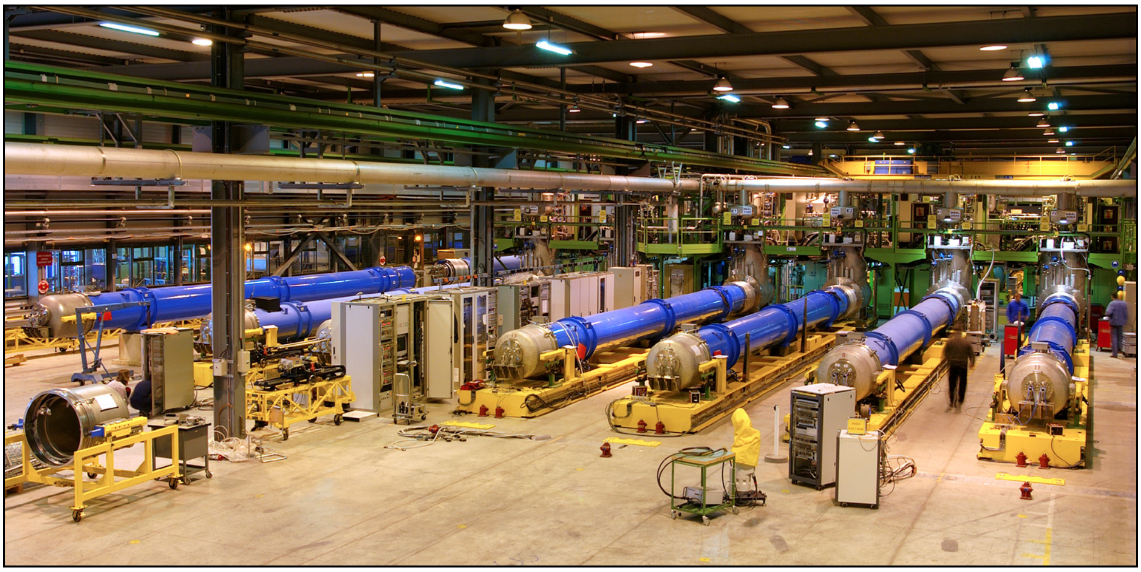

Figure 3.8: Magnet test facility at CERN.

The magnet population sampled at cold is divided into 58 cold masses produced by firm 1 (referred to as 1XXX), 51 cold masses produced by firm 2 (referred to as 2XXX) and 81 cold masses produced by firm 3 (referred to as 3XXX). 31 magnets have the first version of the six-blocks two-dimensional cross-section, 69 dipoles have the second version [56] of the cross-section where the size of the copper wedges of the inner layer was changed. The other 90 dipoles feature the third version of the cross-section [56] geometry characterized by an additional thickness of the mid-plane insulation. These changes were performed to ensure that the multipoles are within the required tolerances. Figure 3.8 shows the cold test benches where these tests are performed.

Figure 3.9 shows the production trend of the normal sextupole harmonic measured at warm [68]. It also shows the production trend of the normal sextupole harmonic measured at cold at the beginning of injection and at nominal current for the different cross-sections. The magnet number is a number assigned to each magnet in the manufacturer and test folders. It should be noted that the number of cold measurements are reduced after about 200 magnets were manufactured. This was done to increase the testing rate. The negative trend is due to the introduction of the second cross-section. The negative trend is furthermore amplified by magnets with the third cross-section.

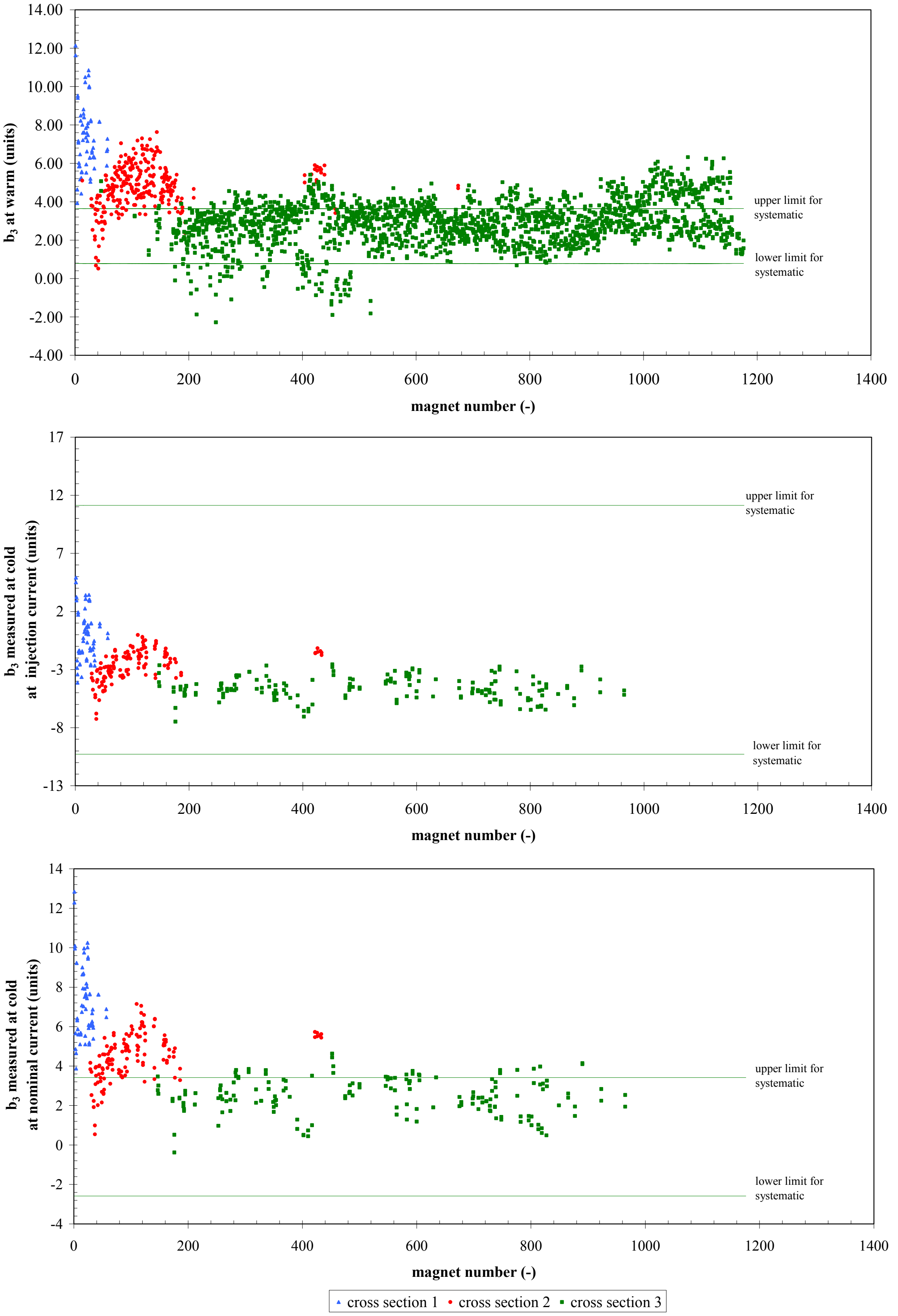

Figure 3.9: The trend in the integrated normal sextupole **(top)** at warm (courtesy MAS group; Ezio Todesco); **(middle)** at cold at the beginning of injection plateau; **(bottom)** at cold at nominal current.

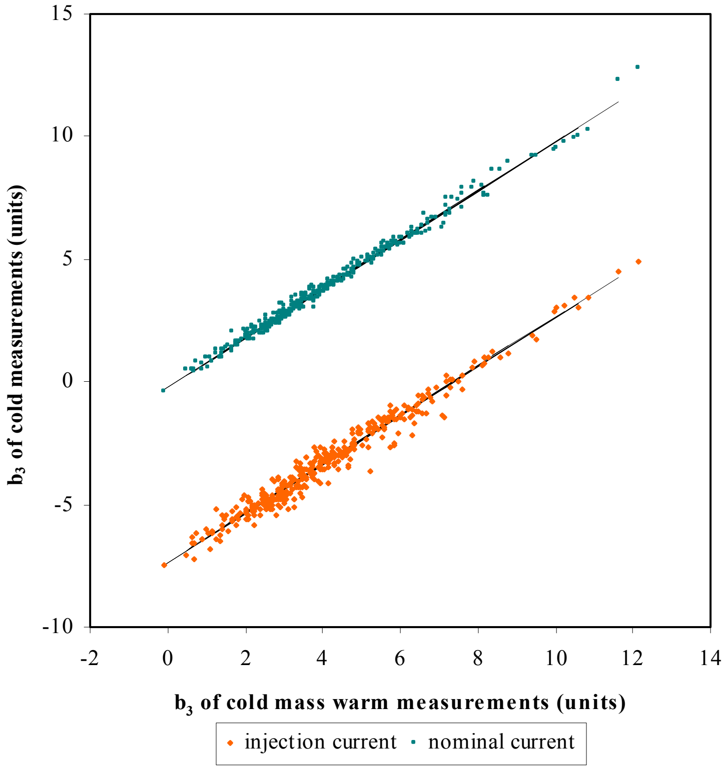

Figure 3.10: The b_3 warm-cold correlation at injection (760 A) and nominal (11850 A) current. (warm data courtesy of MAS group; Ezio Todesco)

Figure 3.10 shows the b_3 warm-cold correlation at injection and at nominal current. The multipoles generally follow a correlation of the type:

$$c_n^{cold} = g_n^{wc} c_n^{warm} + \Delta_n^{wc} \tag{3.9}$$

where the slope g_n^{wc} of the correlations is very close to 1 so the offset Δ_n^{wc} determines the correlation value. The same procedure is performed for all the harmonics. Table 3.3 shows the offset values and the standard deviation (σ) of the difference between the measurements and the correlation line along the y-axis for the transfer function and the harmonics. As will be described in the next chapter, a warm-cold correlation at 5000 A will be used to obtain the average geometric component of the whole magnet population in the static model.

Table 3.3: Correlation offset values and standard deviation (σ) of the difference between the points and the correlation line along the y-axis.

	units	**offset (inj)**	**σ (inj)**	**offset (nom)**	**σ (nom)**
TF	(Tm/kA)	6.89×10^{-3}	5.162×10^{-3}	-5.175×10^{-2}	4.671×10^{-3}
b_2	(units)	−1.455	0.319	−2.920	0.361
a_2	(units)	−0.023	0.412	−0.118	0.191
b_3	(units)	−7.360	0.362	−0.216	0.196
a_3	(units)	0.007	0.086	−0.018	0.093
b_4	(units)	−0.034	0.040	0.167	0.042
a_4	(units)	0.007	0.096	0.014	0.050
b_5	(units)	0.938	0.099	−0.249	0.063
a_5	(units)	0.009	0.024	0.010	0.020

3.4 - Harmonic Tolerances from Beam Dynamics

The tolerances of the harmonics can be calculated from the beam requirements of Table 1.1 so as to provide a specification for the LHC control system. These calculations, performed by Fartoukh and Brüning in [10] yield the tolerances shown in Table 3.4. The commissioning requirements are taken to be the desired feed-forward prediction to be reached by FIDEL. Once the machine is within the commissioning tolerances, it will be in a state that is controllable by beam based feed-back and hence the beam diagnostics will take over to eventually reach the nominal operation control precision required [13].

Table 3.4: The particle injection harmonic tolerance for commissioning and for nominal operation calculated from the beam requirements (values are shown in units).

	commissioning	**nominal operation**
b_1	2	1
b_2 main dipoles	0.2	0.01
b_2 main quadrupoles	4	0.25
a_2	0.2	0.01
b_3	0.35	0.02
a_3	-	0.2
b_4	-	0.04
a_4	-	-
b_5	-	0.1
a_5	-	-

3.5 - Conclusion

The magnetic field in superconducting accelerator magnets is characterized by the coil geometry and is composed of the main field superimposed by the field harmonics. Since the length of the LHC magnets is much larger than their aperture, the magnetic field can be represented by a two-dimensional field. The end-field essentially also behaves like a two-dimensional field provided the integration is carried out over a region that is long enough.

Some of the harmonics are allowed by the coil geometry and are therefore expected to be present. However, limitations in the precision of the manufacturing process also result in the presence of non-allowed harmonics. As highlighted in section 1.2, both allowed and non-allowed harmonics need to be compensated to avoid beam instabilities.

Production is steered by warm measurements in industry. Cold measurements only monitor the production, but they also establish a warm-cold correlation as well as the parameters of FIDEL. The standard cold measurements consist of an LHC cycle and a loadline which are performed at the magnet test facility at CERN using rotating coils.

The commissioning requirements of the LHC are taken as the desired feed-forward prediction to be reached by FIDEL and once these are met, the feed-back system will take over to eventually reach the nominal operation control precision.

Chapter 4

The Static Field Model

Cross section of an LHC cryodipole.

There are two possible outcomes:
if the result confirms the hypothesis, then you have made a measurement;
if the result is contrary to the hypothesis, then you have made a discovery.
- Enrico Fermi

Chapter 4

The Static Field Model

The starting point in establishing the feed-forward control system for the LHC is obtaining a thorough understanding of the reproducible magnetic effects of the machine. In FIDEL, this is referred to as the static field model which is primarily dependent on the excitation current.

The principle of the model is based on the decomposition of the different components that contribute to the magnetic field behaviour. However it is simple enough to be limited to a reasonable number of fitting parameters.

This chapter provides a detailed description of the different components that contribute to the static magnetic field. It provides a mathematical formulation of the effects based on their physical understanding or on empirical formulae when they are too complex to be described analytically. A system is also employed to establish the equation parameters for the main field and its harmonics based on measurements of one sector of the machine.

4.1 - Introduction

The static field model represents the base of FIDEL since it provides a mathematical description of the superconducting magnets' reproducible, current dependent behaviour [70]. It does not provide a description of the field and field error time-dependence or ramp rate dependence. The static field model is constructed by using the following procedure:

a. The different field error components are identified: this is done by determining the main error contributions due to the magnet structural layout and the electromagnetic properties of the materials.
b. A mathematical description of the field errors is formulated on a physical understanding of the phenomena. Where the physical effects are too complex to be represented analytically, an empirical formulation is adopted to approximate the phenomena involved.
c. The series loadline cold measurements are used to obtain the average current-dependence of the magnet population being modelled.
d. A minimization procedure is adopted to determine the parameters of the mathematical formulation.

4.2 - Physical Decomposition of Static Errors

To give an explicit form of the static field model, the field errors can be decomposed in the following components. The advantage of the decomposition relies on the fact that each component has a clear physical origin, and that it can be determined directly from field measurements:

a. *Geometric Contribution* ($C_n^{geometric}$). Since the field in the superconducting magnet is mostly generated by the current in the superconducting cables, the accuracy of the cable position is crucial. In fact the typical target tolerances in the production of the LHC dipoles is very tight: in the order of 25 μm. The geometric contribution is due to the deviation between the conductor position in the real coil winding and the ideal distribution of current that produces the exact desired multipolar field. It is present at all field levels and is proportional to the operating current. However, once the magnet is produced, the geometric errors are fully reproducible.

b. *d.c. Magnetisation Contribution* (C_n^{MDC}), originates from the persistent currents in the superconducting filaments. This contribution is important at low operating fields (e.g. injection current in the main dipoles). It is reproducible provided that the magnet is cycled with the same procedure, in particular maximum and minimum current, irrespective of the time required for cycling.

c. *Saturation Contribution* ($C_n^{saturation}$) which is due to changes of the magnetic permeability in the iron yoke surrounding the coils. This contribution is important at high field, and mostly affects the main field component.

d. *Displacement Contribution* ($C_n^{deformation}$), caused by displacements of the cables in the coil cross-section. Cable movements can take place during powering at high field as a consequence of the changes in the force and stress distribution.

e. *Residual Magnetisation Contribution* ($C_n^{residual}$) of magnetic parts in the cold mass, mostly in the collars and iron surrounding the coils, visible at low current.

The components above are listed in the order of magnitude. They have a specific definition when stored in the magnet reference database and when processed and analysed in the series measurements. This definition is not intended to define the components mathematically but solely provides an idea of the order of magnitude of the particular component. Therefore the components are represented by $\hat{c}_n$. This definition also shows that the components can be determined directly from the field measurements. The definitions of $\hat{c}_n$ for the various components are as follows:

4.2.1 - The Geometric Field

The geometric component is chosen at a current value such that the residual magnetisation and persistent currents are small and the saturation and displacement contribution are not yet significant. The geometric component is therefore taken to be the average between the field at geometric current $I_{geometric}$ (5000 A for a main dipole) during the ramp-up and the field at $I_{geometric}$ during the ramp-down:

$$\hat{c}_n^{geometric} = \frac{1}{2}\left(\hat{c}_n^{down}\left(I_{geometric}\right) + \hat{c}_n^{up}\left(I_{geometric}\right)\right) \tag{4.1}$$

4.2.2 - Effective d.c. Magnetisation

The effective d.c. magnetisation contribution is the difference between the harmonic at injection current I_{inj} (760 A for a main dipole) and the geometric harmonic:

$$\hat{c}_n^{MDC} = \hat{c}_n^{up}\left(I_{inj}\right) - \hat{c}_n^{geometric} \tag{4.2}$$

4.2.3 - Hysteresis

The hysteresis is the difference between the harmonic at injection current I_{inj} during the increasing ramp and the harmonic at the same current during the decreasing ramp:

$$\hat{c}_n^{hyst} = \hat{c}_n^{up}\left(I_{inj}\right) - \hat{c}_n^{down}\left(I_{inj}\right) \tag{4.3}$$

4.2.4 - Effective Saturation

The effective saturation contribution is the difference between the harmonic at nominal current I_{nom} (11850 A for a main dipole) and the geometric harmonic:

$$\hat{c}_n^{sat} = \hat{c}_n^{up}\left(I_{nom}\right) - \hat{c}_n^{geometric} \tag{4.4}$$

Figure 4.1 shows an example of the data obtained from the cold test of an LHC dipole, plotting the dependence of the normal sextupole component as a function of current along a loadline cycle. The figure clearly shows the components as defined in the magnet reference database.

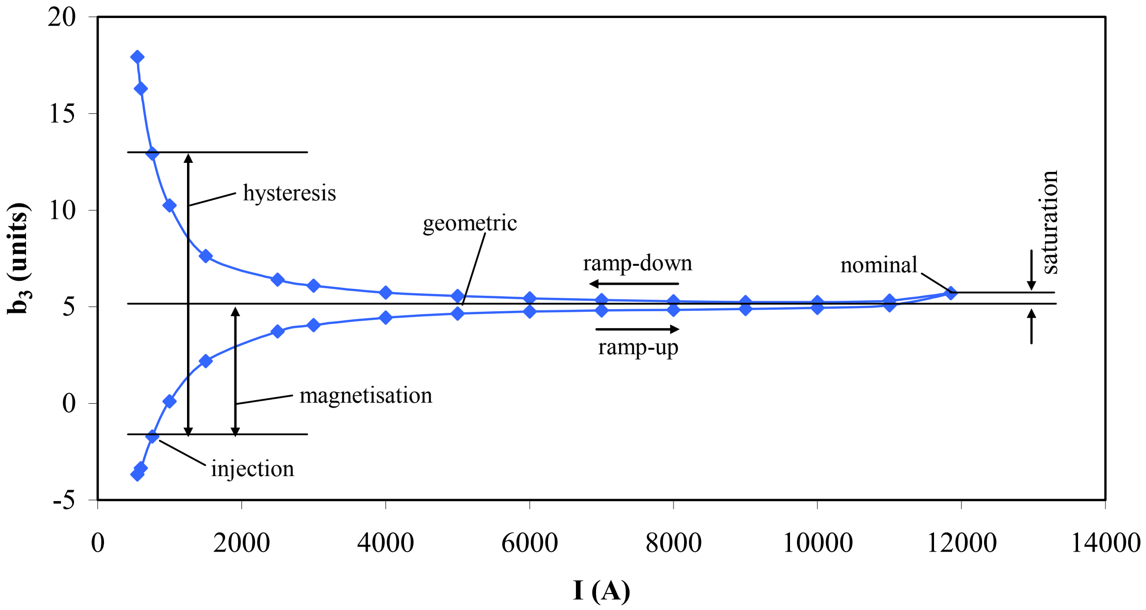

Figure 4.1: Components as defined in the magnet reference database.

4.3 - Mathematical Formulation

The field model relies on the linearity of the field error decomposition i.e. on the mutual independence of the components. This is expected because of the inherent different and independent physical origin of the components. Moreover, as a general rule, superconducting magnets (and especially the main dipoles and quadrupoles) are designed to achieve relative field errors of 1×10^{-4} or better.

Any coupling between the components which results from variations in the field distribution is at most six orders of magnitude smaller than the background field. This coupling effect is an order of magnitude smaller than the required modelling error (typically 0.1 units for b_3 which corresponds to 5 orders of magnitude smaller than the main field) and is therefore negligible. In other words, all deviations from linearity are small perturbations of the ideal field, and the single contributions to the field errors can be added linearly to obtain the total field in the magnet.

Under this assumption, the static field model can be given by the sum of the contributions:

$$C_n^{DC} = C_n^{geometric} + C_n^{MDC} + C_n^{saturation} + C_n^{deformation} + C_n^{residual} \tag{4.5}$$

where C_n^{DC} is the static component.

The analytical formulae that are chosen to describe the various dependencies, with a limited set of free parameters are the following;

4.3.1 - Geometric Contributions

In a magnet aperture, the magnetic field at a particular point is a summation of the contribution from all the strands in the coil and their images in the iron yoke. Essentially, therefore, geometric contributions to the field and field errors can be expressed by:

$$B_m^{geometric} = \gamma_m I \tag{4.6}$$

where the magnetic field $B_m^{geometric}$ is proportional to the excitation current I in the magnet. This means that the normalised geometric multipoles are constant along the magnet loadline. The geometric coefficient, γ_m, in the above definition includes the linear contribution from the iron yoke thus ignoring the saturation and the residual magnetisation. For the transfer function as defined in Eq. 3.7:

$$TF^{geometric} = \gamma_m \tag{4.7}$$

and for the normalized harmonics:

$$c_n^{geometric} = \gamma_n \tag{4.8}$$

Even though only a small sample of the magnets are measured at cold, a warm-cold correlation is good enough to perform extrapolation at cold of the geometric component from warm measurements [48]. This is done using the linear transformation;

$$\gamma_m^{geometric} = g_m^{wc} \gamma_m^{warm} + \Delta_m^{wc} \tag{4.9}$$

where g_m^{wc} is the correlation slope taken to be equal to 1 when correlating with cold mass data (measured at warm), γ_m^{warm} is the main field measured at warm and Δ_m^{wc} is the offset of the correlation line. For the transfer function:

$$\gamma_{TF}^{geometric} = g_m^{wc}\gamma_{TF}^{warm} + \Delta_m^{wc} \qquad (4.10)$$

and for the normalized harmonics:

$$\gamma_n^{geometric} = g_n^{wc}\gamma_n^{warm} + \Delta_n^{wc} \qquad (4.11).$$

Figure 4.2 shows the geometric correlation of the normal sextupole. The geometric component is the only one that can be extrapolated from warm measurements. Eq. 4.11 is general, and holds both for local and integral harmonics in which case it contains the contribution of the change in the magnetic length.

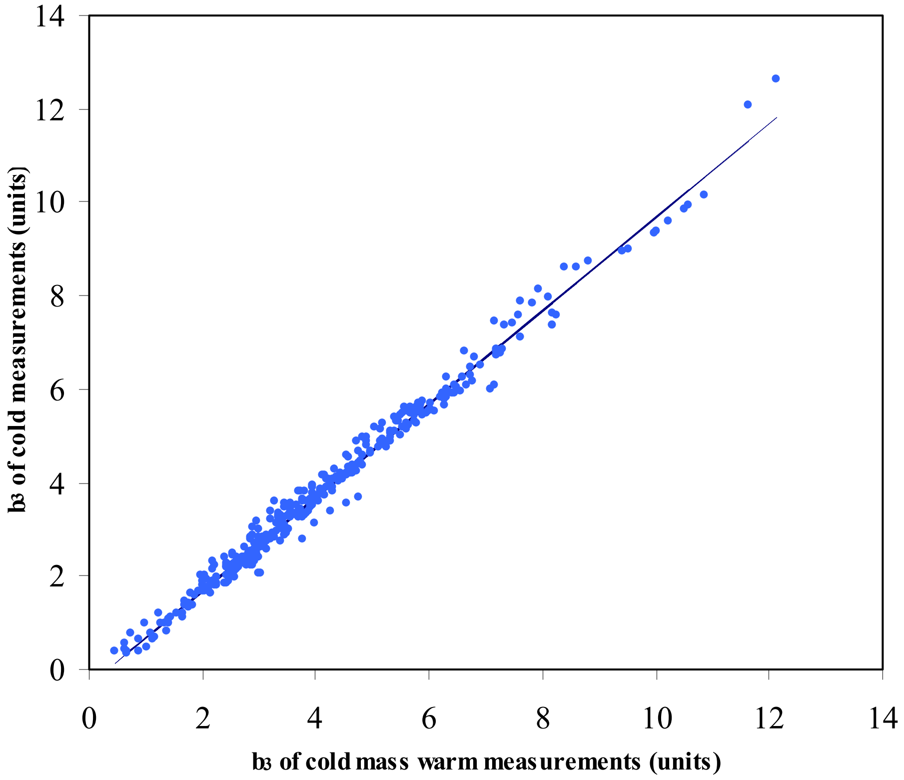

Figure 4.2: Correlation between b_3 geometric (i.e. at 5000 A) at cold (units) and b_3 at warm (units). (warm data courtesy of MAS group; Ezio Todesco)

4.3.2 - d.c. Magnetisation Contributions

Hard superconductors compensate for any background field by inducing a shell of shielding currents to expel the background field from the superconductor centre [71]. Since the superconductor has no resistance, the currents persist with very large time constants. The shielding field and the induced magnetisation are always oriented anti-parallel to the vector of the field change. Theoretically, these persistent currents shield a perfect dipolar field with the same cos(ϕ) current distribution on a circular boundary of the filament cross-section as described in Eq. 3.1. In practice, the current shells are not located on the boundary but penetrate into the superconducting material. As shown in Figure 4.3 a, the current shells can be approximated by ellipses which deviate from this shape as the field increases. In this approximation (known as the Bean model), the induced currents have the highest possible density i.e. the critical current density $J_c(B,T)$ [72].

The penetration field B_p is the highest field that can be shielded where the entire cross-section of the filament is filled with shielding currents. Figure 4.3 b shows the current density in a fully penetrated filament. If the background field is ramped to values much larger than B_p, the shielding currents remain the same as Figure 4.3 b but the field is not entirely shielded in the interior of the filament.

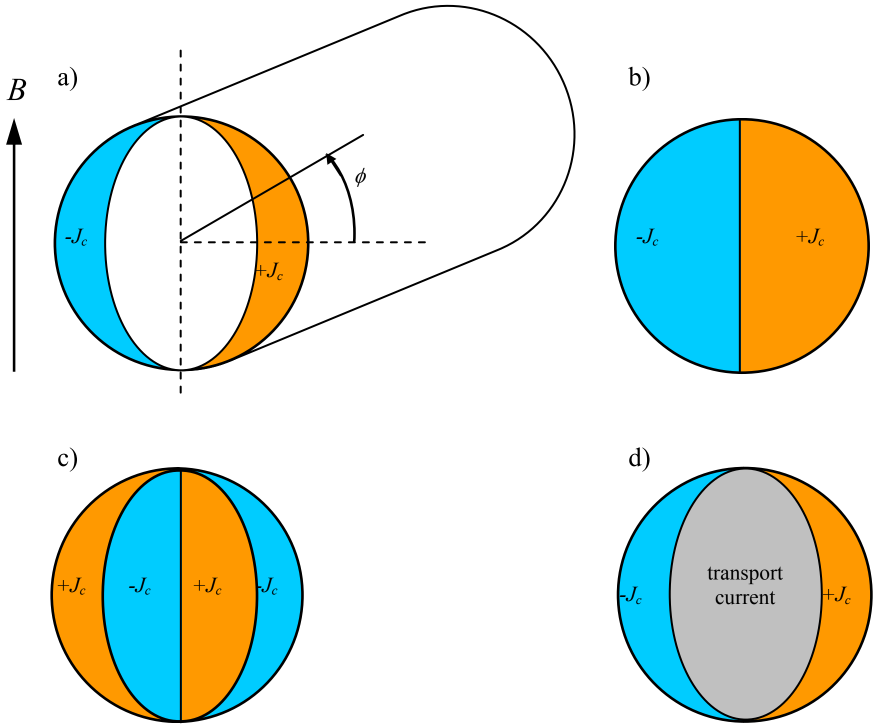

Figure 4.3: The shielding currents induced in a cylindrical superconducting filament by a varying background field B. **(a)** The current boundaries are approximated by ellipses which are induced due to the background magnetic field B. The background field is shielded in the centre of the filament. **(b)** The saturated state **(c)** when the field is decreased, a new shell of shielding currents is induced **(d)** When a filament with transport current is exposed to a background field sweep $\Delta B > B_p$, the transport current is assumed to flow in a central elliptical region.

Consequently, if the ramp direction of the background field is reversed, the decreasing field inverts the polarity of the current distribution in the region close to the surface since these currents oppose the change of magnetic flux in the filament interior. This is shown in Figure 4.3 c.

Figure 4.3 d shows the case in which the filament has a transport current. In this case, the transport current is confined to a small elliptical region in the centre and flows with the critical current density J_c. Therefore, the transport current reduces the magnetisation of an otherwise saturated filament. This effect becomes evident at high currents.

Figure 4.4 depicts a full hysteresis curve where the normalized magnetisation is shown as a function of background field. It should be noted that to proceed from one saturation branch to another and invert the polarity of the magnetisation, the background field has to change by $2B_p$.

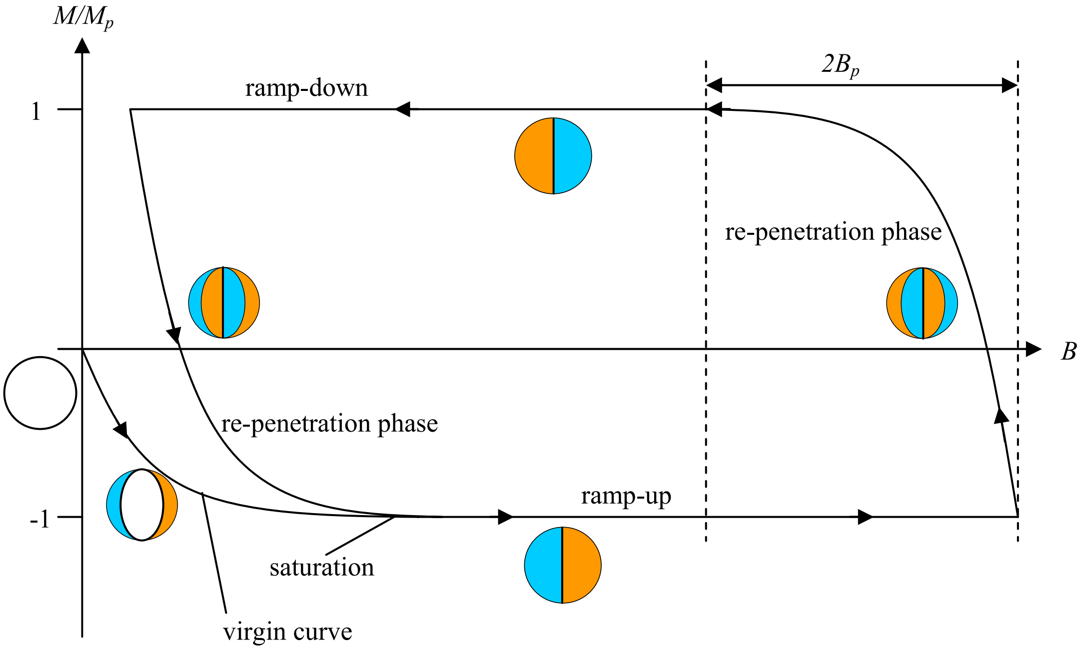

Figure 4.4: The normalized magnetisation M/M_p of a filament in the critical state (constant critical current density i.e. the field dependence of J_c is neglected) as a function of background field B. The hysteresis is a consequence of the persistent currents. The state of the shielding currents are also shown.

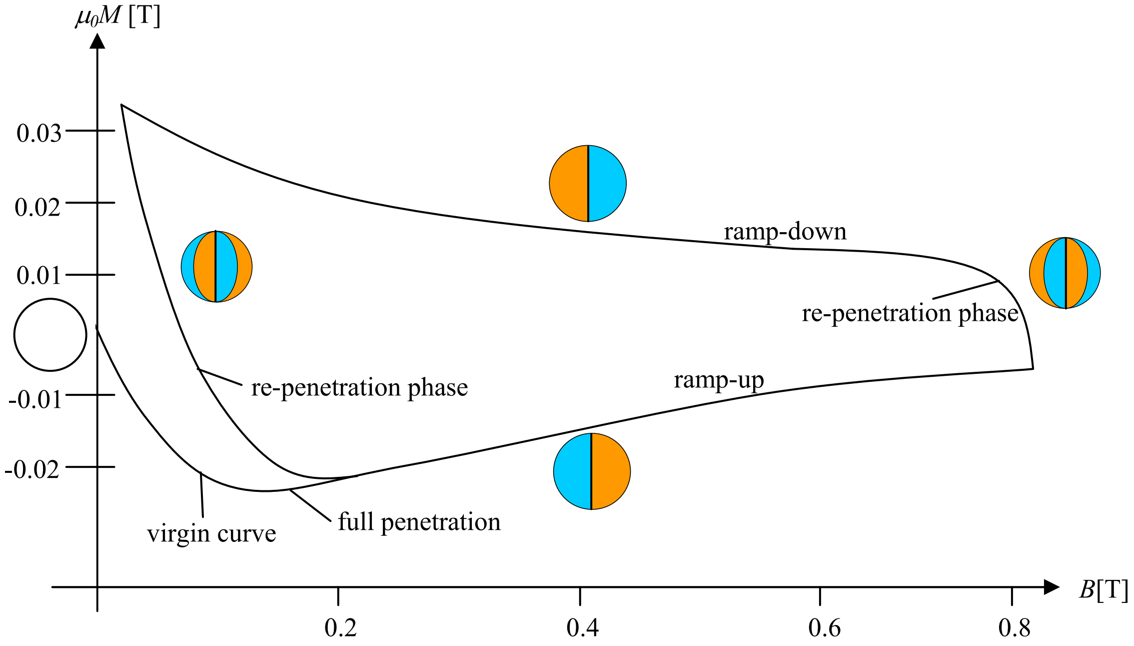

Figure 4.5: A typical magnetisation curve as a function of the magnetic field.

However, Figure 4.4 is a simplification of the magnetisation behaviour. In reality, the penetration field B_p and the saturation magnetisation M_p are not constant, but depend on the field and temperature dependent critical current $J_c(B,T)$. The shielding currents affect the field profile in the filament cross-section and cause an inhomogeneous distribution of the critical current density as shown in Figure 4.5.

To a first approximation, the magnetisation is proportional to the critical current density J_c and the filament diameter D_{fil} [60]:

$$M \propto J_c D_{fil} \tag{4.12}$$

In practical magnetisation calculations, fitting formulae for the critical surface $J_c(B,T)$ for the material in use (in this case Nb-Ti) are commonly used. Bottura in [73] uses expressions for critical temperature [74], critical field and pinning force density [75] to produce a simple but general fit of the critical surface of commercial Nb-Ti. A function which is empirically derived to fit the critical surface hence describing the critical current density as it changes with field is:

$$J_c \propto \frac{1}{B} b^p (1-b)^q \left(1-t^{1.7}\right)^h \tag{4.13}$$

where b is the reduced field defined as:

$$b = \frac{B}{B_c(T)} \tag{4.14}$$

and t is the reduced temperature defined as

$$t = \frac{T}{T_{co}} \tag{4.15}$$

$B_c(T)$ is defined as:

$$B_c(T) = B_{co}\left(1 - t^{1.7}\right) \tag{4.16}$$

B is the background field, B_c is the upper critical field of the material at $T = 0$ (14.5 T for Nb-Ti), B_{co} is the maximum upper critical field (at $T = 0$), T is the temperature, T_{co} is the critical temperature (9.5 K for Nb-Ti) and p, q and h are pinning exponents that are typically in the range $p = 0.5$, $q = 1$ and $h = 2$ for the Nb-Ti alloy used in the LHC cables. Note that J_c in Eq. 4.13 depends on temperature explicitly through the last term and implicitly through the critical field dependence of Eq. 4.16.

To the level of approximation of interest here (assuming flux creep is negligible [76]), M is stationary in time (d.c.) since the persistent currents have infinitely long time constants. Hence, the d.c. magnetisation appears as a hysteretic contribution to the field and field errors that depends on the strength of the magnetisation as well as on the geometric distribution of the magnetisation vectors in the winding cross-section. The strength of the magnetisation decreases with increasing background field, through the J_c dependence of Eqs. 4.13, to 4.16. As a result the magnetisation contribution is important at low field, i.e. injection level, where the magnitude and the variation of M in the coil cross-section is the largest. At high field level the contribution of the persistent current magnetisation decreases rapidly in accordance with Eqs. 4.13 to 4.16.

To provide a scaling for the field generated by the d.c. magnetisation (B_m^{MDC}) the expression for J_c in Eq. 4.13 can be adapted using Eq. 4.12. Current is substituted for field giving:

$$B_m^{MDC} = \mu_m I_{inj} \left(\frac{I}{I_{inj}}\right)^{p_m} \left(\frac{I_c - I}{I_c - I_{inj}}\right)^{q_m} \left(\frac{T_{co}^{1.7} - T^{1.7}}{T_{co}^{1.7} - T_{meas}^{1.7}}\right)^{h_m} \tag{4.17}$$

where the injection current I_{inj} and the measurement temperature T_{meas} are introduced as reference points so that the product of the three terms in I is equal to 1 at I_{inj}, and the term in T is equal to 1 at T_{meas}. With this normalization, the value of μ_m can be interpreted as the value of the contribution of the d.c. magnetisation to the total field measured at injection, which is at present a quantity directly stored in the measurement database. By writing Eq. 4.17 the assumption that the complex convolution of the distribution of magnetisation vectors can be condensed in the fitting exponents p_m, q_m and h_m is made. Dividing Eq. 4.17 by I the contribution to the transfer function is obtained:

$$TF^{MDC} = \mu_m \frac{I_{inj}}{I} \left(\frac{I}{I_{inj}} \right)^{p_m} \left(\frac{I_c - I}{I_c - I_{inj}} \right)^{q_m} \left(\frac{T_{co}^{1.7} - T^{1.7}}{T_{co}^{1.7} - T_{meas}^{1.7}} \right)^{h_m} \tag{4.18}$$

and the normalized harmonics originated by the d.c. magnetisation are:

$$c_n^{MDC} = \mu_n \left(\frac{I_{inj}}{I} \right)^{2-p_n} \left(\frac{I_c - I}{I_c - I_{inj}} \right)^{q_n} \left(\frac{T_{co}^{1.7} - T^{1.7}}{T_{co}^{1.7} - T_{meas}^{1.7}} \right)^{h_n} \tag{4.19}$$

which has a different form from Eq. 4.17 because of the renormalization to make μ_n the measured d.c. magnetisation harmonic at injection.

For a monotonic ramp (ramp-up or ramp-down), Eqs. 4.17, 4.18 and 4.19 hold when the filaments in the coil are in a fully penetrated state, i.e. after the crossing of the hysteresis cycle (penetration phase). The expressions are the same for different ramp directions, but the coefficients μ_m and μ_n for a downward ramp have opposite sign (and approximately same value) to those that best fit an upward ramp.

4.3.3 - Iron Saturation Contribution

The iron saturation contribution to the main field and field errors depends mostly on the iron yoke configuration and on the *B-H* characteristics of the iron structure. The iron yoke saturation appears as a non-linearity of the field and the field errors with respect to the operating current. This deviation is especially visible at high field levels, when the extent of saturation becomes significant. Even though it is highly non-linear and is also affected by the cross-talk between the apertures in the two-in-one design of the LHC lattice magnets (i.e. two magnets/apertures in one common yoke), the saturation is highly reproducible.

It is not easy to establish an a priori fit which can take the saturation into account by simple parameterization of the magnet cross-section. Therefore the choice is to fit the saturation contribution as a sum of rounded step functions for each harmonic. The following function, also plotted in Figure 4.6, was found to be suitable to model the saturation with good accuracy:

$$\Sigma(I,S,I_0,I_{nom}) = \frac{1}{\pi}\operatorname{atan}\left(S\left(\frac{I-I_0}{I_{nom}}\right)\right)+\frac{1}{2} \tag{4.20}$$

The main field is described as:

$$B_m^{saturation} = \sum_{i=1}^{N}\sigma_m^i I\,\Sigma\left(I,S_m^i,I_{0m}^i,I_{nom}\right) \tag{4.21}$$

N is typically 1 or 2 depending on the complexity of the geometry of the iron yoke. The nominal current I_{nom} is used to normalize the equation and σ, S and I_0 are the fitting parameters (omitting subscripts and superscripts).

The transfer function is correspondingly:

$$TF^{saturation} = \sum_{i=1}^{N}\sigma_m^i\Sigma\left(I,S_m^i,I_{0m}^i,I_{nom}\right) \tag{4.22}$$

and the harmonic coefficients are:

$$c_n^{saturation} = \sum_{i=1}^{N}\sigma_n^i\Sigma\left(I,S_n^i,I_{0n}^i,I_{nom}\right) \tag{4.23}.$$

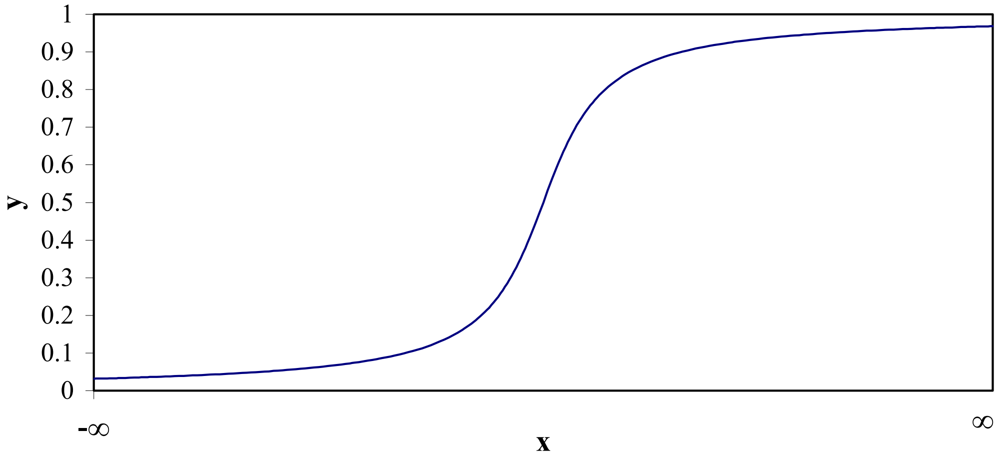

Figure 4.6: Smooth step function used to describe the change in field due to saturation: $\left(y=\frac{1}{\pi}\operatorname{atan}(x)+\frac{1}{2}\right)$.

4.3.4 - Displacement Contributions

Contributions to field and field errors due to coil deformation under electromagnetic loads are proportional to the Lorentz forces, and, in case the restraints defined by pre-stress do not change during powering, these errors are proportional to the square of the current [77]. In the most general situation, however, complex situations of establishment or loss of contact may arise. The contacts may be established or not depending on the amount of pre-stress in the structure. In general, the changes in field and field errors can only be obtained in detail using simulation codes that take into account the actual deformation for the specific pre-load case and therefore reconstruct the change in the field. In practice, the effect of the coil movement in the LHC magnets is small [52]. The static model can therefore be simplified by including any deformation effect in the saturation formulation above.

4.3.5 - Residual Magnetisation Contributions

After powering at nominal current, the magnetic components (e.g. the iron yoke) can be permanently magnetized. The residual magnetisation appears as a field contribution that is particularly important at small excitation currents, e.g. in warm conditions. The contribution to the main field can be described empirically as:

$$B_m^{residual} = \rho_m I \left(\frac{I_{inj}}{I} \right)^{r_m} \tag{4.24}$$

for the transfer function:

$$TF^{residual} = \rho_m \left(\frac{I_{inj}}{I} \right)^{r_m} \tag{4.25}$$

and for the field errors:

$$c_n^{\;residual} = \rho_n \left(\frac{I_{inj}}{I} \right)^{r_n} \tag{4.26}$$

where ρ and r are the fitting parameters.

The expressions discussed in the previous sections contain several fitting parameters with different meanings and units. To maintain a good overview, a summary of the 12 fitting parameters contained in the field model as devised here is reported in Table 4.1.

Table 4.1: Summary of the fitting parameters of the static field model.

	parameter meaning	**units**		
		B_m	TF	c_n
γ	geometric field error	(Tm/kA)	(Tm/kA)	(units)
g^{wc}	warm-cold correlation slope	(-)	(-)	(-)
Δ^{wc}	warm-cold correlation offset	(Tm/kA)	(Tm/kA)	(units)
μ	d.c. magnetisation strength	(Tm/kA)	(Tm/kA)	(units)
p	d.c. magnetisation pinning exponent	(-)	(-)	(-)
q	d.c. magnetisation pinning exponent	(-)	(-)	(-)
h	d.c. magnetisation pinning exponent	(-)	(-)	(-)
σ	iron saturation strength	(Tm/kA)	(Tm/kA)	(units)
I_0	iron saturation current	(A)	(A)	(A)
S	iron saturation current range	(-)	(-)	(-)
ρ	residual magnetisation strength	(Tm/kA)	(Tm/kA)	(units)
r	residual magnetisation exponent	(-)	(-)	(-)

Subscripts (for main field, transfer function and higher order harmonics) and superscripts (for summation indices) have been omitted for clarity. All parameters can be determined univocally from measured data, as shown in the following section.

4.4 - Parameter Computation

4.4.1 - Data Preparation

Based on the above definition of the harmonic components, a method to compute the static field model parameters was implemented. For this analysis, the measurements for currents equal or higher than the injection current I_{inj} (760 A) were selected. The highest measurement current I_{high} was taken to be equal to the nominal current I_{nom} (11850 A). The data used are the magnet integrated transfer function TF and the normalized integrated harmonics c_n obtained from the loadline measurements of the series magnetic measurements at cold (or using the correlation from warm measurements for the geometric component).

Each measurement k is associated to two values: the field harmonic, $b_{n,k}$ and the current measured, I_k. A superscript “up” means that the measurement is performed during the increasing current ramp. A superscript “down” means that the measurement is performed during the decreasing current ramp. Absence of index k means that all the measurements for a ramp-up or a ramp-down are being dealt with (usually two per current plateau). It should be noted that the measurements performed during the plateau at highest current belong to the ramp-up.

The data are first reduced to one value per plateau by taking the average value on each plateau.

$$I_k^{av} = \frac{\sum_{k=a}^{a+Q} I_k}{Q} \qquad\qquad c_{n,k}^{av} = \frac{\sum_{k=a}^{a+Q} c_{n,k}}{Q} \tag{4.27}$$

where Q is the number of measurements performed at $I_{k'}$ on the k'^{th} plateau.

Hence, one obtains the new averaged measurements:

$$c_n = \begin{bmatrix} c_{n,1}^{av\_up} \\ \vdots \\ c_{n,D_{up}}^{av\_up} \\ c_{n,1}^{av\_down} \\ \vdots \\ c_{n,D_{down}}^{av\_down} \end{bmatrix} = \begin{bmatrix} c_n^{up} \\ c_n^{down} \end{bmatrix} \text{, associated to } I = \begin{bmatrix} I_1^{av\_up} \\ \vdots \\ I_{D_{up}}^{av\_up} \\ I_1^{av\_down} \\ \vdots \\ I_{D_{down}}^{av\_down} \end{bmatrix} = \begin{bmatrix} I^{up} \\ I^{down} \end{bmatrix} \tag{4.28}$$

D_{up} is the number of plateaus performed when the current increases and D_{down} is the number of plateaus performed when the current decreases.

4.4.2 - The General Static Model

As described in Eq. 4.5, the model of the harmonics when the ramp direction is positive and negative is:

$$c_n^{DC\_up} = \gamma_n + \mu_n \left(\frac{I_{inj}}{I}\right)^{2-p_n} \left(\frac{I_c - I}{I_c - I_{inj}}\right)^{q_n} \left(\frac{T_{co}^{1.7} - T^{1.7}}{T_{co}^{1.7} - T_{meas}^{1.7}}\right)^{h_n} + \sum_{i=1}^{N} \sigma_n^i \Sigma\left(I, S_n^i, I_{0n}^i, I_{nom}\right) + \rho_n \left(\frac{I_{inj}}{I}\right)^{\gamma_n} \tag{4.29}$$

$$c_n^{DC\_down} = \gamma_n - \mu_n \left(\frac{I_{inj}}{I}\right)^{2-p_n} \left(\frac{I_c - I}{I_c - I_{inj}}\right)^{q_n} \left(\frac{T_{co}^{1.7} - T^{1.7}}{T_{co}^{1.7} - T_{meas}^{1.7}}\right)^{h_n} + \sum_{i=1}^{N} \sigma_n^i \Sigma\left(I, S_n^i, I_{0n}^i, I_{nom}\right) + \rho_n \left(\frac{I_{inj}}{I}\right)^{\gamma_n} \tag{4.30}$$

The model is highly non-linear so the usual minimization functions and fitting methods may not converge and could give results dependent on the initial conditions. Therefore, the fitting procedure had to be implemented in different stages.

4.4.3 - Modelling the Geometric Component

The geometric component is a shift of the whole hysteresis curve. This parameter can be easily computed by determining the offset of the hysteresis curve at 5000 A. However, this value is only the offset of the sample of magnets that were measured at cold. To obtain the real offset of all the magnet population, the warm measurements must also be considered. This is done by using Eqs. 4.1 and 4.11 so that:

$$c_n^{geometric} = \hat{\gamma}_n^{geometric} \tag{4.31}$$

where the cold measurements at 5000 A are correlated with the measurements at warm and where $\hat{\gamma}_n$ is the value of the geometric component to be used in the model.

Since the geometric component is solely calculated using the warm-cold correlation, the average geometric component of the data of Eq. 4.28 is redundant since it only represents the average geometric component of the magnets measured at cold (and not the entire magnet population being considered). Hence this value ($\hat{c}_n^{geometric}$) should be removed. This is done using Eq. 4.1, applying it on the data used for Eqs. 4.29 and 4.30 and then subtracting it from the data used for Eqs. 4.29 and 4.30. This yields:

$$c_n^{-geo} \equiv \begin{bmatrix} c_{n,1}^{up} \\ \vdots \\ c_{n,D_{up}}^{up} \\ c_{n,1}^{down} \\ \vdots \\ c_{n,D_{down}}^{down} \end{bmatrix} - \hat{c}_n^{geometric} \equiv \begin{bmatrix} c_n^{-geo\_up} \\ c_n^{-geo\_down} \end{bmatrix} \text{ associated to } I \equiv \begin{bmatrix} I_1^{up} \\ \vdots \\ I_{D_{up}}^{up} \\ I_1^{down} \\ \vdots \\ I_{D_{down}}^{down} \end{bmatrix} \equiv \begin{bmatrix} I^{up} \\ I^{down} \end{bmatrix} \tag{4.32}$$

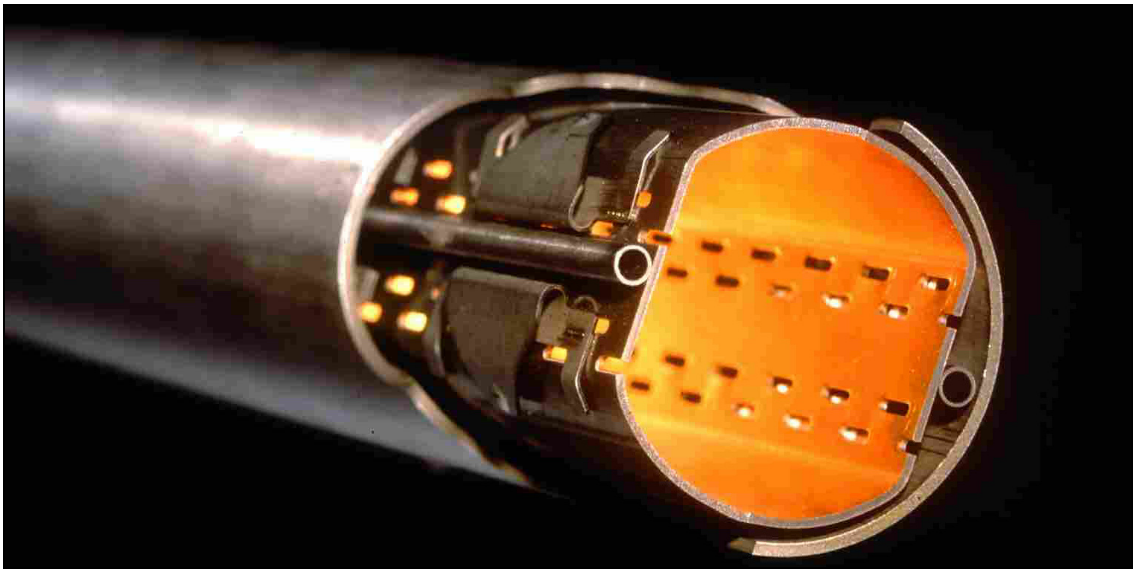

Figure 4.7: The beam screen.

Table 4.2: The shift to be added to the absolute harmonic value to compensate for the beam screen effect on the harmonics.

	TF	b_2	a_2	b_3	a_3	b_4	a_4	b_5	a_5
$c_n^{beamscreen}$	0.000	0.000	0.000	–0.420	0.000	0.000	0.000	0.386	0.000

Another correction needs to be implemented at this point due to the beam screen. The LHC beam screen which is shown in Figure 4.7 is a stainless steel pipe with a 50 μm copper layer coated on its inner surface. It is cooled to a temperature ranging from 5 to 20 K. Its role is to intercept and protect the outer cold bore which is at 1.9 K from the synchrotron radiation power emitted by the LHC proton bunches. The effect of the beam screen on the harmonics is known to be equivalent to a shift of the absolute harmonic value at all excitation currents [78]. Since the cold measurements were performed without the beam screen, the values of the geometric component obtained from the warm-cold correlation must be augmented by the values $c_n^{beamscreen}$ shown in Table 4.2.

Therefore, Eq. 4.31 becomes:

$$c_n^{geometric} = \hat{\gamma}_n^{geometric} + c_n^{beamscreen} \tag{4.33}$$

4.4.4 - Data Pre-treatment

Since the plateaus of the loadline are at the same currents during ramp-up and ramp-down, the average harmonic can be computed by using the formula:

$$\bar{c}_n^{av}(I_k) = \frac{c_n^{-geo\_up}(I_k^{up}) + c_n^{-geo\_down}(I_k^{up})}{2} \tag{4.34}$$

The average value $\bar{c}_n^{av}(I_k)$ along the hysteresis curve is removed and the residual magnetisation and the saturation are modelled on this average data. Therefore the model of the average data is:

$$\bar{c}_n^{av}(I_k) = \sum_{i=1}^{N} \sigma_n^i \Sigma\left(I, S_n^i, I_{0n}^i, I_{nom}\right) + \rho_n \left(\frac{I_{inj}}{I}\right)^{r_n} \tag{4.35}$$

The d.c. magnetisation is symmetric for the ramp-up and the ramp-down, so this component can be modelled on the rest of the data.

4.4.5 - Modelling the Saturation and the Residual Magnetisation

The two terms in Eq. 4.35 describe the saturation and the residual magnetisation. These two components manifest in the two extreme current values; the saturation becomes important at nominal current whilst the residual magnetisation is an effect which is important at low currents, i.e. at injection current. The hysteresis curve is divided in two at $I_{geometric}$ and the two components are therefore separated by modelling them in their respective current value of interest. This division is performed by:

$$\bar{c}_n^{av}\left(I_k^{geo+}\right) \equiv \bar{c}_n^{av}\left(I > I_{geometric}\right) \tag{4.36}$$

$$\bar{c}_n^{av}\left(I_k^{geo-}\right) \equiv \bar{c}_n^{av}\left(I < I_{geometric}\right) \tag{4.37}$$

Therefore Eqs. 4.36 and 4.37 can be used to perform the fits of the saturation and residual magnetisation using the Levenberg-Marquardt algorithm [79-80] to get:

$$\hat{c}_n^{saturation}(I_k^{geo+}) = \sum_{i=1}^{N} \hat{\sigma}_n^i \Sigma\left(I, \hat{S}_n^i, \hat{I}_{0n}^i, \hat{I}_{nom}\right) \tag{4.38}$$

$$\hat{c}_n^{residual}(I_k^{geo-}) = \hat{\rho}_n \left(\frac{I_{inj}}{I}\right)^{\hat{r}_n} \tag{4.39}$$

The result of these fits is a set of optimized parameters $\hat{\rho}_n$, $\hat{r}_n$ $\hat{\sigma}_n^i$, $\hat{S}_n^i$, $\hat{I}_{0n}^i$. These parameters are then substituted in Eq. 4.35 to obtain:

$$\hat{c}_n^{av} = \sum_{i=1}^{N} \hat{\sigma}_n^i \Sigma\left(I, \hat{S}_n^i, \hat{I}_{0n}^i, I_{nom}\right) + \hat{\rho}_n \left(\frac{I_{inj}}{I}\right)^{\hat{r}_n} \tag{4.40}$$

4.4.6 - Modelling the d.c. Magnetisation

The d.c. magnetisation is the ramp direction dependent part of the harmonic. So, for each measurement, one can compute the d.c. magnetisation by first removing the already modelled components:

$$c_n^{MDC\_up} = c_n^{up} - \hat{c}_n^{av} - c_n^{geometric} \tag{4.41}$$

$$c_n^{MDC\_down} = c_n^{down} - \hat{c}_n^{av} - c_n^{geometric} \tag{4.42}$$

The data $c_n^{MDC\_up}$ and $c_n^{MDC\_down}$ are therefore used to model the d.c. magnetisation. Using Eqs. 4.29 and 4.30;

$$\hat{c}_n^{MDC\_up} = \hat{\mu}_n \left(\frac{I_{inj}}{I}\right)^{2-\hat{p}_n} \left(\frac{I_c - I}{I_c - I_{inj}}\right)^{\hat{q}_n} \left(\frac{T_{co}^{1.7} - T^{1.7}}{T_{co}^{1.7} - T_{meas}^{1.7}}\right)^{\hat{h}_n} \tag{4.43}$$

$$\hat{c}_n^{MDC\_down} = -\hat{\mu}_n \left(\frac{I_{inj}}{I}\right)^{2-\hat{p}_n} \left(\frac{I_c - I}{I_c - I_{inj}}\right)^{\hat{q}_n} \left(\frac{T_{co}^{1.7} - T^{1.7}}{T_{co}^{1.7} - T_{meas}^{1.7}}\right)^{\hat{h}_n} \tag{4.44}$$

where $\hat{\mu}_n$, $\hat{p}_n$, $\hat{q}_n$ and $\hat{h}_n$ are the parameters of the model and are equal for both Eqs. 4.43 and 4.44.

4.4.7 - The Static Field Model Parameters

The parameters are fitted with a good accuracy; however, the convergence of the fit highly depends on the initial values assigned to the parameters. Therefore, a check is performed at the end of each fit to verify its convergence. In case the fit does not converge or if the error of the fit with respect to the data is still large, the data are re-fitted with new initial values. The result of the static model is finally:

$$\hat{c}_n^{DC\_up} = \hat{\gamma}_n^{geometric} + c_n^{beamscreen} + \hat{\mu}_n \left(\frac{I_{inj}}{I} \right)^{2-\hat{p}_n} \left(\frac{I_c - I}{I_c - I_{inj}} \right)^{\hat{q}_n} \left(\frac{T_{co}^{1.7} - T^{1.7}}{T_{co}^{1.7} - T_{meas}^{1.7}} \right)^{\hat{h}_n}$$

$$+ \sum_{i=1}^{N} \hat{\sigma}_n^i \Sigma\left(I, \hat{S}_n^i, \hat{I}_{0n}^i, \hat{I}_{nom}\right) + \hat{\rho}_n \left(\frac{I_{inj}}{I} \right)^{\hat{\gamma}_n} \qquad (4.45)$$

$$\hat{c}_n^{DC\_down} = \hat{\gamma}_n^{geometric} + c_n^{beamscreen} - \hat{\mu}_n \left(\frac{I_{inj}}{I} \right)^{2-\hat{p}_n} \left(\frac{I_c - I}{I_c - I_{inj}} \right)^{\hat{q}_n} \left(\frac{T_{co}^{1.7} - T^{1.7}}{T_{co}^{1.7} - T_{meas}^{1.7}} \right)^{\hat{h}_n}$$

$$+ \sum_{i=1}^{N} \hat{\sigma}_n^i \Sigma\left(I, \hat{S}_n^i, \hat{I}_{0n}^i, \hat{I}_{nom}\right) + \hat{\rho}_n \left(\frac{I_{inj}}{I} \right)^{\hat{\gamma}_n} \qquad (4.46)$$

Figures 4.8 and 4.9 show the procedure used to determine the parameters of the static field model applied on the normal quadrupole step-by-step. Figure 4.8 (top) shows the b_2 data obtained from the average of the integrated harmonic of the 130 apertures considered, Figure 4.8 (middle) shows the data with the geometric component removed and Figure 4.8 (bottom) shows the fit of the residual magnetisation after applying Eq. 4.39. Figure 4.9 (top) continues with the procedure and shows the fit of the saturation after Eq. 4.38 is applied. This figure also shows the two step functions used to model the curve. Figure 4.9 (bottom) shows the fit of the ramp-up and ramp-down magnetisation. The result of Figure 4.10 shows the resulting b_2 static model.

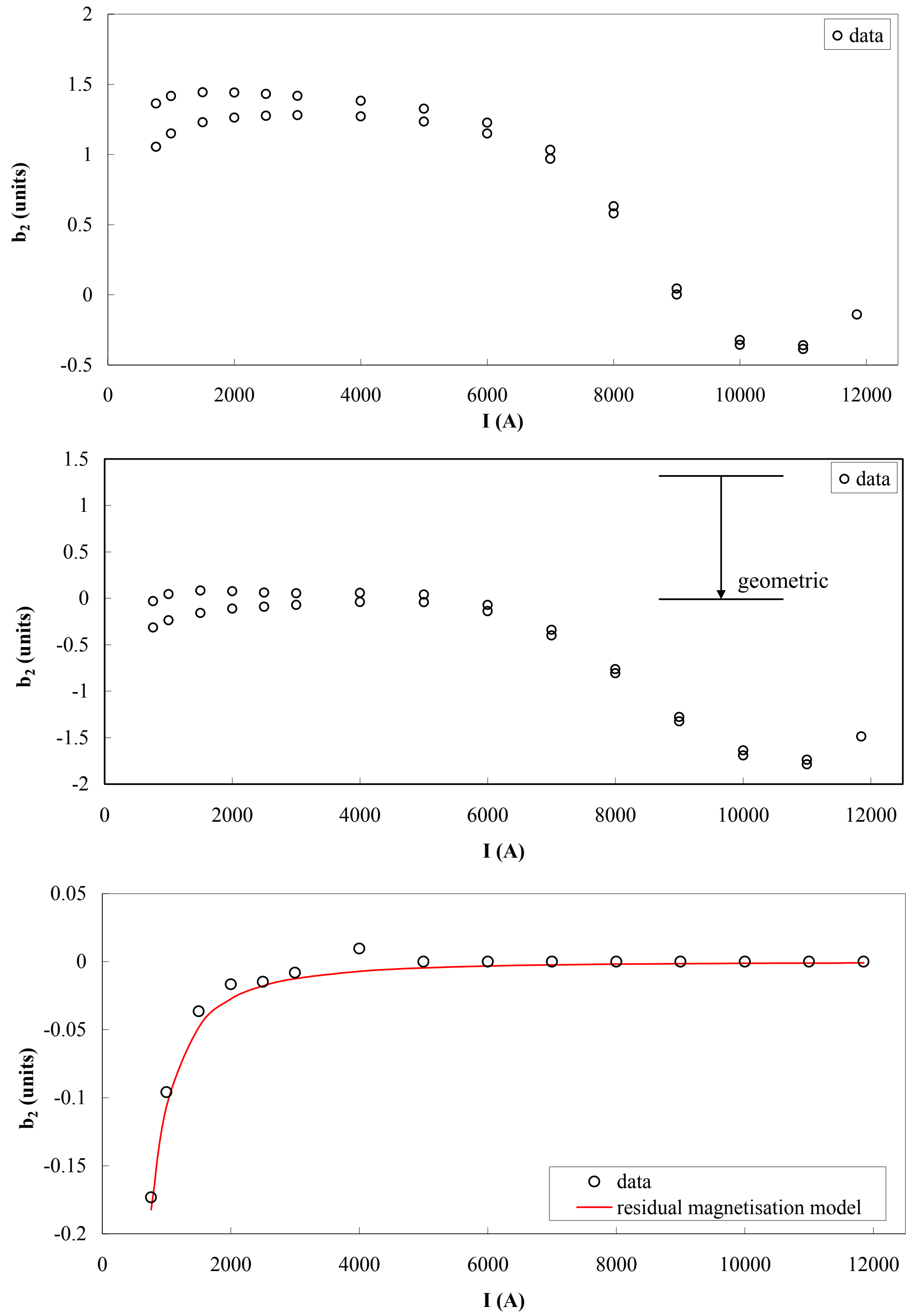

Figure 4.8: The step-by-step procedure used to evaluate the static model parameters. **(top)** average data; **(middle)** data - geometric component; **(bottom)** fit of the residual magnetisation.

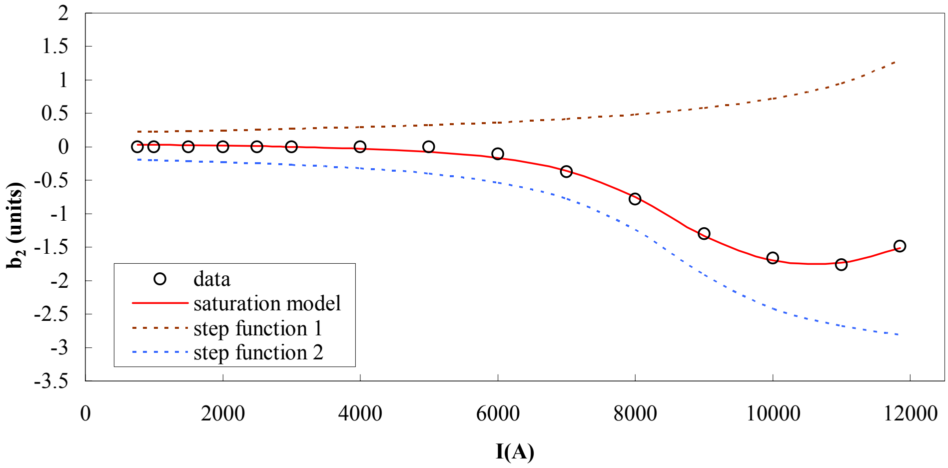

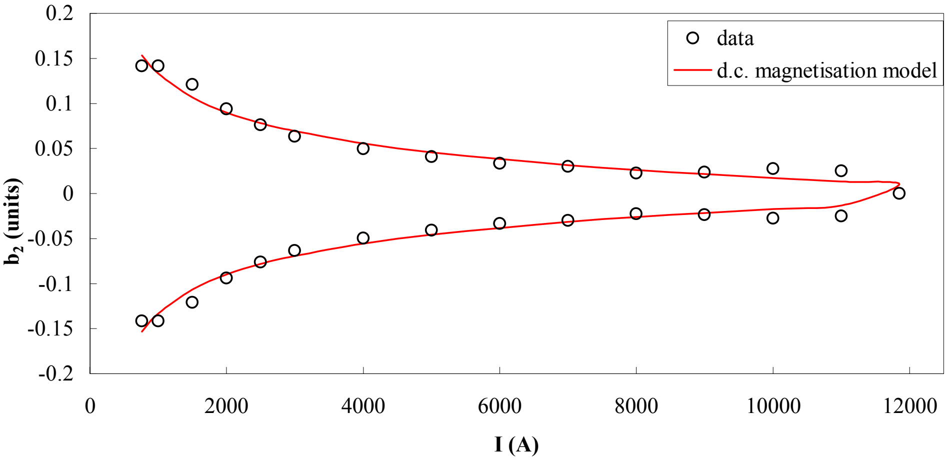

Figure 4.9: The step-by-step procedure used to evaluate the static model parameters. **(top)** the saturation fit; **(bottom)** the d.c. magnetisation fit.

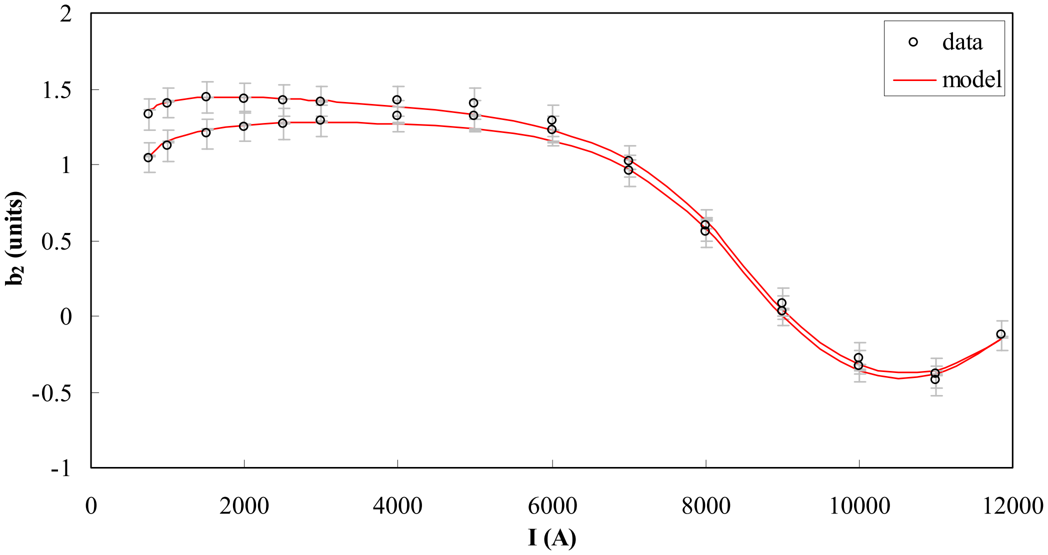

Figure 4.10: Modelling result of b_2. The error bars show the measurement uncertainty. (The repeatability error is an order of magnitude lower).

4.5 - Application of the Model for the Dipoles on a Sector

To test the capability of the static field model, the forecast of the field and the field errors is performed on a sector of the LHC. The data of 65 dipole magnets (130 apertures) to be installed in sector 7-8, collected during the series cold tests, are used as a base to compute the parameters. The measured main field and field harmonics are averaged over the sampled magnets of the sector to obtain an estimate of the integral quantities. The sample of the magnets tested at cold is then extrapolated to the whole magnet population of the sector (164 magnets) by using the warm-cold correlation and adjusting the geometric component as described in the previous section. The results for the main field transfer function and the first harmonics are shown in Figures 4.11 and 4.12. All major features of the current dependence are reproduced very well. Figure 4.13 shows the model error defined as the maximum deviation between the analytical model and the measured data. The model is effective, providing an interpolation of the field and field quality comparable to the rotating coil measurement uncertainty (better than 0.1 units @17mm for the harmonics and 0.44 units for the TF) in the range between injection (760 A) and collision current (11850 A). Table 4.3 and 4.4 show the model parameters.

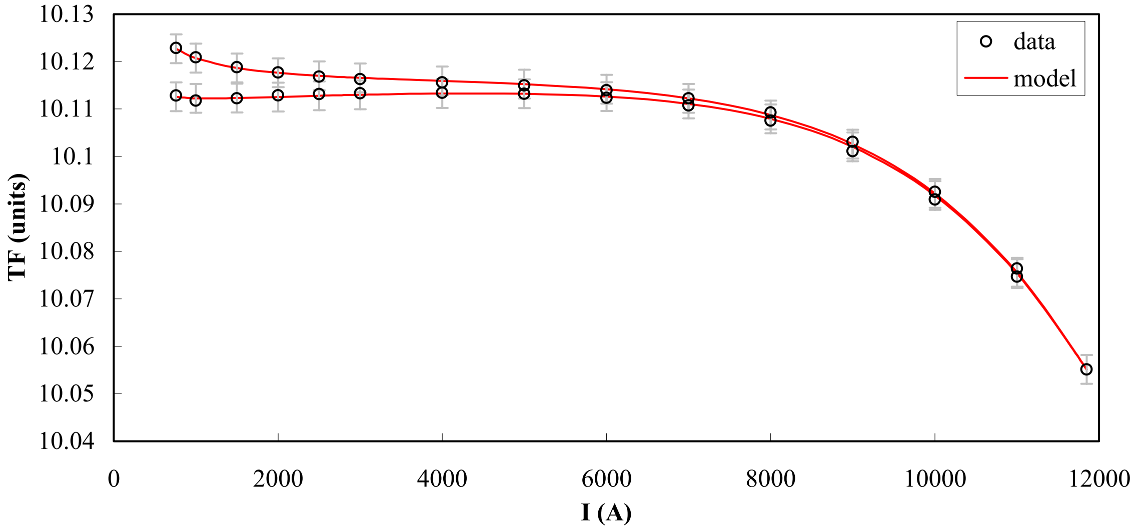

Figure 4.11: Modelling of the integral transfer function (TF) using loadline data from all cold tested magnets in the LHC sector 7-8. The error bars show the measurement uncertainty. (The repeatability error is an order of magnitude lower).

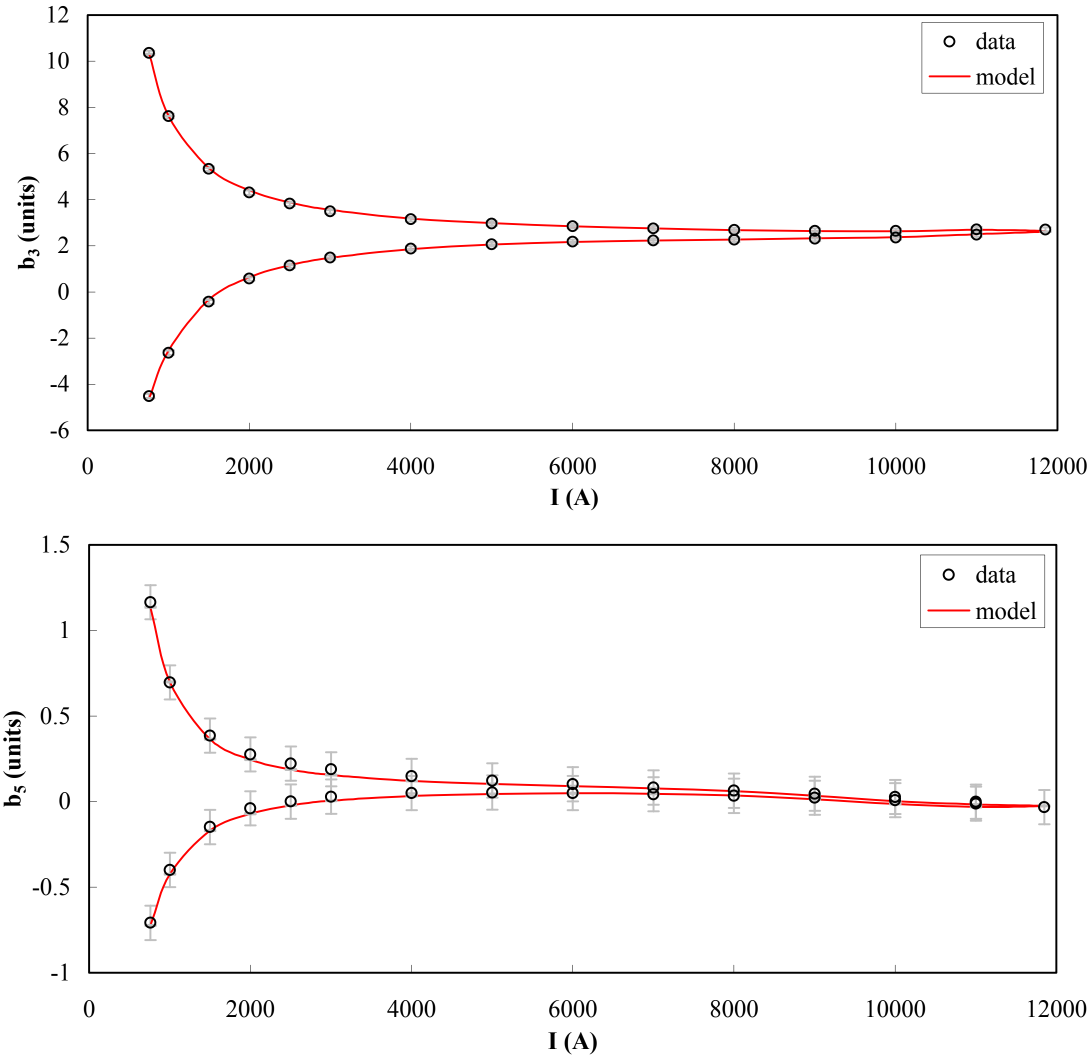

Figure 4.12: Modelling of the normal sextupole and the normal decapole using loadline data from all cold tested magnets in the LHC sector 7-8. The error bars show the measurement uncertainty. (The repeatability error is an order of magnitude lower).

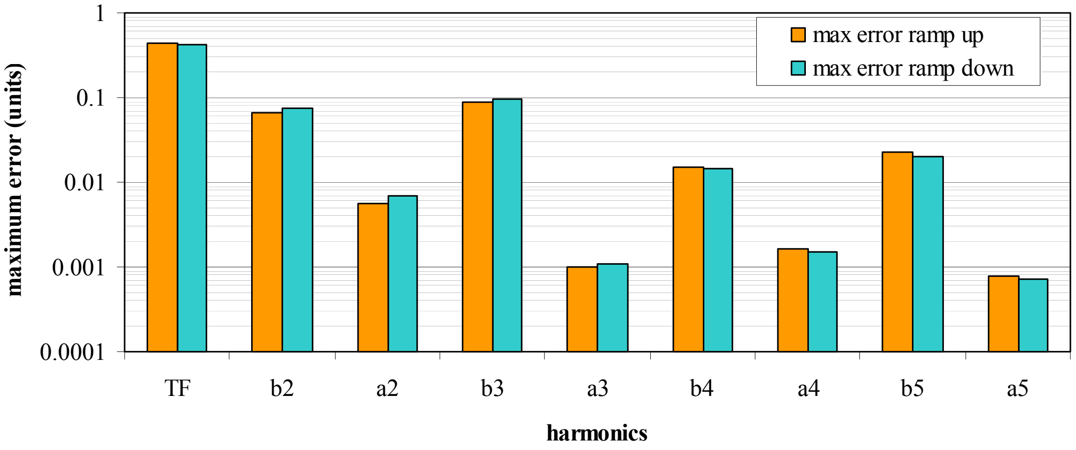

Figure 4.13: Maximum error between measured data and model. (Note that the TF plot of Figure 4.11 is plotted in Tm/kA whilst the TF error here is in units to maintain consistency).

Table 4.3: The values of the warm-cold correlation offset and the standard deviation of the difference between the points and the correlation line along the y-axis. The units are the same as shown in Table 4.1.

	TF	**b_2**	**a_2**	**b_3**	**a_3**	**b_4**	**a_4**	**b_5**	**a_5**
Δ^{wc}	0.0083	−1.370	−0.015	−0.319	−0.002	−0.025	0.015	−0.132	0.012
std dev	0.0047	0.361	0.191	0.196	0.093	0.042	0.050	0.063	0.020

Table 4.4: Parameters used for modelling the field and field errors in the LHC dipoles of sector 7-8. The units of the parameters are the same as shown in Table 4.1.

	TF	**b_2**	**a_2**	**b_3**	**a_3**	**b_4**	**a_4**	**b_5**	**a_5**
γ	**10.1141**	**1.3601**	**0.031**	**2.518**	**−0.132**	**0.072**	**0.025**	**0.088**	**0.057**
μ	**−0.0055**	**0.154**	**−0.032**	**−7.466**	**0.026**	**−0.001**	**−0.008**	**0.929**	**0.003**
p	0.4487	1.532	0.467	0.630	1.116	0.012	0.420	0.168	1.430
q	1.6715	0.929	1.103	0.550	1.015	1.136	1.105	0.000	0.977
h	2.000	2.000	2.000	2.000	2.000	2.000	2.000	2.000	2.000
σ^1	**−0.4203**	**−3.241**	**−0.118**	**−0.095**	**−0.008**	**0.207**	**−0.002**	**−0.142**	**−0.002**
I_0^1	13239	8568	11090	7224	10255	10055	11429	9213	7712
S^1	3.5519	8.088	32.181	9.760	10.453	12.985	13.965	8.150	4.446
σ^2	**0.1657**	**20.131**	**-**	**0.347**	**-**	**-**	**-**	**-**	**0.026**
I_0^2	9735	14107	-	11031	-	-	-	-	16672
S^2	1.7023	25.551	-	16.923	-	-	-	-	21.333
ρ	**0.0037**	**−0.182**	**−0.008**	**0.340**	**−0.018**	**−0.011**	**−0.002**	**0.126**	**−0.009**
r	1.3992	1.953	2.817	10.000	2.522	1.357	1.885	2.851	3.974

The parameters in Table 4.4 are grouped according to the physical origin. Because of the definitions already discussed, the parameters in bold also represent the order of magnitude of the contribution and may give an indication of the relative weight of each component. As expected, and depending on the harmonic considered, some components are dominant. This is consistent with the curves shown in Figure 4.10, 4.11 and 4.12. For instance, in the case of b_3, the geometric and d.c. magnetisation are the dominant components (effect of 7 units) whilst the saturation and the residual magnetisation modelling may be regarded as a fine tuning correction (effect of 0.3 units). By contrast, in the case of the TF and b_2, the saturation component is dominant over the d.c. and the residual magnetisation by two orders of magnitude. Therefore, the modelling of the saturation in this case is very important (effect of 60 units of TF and 2 units of b_2), whilst the modelling of the other components is less critical (effect of 6 units of TF and 0.2 of b_2). In the case of b_2, it should also be noted that the large saturation coefficient (σ^2) is large due to the large saturation current range (S) and the large saturation current (I_0) as indicated by step function 1 in Figure 4.9 (top).

4.6 - Conclusion

The static field model is the foundation of FIDEL since it provides a mathematical formulation of the reproducible magnetic effects in the machine's main magnets. It is based on a parameterisation of the data obtained from warm measurements as well as series loadline magnetic measurements at cold. The model heavily relies on the decomposition and hence on the mutual independence of the different components of the field errors.

The model's components include geometric, d.c. magnetisation, saturation, displacement and residual magnetisation contributions. Based on the physical understanding of these components, a mathematical formulation is drawn up to describe their contribution to the main field and the field harmonics. Where the physical effects are too complicated to be represented analytically, empirical equations are used to approximate the phenomena with good precision.

After formulating the components, a minimisation procedure is set up to overcome non-linearities in the equations and to determine the model parameters. The result of the dipole modelling is very satisfactory providing a maximum error of 0.44 units for the transfer function and 0.1 units for the harmonics. The static model therefore provides a powerful tool to predict the reproducible current dependent magnetic state of the LHC during its operation.

Chapter 5

The Dynamic Field Model

LHC string ready for testing.

Theory without experiment
is like a bird without legs.
- Gordon Kane

Chapter 5

The Dynamic Field Model

As an extension of the static field model, the dynamic field model is based on the understanding of the magnetic effects which are dependent on both current and time and which may not be reproducible from cycle to cycle. The dynamic effects affect the machine mostly at injection and at the beginning of acceleration and include decay, snapback and coupling current contributions.

The dynamic model is established on the understanding of the physical origins of the components. It is based on series and extended magnetic measurements at cold using the rotating coils and the snapback analyser.

In this chapter, the physical origins of the dynamic effects are highlighted and the mathematical formulation to be used in FIDEL is presented. The dependence of the decay amplitude on the powering history of the magnet is also discussed and modelled hence providing a solution to the non reproducibility of the magnetic state from cycle to cycle.

5.1 - Introduction

The dynamic field model is a continuation of the static field model and provides a mathematical description of the superconducting magnets' behaviour in their current and time dependent domain, which to a certain extent is not reproducible from one powering cycle to the following one. The model is constructed in the same manner as the static field model i.e.:

a. Identification of the field error components.
b. Formulation of the mathematical description of the field errors.
c. The use of series LHC cycle measurements to obtain the time-dependence of the magnet population being modeled.
d. Establishment of a minimization procedure to determine the mathematical formulation parameters.

The time dependent domain becomes particularly important when the current is kept constant i.e. on a constant current plateau like the injection plateau and just after the current begins to ramp. The effects associated to the current and time dependent domain are also known as a.c. components and are dependent on the ramp rate of the current excitation and on the powering history of the magnet.

5.2 - Physical Decomposition of Dynamic Field Errors

a. Decay (C_n^{decay}), is an effect due to current redistributions in the superconducting cables. It manifests itself as a change of the main field and of the harmonics and is important during beam injection and in general, whenever the current is kept constant at low field. The magnitude of the decay depends on the waveform and waiting times of previous cycles thus making this effect non-reproducible from cycle to cycle.

b. Snapback ($C_n^{snapback}$), is the rapid re-establishment of the magnetisation after its decay during a constant current plateau and is important at the beginning of the acceleration ramp. The same considerations on reproducibility are valid as for the decay.

c. *Coupling currents* (C_n^{MAC}), component which is the contribution due to interfilamentary currents within the strand and interstrand currents within the cable. This contribution is only present during changes in the operating field, e.g. during energy ramp. It is reproducible and depends on the ramp rate (*dI/dt*).

Figure 5.1 shows the typical variation of the b_3 harmonic during the LHC cycle as a function of time. The decay phenomenon can be clearly identified as a drift whilst the current is kept constant. The snapback can be clearly identified as the re-establishment of the magnetisation as soon as the current begins to ramp.

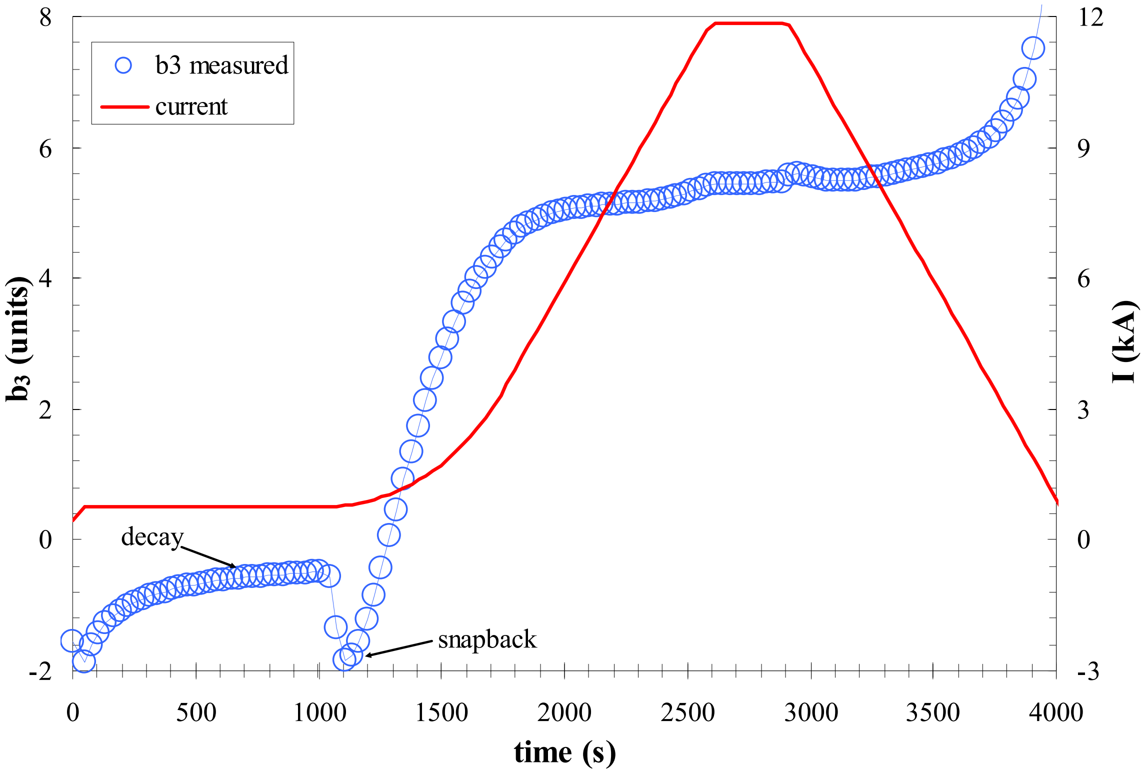

Figure 5.1: Integral Sextupole variation of a typical dipole magnet plotted vs. time (in blue, left axis) and the excitation current during the simulated LHC cycle (in red, right axis).

5.3 - Mathematical Formulation

As was the case for the static field model, the dynamic field model relies on the mutual independence of the components. This is perfectly justified since the effects can be isolated in different time periods of the cycle i.e. the decay on the injection plateau, the snapback as soon as the acceleration starts and the coupling current when there is a fast change in current. The eddy current effect can be ignored at the beginning of the acceleration since the LHC PELP acceleration was optimized to significantly reduce this effect on this part of the cycle [65]. The eddy current effect is, however, still monitored by using a different kind of measurement excitation cycle. This will be discussed in section 5.7.

Under this assumption, the field model can be given by the sum of the contributions:

$$C_n^{AC} = C_n^{decay} + C_n^{snapback} + C_n^{MAC} \tag{5.1}$$

where C_n^{AC} is the dynamic component. Using this equation and Eq. 4.5 yields:

$$C_n = C_n^{DC} + C_n^{AC} \tag{5.2}$$

which therefore combines the static and dynamic domains and hence provides a full description of the main field and its harmonics of the magnet population being considered.

5.4 - The Field Decay

5.4.1 - The Decay Phenomenon

The decay effect was discovered at the commissioning of the Tevatron in 1987 [81] where it caused the chromaticity to change by as much as 70 units over a few hours. Originally, the decay was thought to originate from flux creep. However, magnetisation measurements performed by Kuchnir and Tollestrup [82] revealed that flux creep rates where an order of magnitude smaller than those observed in cables. This was confirmed by Le Naour [83] who performed magnetisation measurements on LHC strands. Eventually, the dominant contribution was found to be the result of a non uniform current distribution in the Rutherford cable as it is wound in the magnet coil. An illustration of the current imbalance is shown in Figure 5.2.

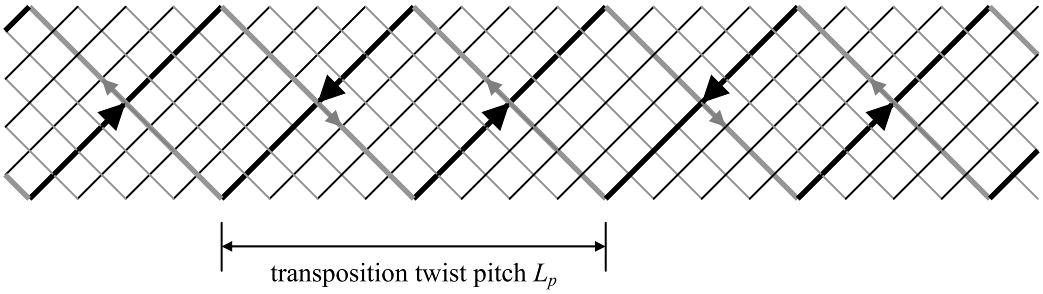

Figure 5.2: Two strands in a Rutherford-type cable carrying a larger current, flowing in a long loop.

The non uniform current distribution originates in parts of the magnet where there are spatial gradients in the field sweep rate (perpendicular to the large face of the cable) [84]. These gradients especially appear in the coil ends, in cable-to-cable connections and in connections of the cable to the current leads. Less importantly, the non uniform current distribution can also be induced in gradients of the cross-contact resistances which exist along the cable. These mainly appear in gradients in the transverse pressure, soldered connections or local shorts between strands or key-stoning of the cable.

Krempasky and Schmidt in [85-86] demonstrated how the non uniform current distribution diffuses in a twisted two-wire cable. The same effect was extended to a cable with a generic number of strands by Bottura, Breschi and Fabbri [87]. The non uniform current distribution diffusion was also demonstrated experimentally by Sampson and Ghosh in [88] where they exposed a cable winding without transport current to a variable external field hence inducing a periodic field pattern.

In the magnet aperture, the current imbalance is observed as a spatially Periodic Field Pattern (PFP) in all field components with a period comparable to the transposition twist pitch of the Rutherford cable. This phenomenon was first observed in HERA dipole magnets [89] and can be approximated by a sinusoid. Effectively, the PFP results from a superposition of the fields induced by the current imbalances in all the turns of the coil. Fortunately, the PFP does not affect the proton beam emittance in the machine since the oscillations are orders of magnitude smaller than the betatron wavelength.

Wolf in [90], shows how the decay can be explained as the reduction of filament magnetisation due to the current imbalances diffusing along the length of the cables inside the coil. As currents redistribute and the PFP forms, the superconducting filaments within the strands see minute changes of the local magnetic field. If these local changes in magnetic field are not overwhelmed by the change of field caused by a change in transport current in the magnet (such as during ramping), the superconductor magnetisation will also change as a result of it. As was already described in chapter 4, when a superconductor is exposed to an external magnetic field, shielding super-currents are generated that partially shield the inside of the filaments from that field. As the external field is decreased the superconductor traps field inside, again generating a magnetic moment that is opposed to the external field change. This magnetisation produces most of the low field hysteresis in the superconducting magnets.

When the field is ramped up, the strand magnetisation evolves along the hysteretic loop. When on the constant current injection plateau, the current imbalance forms resulting in a PFP. At this point two cases should be considered which are also illustrated in Figure 5.3:

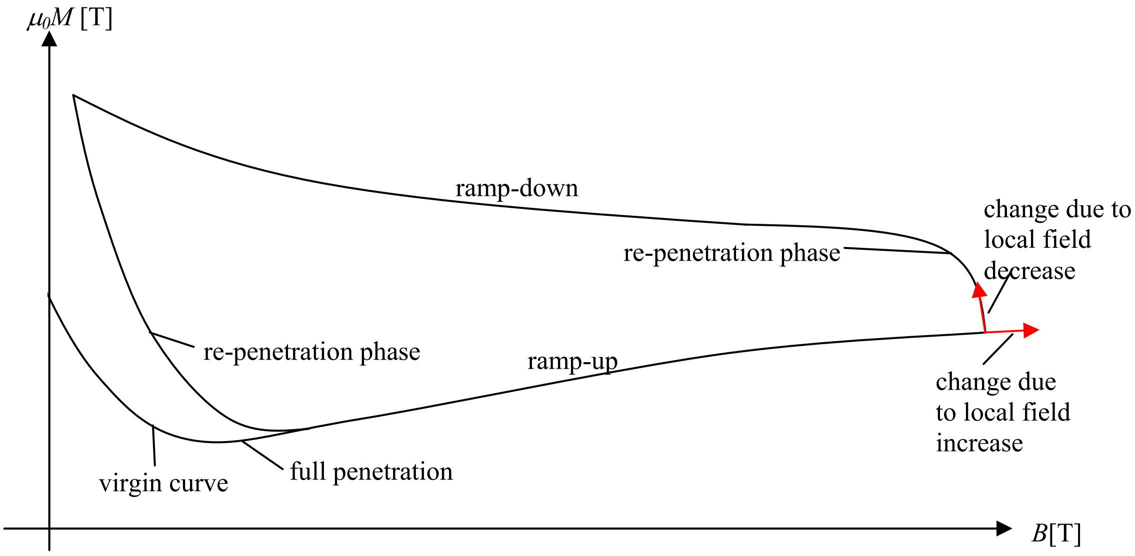

Figure 5.3: A filament magnetisation curve showing a large change in magnetisation due to a local field decrease and a small change in magnetisation due to a local field increase.

a. *local field decrease:* a sudden opposition to a decreasing field produces a very strong change of the superconductor magnetisation, as one flips to the "other" side of the loop through the re-penetration phase. This strong change is the result of an instantaneous excitation of a new shielding current with opposite polarity.

b. *local field increase:* an opposition to an increasing field produces a very weak change of the superconductor magnetisation as one remains on the ramp-up phase.

Therefore the shielding current reversal has a much larger effect on the superconductor magnetisation than a small change of field along the hysteretic loop. Hence as the current imbalances diffuse with time along the cable, a decay in the magnetisation occurs due to a lowering of the average magnetisation. This is shown in Figure 5.4.

Unfortunately, the number of pitch lengths between coil heads and the value of the cross-contact resistance vary from magnet to magnet and from turn to turn. Both these two parameters affect the formation of the PFP but are very difficult to control and vary a lot from magnet to magnet. This results in a large decay spread in the magnet population. In the case of the LHC, the standard deviation is 0.5 units for b_3.

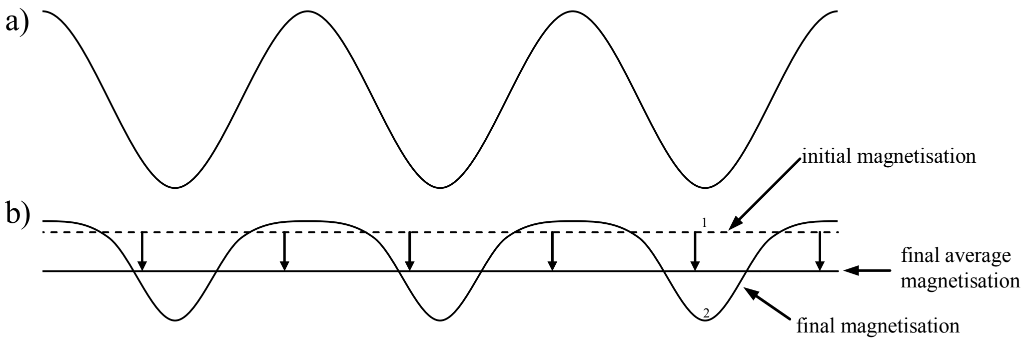

Figure 5.4: (a) The current redistribution causes a change of the local external field along the cable; **(b)** The local field change has a non-linear impact on the magnetisation. This results in a decay in the allowed field harmonics. The magnetisation changes from the dotted line distribution to the straight line distribution in sequence as indicated by the numbering.

5.4.2 - Mathematical Decay Formulation

From the solution of the current diffusion equation [87], a mathematical formulation can be derived to describe the decay evolution in time. The terms that contain parameters that are impossible to determine (such as the cross-contact resistance and its variation along the coils) are substituted by constants that can be determined by fitting the equation curves to cold magnetic measurement data. The normalised decay can therefore be modelled by the following equation:

$$\Delta\left(t,t_{inj},\tau,d\right)=d\left(1-e^{-\frac{t-t_{inj}}{\tau}}\right)+\left(1-d\right)\left(1-e^{-\frac{t-t_{inj}}{9\tau}}\right) \tag{5.3}$$

which holds for $I = I_{inj}$ and $t > t_{inj}$. t is the instantaneous time, t_{inj} is the time when injection starts, I_{inj} is the current at injection, τ is the time constant. The parameter d gives the normalized weight of the fast mode of the decay and its complement to one, $1-d$, gives the normalized weight of the slow mode. Making the hypothesis that the cable current distributes continuously among the strands of a uniform cable, the time evolution of the currents is governed by an infinite series of harmonic modes damped by an exponential with time constants $\tau_n = \frac{\tau}{(2n-1)^2}$ [87]. Eq. 5.3 is limited to the first two modes. The main field decay, using Eq. 5.3, is given by:

$$B_m^{decay} = \delta_m I \frac{\Delta\left(t,t_{inj},\tau_m,d_m\right)}{\Delta\left(t_{inj}^{std},t_{inj},\tau_m,d_m\right)} \tag{5.4}$$

where the parameter δ_m represents the decay amplitude at a reference time t_{inj}^{std}. The contribution of decay to the transfer function is modelled by:

$$TF^{decay} = \delta_m \frac{\Delta\left(t,t_{inj},\tau_m,d_m\right)}{\Delta\left(t_{inj}^{std},t_{inj},\tau_m,d_m\right)} \tag{5.5}$$

and by analogy the contribution to the harmonics is given by:

$$c_n^{decay} = \delta_n \frac{\Delta\left(t,t_{inj},\tau_n,d_n\right)}{\Delta\left(t_{inj}^{std},t_{inj},\tau_n,d_n\right)} \tag{5.6}.$$

where δ_n are in units and δ_m are in Tm/kA for LHC dipoles. However, for b_1, δ_m will be expressed in units in this work so as to render the comparison of the decay amplitude with the specification and with other harmonics easier.

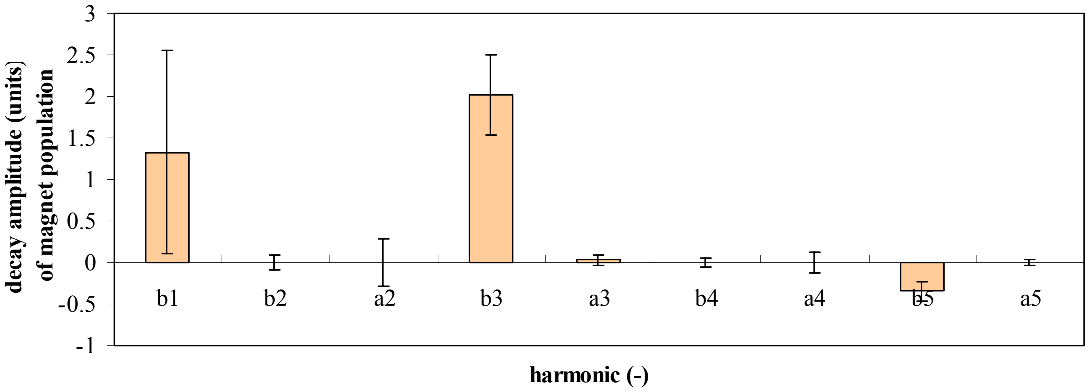

Figure 5.5: The average decay amplitude of the main field and the harmonics for sector 7-8.

The average decay variation after 1000 s of sector 7-8 can be calculated by averaging the standard LHC cycle measurements at injection. The sample consists of 165 apertures and is almost equally distributed amongst the three different manufacturers (Alstom®, Ansaldo Superconduttori® and Babcock Noell®). Figure 5.5 shows the average decay amplitude of the main field and the harmonics. In the case of the allowed harmonics, the decay manifests itself as a systematic behaviour and so must be modelled and compensated in the machine. The allowed harmonic decay always results in a net decrease of the persistent current contribution to the field. From this observation, the decay modelling is limited to the main field and the first two allowed harmonics which can be compensated by using corrector magnets.

Figure 5.6 shows the variation of b_1, b_3 and b_5 during a 1000 s injection, arbitrarily shifted along the vertical axis to make the initial value at injection equal to zero. Note that only 58 apertures are included in the figure so as to limit the cluttering effect of having all the data in one graph. However, the average shown is the average of all the 165 apertures measured. Table 5.1 shows the average decay amplitude and the related 99 per cent confidence interval for the allowed harmonics.

Table 5.1: The average decay amplitude at 1000 s for sector 7-8 and the 99 per cent confidence interval for the allowed harmonics

	units	**b_1**	**b_3**	**b_5**
average decay amplitude after 1000 s (δ_{std})	(units)	1.41	2.01	–0.34
99 % confidence interval	(units)	0.22	0.07	0.02

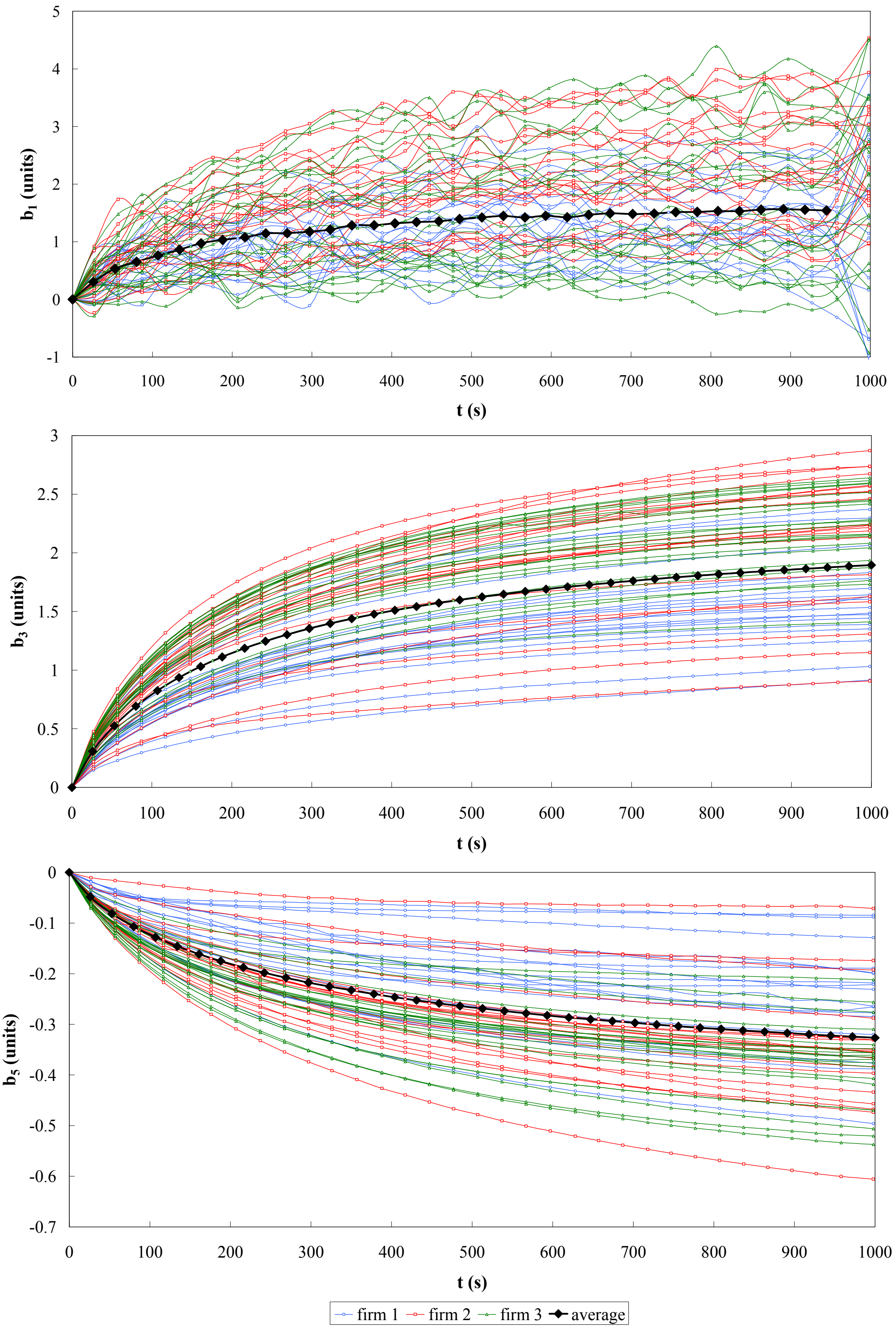

Figure 5.6: (top) Decay of b_1, **(middle)** b_3 and **(bottom)** b_5, (units @ 17mm), measured during a 1000 s simulated injection plateau following a standard pre-cycle. The values have been normalized by arbitrarily shifting them along the y-axis to cancel the initial value.

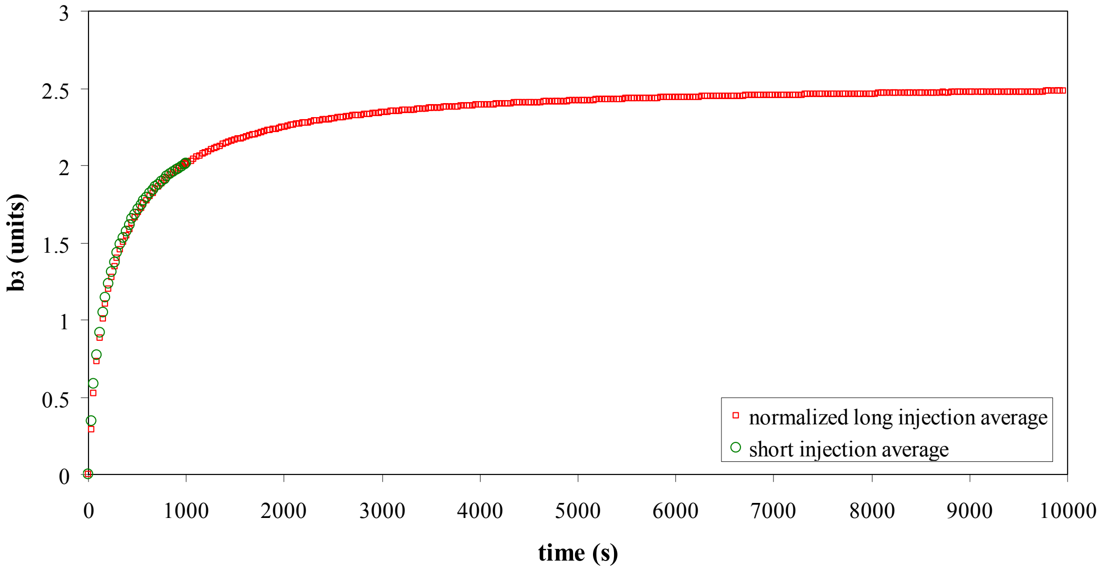

Figure 5.7: The short b_3 decay average data and the normalized long b_3 decay average data.

The standard series measurements at cold are performed on a pre-defined injection plateau for a duration of 1000 s. However, it is possible that the particle injection will take longer than this, particularly during initial tests if there happens to be a technical problem in the injector chain.

Therefore dedicated decay measurements on 13 apertures lasting 10000 s were performed to ensure that the decay model is valid over longer injection plateaus. The decay does not vary by more than the measurement repeatability for the respective harmonics after 7000 s. So 10000 s are enough to ensure that the decay model is valid for even longer injection plateaus. Figure 5.7 shows the b_3 short injection average data of sector 7-8 and the b_3 average decay of the long measurements normalized at 1000 s. This normalisation (scaling) procedure will be described in more detail in the next chapter.

The values of the parameters obtained from the fits of the average decay and the maximum difference between the sample average and the model are reported in Table 5.2. Figure 5.8 shows the average short injection decay of the 165 apertures of sector 7-8 extended by the normalized long injection average decay based on the 13 dedicated measurements. It also shows the model and the modelling error. This error is comparable to the maximum error of the static field model and therefore demonstrates that using two modes to model the decay is sufficient. The maximum error occurs in the first minute of the injection plateau and indicates that there is a fast decay component as reported by Velev [91]. After 250 s the maximum error reduces by an order of magnitude for b_3 and b_5.

Table 5.2: Parameters obtained fitting the model of Eq. 5.6 to the average decay of the population analysed, representing the behaviour of sector 7-8.

parameter	units	b_1	b_3	b_5
τ	(s)	227.58	189.04	284.15
d	(-)	0.978	0.660	0.660
δ	(units)	1.41	2.01	–0.34
max error	(units)	0.32	0.13	0.04

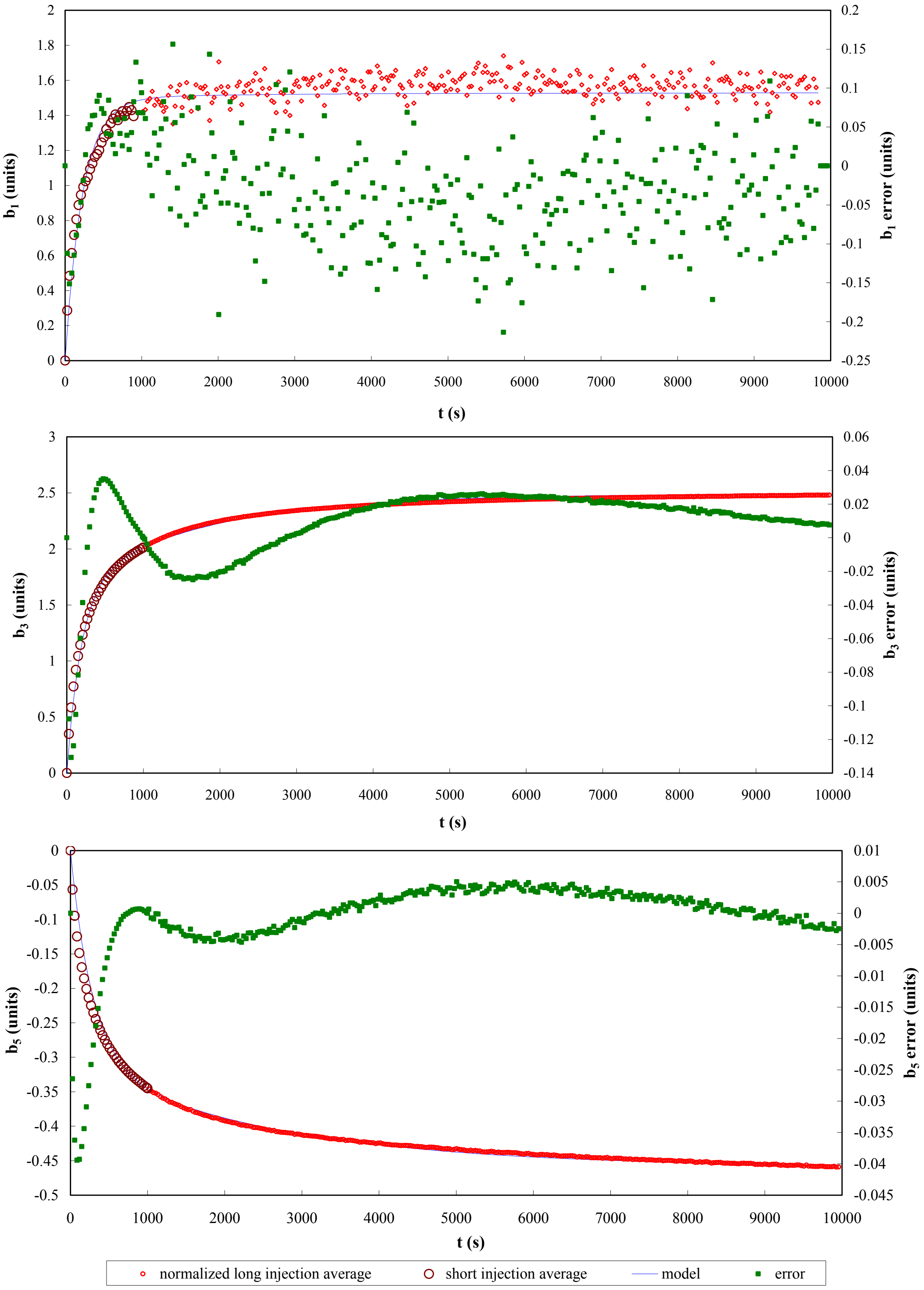

Figure 5.8: The average decay and the decay model of b_1, b_3 and b_5.

5.5 - The Powering History Dependence of the Decay

The decay amplitude of the allowed multipoles in the LHC dipole magnets is known to be strongly dependent on the magnet powering history [92]. By comparing the pattern evolution along the machine cycle to a charging and discharging capacitor, Schreiner [93] showed that this dependence could be explained by the way the non uniform current distributions are formed and are diffused in the Rutherford cable:

a. During ramp-up, the cable is charged with a non-uniformly distributed current.
b. On the pre-cycle plateau, the current imbalance diffuses slowly and is redistributed along the cable.
c. During the ramp-down, the cable is charged with a non-uniformly distributed current with the opposite sign.
d. Again, during the slow ramp-up to injection, the cable is charged with a non-uniformly distributed current with the original sign.
e. Finally, on the injection plateau, the current imbalance diffuses slowly redistributing along the cable and causing the decay.

Studies performed by Haverkamp [94] and Schneider [95] on 1 m short LHC dipole model magnets based on a single powering pre-cycle have shown that the decay amplitude is mostly dependent on the pre-cycle flat-top current I_{FT}, flat-top duration t_{FT} and the preparation plateau duration time $t_{preparation}$. These parameters are illustrated in Figure 5.9.

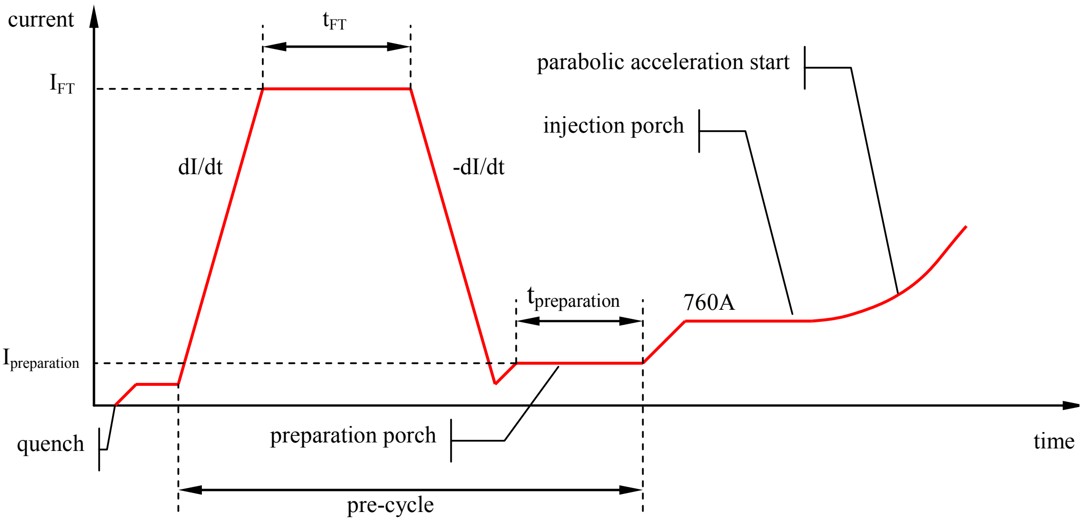

Figure 5.9: Definition of the parameters affecting decay during LHC injection.

The other parameter variations studied by Haverkamp and Schneider on the model dipoles include: pre-injection duration, pre-injection current, ramp rate to injection, pre-cycle flat top current, pre-cycle flat top duration and pre-cycle ramp rate. However all these effects are very small compared to the decay amplitude variation caused by changes in I_{FT}, t_{FT} and $t_{preparation}$.

The measurement procedure performed on series dipole magnets to study the powering history effect was carried out by first performing a quench to erase all persistent currents. The measurement then proceeded by performing an LHC cycle with a pre-cycle whose current values and duration have been varied parametrically as is shown in Figure 5.10.

When testing the influence of one parameter (e.g. the flat-top current) the second and third parameters (e.g. the flat-top time and the preparation time) were held constant at the value corresponding to the standard pre-cycle. Table 5.3 shows a full powering history measurement programme. The cycle in blue is the standard series LHC cycle magnetic measurement whilst the others are the cycles with the different pre-cycle parameters.

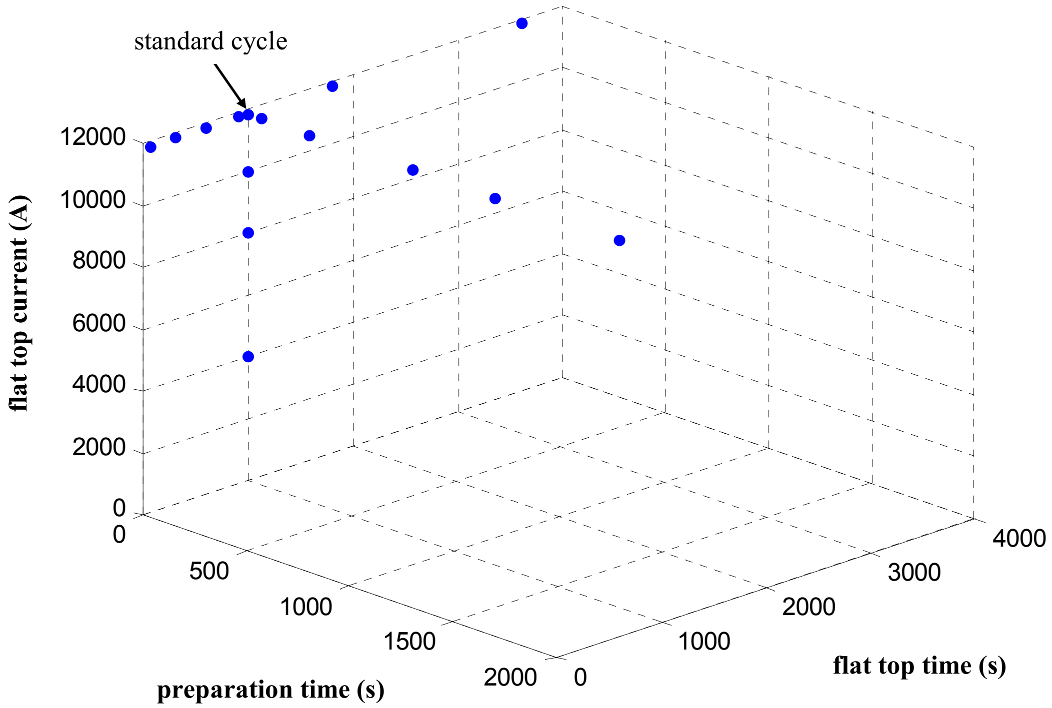

Figure 5.10: A graphical representation of the full powering history test programme.

Table 5.3: The full powering history test programme. The first test is the standard LHC cycle.

Test	**Pre-cycle Parameters**		
	I_{FT}	t_{FT}	$t_{preparation}$
1	11850	1000	0
2	**4000**	1000	0
3	**8000**	1000	0
4	**10000**	1000	0
5	11850	**60**	0
6	11850	**300**	0
7	11850	**600**	0
8	11850	**900**	0
9	11850	**1000**	0
10	11850	**1800**	0
11	11850	**3600**	0
12	11850	1000	**60**
13	11850	1000	**300**
14	11850	1000	**800**
15	11850	1000	**1200**
16	11850	1000	**1800**

The measurements are performed with the twin rotating coils [45]. Each cycle takes around 1.5 hours to run and a quench has to be performed between every cycle. A quench recovery usually takes around 3 hours. Therefore, if the test sequence is launched and is performed with full efficiency and without any hardware problems, it would last for 70 hrs. This imposes a very large demand on cold test scheduling so a statistical optimisation study had to be performed to decide what is the best way of distributing the allocated magnetic measurement time between the powering history magnetic measurements and the series magnetic measurements that were determining the warm-cold correlation discussed in chapter 4 [96]. The results of this study showed that performing 12 powering history tests over 2 years is the best compromise.

Furthermore, as a part of the overall optimisation, it was decided to distribute the test time on several magnets. Therefore, sometimes, only the influence of one of the three parameters was measured. Moreover, in some cases, only part of the parameter space of one particular parameter was studied. A summary of the powering history measurements performed can be found in Table 5.4.

Table 5.4: Magnets considered in the analysis of the powering history influence on decay and snapback at injection.

Magnet	I_{FT}	t_{FT}	$t_{preparation}$
1004	✓		
1007	✓		
1010		✓	
1011		✓	
1012	✓		
1018		✓	
1225		✓	✓
2010		✓	
2123	✓	✓	✓
2168			✓
3007	✓		
3028		✓	
3042		✓	
3117	✓	✓	✓
3130	✓	✓	✓
3219	✓	✓	✓
3284	✓	✓	✓

In terms of the results reported in the previous section, the change in the decay amplitude can be described through a change of the parameter δ in Eqs. 5.4, 5.5 and 5.6. To model the changes in δ_n the following equations can be used:

$$\delta_n^{I_{FT}} = \delta_{std}^{I_{FT}} \left(\frac{E_0^n - E_1^n e^{-\frac{I_{FT}}{\tau_E^n}}}{E_0^n - E_1^n e^{-\frac{I_{FT}^{std}}{\tau_E^n}}} \right) \tag{5.7}$$

$$\delta_n^{t_{FT}} = \delta_{std}^{t_{FT}} \left(\frac{T_0^n - T_1^n e^{-\frac{t_{FT}}{\tau_T^n}}}{T_0^n - T_1^n e^{-\frac{t_{FT}^{std}}{\tau_T^n}}} \right) \tag{5.8}$$

$$\delta_n^{t_{preperation}} = \delta_{std}^{t_{preperation}} \left(\frac{P_0^n + P_1^n e^{-\frac{t_{preparation}}{\tau_P^n}}}{P_0^n + P_1^n e^{-\frac{t_{preparation}^{std}}{\tau_P^n}}} \right) \tag{5.9}$$

where δ_{std} is the decay amplitude measured for a standard pre-cycle, i.e. with flat-top current of $I_{FT}^{std} =$ 11850 A, flat-top time $t_{FT}^{std} =$ 1000 s and preparation time $t_{preparation}^{std} = 0$ s. τ_E^n, τ_T^n and τ_P^n are the time constants for the magnet memory for flat-top current, flat-top duration and preparation time, respectively. E_0^n, E_1^n, T_0^n, T_1^n, P_0^n and P_1^n are the fitting parameters. These three equations are a direct consequence of the assumption of exponential decay during constant current excitation, i.e. Eqs. 5.3 to 5.6, where only the longest time constant has been retained for simplicity.

As mentioned above, resource constraints sometimes limited the range of investigation in the parameter space and therefore one particular parameter value may not have a value for all the magnets considered. For example: not all measurements investigating t_{FT} dependence were measured at 3600 s. Therefore, to avoid having inhomogeneous averaging, the average value was calculated after every single curve was first fitted with Eqs. 5.7, 5.8 and 5.9.

Figure 5.11 shows the measurement results and the average variation of decay amplitude vs. pre-cycle flat-top current for the measurements shown in Table 5.4. b_1, b_3 and b_5 all have a general asymptotic systematic dependence. The b_1 dependence is, however, very close to the measurement accuracy limit.

Figure 5.12 and 5.13 show the measurement results and the average variation of decay amplitude vs. pre-cycle flat-top duration and the decay amplitude vs. preparation duration, respectively, for the measurements shown in Table 5.4. b_1, b_3 and b_5 all have a general asymptotic systematic dependence. However, the dependence for b_1 and b_5 in both the cases is considered to be negligible since it is not fully systematic and is comparable to the rotating coils measurement repeatability. Therefore, these dependencies are only considered to be important for b_3.

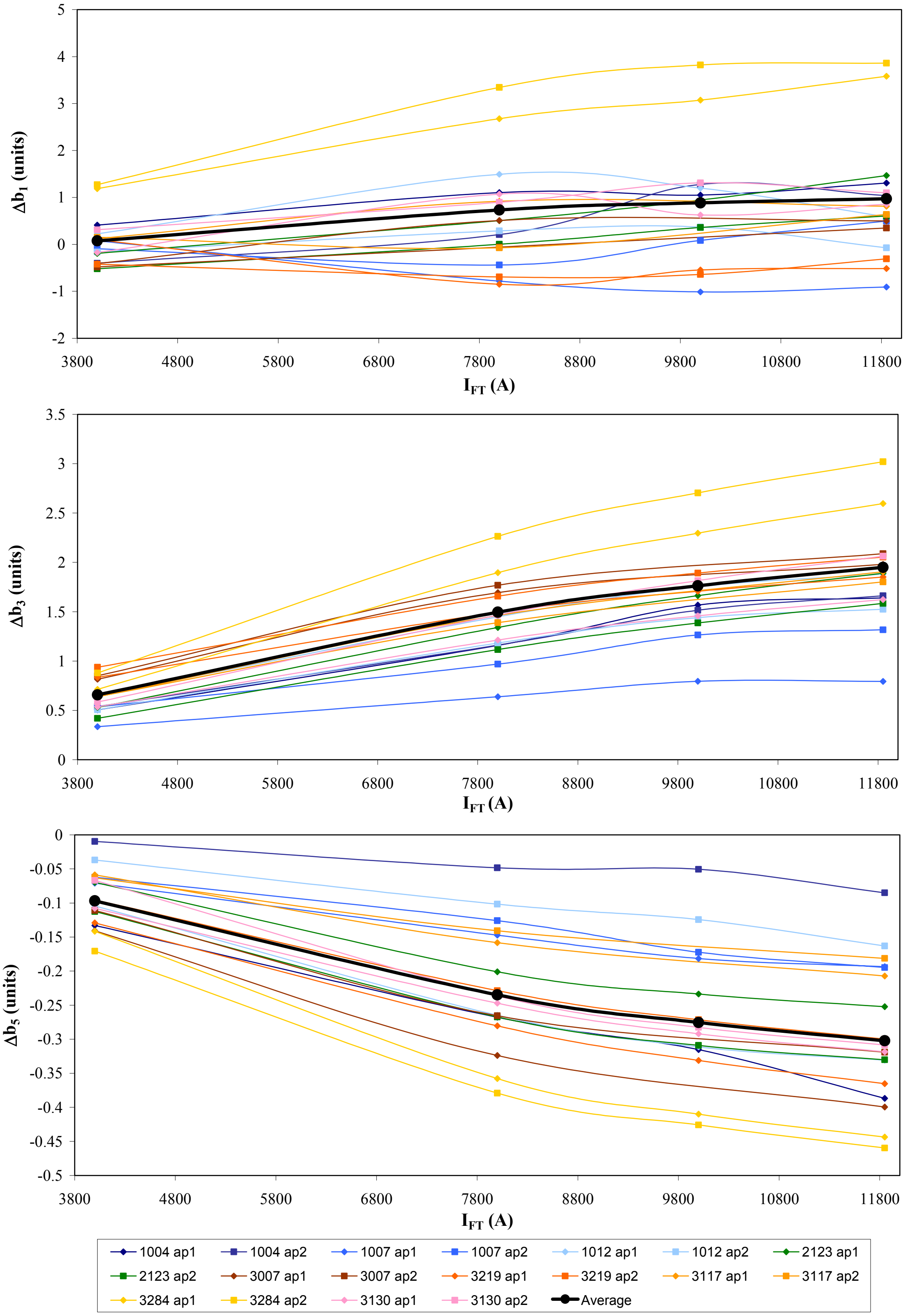

Figure 5.11: The variation of the decay amplitude with flat-top current for **(top)** b_1, **(middle)** b_3, and **(bottom)** b_5.

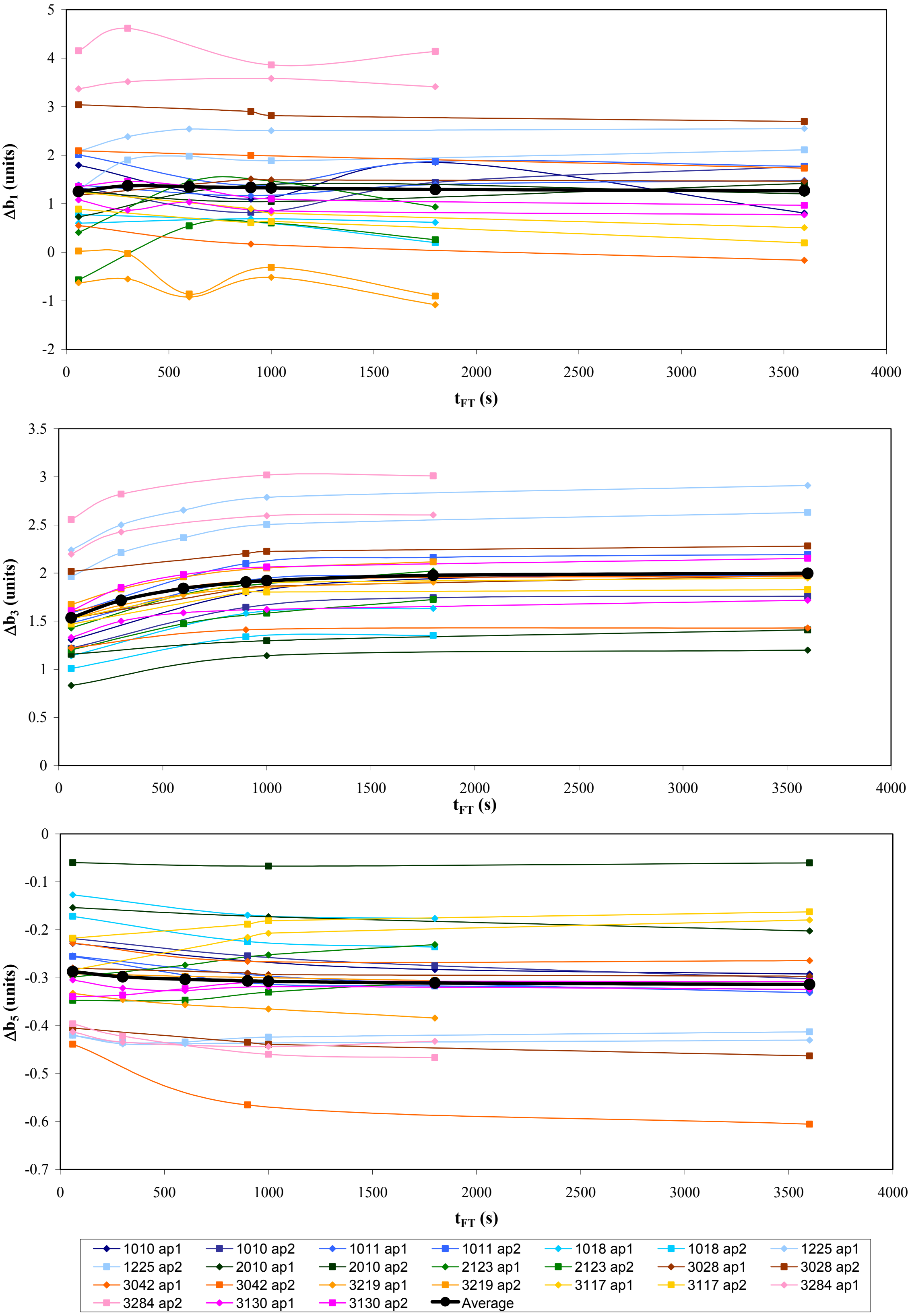

Figure 5.12: The variation of the decay amplitude with flat-top duration for **(top)** b_1, **(middle)** b_3, and **(bottom)** b_5.

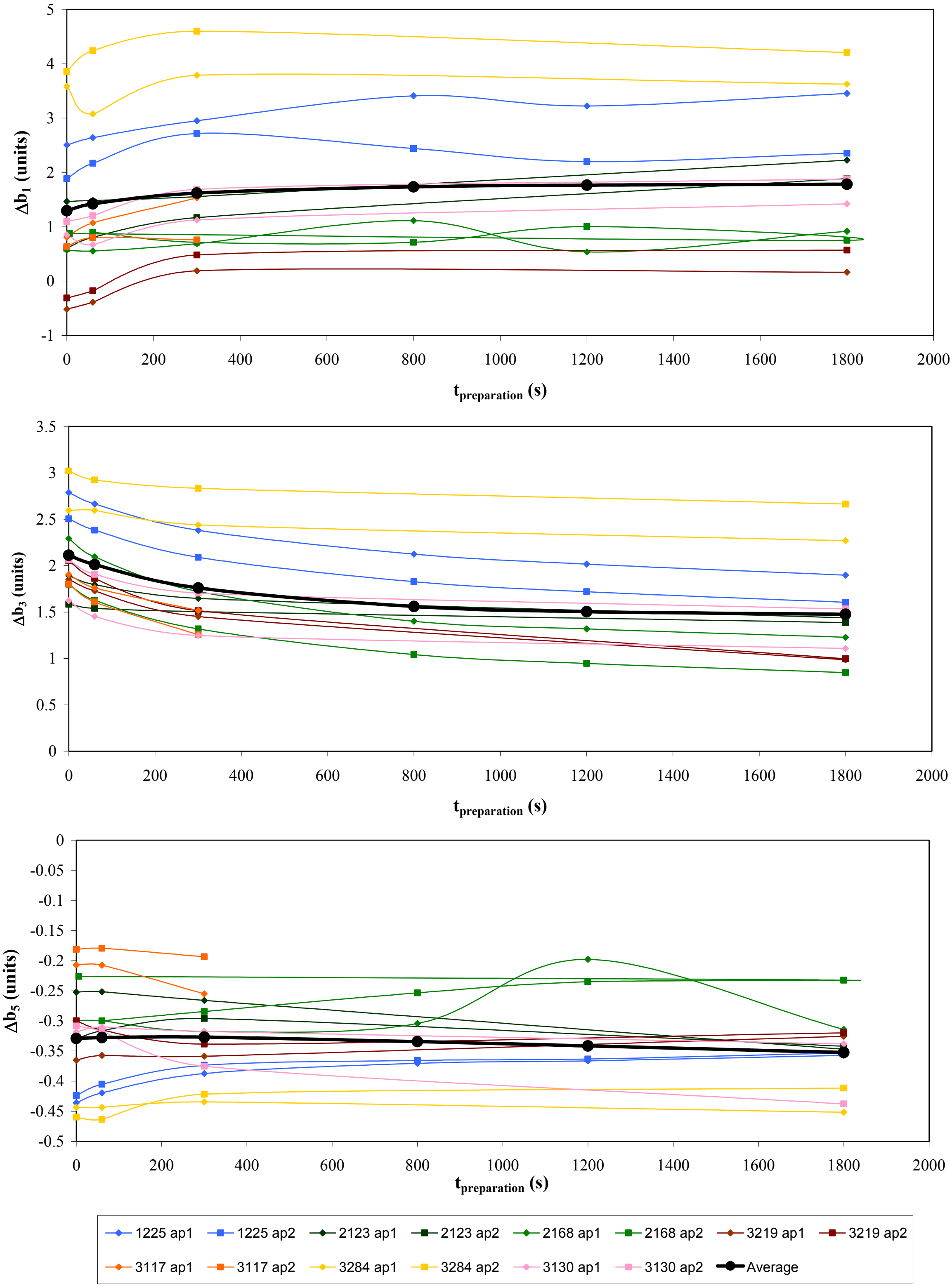

Figure 5.13: The variation of the decay amplitude with preparation duration for **(top)** b_1, **(middle)** b_3, and **(bottom)** b_5.

Considering the average curves of the measurements, the importance of the three parameters can be determined for the main field and the harmonics being considered. The difference between the maximum and minimum value of the curves is shown in Table 5.5. This table therefore shows that the most important dependence is I_{FT} since variations of this parameter cause the largest change. Table 5.6 also indicates which parameters are important for modelling in FIDEL. The I_{FT} dependence, and all the three parameter dependencies for b_3, are important for modelling. The I_{FT} and $t_{preparation}$ dependence for b_1 and b_5 can be ignored.

The maximum error between the fitting curves and the data of every single aperture are shown in Table 5.7. Table 5.8, 5.9 and 5.10 show the parameters of the fit of the average data calculated as explained above using Eqs. 5.7, 5.8, 5.9, respectively. Figure 5.14 shows the curves of these fits for b_3. The maximum error between the average data and the fit of the average is negligible and is shown in Table 5.11. This is expected since the errors due to inhomogeneities in the data were removed when calculating the fit of the individual apertures.

Table 5.5: The difference between the maximum and minimum value of the average powering history dependence (all values in units).

	b_1	b_3	b_5
I_{FT}	0.9	1.29	0.21
t_{FT}	0.02	0.46	0.03
$t_{preparation}$	0.49	0.6	0.02

Table 5.6: The systematic powering history effects that should be modelled are shown as a green tick. The effects marked with a red cross are negligible and may be ignored (all values in units).

	b_1	b_3	b_5
I_{FT}	✓	✓	✓
t_{FT}	✗	✓	✗
$t_{preparation}$	✗	✓	✗

Table 5.7: The maximum error between the data and the fits of every individual aperture (all values in units).

	b_1	b_3	b_5
I_{FT}	0.507	0.088	0.007
t_{FT}	-	0.028	-
$t_{preparation}$	-	0.033	-

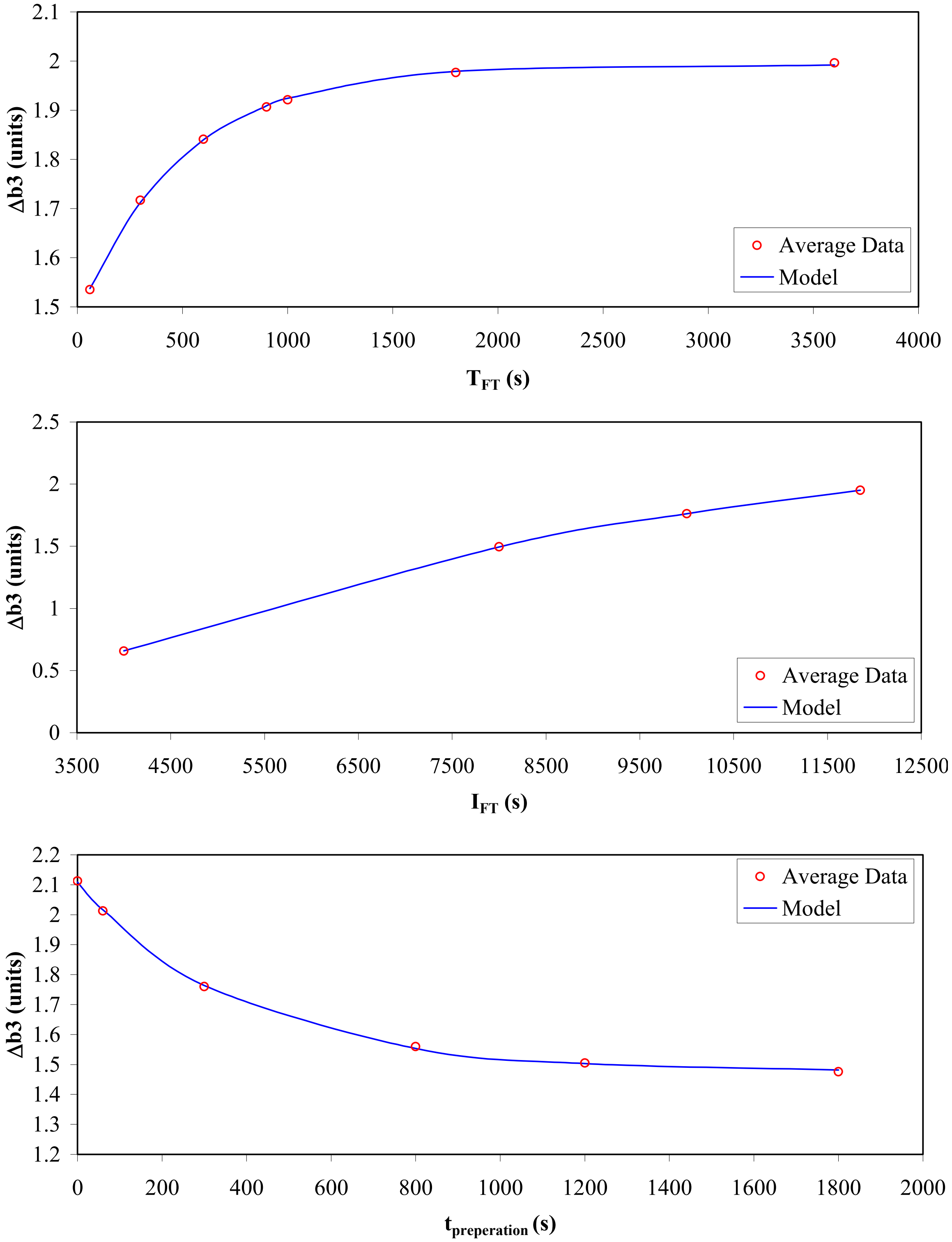

Figure 5.14: The average data and model of b_3 for **(top)** the pre-cycle current dependence, **(middle)** the pre-cycle time dependence and, **(bottom)** the preparation time dependence.

Table 5.8: The model parameters for I_{FT}.

component	units	parameter	b_1	b_3	b_5
I_{FT}	(-)	E_0	–0.4669	1.2807	–0.7025
	(-)	E_1	–1.0266	1.6991	–1.0329
	(A)	τ_E	4665.0	6900.2	5843.0
	(units)	$\delta_{std}^{I_{FT}}$ (1000 s)	0.9855	1.9500	–0.3024

Table 5.9: The model parameters for t_{FT}.

component	units	parameter	b_1	b_3	b_5
t_{FT}	(-)	T_0	-	–0.1986	-
	(-)	T_1	-	–0.0512	-
	(s)	τ_T	-	494.5232	-
	(units)	$\delta_{std}^{t_{FT}}$ (1000 s)	-	1.9213	-

Table 5.10: The model parameters for $t_{preparation}$.

component	units	parameter	b_1	b_3	b_5
$t_{preparation}$	(-)	P_0	-	0.9172	-
	(-)	P_1	-	–0.3934	-
	(s)	τ_P	-	380.5939	-
	(units)	$\delta_{std}^{t_{preperation}}$ (1000 s)	-	2.1090	-

Table 5.11: The maximum error between average data and its fit (all values in units).

component	b_1	b_3	b_5
I_{FT}	0.01	0.001	0.007
t_{FT}	-	0.007	-
$t_{preparation}$	-	0.007	-

5.6 - Snapback

The snapback phenomenon was discovered two years after the decay phenomenon at the Tevatron [92]. During snapback the field bounces back to its pre-decay level once the current in the magnet starts to ramp-up after a current plateau, e.g. at injection.

The mechanism described in section 5.4.1 also explains why the snapback occurs. As the current ramp resumes, the regions which saw a decreasing field due to the local current redistribution fields, suddenly experience a positive field change again, which quickly overcomes the redistribution field. Therefore the magnetisation is re-established. This is shown graphically in Figure 5.15.

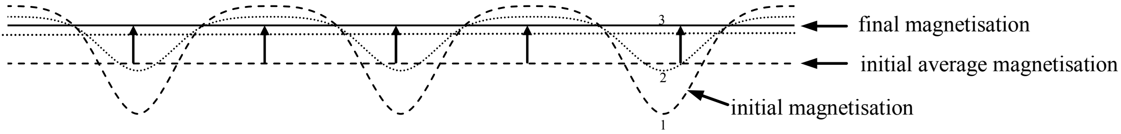

Figure 5.15: The regions which experienced a local field decrease, now experience a positive field change. Hence the magnetisation quickly snaps back to its original value (the magnetisation changes from the dotted lines distribution to the straight line distribution in sequence as indicated by the numbering).

Snapback can be described empirically by an equation of the type [18]:

$$b_3^{snapback}(t) = b_3^{decay} e^{\frac{I_{inj}-I(t)}{\Delta I}} \tag{5.10}$$

where $b_3^{snap-back}(t)$ is the sextupole change during the snapback, *I(t)* is the instantaneous value of the current, initially at the injection value I_{inj}. The decay amplitude (or snapback amplitude) b_3^{decay} and the current change ΔI are the two fitting constants. Based on this observation the snapback can be modelled by an expression of the type given above so that:

$$B_m^{snapback} = B_m^{decay}(t_{ramp}) e^{\frac{I_{inj}-I(t)}{\Delta I_m}} \tag{5.11}$$

$$TF^{snapback} = TF^{decay}(t_{ramp}) e^{\frac{I_{inj}-I(t)}{\Delta I_m}} \tag{5.12}$$

$$c_n^{snapback} = c_n^{decay}(t_{ramp}) e^{\frac{I_{inj}-I(t)}{\Delta I_n}} \tag{5.13}$$

where the factors $B_m^{decay}(t_{ramp})$, $TF^{decay}(t_{ramp})$, and $c_n^{decay}(t_{ramp})$ are the change of the main field, the transfer function and the normalized harmonics, respectively, during the decay evaluated at the instantaneous time of the beginning of the ramp t_{ramp}.

The measurement of the snapback is performed with the snapback analyser (locally in the straight part of the magnet) since the rotating coils are too slow to measure enough points for modelling. A typical snapback measurement campaign consists of several LHC cycles with the pre-cycle parameters changed so as to vary the decay amplitude and hence the current change ΔI. The cycles are separated by a quench to erase the persistent currents. A typical snapback measurement campaign lasts around 40 hrs which demands a lot of resources. As was done for the powering history measurements, a study was performed to determine how to share the time between snapback measurements and series tests [96]. From the results of this study, it was decided to perform measurements on about 12 magnets over 2 years.

Table 5.12 shows the number of snapback measurements performed on the sampled LHC magnets. In total 96 b_3 measurements were performed and 70 b_5 measurements were performed.

Figure 5.16 shows typical LHC snapback curves for b_3 and b_5 measured using the snapback analyser. The signal to noise ratio of the b_5 snapback measurement is small due to the hardware resolution limitations [97].

Table 5.12: The number of snapback measurements performed on the LHC dipoles. (Measurements in blue courtesy of Markus Haverkamp [98]; Measurements in orange courtesy of Tatiana Pieloni [99], measurements in black are part of this work).

Magnet	b_3		b_5	
	Aperture 1	Aperture 2	Aperture 1	Aperture 2
MBP202	4	0	0	0
1001	4	0	0	0
1009	3	0	1	0
3005	2	1	1	0
1024	1	1	1	0
2020	2	0	1	0
3164	4	0	0	0
2043	4	0	0	0
3370	0	4	0	4
2259	4	2	4	2
2211	4	4	4	4
1310	4	4	4	4
2142	0	1	0	1
2236	5	10	8	10
1292	5	6	5	6
2358	8	9	6	4

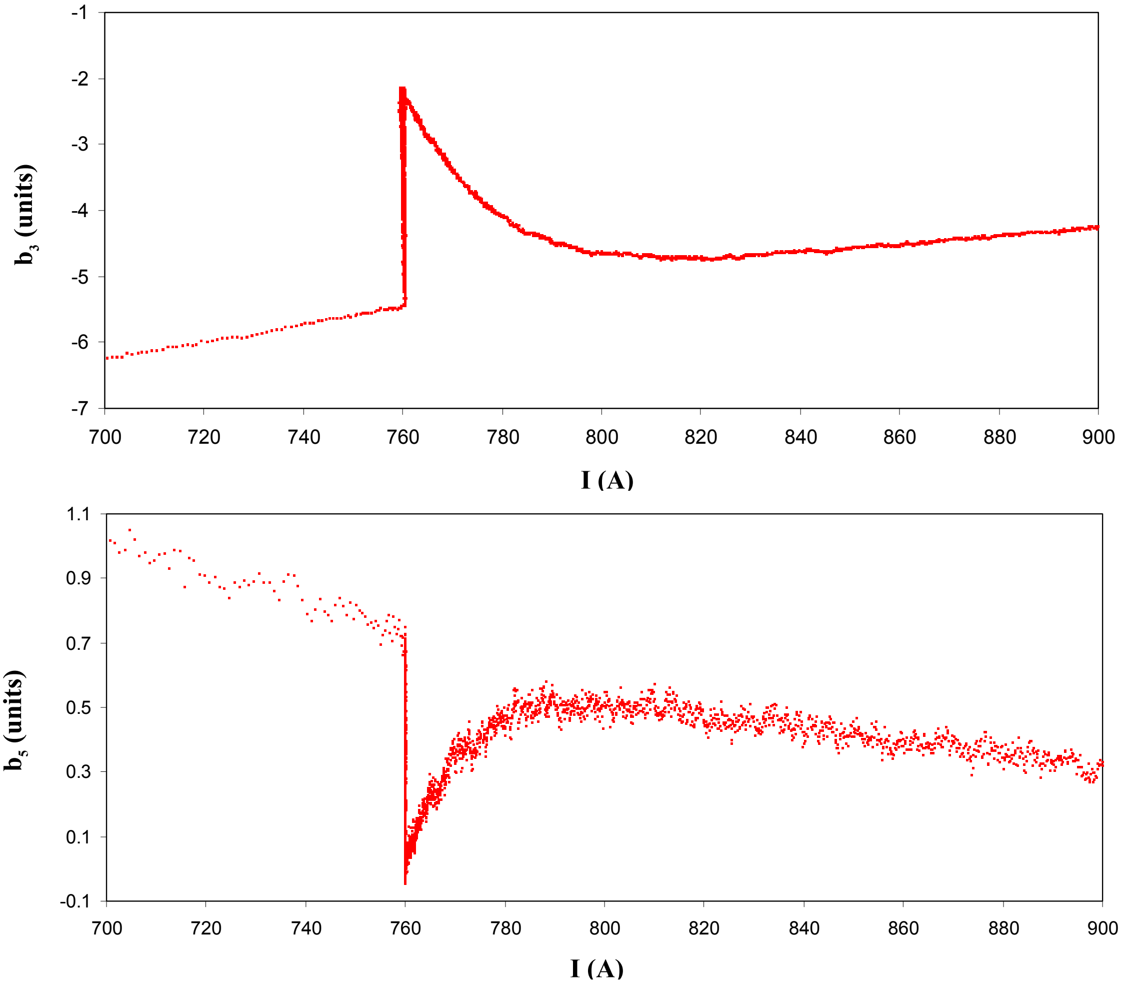

Figure 5.16: The decay during the injection plateau of an LHC cycle and the subsequent snapback when the current begins to ramp. **(top)** b_3 decay and snapback **(bottom)** b_5 decay and snapback.

Table 5.13: Snapback modelling results.

		b_3	b_5
ΔI	(A)	19.1	12.1
decay amplitude	(units)	3.4	0.6

Figure 5.17 shows the b_3 and b_5 snapback modelling for the measurement shown in Figure 5.16. On the log scale, the data follow a straight line hence demonstrating that the phenomenon can indeed be modelled using an exponential relationship. The values of the parameters of this measurement are shown in Table 5.13. The standard deviation of the error between the measurements performed and their model is in general less than 0.03 units.

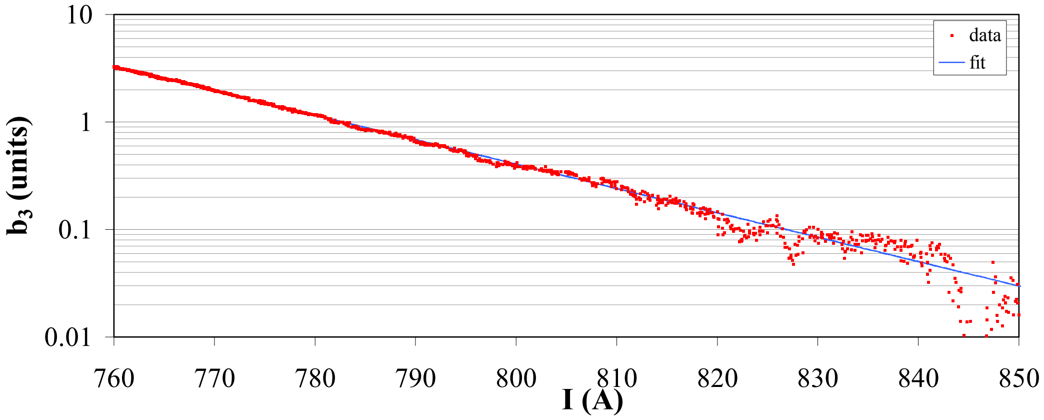

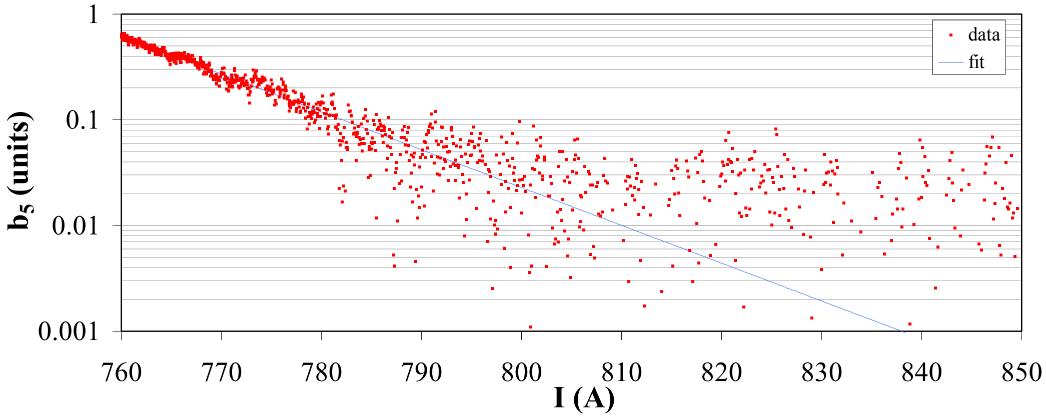

Figure 5.17: Snapback modelling for **(top)** b_3 and **(bottom)** b_5.

5.7 - Coupling Currents Contributions

Eddy currents are induced by moving magnetic fields (or time-varying magnetic fields) that intersect conducting materials. This effect is a consequence of Lenz’s Law and has been highlighted in chapter 4 for the case of superconducting materials when they are in their superconducting state. Eddy currents in superconductors have very large time constants and hence are known as persistent currents.

Eddy currents are also induced in the normally conducting materials such as the copper matrix of the Rutherford cable. They also form in the iron yoke and the copper wedges but these are negligible compared to the ones induced in the cables. Eddy currents are distinguished from each other according to the part of conductor through which they flow, their characteristic loop length and their characteristic time constants.

Strand coupling currents are eddy currents that flow between the superconducting filaments through the copper matrix of the strands. Therefore, they are both normal and superconducting in nature. Filament coupling is highly dependent on the twist pitch of the filaments in the strand and on the resistivity of the matrix material (copper in the case of the LHC). Hence, strand coupling currents are effectively reduced by twisting the strand so that the length of the loop that is exposed to the time-varying field is considerably shortened. In this way, contributions from adjacent loops alternate in sign. In the case of the LHC, the strand coupling current time constant is a few tens of milliseconds [84].

Cable coupling currents are eddy currents that flow between and in the strands of the cable. Their magnitude increases with increasing twist length of the strands and the decrease of the electrical cross-contact resistance. The contributions of cable coupling currents can be simulated by network models [100]. Cable coupling currents do not obey coil symmetry because the cross-contact resistances vary from turn to turn as well as in the longitudinal direction and therefore create both allowed and non-allowed multipoles. In the case of the LHC, the cable coupling currents time constant is a few hundred milliseconds [84] for magnetic field variations uniform along the length of the cable.

Since the coupling currents have very short time constants, for the typical ramp times to be used in the LHC operation, they can be assumed to be fully developed in the resistive regime, that is all inductive and shielding effects have already decayed. The field dependence of the total resistance of the coupling current loops can also be neglected. With this assumption, the contribution of coupling currents to the main field and the field errors is linear with the ramp rate. Therefore, for the main field component:

$$B_m^{MAC} = \theta_m I_{inj} \frac{1}{10} \frac{dI}{dt} \tag{5.14}$$

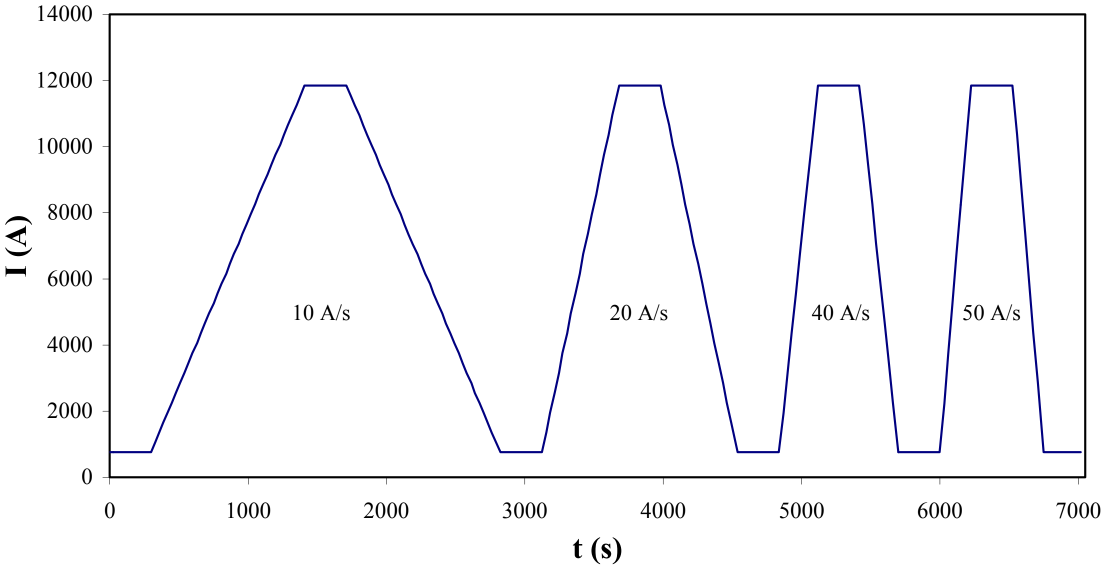

Figure 5.18: The eddy current measurement cycle.

where the normalization factor (1/10) is used to refer the contribution to the nominal ramp rate of the LHC (10 A/s). θ is the coupling current coefficient. The contribution to the transfer function is:

$$TF^{MAC} = \theta_m \frac{I_{inj}}{I} \frac{1}{10} \frac{dI}{dt} \qquad (5.15)$$

while for the normalized harmonics:

$$c_n^{MAC} = \theta_n \frac{I_{inj}}{I} \frac{1}{10} \frac{dI}{dt} \qquad (5.16).$$

Note that normalization is such that the multiplication constant corresponds to the effect of the coupling currents at injection current and nominal ramp rate in both cases.

The effect of the coupling currents on the field quality of the LHC dipole magnets is tested by exciting the magnet with a dedicated rotating coil measurement which forms part of the extended cold magnetic programme. Since the eddy currents are directly proportional to the current ramp rate, this measurement consists of four cycles each with a different ramp rate as shown in Figure 5.18.

To quantify the eddy currents contribution, the difference of the harmonic value between the ramp-up and the ramp-down (i.e. the hysteresis width) for each current is computed. Figure 5.19 shows an example of the variation of the hysteresis width as a function of ramp rate for the sextupole harmonic at different current values. The average slope of these curves transformed into units and multiplied by 10 A/s (nominal LHC cycle ramp rate) consequently results in the eddy current contribution to the b_3 harmonic for a typical LHC cycle.

Figure 5.20 shows the average eddy current contribution to the harmonics based on a sample of 103 LHC dipole apertures. The average for LHC dipoles is negligible for all harmonics and therefore for the LHC dipoles this component may be ignored by FIDEL. In the case of the main field, the contribution is also very small (smaller than 1 unit) [101].

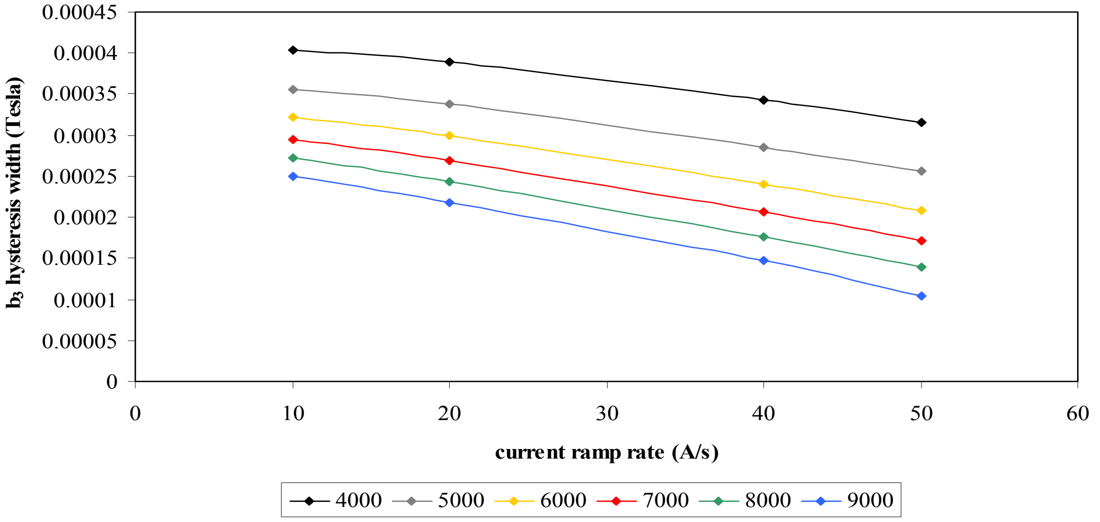

Figure 5.19: b_3 ramp rate dependence for an LHC magnet. (Dipole 2212 ap1).

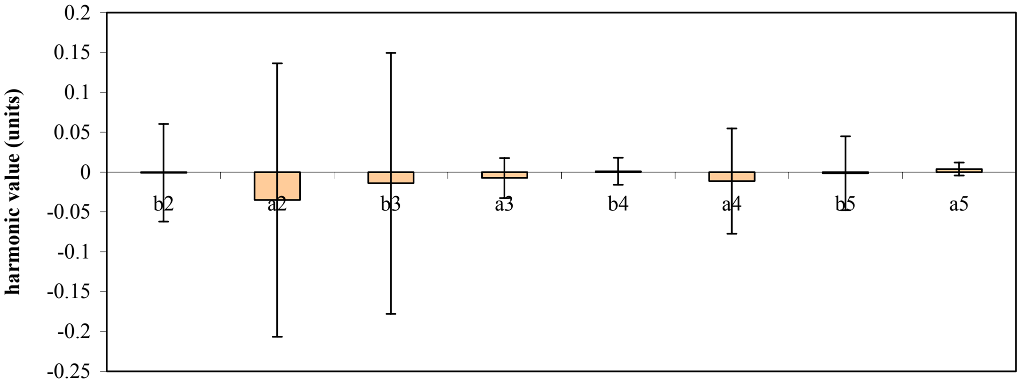

Figure 5.20: The eddy current contribution to the harmonics at 10 A/s. Error bars show the standard deviation.

5.8 - Conclusion

The dynamic field model is an important part of FIDEL since it provides a mathematical description of the current and time dependent components of the LHC dipole magnets. By modelling the pattern of the powering dependence of the decay amplitude, the dynamic model is also equipped to predict the state of the machine even though it is not reproducible from cycle to cycle.

The harmonic decay is established to be mostly due to current imbalances and their re-distribution in the Rutherford cable due to spatial gradients of the field sweep rate. The mathematical formulation of the decay is therefore derived as a direct consequence of the diffusion equation of the current imbalances of the cable. The modelling result is acceptable having the maximum difference of 0.13 units for the normal sextupole between the average data and the model within the considered time range.

The powering dependence is also formulated based on the first mode of the series that forms the solution of the diffusion equation of the current imbalances through the Rutherford cable. The maximum error of this model within the measurement range for the three parameters considered is very promising: less than 0.1 units for the normal sextupole harmonic.

In the case of the snapback, an empirical model is adopted based on its observed exponential behaviour. Since snapback is a fast effect, the snapback analyser is used to provide enough measurement points for modelling. The standard deviation between the model and the data is less than 0.03 units for the normal sextupole.

In the case of the coupling currents, their effect is negligible compared to the static field model error. Therefore, even though a mathematical construct is formulated based on their physical origin, this component can be omitted altogether from the dynamic field model.

Chapter 6

The Scaling Laws

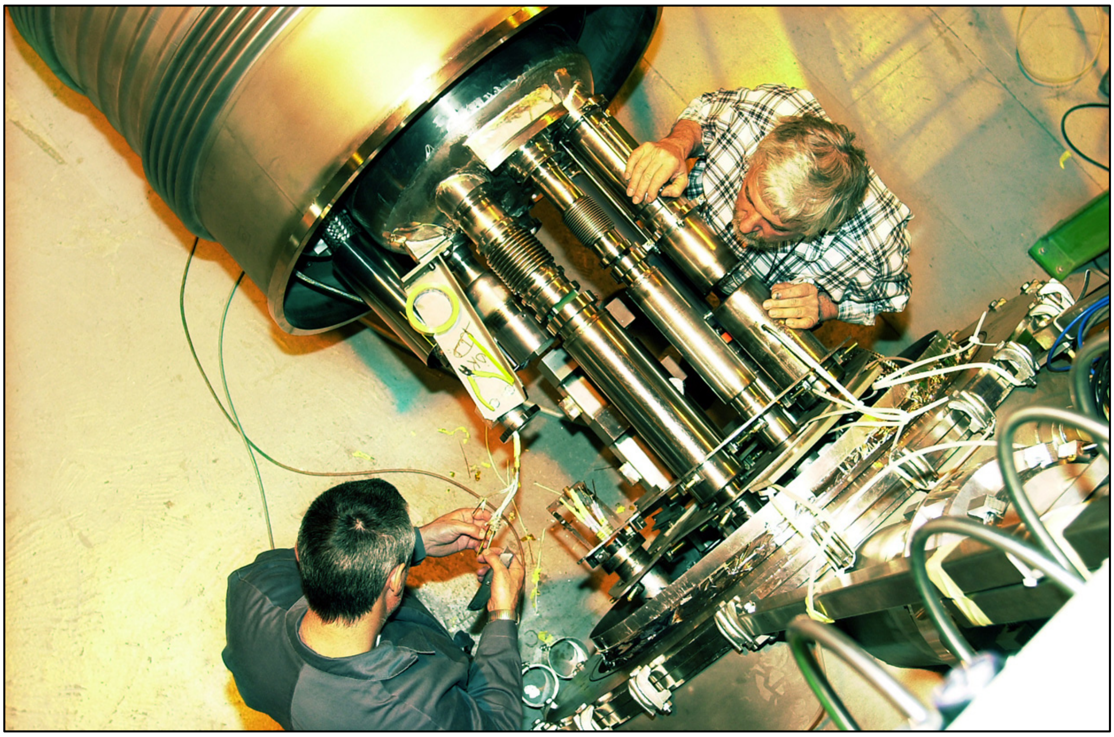

Magnet connected to cryogenic test station.

Everything should be made as simple as possible,
but not simpler.
- Albert Einstein

Chapter 6

The Scaling Laws

The machine magnetic state as predicted by the static model and, to a larger extent, by the dynamic field model, is expected to deviate somewhat from the actual machine magnetic state. This means that the parameters of the models will need to be recalibrated every so often to keep the feed-forward prediction as close as possible to the real machine magnetic state.

Recalibration information will be provided by beam-based measurements and by off-line reference magnets. The model therefore requires a mechanism that relates this information to the whole magnet population. The model also requires a mechanism that allows the model's powering history dependence parametric space to be extended. It also has to be powerful enough to project any changes measured in one component onto the other components. The latter mechanism is particularly important in the case of the snapback, which is closely related to the decay amplitude and which is too fast for measurements to be performed for the beam based feed-back system.

The mechanisms that provide the required model flexibility are referred to as model scaling laws. The main purpose of this chapter is to describe the principles of the scaling laws and qualify their performance in FIDEL. Where relevant, results from other magnet productions are referred to.

6.1 - Introduction

So far, the magnetic state of the machine is based on the standard measurements and an extended measurement programme of the LHC dipole magnets. This magnetic state will be used in FIDEL at the machine start up. However, the experience accumulated in the three major operating superconducting accelerators, Tevatron, HERA and RHIC, shows that after commissioning there will be a constant need of improving the knowledge of the machine magnetic state.

Deviations from the initial magnetic state will occur for the following reasons:

a. the sample of the magnets is not large enough to represent the whole magnet population; statistically the sample taken represents a good sample of the population, but unfortunately, it is not distributed evenly amongst the machine sectors. Besides, more measurements were performed at the beginning of the production than at the end, so any deviations due to production trends may be hidden statistically by the biased sample.
b. the magnetic state of the magnets might begin to change with age. For instance, the current distribution diffusion is dependent on the cross contact resistance. This parameter may change due to aging of the coils in the tunnel and hence cause a change in the decay and snapback amplitudes. This means that the model parameters will have to be recalibrated.
c. if systematic errors in the measuring instruments escape the calibration procedure the real machine magnetic state may be different from what was modelled.

New calibration data will be obtained using direct beam measurements (both in the cycle to cycle feed-forward paradigm and in the feed-back paradigm) and by using the new fast rotating coils described in chapter 2 together with the off-line reference magnet system. The latter has been proven to be extremely valuable to establish expected behaviours. One such example is given by the recent study of the sextupole in the Tevatron dipoles [102-103].

The method of compensating for these deviations in the static regime is of course to re-compute the model parameters once a suitable set of data is available. In the dynamic regime, this can be done in two ways:

a. By re-computing the model parameters
b. By employing a set of scaling laws.

For adjustment purposes, the re-computation of the model parameters is the ideal way of guaranteeing the precision of the model. However, when the fast measurement system and the off-line reference magnets are used, their magnetic state must be extrapolated to the magnetic state of the whole magnet population. The deviation in the static regime is primarily based on the geometric component, which is easily measured and corrected for. However, inferring the dynamic regime is not straightforward. The decay amplitude varies from magnet to magnet with a spread of 0.5 units. In this case, a scaling law can be employed on the decay model to allow a single magnet to be representative of the whole magnet population and hence provide a base on which to adjust the model. This procedure may also be used in case the number of beam-based measurements on the decay plateau is not enough for modelling. In this case, one single measurement on the decay plateau can be used to scale the model based on the magnetic measurements. These two applications are the motivation for the decay scaling law.

As described in chapter 5, the decay amplitude is dependent on the powering history. The dependence on the important pre-cycle parameters has been measured and a systematic behaviour has been identified and modelled for each parameter. However, this is not enough. A scenario in which more than one parameter change occurs is possible. Therefore, the dependence of the three parameters must be joined to a 3-dimensional parameter space to allow the parametric behaviour to be extrapolated. The inference of the influence of the powering history to unknown magnetic states due to the change of more than one parameter is the principle of the powering history scaling law.

As described in chapter 5, the change of the harmonics during the snapback is based on the two parameters namely: the decay amplitude at the end of injection and the current constant. Therefore, if the decay amplitude is changed as described previously, the snapback will also change. Due to instrumentation bandwidth limitations, snapback is difficult to measure and compensate quickly enough. Therefore, a modeled relation between the decay amplitude and the snapback current constant would be the ideal way of scaling the snapback to be representative of the magnet population behaviour once the decay amplitude varies. The relation between the two snapback parameters is the principle on which the third scaling law is based.

6.2 - The Decay Scaling Law

6.2.1 - LHC dipoles

When designing the off-line reference magnet system, the primary issue that must be settled before developing the instrumentation is to what extent the decay of the reference magnet can be scaled in case it is not representative of the whole magnet population. Observing the single magnet data, it seems that a simple scaling factor applied to the decay of a single magnet could stretch the measured data in the y direction to match the average curve. This is clearly true if the dynamics of the decay do not change from magnet to magnet. Starting with this assumption, it can be verified whether the scaling law:

$$\Delta_n\left(t, t_{inj}, \tau_n, d_n\right) = f_n^{decay} \cdot \Delta_n^i\left(t, t_{inj}, \tau_n, d_n\right) \qquad (6.1)$$

produces a satisfactory result. In Eq. 6.1 $\Delta_n\left(t, t_{inj}, \tau_n, d_n\right)$ is the average decay (i.e. the value for the sector or for the ring), $\Delta_n^i\left(t, t_{inj}, \tau_n, d_n\right)$ is the decay of the reference magnet *i*, and f_n^{decay} is the scaling factor. The latter is determined as the ratio of the measured decays for the sample average and for the reference magnet chosen at the end of the simulated injection, i.e. in the above notation:

$$f_n^{decay} = \frac{\Delta_n\left(t, t_{inj}, \tau_n, d_n\right)\left(t = 1000\right)}{\Delta_n^i\left(t, t_{inj}, \tau_n, d_n\right)\left(t = 1000\right)} \qquad (6.2)$$

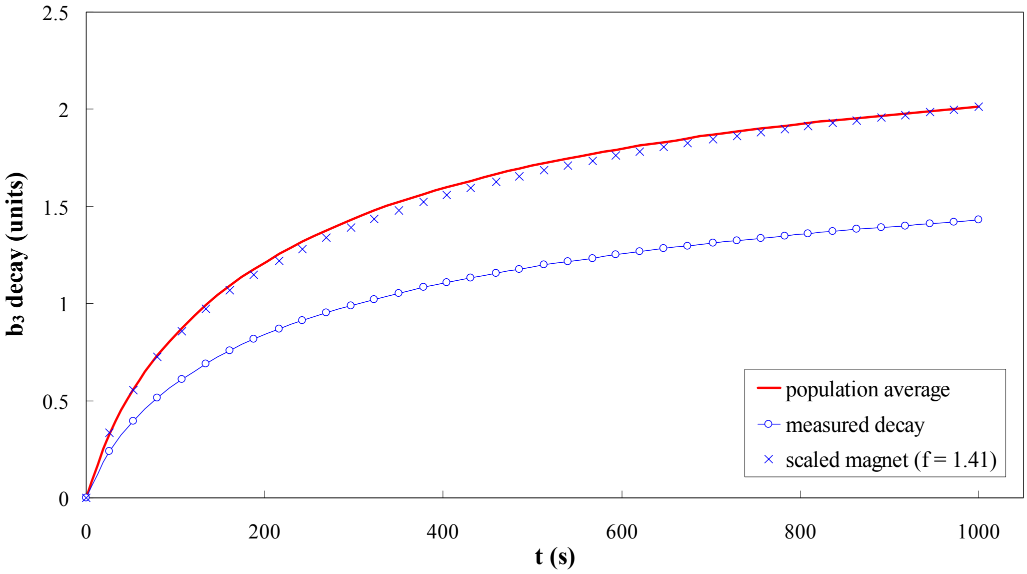

Figure 6.1: Example of scaling and comparison of scaled sextupole decays in magnet 3154, aperture 1.

It should be noted that there is no free parameter in the above scaling since all quantities will be known once the measurement on the beam is performed or once the reference magnet, or a suitable sample, is measured in cold conditions.

Eqs. 6.1 and 6.2 are used to scale the decay of each magnet measured, producing curves of the type represented in Figure 6.1 for a selected magnet (in this case sextupole harmonic of magnet 3154 aperture 1). The difference between the scaled decay and the average of the magnet population at all times during the injection plateau is then computed.

A histogram of the maximum error of all the magnets as well as a lognormal cumulative distribution function (cdf) for b_1, b_3 and b_5, respectively, are shown in Figure 6.2. The lognormal distribution is used because it can fit a data set that is skewed and can also be used to describe data that cannot fall below zero but that might increase without limit. A typical lognormal probability density function is shown in Figure 6.3. The goodness of fit is tested using the Kolmogorov-Smirnov test [104], which is satisfied for b_3 and b_5. b_1 does not pass the test due to the noise inherent in the measurements (Figure 5.6) but is graphically seen to approach a lognormal distribution.

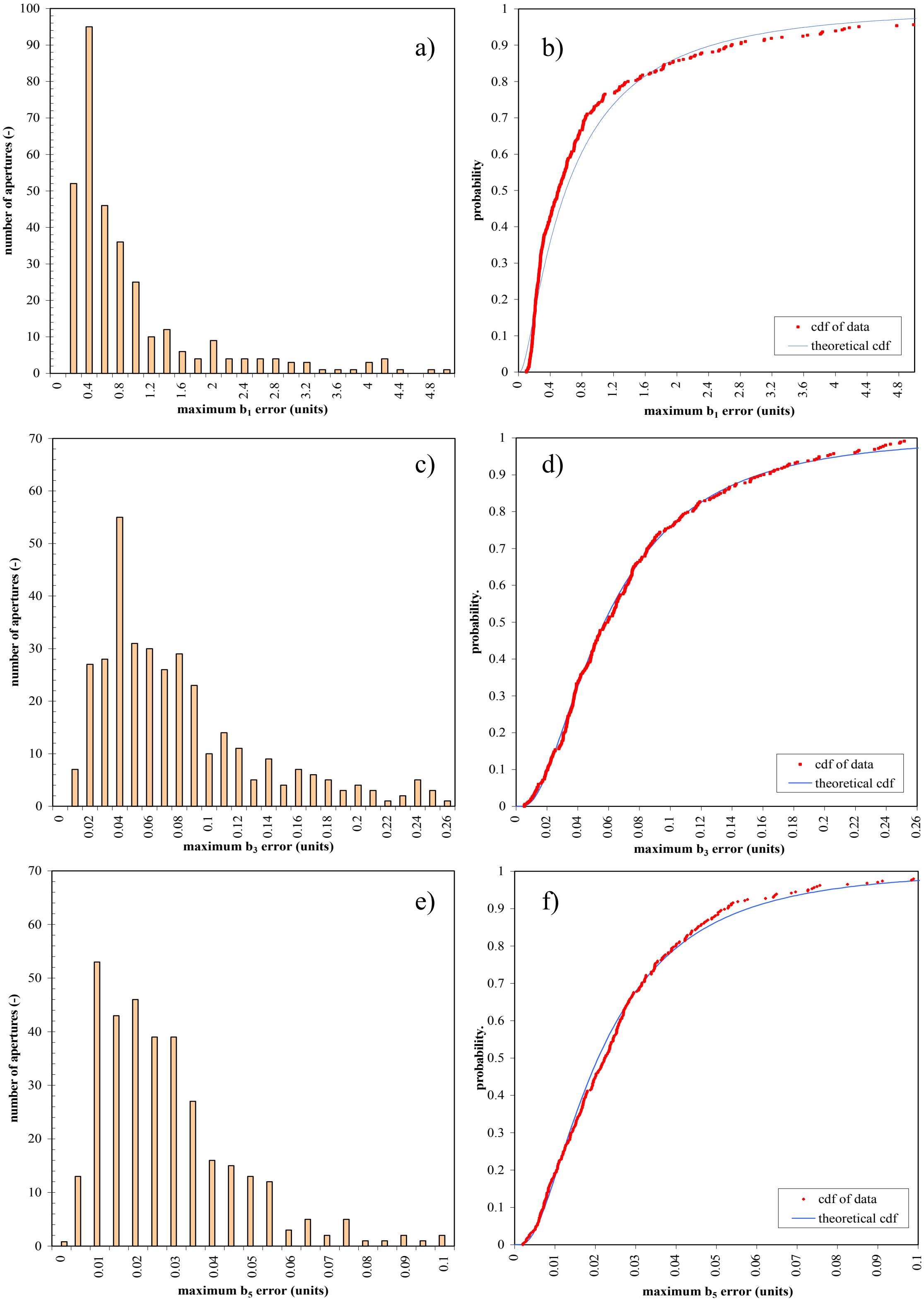

Figure 6.2: (a) (c) and **(e)** Histograms of the maximum error for b_1, b_3, and b_5, respectively, between the scaled harmonic decay and the average harmonic decay of the magnet set analysed. **(b), (d)** and **(f)** cumulative distribution function for b_1, b_3, and b_5, respectively, between the scaled harmonic decay and the average harmonic decay of the magnet set analysed.

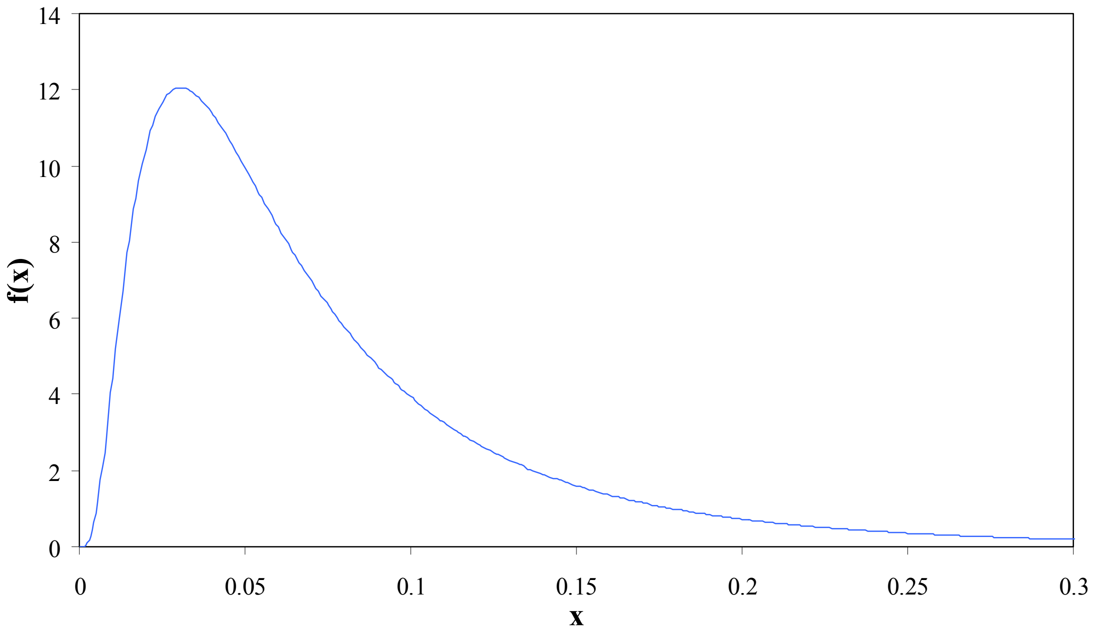

Figure 6.3: A lognormal probability density function (for $\sigma < 1$).

The scaling law tested produces typical maximum scaling errors in the range 0.1 to 5 units @ 17 mm for b_1, 0.01 to 0.26 units @ 17 mm for b_3, and 0.005 to 0.1 units @ 17 mm for b_5. There are few outliers that are not shown in the figure. These are generally related to magnets that have a large scaling factor or that have anomalous behaviour and that appear as a tail in the distributions.

Since the data distribution is skewed as shown in the histograms, the most probable errors (i.e. the mode) are less than the medians of the distribution. A conservative choice can be made by taking the median as an indication for the typical error in a reference magnet selected at random i.e. 0.5 units @ 17 mm for b_1, 0.06 units @ 17 mm for b_3 and 0.02 units @ 17 mm for b_5. In fact, in principle, it would be possible to achieve better results by selecting magnets based on their scaling error, and defining the scaling factor based on a general optimization over the time span available in measured data. This is not done here to keep the reasoning simple, and as it has little influence on the final conclusions.

6.2.2 - An Example: The Tevatron Dipoles

As a part of the overall optimization of the Tevatron Run II, several dipole magnets were re-measured at the Magnet Test Facility in Fermilab [105-106] aiming at reducing beam losses associated with residual correction errors during injection and snapback. Thanks to the copious results obtained in this measurement campaign, it was possible to compare the behaviour of the sextupole during injection in specific magnets to the chromaticity measurements taken during the injection plateau in the accelerator [102]. The result of this test is shown in Figure 6.4, and it demonstrates that the good agreement between the average behaviour of a magnet population and the scaled results from a single magnet is not accidental.

In the case shown in Figure 6.4 the scaled magnet behaviour reproduces the dynamics of the Tevatron chromaticity evolution to within 0.04 units @ 25.4 mm over a time span of nearly 2 hours. This gives confidence that the scaling of Eq. 6.2 can produce results accurate enough for precise control.

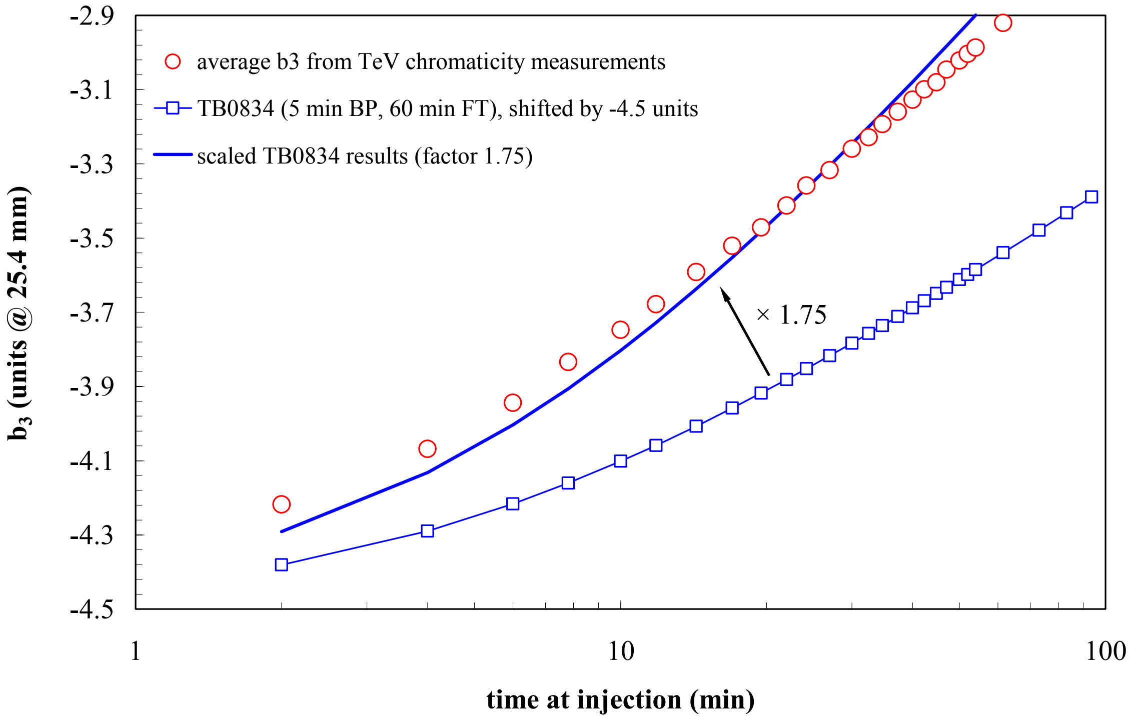

Figure 6.4: Comparison of the sextupole deduced from chromaticity measurement during an injection at Tevatron, and the scaled measurements in a spare dipole. The scaling factor was optimized to minimize the error over the complete injection plateau, of 100 minutes. Courtesy of P. Bauer, FNAL [102].

6.2.3 - A Second Example: The HERA Dipoles

The correction scheme employed by HERA at DESY makes use of on-line reference magnets and look up tables. As mentioned before, two reference magnets, one for each magnet production line, have been chosen to represent the behaviour of the two halves of the proton ring. The reference magnets were chosen to be at the centre of the drift spread of their respective magnet family.

The beam parameters can be controlled automatically using the rotating coils in the reference magnets to measure the drift of the b_3 component, and using NMR probes to detect the b_1 change [40]. The corrections obtained are applied without scaling to the corrector magnets in the ring. This corresponds to the scaling procedure outlined above for the LHC magnets, where the scaling factor f_{decay} of the single magnet to the average of the population is 1 because of the magnet selection adopted.

As shown in [107] and [36], the effect of decaying persistent currents leads to a change in the horizontal and vertical chromaticities in opposite directions. Without correction, the chromaticity reaches unacceptable values within a few minutes. However, if the correction system is switched on, the use of reference magnet data counteracts the decaying persistent current sextupole fields and the chromaticity in both planes is kept close to the desired values. As in the case of the Tevatron dipoles, these results show that a single magnet can be taken to represent the behaviour of a whole family.

6.3 - The Powering History Scaling Law

Eqs. 5.7, 5.8 and 5.9 can be combined to yield an equation that extrapolates the powering history dependence to a 3-dimensional parameter space [108]:

$$\delta_n = \delta_{std} \left(\frac{E_0^n - E_1^n e^{-\frac{I_{FT}}{\tau_E^n}}}{E_0^n - E_1^n e^{-\frac{I_{FT}^{std}}{\tau_E^n}}} \right) \left(\frac{T_0^n - T_1^n e^{-\frac{t_{FT}}{\tau_T^n}}}{T_0^n - T_1^n e^{-\frac{t_{FT}^{std}}{\tau_T^n}}} \right) \left(\frac{P_0^n + P_1^n e^{-\frac{t_{preperation}^{std}}{\tau_P^n}}}{P_0^n + P_1^n e^{-\frac{t_{preperation}^{std}}{\tau_P^n}}} \right) \tag{6.3}$$

The standard cycle is a pivot point that is common to all three powering history parameters. However, this pivot point has different values for the three parameters (δ parameters in Table 5.8, 5.9 and 5.10) due to the limited sample of measurements taken. To homogenise the pivot point and to have a powering history prediction for the entire magnet population, the decay scaling law is used to scale the average curves of Figures 5.11 to 5.13. Eq. 6.3 is then used to fit the three scaled average curves to a 3-dimensional parameter space. The fit yields the parameters reported in Table 6.1. The corresponding surface plots are shown in Figure 6.5, 6.6 and 6.7.

Table 6.1: The b_3 fit parameters of the 3-dimensional powering history dependence.

component	parameter	units	b_3
Decay amplitude	δ_{std}	(units)	2.004
Pre-cycle flat-top current (I_{FT})	E_0	(-)	1.2807
	E_1	(-)	1.6991
	τ_E	(A)	6900.1692
Pre-cycle flat-top duration (t_{FT})	T_0	(-)	–0.1986
	T_1	(-)	–0.0512
	τ_T	(s)	494.5232
Preparation duration ($t_{preparation}$)	P_0	(-)	0.9172
	P_1	(-)	–0.3934
	τ_P	(s)	380.5939
Standard deviation	σ	(units)	0.0002
Maximum error	max	(units)	0.0007

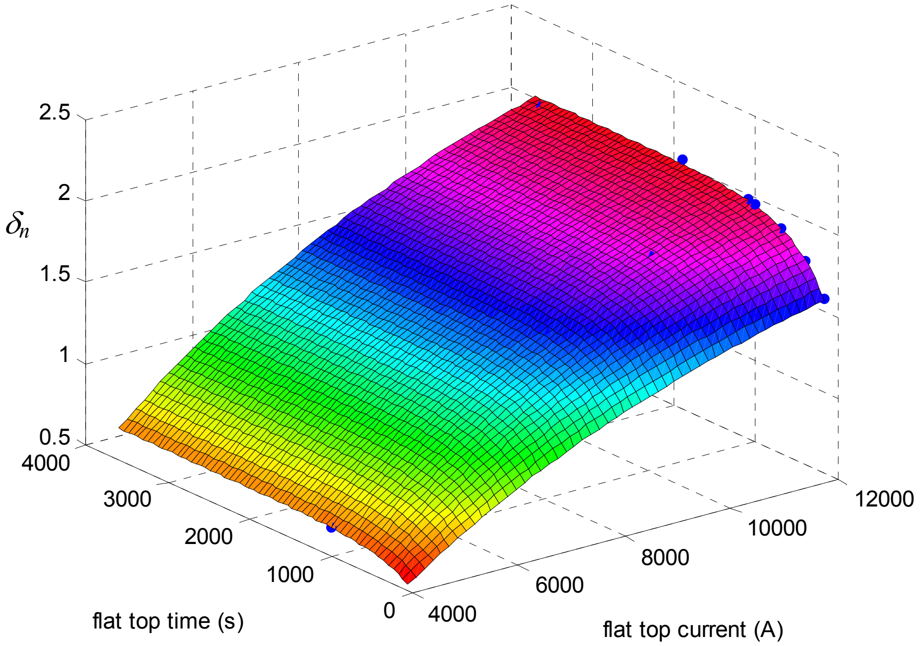

Figure 6.5: Plot of the surface of b_3 in the space defined by variations of flat top time (t_{FT}) and flat top current (I_{FT}) as generated with the parameters of Table 6.1 and representative for the LHC behaviour. The measured values are depicted by the blue points.

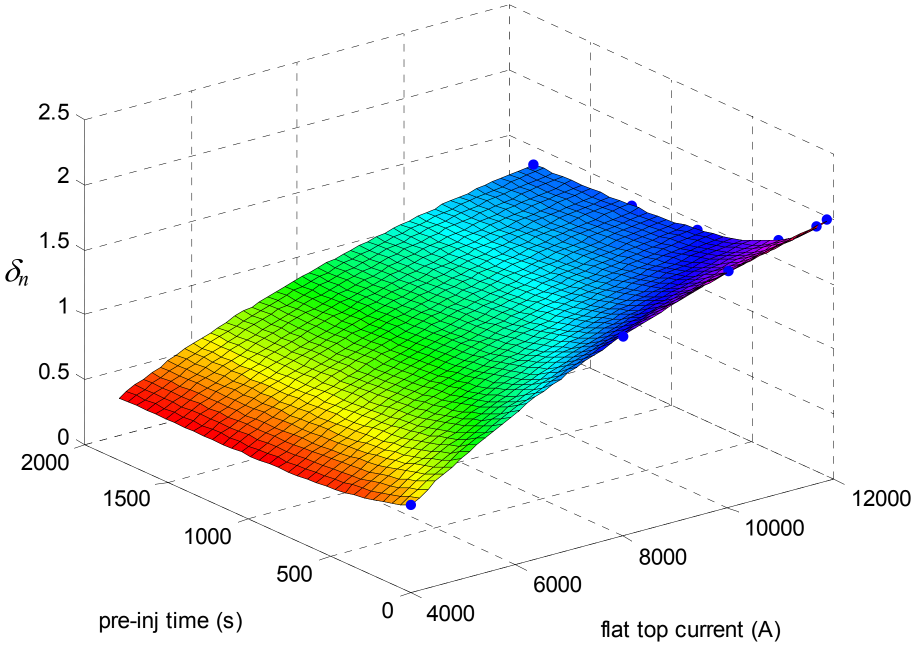

Figure 6.6: Plot of the surface of b_3 in the space defined by variations of pre-injection time ($t_{preparation}$) and flat top current (I_{FT}) as generated with the parameters of Table 6.1 and representative for the LHC behaviour. The measured values are depicted by the blue points.

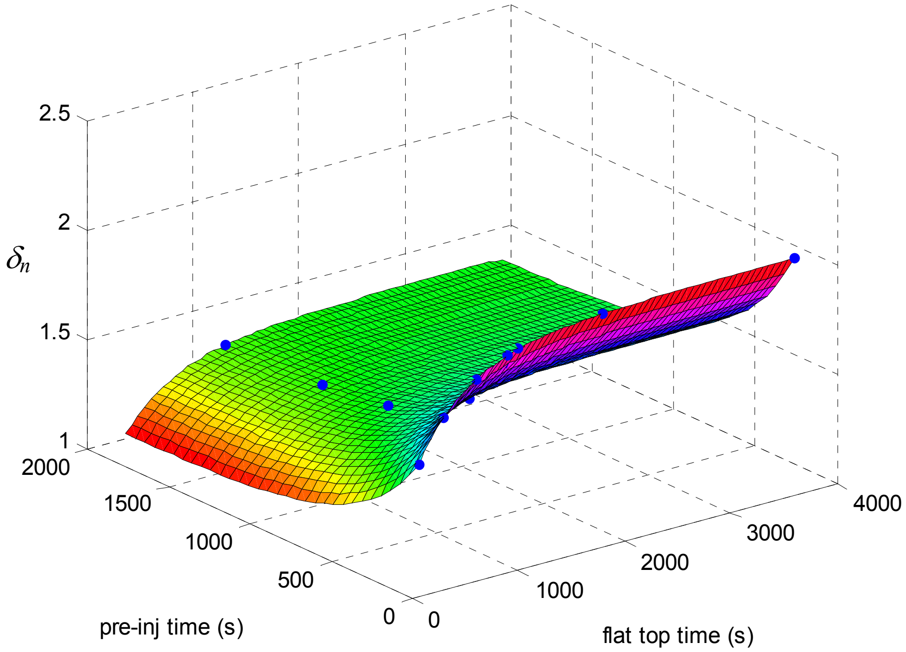

Figure 6.7: Plot of the surface of b_3 in the space defined by variations of pre-injection time ($t_{preparation}$) and flat top time (t_{FT}) as generated with the parameters of Table 6.1 and representative for the LHC behaviour. The measured values are depicted by the blue points.

As was done for the dynamics of the decay, it can be assumed that the linear scaling:

$$\delta_n = f_n^{decay} \cdot \delta_n^i \tag{6.4}$$

can be used to deduce the magnet population behaviour from the measurement of one magnet. In this case δ_n is the average decay in standard powering conditions, whilst δ_n^i is the decay of the reference magnet *i*. The scaling factor f_n^{decay} is given by the ratio of the average decay in the magnet population (sector or ring) and the decay of the reference magnet chosen. This is the same ratio as computed for the decay dynamics, through Eq. 6.2. Again, once the parameterization is fixed, the scaling has no free parameter. The parameters of Table 6.1 can be used in Eq. 6.3 to compute the difference between the scaled behaviour of a single magnet and the 3d fits. The maximum error between these two can be taken as a measure of the quality of the scaling. The histograms and the lognormal cdf for the three powering history parameters are shown in Figure 6.8. The use of the lognormal distributions is justified by the reasons described in the section 6.2 and confirmed by checking their goodness of fit with the Kolmogorov-Smirnov test.

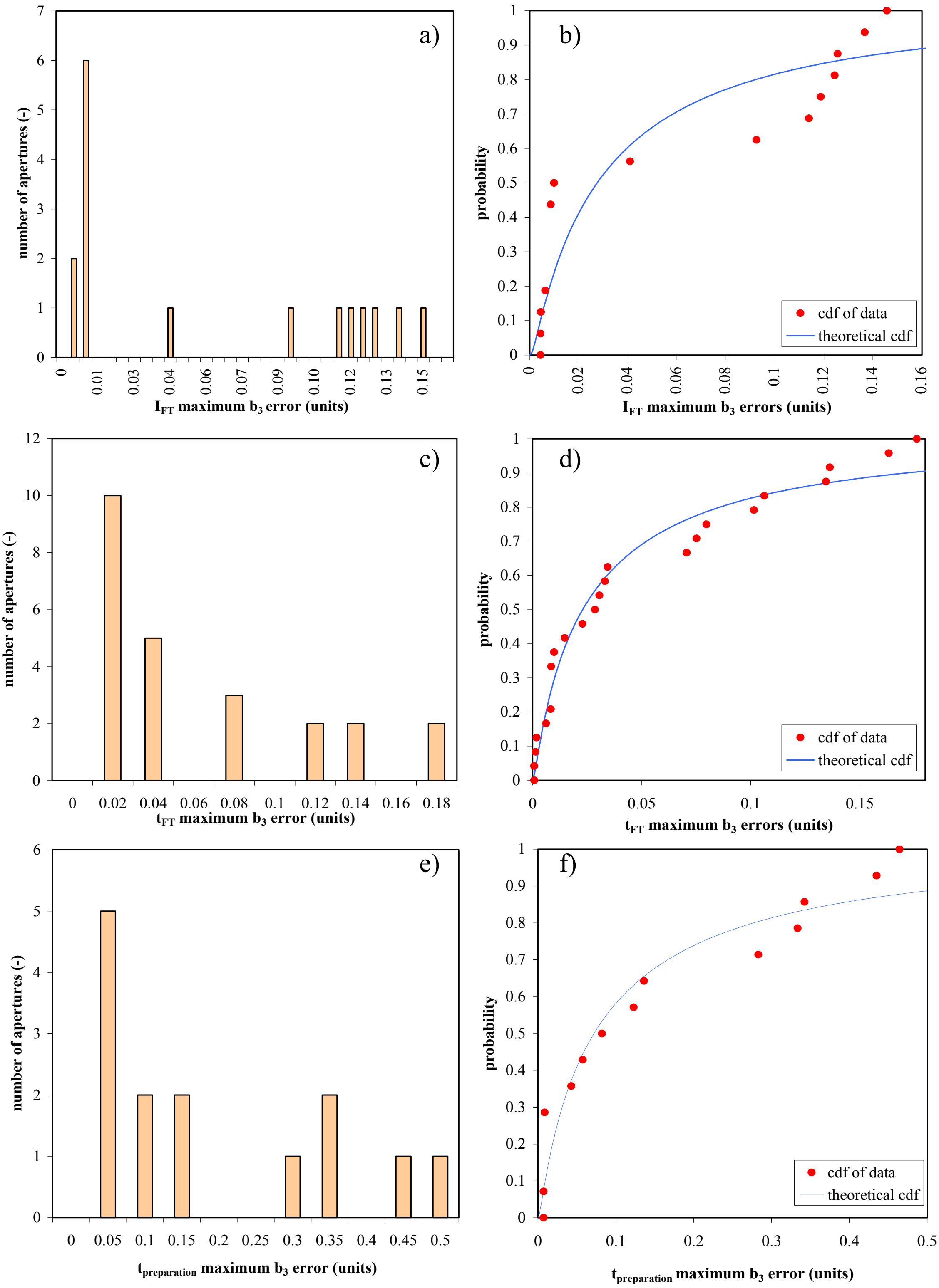

Figure 6.8: (a), (c) and **(e)** Histograms of the maximum error for I_{FT}, t_{FT}, and $t_{preparation}$, respectively, between the scaled harmonic decay and the average harmonic decay of the magnet set analysed. **(b), (d)** and **(f)** cumulative distribution function for I_{FT}, t_{FT}, and $t_{preparation}$, respectively, between the scaled harmonic decay and the average harmonic decay of the magnet analysed.

As done earlier, the medians can be taken as an indication of the error in a reference magnet selected at random. For the b_3 flat top current dependence, the maximum error ranges from 0.004 to 0.15 units, with a median value of 0.03 units. For the b_3 flat top time dependence, the maximum error ranges from 0.001 to 0.18 units, with a median value of 0.02 units @ 17 mm. For the b_3 pre-injection time dependence, the maximum error ranges from 0.008 to 0.46 units, with a median value of 0.07 units.

For the b_1 flat top current dependence modelled with Eq. 5.7, the maximum scaling error ranges between 0.33 and 2.5 units with a median value of 0.84 units. For the b_5 flat top current dependence modelled with Eq. 5.7, the maximum scaling error ranges between 0.005 and 0.11 units with a median value of 0.016 units.

6.4 - The Snapback Scaling Law

6.4.1 - LHC Dipoles

Having a relation between the decay amplitude and the current constant of Eq. 5.10 would be highly instrumental for predicting the snapback behaviour since this would imply that only the decay amplitude resulting after a decay change would need to be known for a snapback forecast.

Based on a few measurements, it was observed in [18] that the decay amplitude and the current constant are strongly correlated with each other and once represented on a scatter plot $c_n^{decay}(t_{ramp})$ vs. ΔI_n they lie on a straight line. Figure 6.9 shows the b_3 correlation between these two parameters for the LHC dipoles measured using the snapback analyser.

The most interesting property, however, is that the b_3 correlation between the fit parameters $b_3^{decay}(t_{ramp})$ and ΔI_n is the same, in all magnets tested. This fact suggests that the scatter plot representation adopted and the correlation found is an invariant property of a magnet design family within the standard deviation of the correlation, independent of the specific properties of each magnet instance.

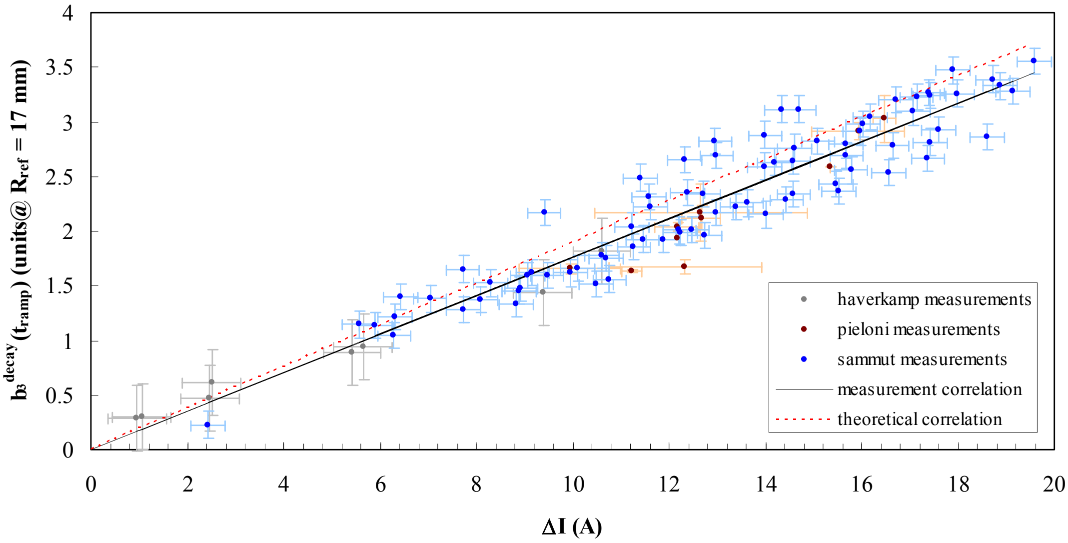

Figure 6.9: Scatter plot of the sextupole fit parameters $b_3^{decay}(t_{ramp})$ (units @ R_{ref} 17 mm) and ΔI_n that correspond to sets of different powering cycles in the LHC dipoles tested and analysed to date.

This postulate is substantiated by the fact that the magnets tested were not specially selected (e.g. with respect to cable properties) and comparable results are found performing the same measurements and data analysis on both the LHC and Tevatron dipoles, as discussed later. This therefore demonstrates that the correlation plot can be used to characterize the behaviour of the dipoles in the whole accelerator, i.e. it can work as a scaling law.

In practice, the waveform of the snapback can be predicted by taking the observed decay $c_n^{decay}(t_{ramp})$, at the time of the start of the ramp (e.g. computed using Eq. 6.2), and computing the corresponding ΔI_n using the linear snapback correlation coefficient g_n^{SB}:

$$c_n^{decay}(t_{ramp}) = g_n^{SB} \cdot \Delta I_n \tag{6.5}$$

From b_3 measurements, g_3^{SB}= 0.176 units/A which is comparable to the theoretical value $g_3^{SB\_theoretical} = 0.19$ units/A obtained by Bottura [109]. The R-squared value of the correlation line is 0.911. To have a better indication of the quality of the snapback scaling law, the same procedure as used in the decay scaling analysis described above is employed. This is done by taking the error as being the maximum deviation of the fit parameter $b_3^{decay}(t_{ramp})$ from the correlation of Eq. 6.5 for all measurement sets analysed. The histogram and the cdf of the difference between the sextupole snapback amplitudes and the correlation line are shown in Figure 6.10.

The use of the lognormal distribution is justified by the same reasons discussed earlier. The errors range from 0.01 to 0.6 units @ 17 mm, with a median value of 0.14 units @ 17 mm. The above values for the median error can be taken as an estimate for the deviation between the predicted and the actual snapback waveforms in the accelerator.

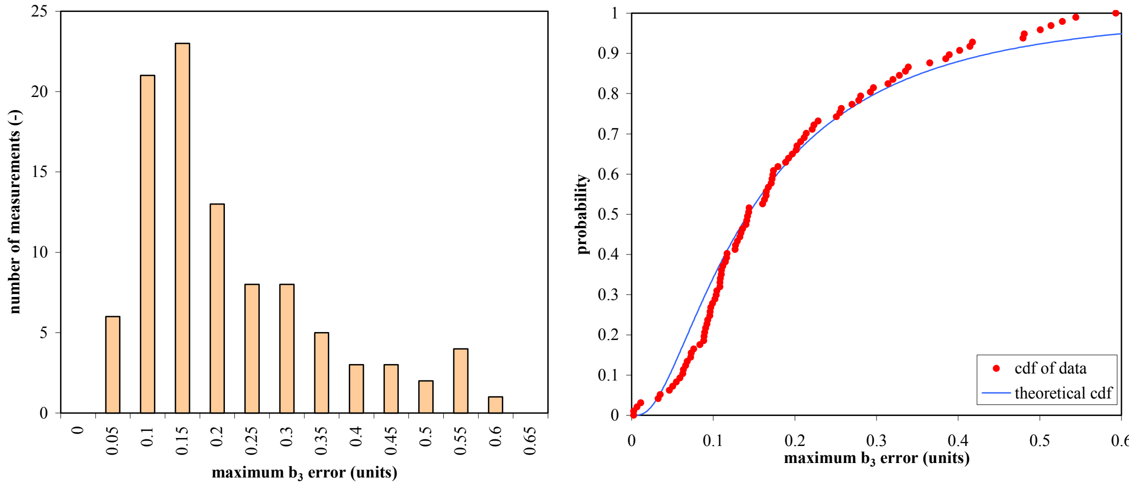

Figure 6.10: (left) The histogram and **(right)** the cdf of the difference between the sextupole snapback amplitudes and the correlation line.

6.4.2 - Tevatron Dipoles

Sextupole snapback measurements of the same type as described above were performed by Velev on 12 Tevatron dipoles [110]. Following the same analysis procedure as for the LHC dipoles, the results can be represented in the same scatter plot of Figure 6.11, and lead to the same conclusion, namely that the two parameters $c_n^{decay}(t_{ramp})$ and ΔI_n are strongly correlated.

The fact that the same result is obtained on two different families of dipole magnets, with major design and manufacturing differences (both on the superconducting cable and coil) supports the idea that the correlation found has some fundamental origin, and can thus be used for a robust prediction.

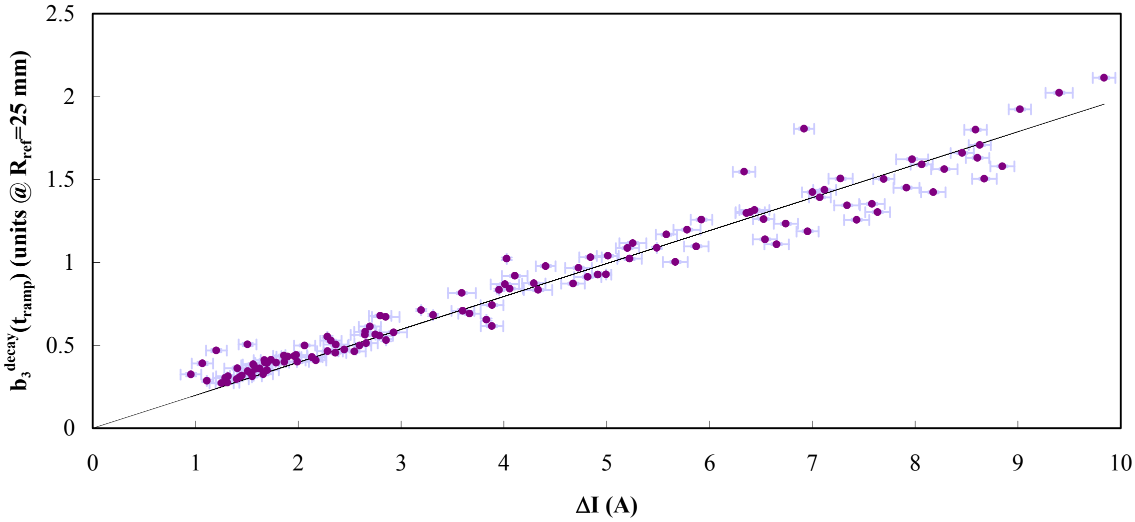

Figure 6.11: Scatter plot of the fit parameters $b_3^{decay}(t_{ramp})$ (units @ R_{ref} = 25 mm) and ΔI_3 that correspond to sets of different powering cycles in four Tevatron dipoles tested and analysed to date. $g_3^{SB} = 0.198$. Courtesy of G. Velev and P. Bauer from FNAL [110].

6.5 - Conclusion

It has been shown in this chapter that a set of scaling laws deduce the decay and snapback behaviour of a set of several magnets in different magnetic states, representing a sector or the whole ring in the LHC, from:

a. The series measurements on 18 per cent of the magnets.
b. Single measurements on selected magnets i.e. off-line reference magnets.
c. Direct beam measurements during machine development time.

In the case of point b above, the error of the scaled predictions does not depend drastically on the magnet selected, so that the selection of a *good* reference magnet will not be a critical process. In practice, following the reasoning of this chapter, half of the magnets produced can be used as reference magnets.

Table 6.2 reports a summary of the maximum expected errors due to the dynamic model and the scaling procedure. For the injection plateau, this is obtained as the quadratic sum of the error on the decay and on the prediction of the powering history dependence. These values correspond to about 7 units of chromaticity.

Table 6.2: Summary of the maximum error expected due to the dynamic model and scaling procedure. (All values are in units @ R_{ref})

		b_1	b_3	b_5
decay model		0.32	0.13	0.04
decay scaling		0.5	0.06	0.02
powering history model	I_{FT}	0.01	0.0007	0.007
	t_{FT}	-		-
	$t_{preparation}$	-		-
powering history scaling	I_{FT}	0.84	0.03	0.016
	t_{FT}	-	0.02	-
	$t_{preparation}$	-	0.07	-
total decay error		1.02	0.16	0.05
snapback model		-	0.03	0.03
snapback correlation		-	0.14	-
total snapback error		-	0.14	-

Chapter 7

Further Model Considerations

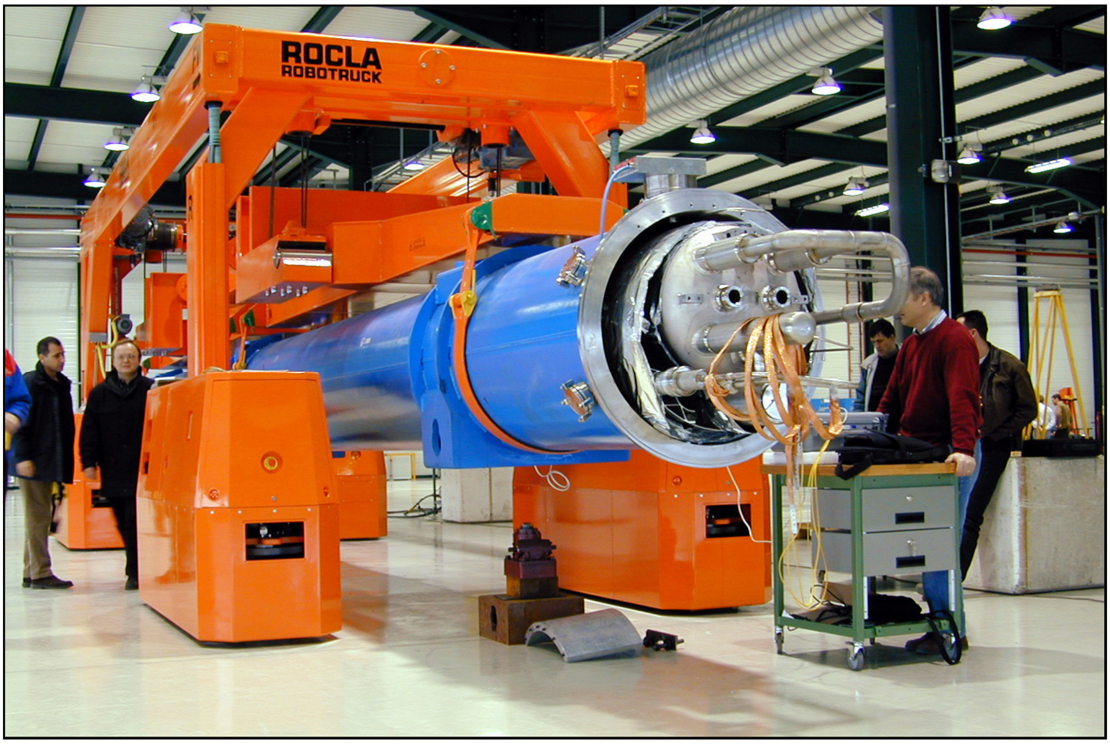

LHC magnet transported by robotruck.

> You see things, and you say, “Why?”
> But I dream things that never were, and say, “Why not?”
> - George Bernard Shaw

Chapter 7

Further Model Considerations

During the design of FIDEL, a number of additional considerations must be evaluated to ensure that the feed-forward strategy is optimised.

One of the most important considerations is to verify whether the dipoles should be grouped up into families according to their magnetic field variations with the aim of reducing the spread. This is important since it indicates whether parts of the model should be modified to represent different magnet groups and determines how many off-line reference magnets should be used to ensure that they can represent the entire population.

Other aspects that must be considered include the effect of multiple LHC cycles on the decay amplitude of the main field and the allowed harmonics as well as the magnetic effects due to aging or due to Lorentz forces after many machine cycles.

It is also important to consider the adaptability of the field model when used to predict the magnetic field variation of magnet types other than that of the LHC dipoles. Therefore, in this chapter, the static and decay model are applied on the LHC main quadrupoles and the insertion region wide aperture quadrupoles. The static model is also tested on the long trim quadrupole correctors. The results of this modelling hence give a good insight to the robustness and the scope of the field model.

7.1 - Magnet Families

In an effort to minimise the spread of the magnetic field variation in the machine, the LHC superconducting dipole magnets are installed in the ring such that magnets with the same type of inner cable are placed in each sector. As shown in Figure 7.1, the cross-section of the two cable types (01B and 01E) is very different. 01B cables are manufactured using the single stack method whilst 01E cables are manufactured using the double stack method.

This sorting procedure was an initial recommendation followed by the MEB and was used as a working hypothesis. However, it eventually placed a very large constraint on the installation of the magnets and this triggered a detailed analysis of the magnetic data to check whether the two magnet families really do have two distinct systematic behaviours.

The way the dipoles are grouped up into families is important for FIDEL since it gives a good insight as to how many dipole off-line reference magnets should be measured to ensure proper predictability of the field and its harmonics. The grouping strategy also indicates whether variations of the static and dynamic models need to be considered for the different sectors based on the different behaviours of the magnet families.

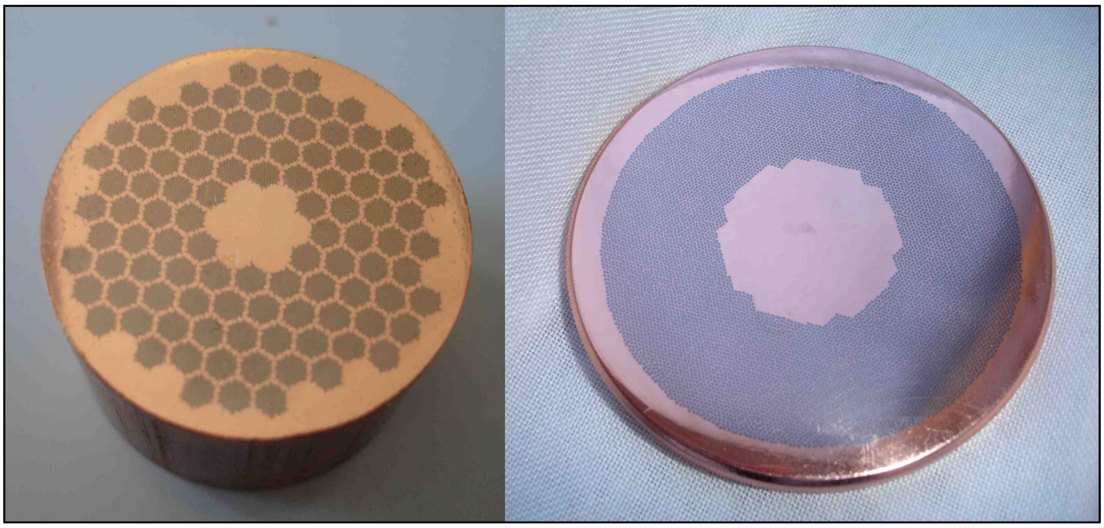

Figure 7.1: **(left)** The double stacked O1E cable cross-section, courtesy of EAS®; **(right)** the single stacked O1B cable cross-section, courtesy of Alstom®.

A similar sorting strategy was used at DESY in the HERA machine where the magnets were divided into two families according to manufacturer and hence controlled with two different reference magnets [40].

7.1.1 - Magnet Families in the Static Domain

The distinct systematic difference of the two magnet families in the static domain can be checked by considering their hysteresis and effective magnetisation components. In this analysis, 314 apertures are considered and are also separated by outer cable so as to investigate whether the outer cables also contribute to the distinct systematic difference. Table 7.1 shows the number of apertures considered for the magnets with the different cable combinations.

Considering the hysteresis as defined in section 4.2, a clear difference of 5.5 units on the main field can be observed between the apertures that have 01E cables and the ones that have 01B cables. This is clearly shown in Figure 7.2. However, Figure 7.3 shows that there is no significant distinction in the case of the effective magnetisation. These figures also show that in the static domain, the outer cables can be ignored when grouping the magnets into families. No distinct difference can be observed for b_3 and b_5.

Table 7.1: The number of apertures measured for the different cable combinations.

	02B5	**02B8**	**02C0**	**02C9**	**02D**	**02G**	**02K**
01E	0	15	N/A	6	16	7	20
01B	98	11	14	N/A	0	18	109

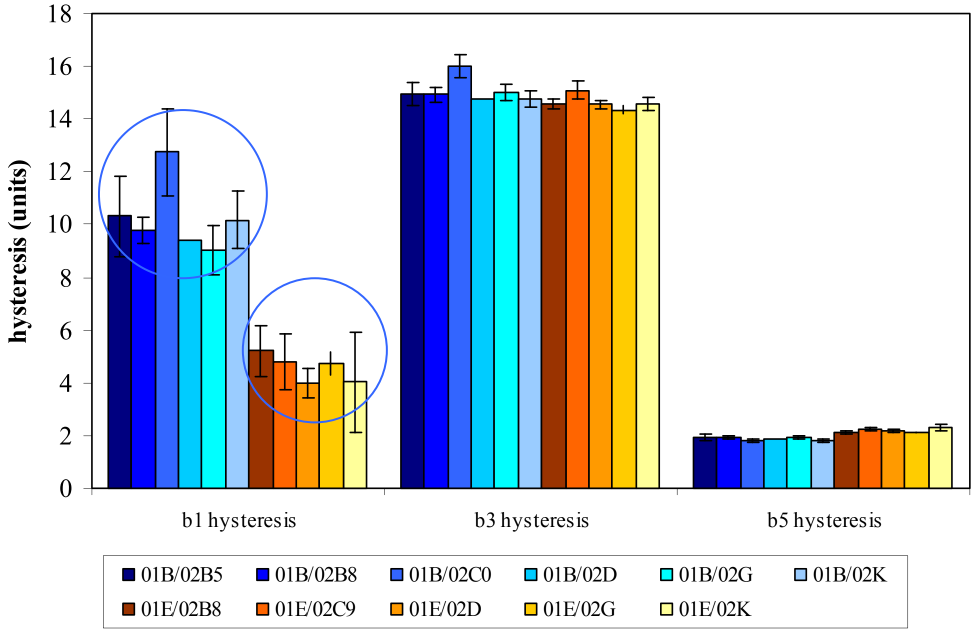

Figure 7.2: The hysteresis for the various cable types. Bars indicate the standard deviation.

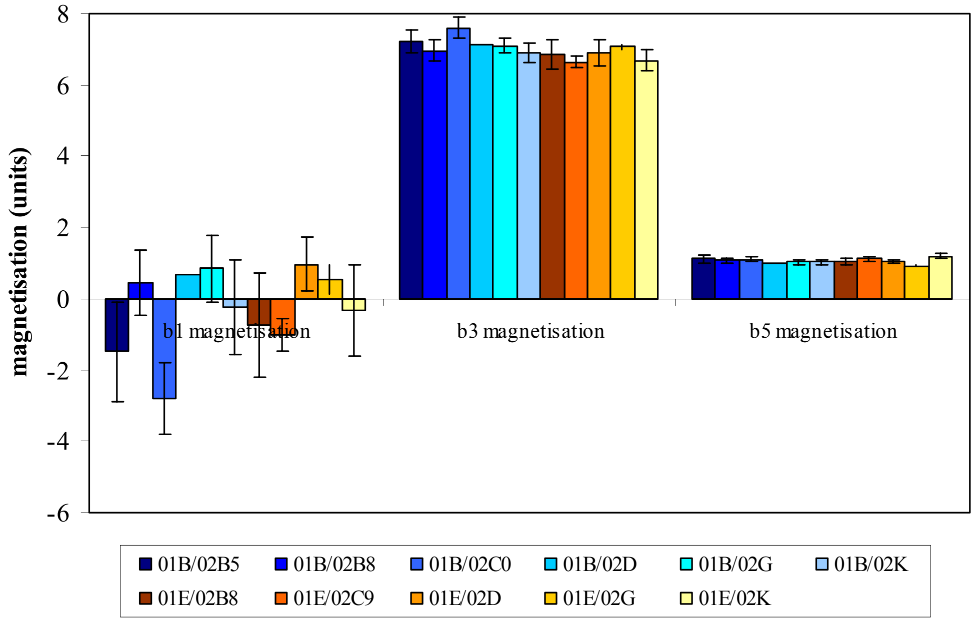

Figure 7.3: The effective magnetisation for the different cable combinations. Bars indicate the standard deviation.

To investigate further, the average transfer functions of the two families during the ramp-up can be compared with each other as shown in Figure 7.4. Every magnet in each family is first normalized with respect to the geometric value before averaging. Figure 7.4 (bottom) shows a close up of the TF where the difference between the two curves is greatest. Figure 7.5 shows the difference as a function of current and Table 7.2 shows the actual values. These results demonstrate that, during the ramp-up, the difference between the two families only becomes important at very low currents. However, the difference is comparable to the rotating coil measurements repeatability in the range of operation of the LHC (760 A to 11850 A).

Table 7.2: The average TF values and the difference of the TF during the ramp-up.

current (A)	average 01B (units)	average 01E (units)	difference (units)
400	10.99	0.97	10.02
550	3.68	1.34	2.34
600	2.02	1.23	0.79
760	−0.72	−0.14	−0.58
1000	−1.90	−1.54	−0.36
1500	−1.67	−1.60	−0.07
2000	−1.11	−0.99	−0.12
3000	−0.54	−0.34	−0.20
4000	−0.52	−0.23	−0.29
5000	−0.73	−0.53	−0.21
6000	−1.52	−1.34	−0.18
7000	−3.13	−2.99	−0.14
8000	−6.08	−6.06	−0.02
9000	−12.25	−12.29	0.04
10000	−22.64	−22.70	0.06
11000	−38.50	−38.69	0.19
11850	−58.55	−58.72	0.17

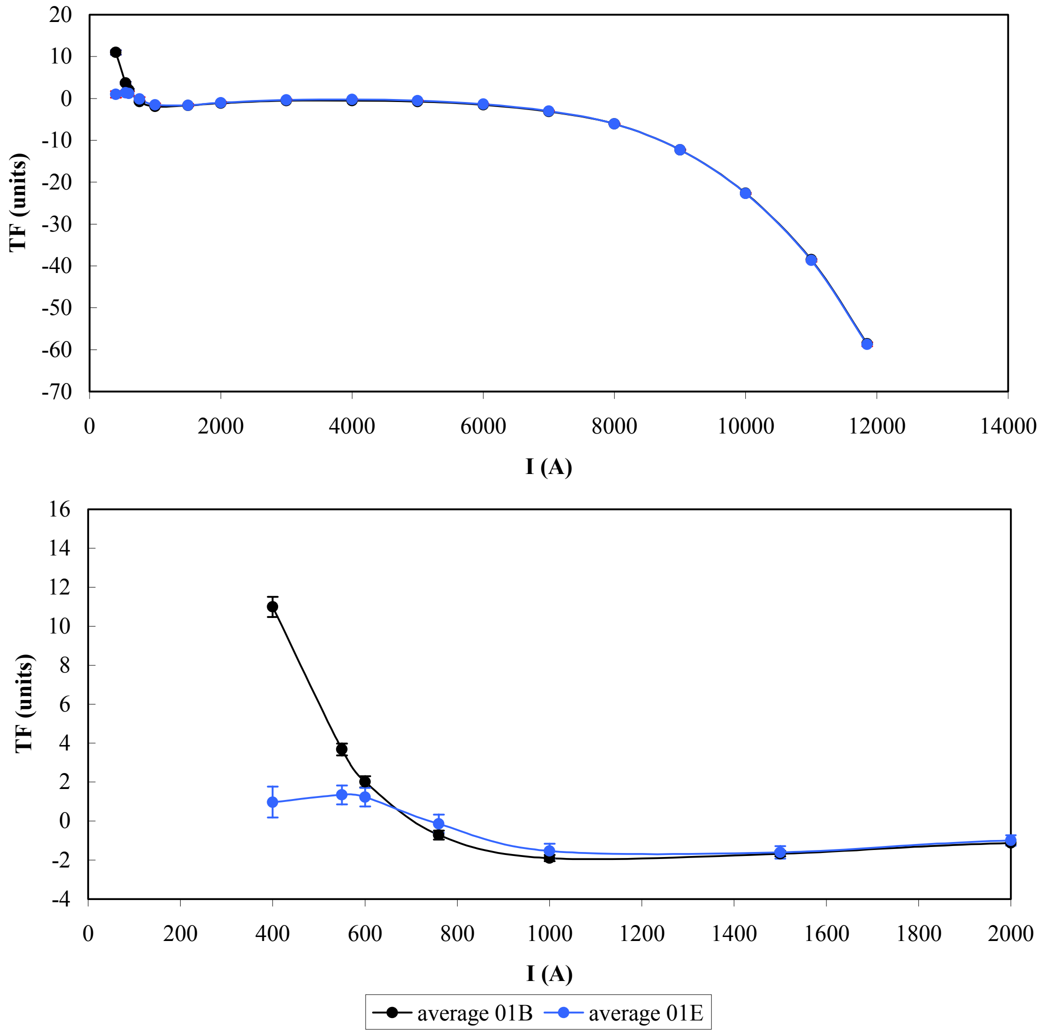

Figure 7.4: The normalized average of the TF for the two families. The error bars show the 95 per cent confidence interval. **(top)** full TF and **(bottom)** close up at low current.

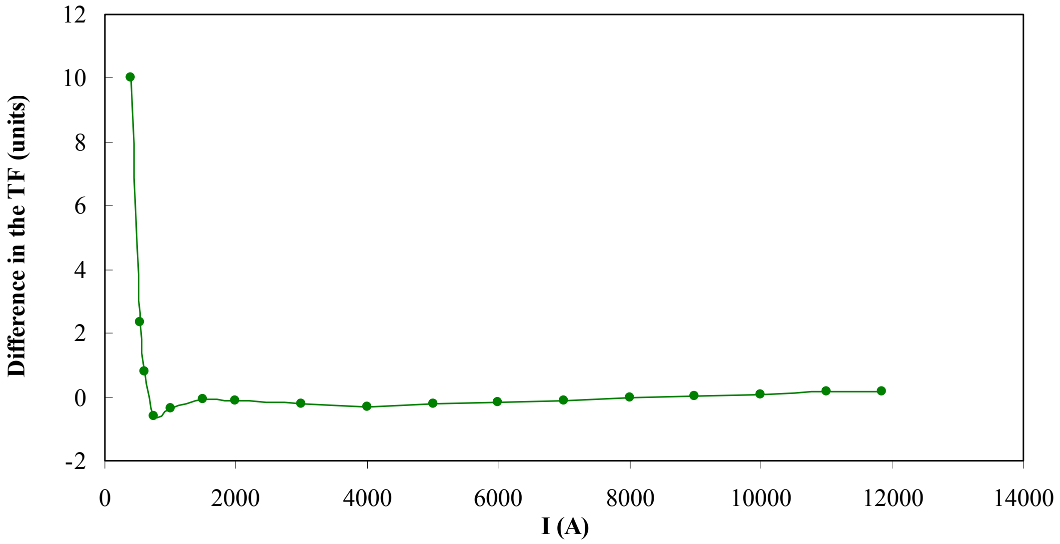

Figure 7.5: The difference of TF between the two families (Normalized to the geometric value).

From the effective magnetisation and the hysteresis definitions of section 4.2, the large distinction between the two magnet families, observed in the hysteresis component (Figure 7.2), can only be explained by an important difference in the transfer function during ramp-down. A comparison can be made between two magnets selected at random from the different families namely, MB3127 of the 01B family and MB3005 of the 01E family. Figure 7.6 shows the difference between the transfer function of the two magnets. At injection current (760 A), the difference is only 0.8 units during the ramp-up (close to the average of 0.58 units). However, during the ramp-down at injection current, the difference is -6.5 units which is close to the average hysteresis difference of 5.5 units between the two families.

Therefore, these results show that from the static model point of view, it is not necessary to separate the magnets into families since the difference between them is not important in the LHC range of operation.

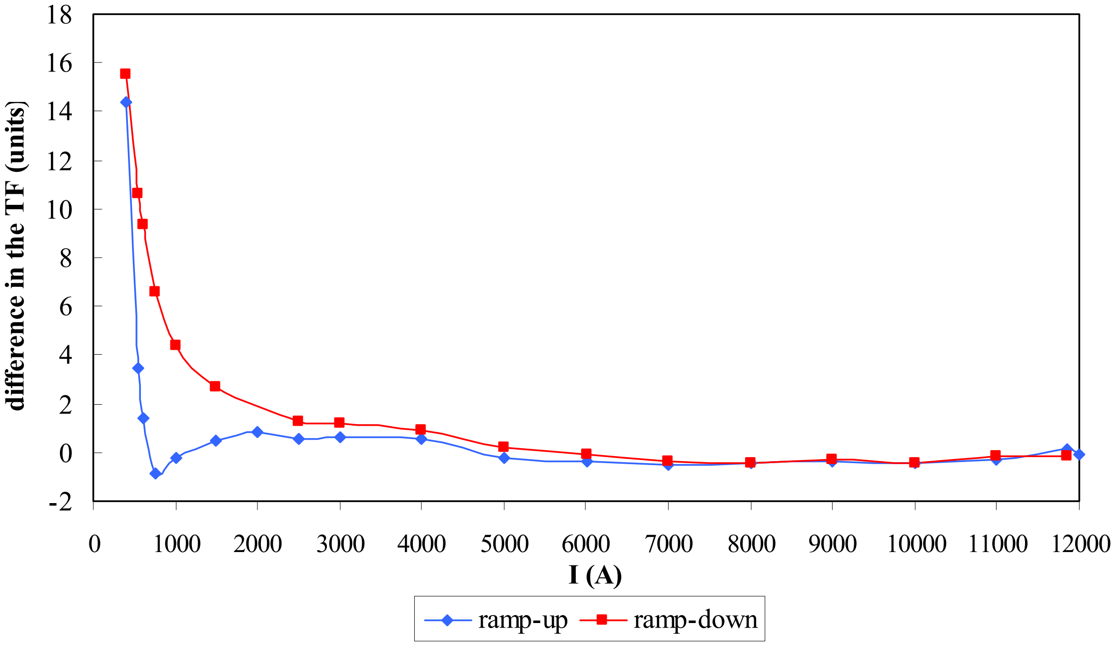

Figure 7.6: The difference of TF between two magnets coming from the two families.

7.1.2 - Magnet Families in the Dynamic Domain

The distinct systematic difference of the two magnet families in the dynamic domain can be checked by considering the magnet decay of the main field and the main harmonics at injection. The apertures considered in the previous section are grouped by inner cable and their average decay is computed. As was seen in the static domain, no distinct systematic difference is observed for b_3 and b_5. However, a difference in the average decay of the main field of the two families can be observed, as shown in Figure 7.7.

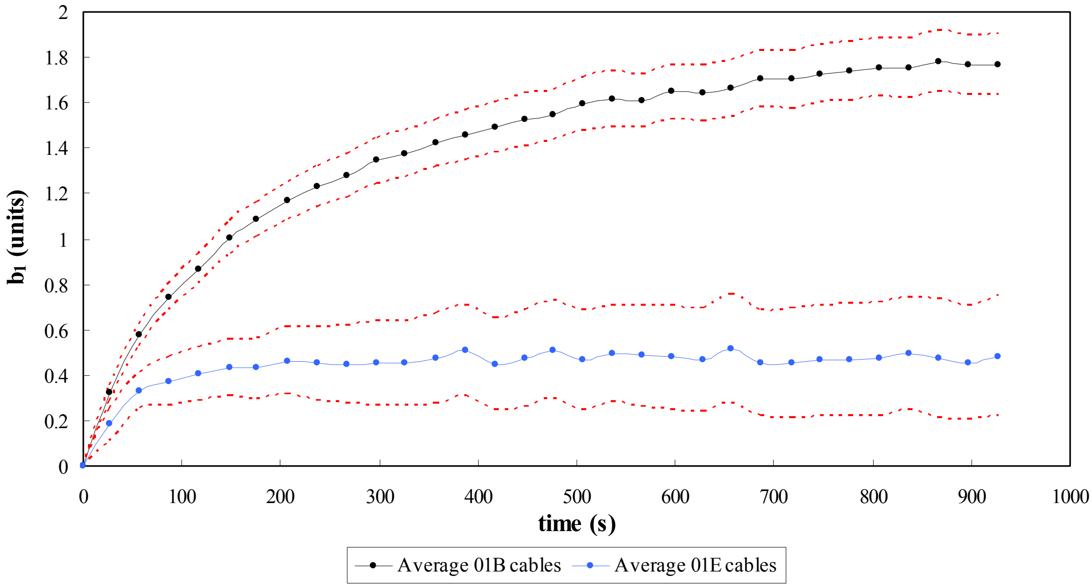

Figure 7.7: b_1 decay for the average of the 01B and 01E cables at injection current. The red dashed lines show the 95 per cent confidence interval.

The above analysis can be taken one step further to check the influence of the outer cables. The results of this analysis are shown in Figure 7.8. These graphs show that the behaviour of the decay is mostly affected by the inner cables though the outer cable may also have some influence. All the 01B cables show an exponential decay behaviour even though this is debatable for 01B-02G magnets. In contrast to this, 01E cables show practically no decay at all with the exception of the 01E-02B8 magnets which behave like magnets with 01B cables. Ideally, the machine would be grouped into inner and outer cable families. However, this is not practical for installation.

From this analysis, it is possible to predict what the b_1 decay behaviour would be for the entire population when sorted by inner cable. To do this the sampled average of each inner and outer cable group is multiplied by the number of magnets that are produced with that specific cable combination. The average is then computed for the magnets sorted by inner cable type. Figure 7.9 shows the sampled average and the predicted population b_1 decay average.

The 01B population average is expected to be the same as the sampled decay average whilst the 01E population average is expected to decrease by about 0.2 units with respect to the sampled decay average.

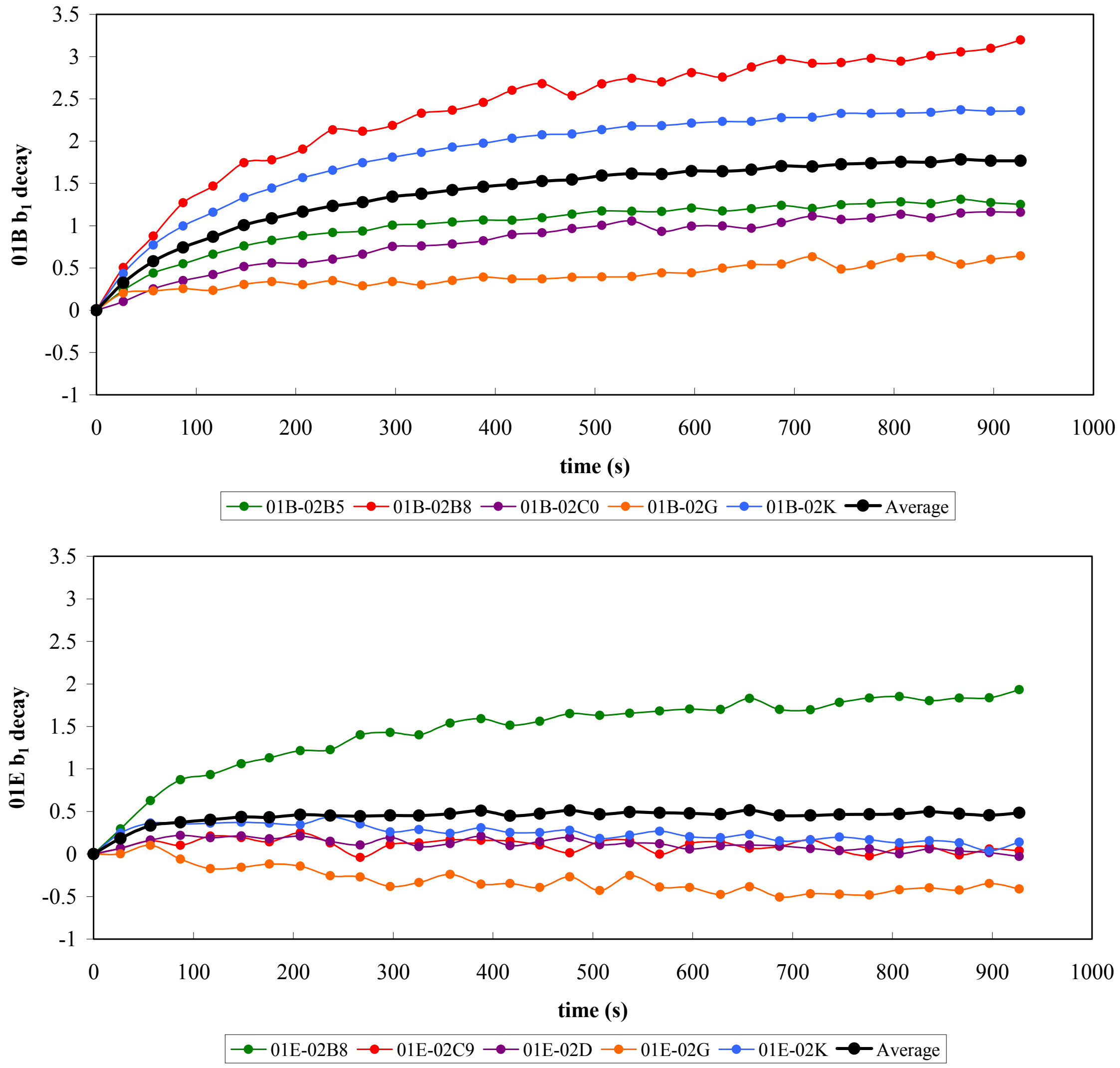

Figure 7.8: b_1 decay for the average of the **(top)** 01B and **(bottom)** 01E cables at injection current sorted also by outer cable type.

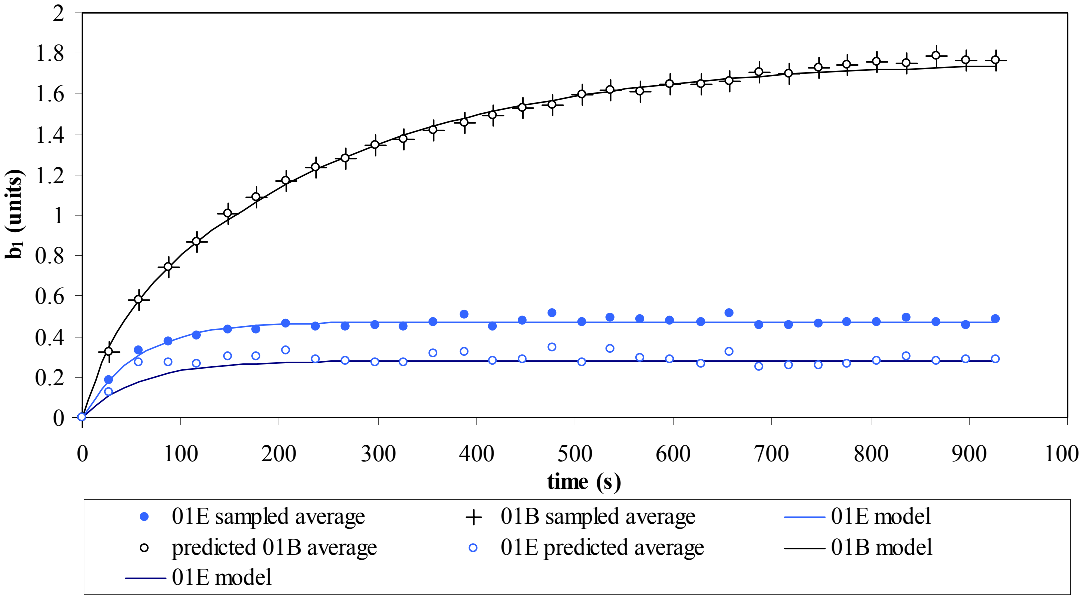

Figure 7.9: b_1 decay for the sampled average and the predicted b_1 decay of the entire population of the **(top)** 01B and **(bottom)** 01E cables at injection current sorted by inner cable type.

It can be observed from Figure 7.9 that on average, magnets with 01B cables exhibit a more pronounced exponential decay behaviour (Eq. 5.3). For 01E magnets Eq. 5.3 can be written as:

$$\Delta(t, t_{inj}, \tau, d) = d\left(1 - e^{-\frac{t - t_{inj}}{\tau}}\right) \tag{7.1}$$

where the parameters have the same meaning as in Eq. 5.3. The values of the fitting parameters of the 01E cables are shown in Table 7.3.

The decay scaling law can be tested separately for the predicted 01E cable decay in the same way as was done in chapter 6. The pdf and the cdf of this analysis is shown in Figure 7.10. The typical maximum scaling errors in this case are in the range of 0.12 to 1.5 units @ 17 mm. The median is 0.29 units. The median maximum error of the scaling is also comparable to the decay amplitude of the 01E cables, since the latter is very small and comparable to the measurement repeatability.

Table 7.3: The model parameters for 01E cables based on a sample of 65 apertures taken from the whole magnet population.

parameter	units	b_1 (01E)
τ	(s)	54.89
d	(-)	0.98
δ	(units)	0.285
max error	(units)	0.09

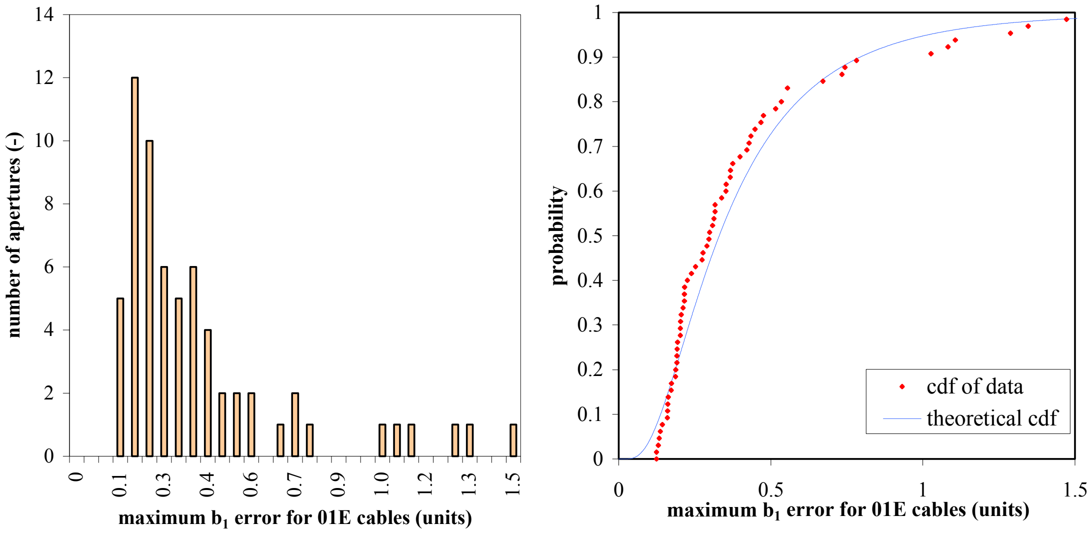

Figure 7.10: (left) The histogram and **(right)** the cdf, for b_1 of the maximum difference between the scaled decay and the predicted decay of 01E cables.

Therefore, the above analysis has shown that magnets with a different type of inner cable have a different magnetic behaviour. The same conclusion was drawn by Bellesia from warm measurement data [111]. In the static domain, the difference is small in the machine operation range and can be neglected. In the dynamic domain, the difference is larger but still within the measurement uncertainty and hence, not necessarily critical.

From these results, the MEB at first decided to maintain the policy of sorting the magnets by inner cables. However, as installation proceeded this criterion was relaxed and the magnets were mixed when the sorting constraints became tight.

7.2 - Multiple LHC Cycle Effect

Another consideration that needs to be taken into account in the dynamic field model is the effect of many LHC cycles on the decay amplitude. In the powering history analysis, the powering history is condensed into a single powering pre-cycle. In practice, there will be many LHC cycles following each other. Therefore, a dedicated measurement as shown in Figure 7.11 was performed on the dipole MB1225 to investigate whether the decay preceded by many LHC cycles has the same amplitude as the decay preceded by one single powering pre-cycle.

Figure 7.12 shows the decay amplitude of the allowed harmonics in the two apertures vs. the number of LHC cycles preceding the measurement. For b_3 and b_5, the maximum difference between two consecutive cycles is 0.05 units and 0.004 units, respectively. This difference is therefore very small and comparable to the median of the maximum scaling error for the powering history dependence (section 6.3). The decay amplitude variation of b_1 is also negligible and is less than the measurement repeatability. These results are consistent with those achieved by Haverkamp [94] and Schneider [95] on 1 m short LHC dipole model magnets.

Therefore, based on this measurement, the indication is that many cycles of the same type can be condensed into a single pre-cycle. This measurement, however, does not check several other variations of the multiple pre-cycles, for example, the effect of a low current (e.g. I_{FT} = 4 kA) pre-cycle preceded by a high current (e.g. I_{FT} = 11.85 kA) cycle.

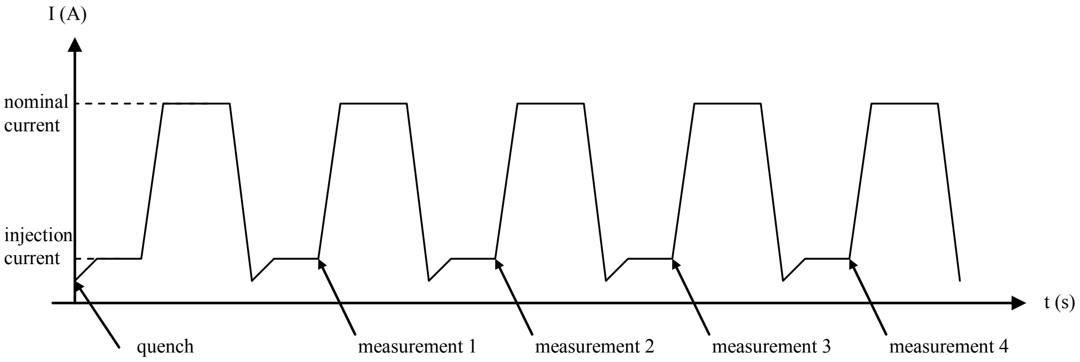

Figure 7.11: The multiple LHC cycle test.

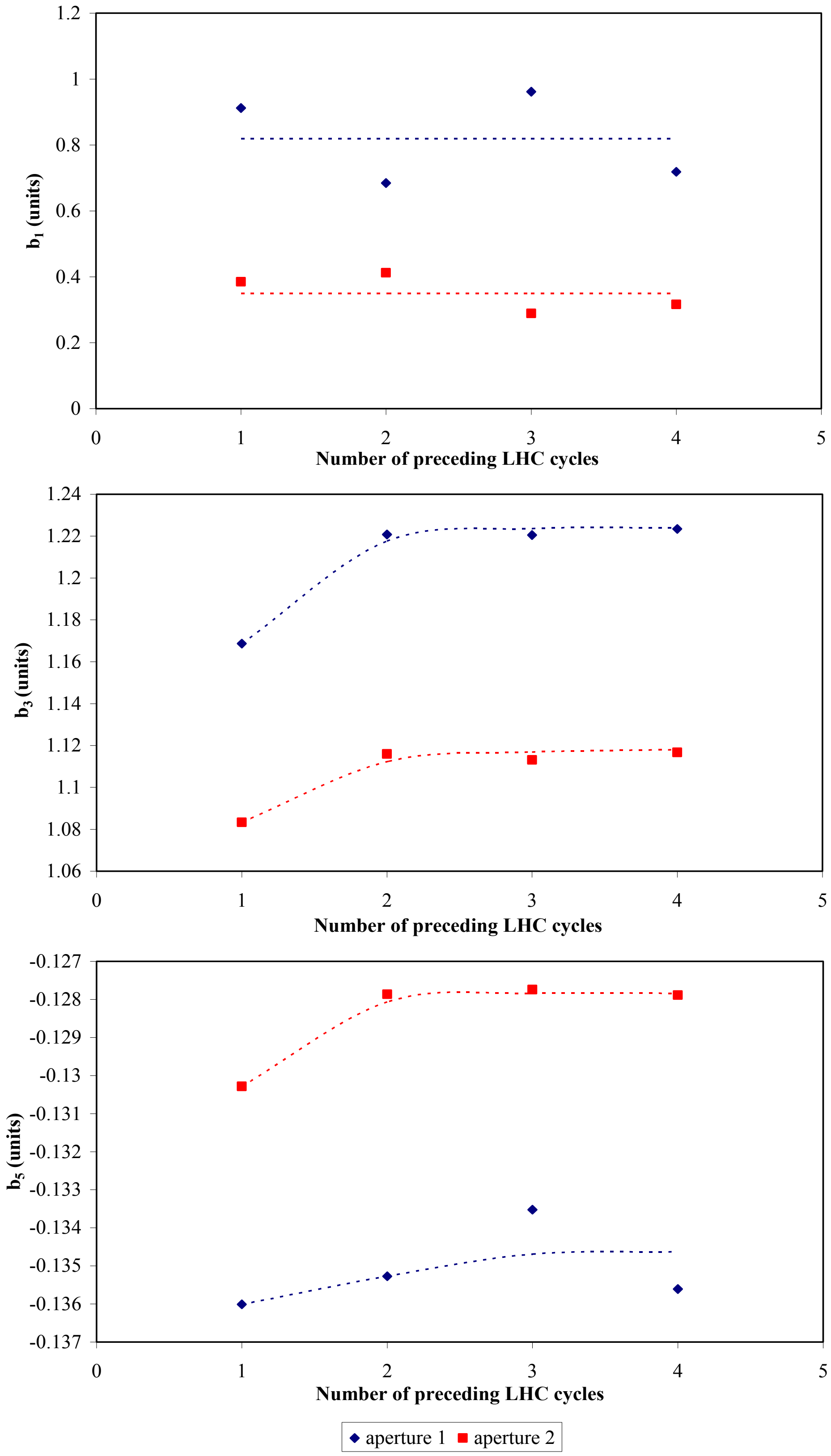

Figure 7.12: The decay amplitude for a number of identical pre-cycles for **(top)** b_1, **(middle)** b_3 and **(bottom)** b_5.

7.3 - Magnet Aging

During the LHC lifetime, it is possible that slight changes in the magnetic field occur due to aging. If these changes are significant, a strategy can be adopted to determine a systematic aging effect. This can be done by performing a standard loadline and LHC cycle on a magnet every so often. Unfortunately, this is not possible during installation since magnetic measurement bench time is entirely dedicated to establishing the warm-cold correlation and to perform extended magnetic measurements (powering history, snapback, coupling currents).

However, one dedicated magnetic measurement was performed to establish the aging effect's order of magnitude. A loadline and LHC cycle measurement was done on dipole MB1017 once in April 2003 and then again in September 2005. Figure 7.13 shows the difference between the two loadline measurements at injection and at nominal current. The change is not large and is comparable to the maximum error of the static model.

The aging effect of these 28 months on the decay amplitude is shown in Figure 7.14. The effect is small and within measurement uncertainty but is still larger than the measurement repeatability in the case of b_3.

The results of this measurement have demonstrated that the effect of magnet aging over 28 months is rather small and so far does not need to be considered in FIDEL. However, this effect might become significant in time. Unless a measurement campaign is performed to try to establish a systematic aging effect that can be included in FIDEL, this effect can only be compensated by the calibration of the model parameters from beam-based measurements.

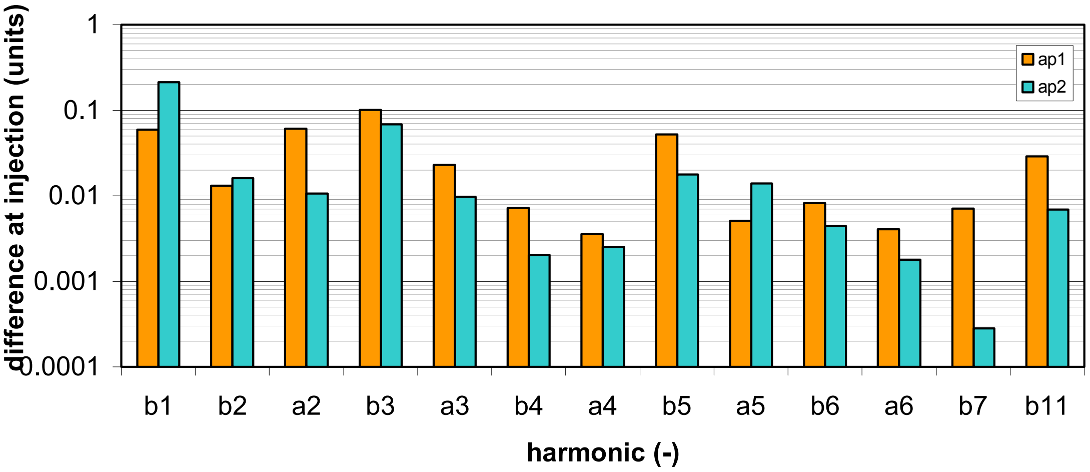

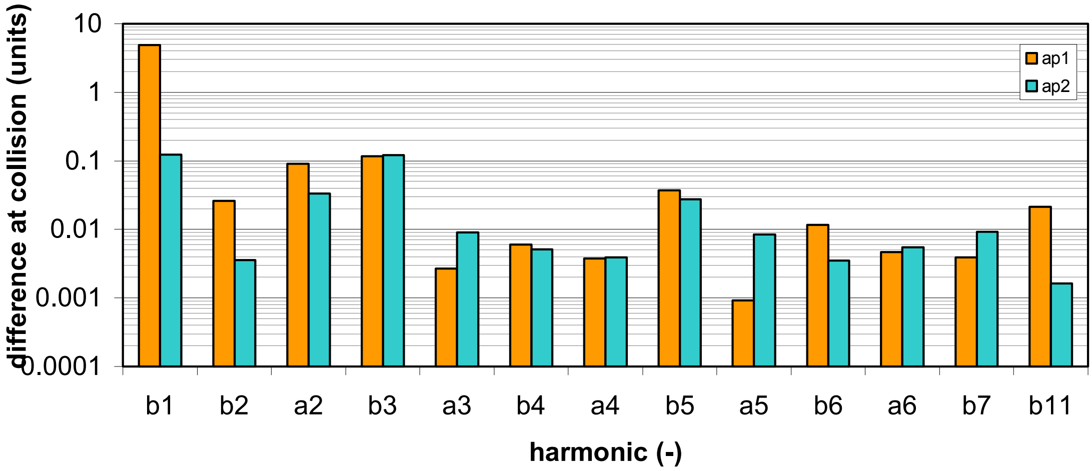

Figure 7.13: The aging effect of 28 months on the harmonics at **(top)** injection and **(bottom)** nominal current.

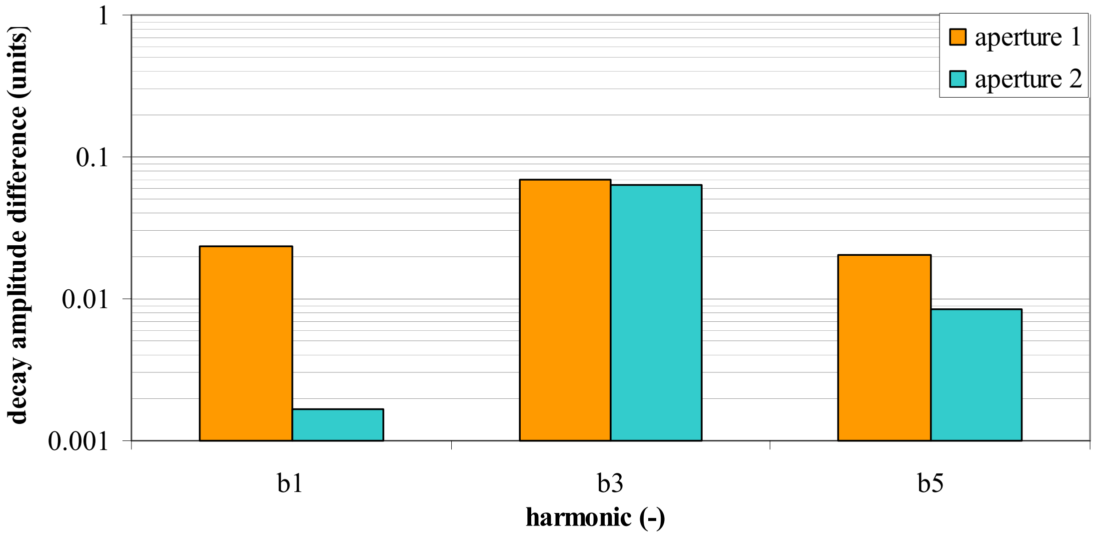

Figure 7.14: The aging effect of 28 months on the decay at injection.

7.4 - Geometric Component Changes due to Many Machine Cycles

The impact of Lorentz forces on the dipole geometric component due to many powering cycles is an important aspect that must be checked when designing FIDEL. After many cycles, it is possible that some changes in the coil geometry occur hence affecting the magnetic field. If the changes are important they might give an a priori ballpark figure on how many times the model parameters must be recalibrated.

A dedicated measurement was performed on magnet MB1017 to check these changes. Six loadline measurements were performed separated by 100 cycles that varied from 350 A to 11850 A. The b_3 geometric component of these measurements as defined in section 4.2 is shown in Figure 7.15. The standard deviation for both apertures is smaller than 0.01 units which is comparable to measurement repeatability.

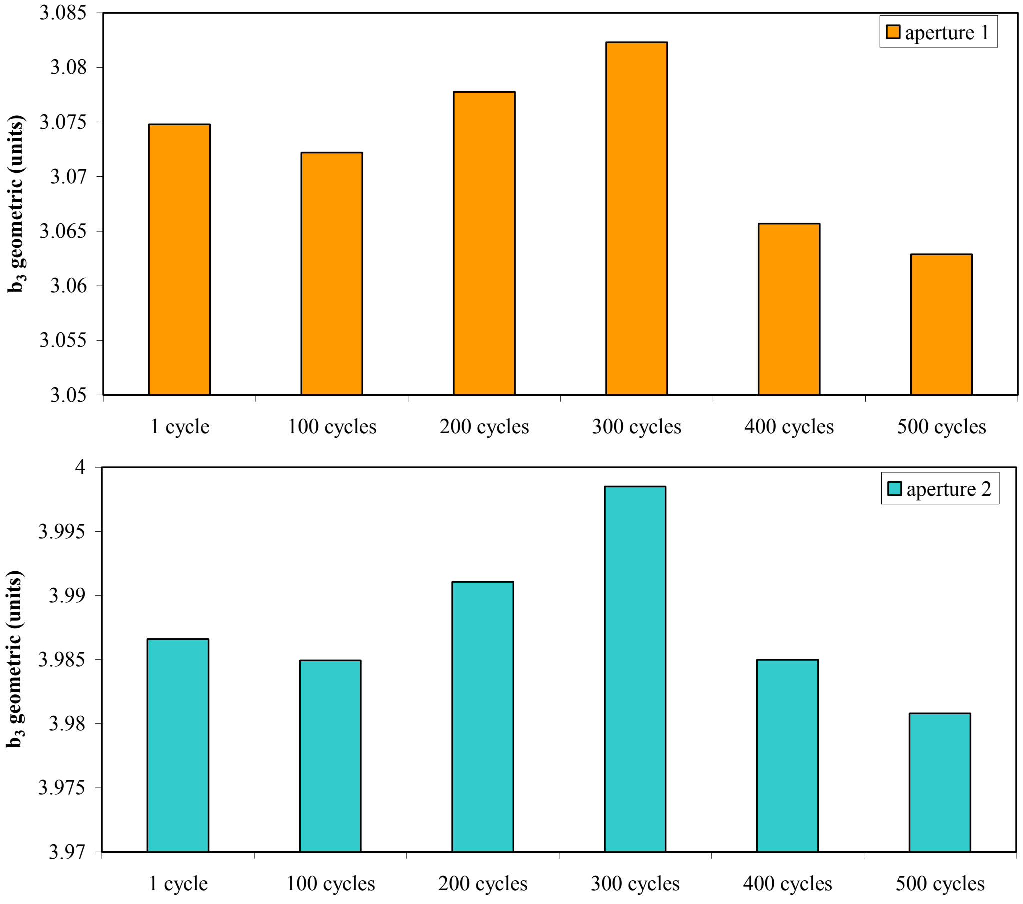

Figure 7.15: Six b_3 geometric measurements separated by 100 cycles for **(top)** aperture 1 and **(bottom)** aperture 2.

The same result is obtained for all the harmonics. In the case of b_1, the standard deviation is smaller than 0.4 units which is comparable to the measurement repeatability. Therefore, the indication is that ramping the magnets up and down many times does not affect the coil geometry and hence this effect does not need to be considered in FIDEL.

7.5 - Applying the Field Model to other Magnet Types

7.5.1 - The Field Model Applied to the Main Quadrupoles (MQ)

Apart from being applied on the dipole magnets, the field model was also applied on the average data of 61 apertures of the main quadrupoles [112]. These were measured with the rotating coils which were cross calibrated with the single stretch wire system [113].

Figure 7.16 shows the FIDEL static model for the MQs during ramp-up. The fitting parameters of the TF in the static domain are shown in Table 7.4. The other non allowed harmonics may be neglected since their average magnitude is well below the measurement repeatability. For the quadrupoles the integrated TF is expressed in T/kA which corresponds to the TF of the field gradient [61] and from Eq. 3.9.

The injection current I_{inj} for MQs is 760 A, the nominal current I_{nom} is 11850 A and the critical current I_c is 15000 A. The fit during the ramp-up of the magnet operation range ($760 \text{ A} < I < 11850 \text{ A}$) has a maximum error of 0.36 units for the main field which is less than the measurement repeatability.

Figure 7.17 shows the MQ decay model for a 1000 s injection based on 27 aperture measurements. The values of the parameters are shown in Table 7.5. The maximum error is very small (0.1 units for the main field) and is much less than the measurement repeatability.

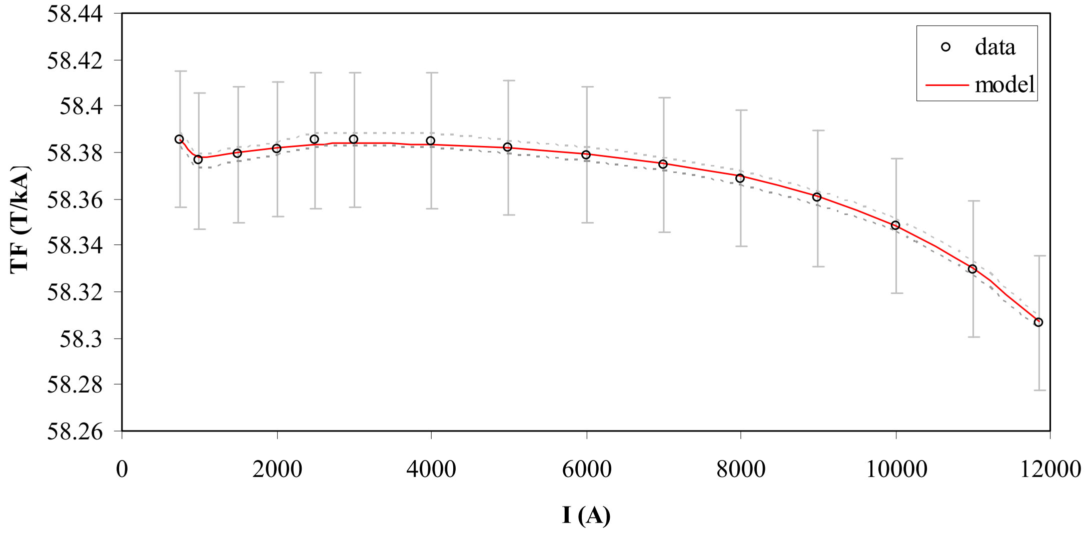

Figure 7.16: MQ measurements and the FIDEL model fit for the main field. The error bars show the measurement uncertainty and the grey lines show the measurement repeatability error.

Table 7.4: The static model parameters used for the MQs.

parameter	units	TF
Δ^{wc}	(T/kA)	0.203
γ	(T/kA)	58.387
μ	(T/kA)	−0.128
p	(-)	−0.677
q	(-)	5.486
h	(-)	2.000
σ^1	(T/kA)	−0.949
I_0^1	(A)	1555
S^1	(-)	3.987
σ^2	(T/kA)	0.253
I_0^2	(A)	1211
S^2	(-)	1.152
ρ	(T/kA)	0.127
r	(-)	2.422

Table 7.5: The decay parameters of the TF of the MQs.

parameter	units	TF
τ	(s)	138.490
d	(-)	0.353
δ	(units)	−1.618

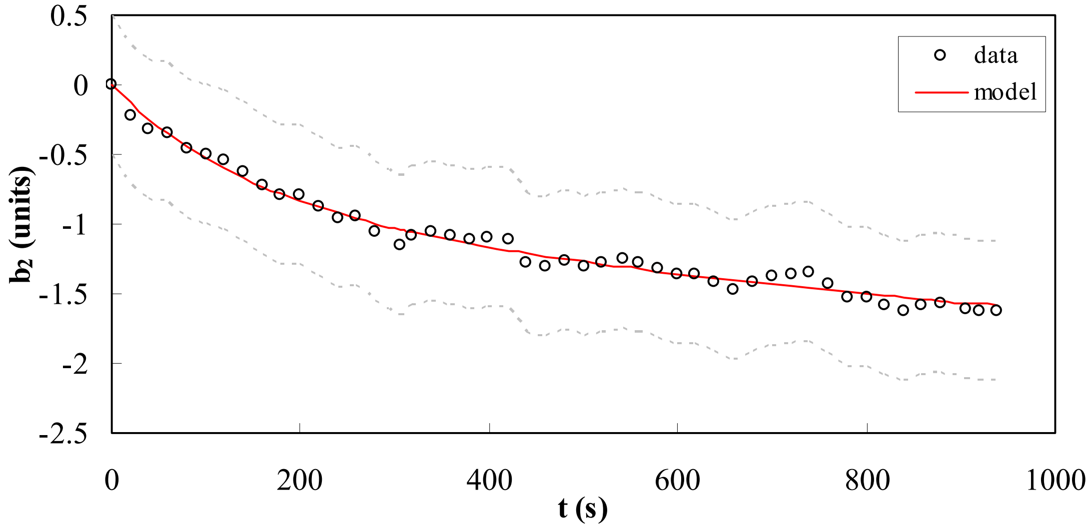

Figure 7.17: The decay fit for the MQ for the main field. The dotted grey lines show the measurement repeatability error. (The uncertainty is an order of magnitude larger).

7.5.2 - Results for the Insertion Region Wide Aperture Quadrupole 3.4 m (MQY)

The FIDEL static model was also applied to the average data of 6 aperture measurements of the MQYs [114]. The measurements were also performed with the rotating coils and the single stretched wire system.

Figure 7.18 shows the static model for the MQY during ramp-up. The fitting parameters are shown in Table 7.6. As in the MQs, the other non allowed harmonics are well below the measurement repeatability and hence may be ignored.

For MQYs, the injection current I_{inj} is 176 A, the nominal current I_{nom} is 3610 A and the critical current I_c is 15000 A. The fit during the ramp-up in the range $150\ \mathrm{A} < I < 3610\ \mathrm{A}$ has a maximum error of 0.96 units for the main field. If the magnets need to be excited below 150 A in the range where the superconducting filaments are not fully penetrated, further model developments would be required.

Figure 7.19 shows the decay model based on 4 aperture measurements during the first 1000 s of the injection plateau. The maximum error of the fit is very small (0.42 units for the main field) and is within measurement repeatability. The values of the decay parameters are listed in Table 7.7.

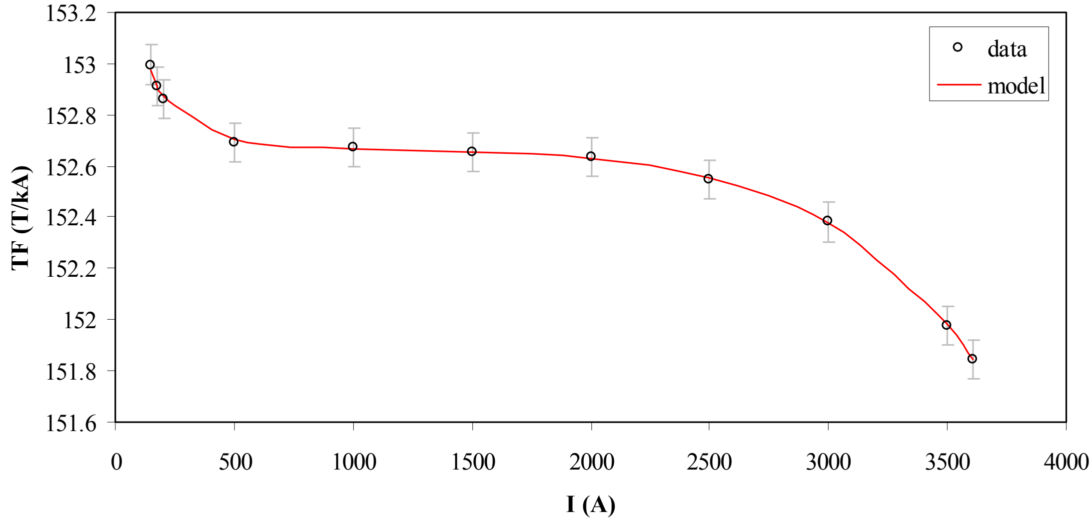

Figure 7.18: MQY measurements and the FIDEL model fit for the main field. The error bars show the measurement uncertainty. (The repeatability error is an order of magnitude lower).

Table 7.6: The static model parameters used for the MQYs.

parameter	units	TF
Δ^{wc}	(T/kA)	–0.309
γ	(T/kA)	152.6384
μ	(T/kA)	0.6046
p	(-)	0.000
q	(-)	1.602
h	(-)	2.000
σ^1	(T/kA)	–29.79
I_0^1	(A)	5027.8
S^1	(-)	9.414
σ^2	(T/kA)	2.890
I_0^2	(A)	2776.06
S^2	(-)	1.329
ρ	(T/kA)	–0.323
r	(-)	0.795

Table 7.7: The decay parameters of the TF of MQYs.

parameter	units	TF
τ	(s)	32.873
d	(-)	0.154
δ	(units)	–4.640

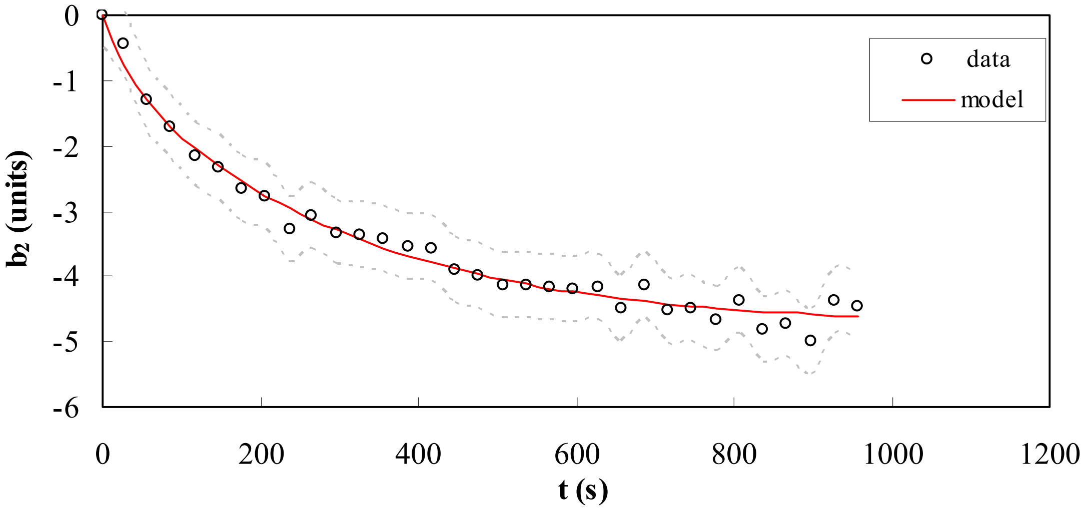

Figure 7.19: The decay fit for the MQY for the main field. The dotted grey lines show the measurement repeatability error. (The uncertainty is an order of magnitude larger).

7.5.3 - Application of the Model to the Long Trim Quadrupole Corrector (MQTL)

The static model was applied on one aperture measurement of the MQTL [115]. The measurement was performed with rotating coils in the vertical cryogenic test setup (Block 4) used to measure corrector magnets [116]. Figure 7.20 shows the static model for the MQTL TF during ramp-up and ramp-down of one polarity [117]. The static model fitting parameters are shown in Table 7.8.

I_{inj} is taken to be 1 A, I_{nom} is 550 A and I_c is 930 A. The model is valid over the entire operation range of the magnet which is $-550\text{ A} < I < 550\text{ A}$. The maximum error is less than 0.0015 Tm which is within the desired tolerance [118]. This error may be reduced even further by considering that the filaments are not fully penetrated during the ramp-up at very low currents.

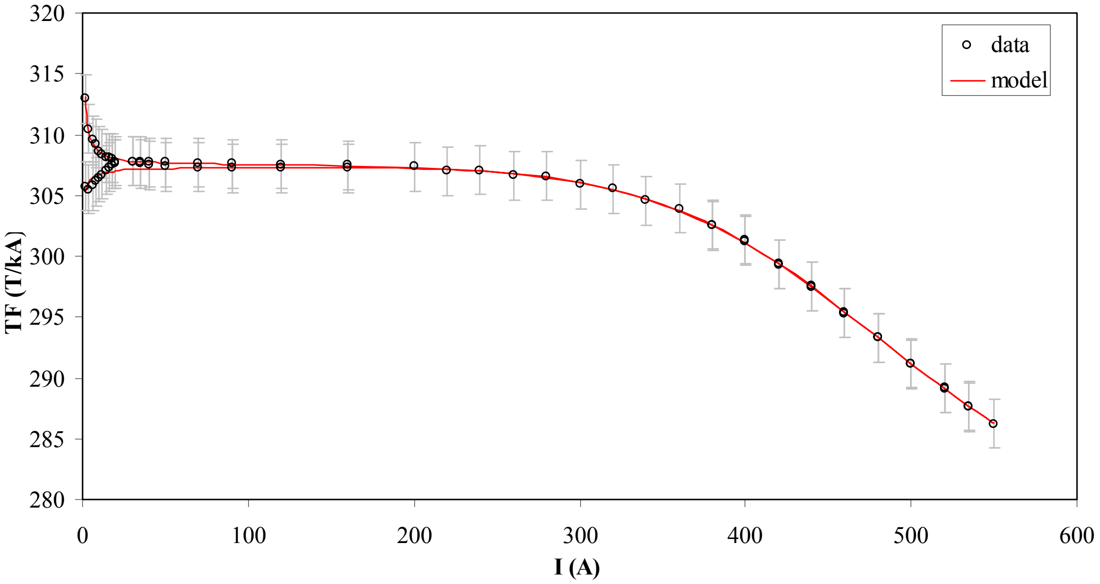

Figure 7.20: The TF of the MQTL magnet modelled with the FIDEL static model. The error bars show the measurement uncertainty.

Table 7.8: The static model parameters used for the MQTL.

parameter	units	TF
γ	(T/kA)	307.362
μ	(T/kA)	−7.041
p	(-)	0.142
q	(-)	2.000
h	(-)	2.000
σ^1	(T/kA)	333.105
I_0^1	(A)	433.118
S^1	(-)	2.571
σ^2	(T/kA)	−368.906
I_0^2	(A)	447.758
S^2	(-)	2.795
ρ	(T/kA)	3.893
r	(-)	1.096

7.6 - Conclusion

The results obtained show that the LHC magnets exhibit different behaviours when grouped up into families according to the inner cable type. In the static domain, the average transfer function is different for the two families at low fields. This effect is large during ramp-down and for current values below injection during the ramp-up. However, it is small in the operation range of the LHC cycle.

In the dynamic domain the difference is observed in the b_1 decay behaviour. The average decay of 01B cable magnets can be modelled by a double exponential function whilst the average decay of 01E cable magnets can be modelled by a single exponential function.

From these results, the MEB at first decided to maintain the policy of sorting the magnets by inner cables. However, as installation proceeded, this criterion was relaxed and eventually was removed and the magnets were mixed since the sorting constraints became tight.

An investigation targeted at checking whether the decay amplitude is affected by multiple LHC cycles showed that the effect can be neglected. This is the case particularly if the multiple LHC cycles are all the same.

Magnet aging and geometric component changes due to many machine cycles were also investigated but turned out to have a small effect on the magnetic field.

The robustness and adaptability of FIDEL was tested by applying the static and decay model on the main quadrupoles (MQ) and insertion region wide aperture quadrupoles (MQY). The static model was also tested on the long trim quadrupole correctors (MQTL). The results show that the field model performs well in the major hysteresis loop of these magnets with maximum errors comparable to the measurement repeatability.

Chapter 8

The Snapback Analyser

Cryodipoles stored during manufacturing.

> If a man empties his purse into his head, no man can take it away from him.
> An investment in knowledge always pays the best interest.
> - Benjamin Franklin

Chapter 8

The Snapback Analyser

The twin rotating coil system is the standard magnetic instrument in cryogenic conditions. However, even though this system has a very high resolution, it is far too slow to measure the snapback and provide enough data points for modelling.

To this end, a state of the art instrument was developed to provide a high resolution measurement of the snapback at a relatively high frequency. The snapback analyser is a Hall plate based probe that is designed to measure the main field and the first two allowed harmonics of the LHC dipole magnets at the beginning of the current ramp.

In this chapter the instrument's principle of operation, its mechanical arrangement and an analytical description of its uncertainty sources are described. A detailed description of the compensation system and the digital acquisition system is also provided. The performance of two different techniques implemented to achieve the necessary measurement resolution of 6 orders of magnitude lower than the main superimposed dipole field is also discussed. Finally, the analysis procedure and the results obtained are highlighted.

8.1 - Instrument Specification

As was described in chapter 5, the snapback occurs at the beginning of the particle acceleration and manifests itself as a rapid re-establishment of the magnetisation after its decay during the injection plateau.

The rotating coil system is the standard general field quality instrument used in series tests. It has a maximum acquisition frequency of 0.1 Hz and is well suited to measure the slow decay integrated in sectors of 1.25 m long over one entire 15 m superconducting LHC dipole magnet [45]. Unfortunately, even though this system has a relative resolution of 1 part per million (ppm) of the main field, its measurement accuracy of the dynamics of the snapback is rather limited by its time resolution since the phenomenon occurs in a few tens of seconds.

This limitation motivated the development of the Hall plate based instrument to measure the snapback in the first two allowed harmonics. The snapback lasts for one to two minutes for the standard LHC cycle, so a measurement frequency between 1 Hz and 10 Hz is required to allow adequate understanding and modelling of the phenomenon. The b_3 decay amplitude is 2 units ± 0.5 units (200 ± 50 ppm) and the b_5 decay amplitude is 0.34 ± 0.12 units (34 ± 12 ppm). This effect causes a change of about 60 units of chromaticity which is critical for high intensity beams since they become unstable if not controlled to between 2 and 10 units. The decay amplitude therefore imposes a required measurement resolution and hence measurement uncertainty of 0.15 units (15 ppm) for a signal to noise ratio of 10 for b_3 and a preferable resolution (though not strictly required) and hence measurement uncertainty of 0.02 units (2 ppm) to have the same signal to noise ratio for b_5. This requirement represents a considerable challenge particularly since the resolution requirement is 6 orders of magnitude smaller than the superimposed dipole field of 0.537 T at injection.

The instrument also needs to be stable with minimum drift at this resolution at least over one measurement cycle of typically 6000 s. It is however not required to have an absolute measurement of the magnetic field harmonics. The absolute value of the field can be obtained by cross calibrating the instrument with the rotating coils.

To reduce the complexity and the cost, it is not required to perform an integral measurement of the field over the whole magnetic length of the magnet. It is, however, important that the length of the probe spans over one transposition twist pitch (115 ±5 mm) of the periodic field pattern [89] of the superconducting magnet cable so as to compensate this latter effect. This inherently imposes the assumption that the local dynamics of the snapback do not vary significantly when compared to the dynamics of the integral over the length of the magnet.

Having these stringent targets, the design is tackled with two different techniques (analogue technique and digital technique) to examine their strengths and weaknesses and finally compare their performance.

8.2 - Principle of Operation

A sensor that measures high order harmonics must be capable of strongly suppressing the dipole component. As explained in [119] and as shown in Figure 8.1 the compensation of the dipole field and the measurement of the *n-th* order harmonic can be performed using an appropriate arrangement of *n* Hall plates. If these plates are placed tangentially to a ring at a radial distance *R* and at an azimuthal angle of 2π/n, where n is the harmonic order, all the lower order components are compensated and the arrangement yields a signal proportional to the *n-th* order harmonic only.

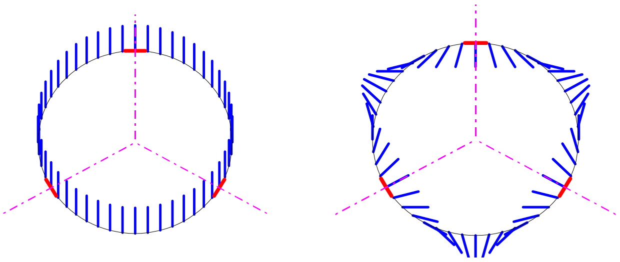

Figure 8.1: (left) In a dipole field: Sum $\propto B_1 - B_1/2 - B_1/2 = 0$ $\therefore$ The dipole field contribution is cancelled. **(right)** In a sextupole field: Sum $\propto -B_3 - B_3 - B_3 = -3B_3$ $\therefore$ Sextupole field is isolated.

Figure 8.1 considers the case where n = 3 and shows the dipole and sextupole field in the magnet aperture. In the case of b_3, the top hall plate measures the dipole field and the bottom hall plates each measure half of the dipole field with an opposite polarity. Hence, if all the signals are summed together as shown in Figure 8.1 (left), the dipole main field is compensated. In the case of the sextupole field, all three plates measure the negative component of the sextupole. If the signal is summed up as shown in Figure 8.1 (right), the resulting output is a measurement proportional to the sextupole component. Hence for the dipole field:

$$\text{Sum} \propto B_1 - B_1/2 - B_1/2 = 0 \qquad (8.1)$$

In the same way, A_1, B_2, A_2, are also cancelled. For the sextupole field;

$$\text{Sum} \propto -B_3 - B_3 - B_3 = -3B_3 \qquad (8.2)$$

The measurement of the b_5 snapback is based on the same principle. However, in the case of the decapole rings, B_1, A_1, B_2, A_2, B_3, A_3, B_4, A_4 harmonics are cancelled.

With this ideal geometry, the total signal, S_n, from the Hall plates is given to first order by [119]:

$$S_3 \approx 3B_1 10^{-4}\left(\frac{r}{R_{ref}}\right)^2 b_3 \qquad (8.3)$$

$$S_5 \approx 5B_1 10^{-4}\left(\frac{r}{R_{ref}}\right)^4 b_5 \qquad (8.4)$$

where S_3 and S_5 is the total signal for b_3 and b_5, respectively, r is the radius and R_{ref} is the reference radius.

This means that, to a first approximation (ignoring higher order terms), the signals coming from the *ideal arrangement* of the sensors in the rings are proportional to the normal sextupole and decapole harmonic, respectively, whilst the dipole field component is completely compensated by the symmetry.

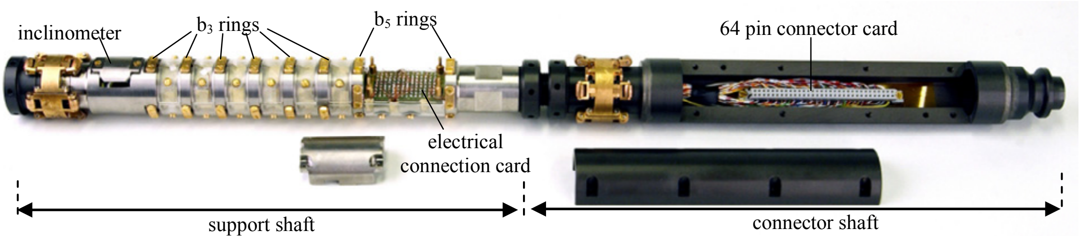

Figure 8.2: The Hall Probe.

8.3 - Probe Mechanical Arrangement

The Hall plate based probe as shown in Figure 8.2 consists of six rings each supporting 3 sensors for the sextupole measurements and two rings each supporting 5 sensors for the decapole [99].

The support shaft is designed to provide good mechanical stability for the sensors. It is made of Ti_6A1_4V alloy purposely chosen for its relatively high electrical resistivity ($\rho \approx 1.7\ \mu\Omega$m), its adequate thermal conductivity ($k \approx 7$ W/mK) and its weak paramagnetic behaviour ($\mu_r \approx 1.0002$). The support shaft is 300 mm long with a diameter of 33 mm and has a hole of 15 mm diameter carved inside it in order to allow cabling and to minimize the quantity of Ti_6Al_4V. The front end of the shaft is equipped with ball bearings and rollers to insert and rotate the device inside the anti-cryostat of the magnet. The six b_3 rings are placed at a distance of 19.17 mm from each other in order to cover the average wavelength of the cable transposition twist pitch (115 mm) in the superconducting magnets. The two b_5 rings are spaced by half a pattern wavelength (57.5 mm). This spacing is purposely intended to compensate for the periodic field pattern inherent in the superconducting magnets by taking the average value of the six b_3 rings and the average value of the two b_5 rings to compute the harmonics. Apart from the ring supports, the support shaft has two flat surfaces: one for the electrical connection card and one for the inclinometer.

The inclinometer built by Spectron® provides an absolute reference for the angular position of the shaft with respect to gravity. It is hermetically sealed with a resolution of 30 arc seconds, a sensitivity of 0.1 V/degree, a linearity half scale of 0.3° and a nominal range of ± 60° [120]. The sensor has a signal conditioner provided by Spectron®. The Hall plates are mounted into grooves at a radius r of 14.9 ± 0.02 mm on the rings at an angular spacing of 120° and 72° for the sextupole and the decapole, respectively. They are provided by AREPOC® and are of the unpackaged type (HHP-NU) made of InSb. The Hall plates have a typical sensitivity of 220 mV/T at an excitation current of 50 mA. The Hall plates are connected in series and are supplied with a common current source having a maximum drift of 100 nA. The Hall plate wires have a diameter of 0.1 mm and are soldered to the electronic connection card.

The aluminium connector shaft is fixed to the support shaft and houses the 64-pin cable connector. It too is equipped with ball bearings and rollers to make the installation of the probe in the anti-cryostat easier. Four extension shafts of 1 m each are added to the connector shaft to extend the probe into the superconducting magnet and allow it to measure the field harmonics in the straight part of the magnet. An angular adjustment mechanism with a manual coarse and fine tuning is attached to the end of the extension shafts to allow angular positioning during installation. A shielded twisted pair cable is passed through the hollow interior of the extension shafts to connect the 64-pin connector to the analogue and digital compensation systems.

8.4 - Analytical Description of Uncertainty Sources

A complete characterisation of the Hall Probe is necessary to quantify all the uncertainty sources and to implement strategies that minimize them. The sources of these uncertainties are:

a. geometrical uncertainties inherent in the Hall probe due to manufacturing tolerances assuming that the geometric axis of the instrument coincides with that of the superconducting magnet to be measured.
b. noise inherent in the probe due to electromagnetic interference and thermocouple effects
c. errors due to drifts and noise inherent in the electronics
d. variations in the supply current, errors in the Hall plate sensitivity determination and the Hall generator offset.

8.4.1 - Formulation of Geometrical Errors

By using the basic equation for a homogenous, isotropic and rectangular Hall generator of finite dimensions with point Hall and ohmic contacts not connected to the load and considering only a uniform magnetic field B normal to the Hall plate, the Hall voltage V_j^H for Hall plate j can be given by:

$$V_j^H = \gamma_j I_{cs} B \tag{8.5}$$

where γ_j is the sensitivity of the Hall plate (V/TA) at the supply current of I_{cs}. For an error due to a tilt of the Hall plate, Eq. 8.5 can be expressed by:

$$V_j^H = \gamma_j I_{cs} B \cos\left(\angle\left(\vec{B} \cdot \vec{p}_j\right)\right) \tag{8.6}$$

where $\vec{p}_j$ is a unit vector orthogonal to the plane of the ideally placed Hall plate.

For a plate with a pitch angle error $\delta\alpha$ and a roll angle error $\delta\beta$ both with respect to the ideal orientation of the Hall plate (in radians) in the superconducting magnet frame,

$$\cos\left(\angle\left(B \cdot \vec{p}\right)\right) = \sqrt{1 - \sin^2(\delta\alpha) - \sin^2(\delta\beta)} \tag{8.7}$$

Hence Eq. 8.5 becomes:

$$V_j^H = \gamma_j I_{cs} B \sqrt{1 - \sin^2\left(\delta\alpha_j\right) - \sin^2\left(\delta\beta_j\right)} \tag{8.8}$$

Considering a displacement Δr_j from the ideal radial position of the Hall plate j, becomes:

$$B_r = 10^{-4} B_1 \sum_{n=1}^{\infty} \left(\frac{r + \Delta r_j}{R_{ref}}\right)^{n-1} \left(b_n \sin(n\theta) + a_n \cos(n\theta)\right) \tag{8.9}$$

For a displacement $\Delta\theta$ in the θ coordinate from the ideal position of the Hall plate j, Eq. 8.9 becomes:

$$B_r = 10^{-4} B_1 \sum_{n=1}^{\infty} \left(\frac{r + \Delta r_j}{R_{ref}}\right)^{n-1} \left(b_n \sin\left(n\left(j\frac{2\pi}{m} + \frac{\pi}{2} + \Delta\theta\right)\right) + a_n \cos\left(n\left(j\frac{2\pi}{m} + \frac{\pi}{2} + \Delta\theta\right)\right)\right) \tag{8.10}$$

where m is the number of Hall plates in one ring.

For a displacement Δz_j of the Hall plate j along the z-axis of the magnet, the effect of the periodic field pattern that varies also in time must be considered. This effect can be expressed by:

$$D(t,z_j,k)=\left(1+A_{pp}(t)\cdot\left(\sin\left(\frac{2\pi}{R}k\right)+\sin\left(\frac{2\pi}{R}k+\frac{2\pi}{L_{pp}}\cdot\Delta z_j\right)\right)\right) \tag{8.11}$$

where A_{pp} is the periodic field pattern amplitude which changes in time t, L_{pp} is the transposition twist pitch of the cable of the magnet in meters, k is the ring number and R is the number of rings. Therefore, Eq. 8.10 becomes:

$$B_r=10^{-4}B_1D_1(t,z_1,k)\sum_{n=1}^{\infty}\left(\frac{r+\Delta r_j}{R_{ref}}\right)^{n-1}\left(\begin{array}{l} b_nD_n(t,z_n,k)\sin\left(n\left(j\frac{2\pi}{m}+\frac{\pi}{2}+\Delta\theta\right)\right)\\ +a_nD_n(t,z_n,k)\cos\left(n\left(j\frac{2\pi}{m}+\frac{\pi}{2}+\Delta\theta\right)\right)\end{array}\right) \tag{8.12}$$

Therefore Eqs. 8.11 and 8.12 include all the geometrical errors for one Hall plate including the error due to the planar effect.

The total signal including the geometrical error for one ring can be expressed as:

$$V_k^H=\sum_{j=1}^{m}V_j^H \tag{8.13}$$

For the total multipole signal from the Hall probe, Eq. 8.13 yields:

$$V_{probe}^H=\sum_{k=1}^{R}V_k^H\cdot P_{Lpp-Lhp}^H\cdot P_{k\Delta z}^H \tag{8.14}$$

where $P_{Lpp-Lhp}^H$ is the relative voltage error due to the difference between the period of the periodic field pattern and the period covered by the Hall probe (i.e. the error due to the periodic field pattern not being totally compensated). This is defined as:

$$P_{Lpp-Lhp}^H=1+\left(\frac{A_{pp}(t)}{R}\cdot\sin\left(\frac{2\pi}{L_{pp}}\cdot(L_{pp}-L_{hp})\right)\right) \tag{8.15}$$

where L_{hp} is the length covered by the Hall probe. $P_{k\Delta z}^H$ is the relative voltage error due to the misalignment of the plane of the ring Δz_k with respect to the ideal spacing in the period covered by the Hall probe. This error can be defined as:

$$P_{k\Delta z}^H=1+A_{pp}(t)\left(\sin\left(\frac{2\pi}{R}k\right)+\sin\left(\frac{2\pi}{R}k+\frac{2\pi}{L_{pp}}\Delta z_k\right)\right) \tag{8.16}$$

8.4.2 - Formulation of Non-Geometrical errors

For the non-geometrical inherent errors of the system, Eq. 8.8 becomes:

$$V_j^H = \left(\left(\gamma_j(B) + \Delta\gamma_j(B)\right)\left(I_{cs} + \Delta I_{cs}\right)B\sqrt{1-\sin^2\left(\delta\alpha_j\right)-\sin^2\left(\delta\beta_j\right)}\right)$$
$$+V_{offset}^H + V_{offset}^{PXI} + V_{ADCdrift}^{PXI} + V_{ADCsettling}^{PXI} + V_{noise} \qquad (8.17)$$

where $\Delta\gamma_j(B)$ is Hall plate j error in the value of the sensitivity $\gamma_j(B)$ which has an inherent second order dependence on the applied magnetic field B. ΔI_{cs} is the error of the ideal direct current supplied to the Hall plates in Amps; V_{offset}^H is the Hall voltage due to the Hall generator offset; V_{offset}^{PXI} is the voltage offset of the PXI data acquisition (DAQ) analogue to digital converter (ADC), $V_{ADdrift}^{PXI}$ is the voltage due to the ADC drift; $V_{ADsettling}^{PXI}$ is the voltage due to the ADC settling time and V_{noise} is the voltage due to noise from the whole system.

8.4.3 - Estimation of the Error Contribution

So as to calculate the contribution of each individual error to the final measurement uncertainty of the instrument, it can be assumed that all errors are mutually independent. Hence, the perturbations of each error can be calculated by formulating their partial derivative and then adding them to an otherwise ideal Hall voltage. Considering one error at a time and assuming that it approaches zero and also assuming that all the other errors are equal to zero then the contribution to the total error can be estimated. Hence, starting again with the geometrical errors, if the Hall pitch angle error $\alpha \neq 0$ and all the other errors are equal to zero and assuming that $\alpha \to 0$ so that from the Taylor theorem:

$$\cos\alpha \approx 1 - \frac{(\delta\alpha)^2}{2} \qquad (8.18)$$

$$\sin\alpha \approx \delta\alpha \qquad (8.19)$$

Eq. 8.17 yields;

$$\frac{\delta V_j^H}{\delta\alpha} = -\gamma_j I_{cs} B \sin\left(\delta\alpha\right) = -\gamma_j I_{cs} B\delta\alpha \qquad (8.20)$$

and the effect of the pitch angle error on the Hall voltage is:

$$\frac{\delta V_j^H}{V_j^H} = \delta_e \alpha = \frac{\gamma_j I_{cs} B \delta\alpha}{\gamma_j I_{cs} B\left(1 - \frac{(\delta\alpha)^2}{2}\right)}\delta\alpha = \frac{2(\delta\alpha)^2}{2-(\delta\alpha)^2} = (\delta\alpha)^2 \qquad (8.21)$$

Therefore;

$$V_{meas\alpha}^H = V_{ideal}^H\left(1+(\delta\alpha)^2\right) \qquad (8.22)$$

where V_{ideal}^H is the voltage from an ideally placed Hall plate. Similarly for the roll angle error;

$$V_{meas\beta}^H = V_{ideal}^H\left(1+(\delta\beta)^2\right) \qquad (8.23)$$

For a displacement from the ideal radial position of the Hall plate *j*, Eq. 8.8 combined with Eq. 8.12 becomes:

$$\frac{\delta V_j^{\boldsymbol{H}}}{\delta r} = \gamma_j I_{cs}\left(10^{-4} B_1 \sum_{n=1}^{\infty}(n-1)\frac{1}{R_{ref}}\left(\frac{r}{R_{ref}}\right)^{n-2}\left(b_n \sin(n\theta) + a_n \cos(n\theta)\right)\right) \qquad (8.24)$$

and normalizing with respect to V_j^H

$$\frac{\delta V_j^H}{V_j^H} = \delta_e r_j \frac{n-1\left(r/R_{ref}\right)^{n-2}\delta r_j}{R_{ref}\left(r/R_{ref}\right)^{n-1}} = (n-1)\frac{\delta r_j}{r} \qquad (8.25)$$

Therefore the effect of the error in the radial position of Hall plate *j* on the Hall voltage yields:

$$V_{measr}^H = V_{ideal}^H\left(1+(n-1)\frac{\delta r_j}{r}\right) \qquad (8.26)$$

For a displacement $\Delta\theta$ in the θ coordinate from the ideal position of the Hall plate *j,* there are two effects:

a. A reduction of the wanted component (b_3 or b_5 in our case) which is multiplicative and can be expressed by differentiating Eq. 8.10.
b. An addition due to the adjacent b_2 and b_4 contribution which is additive and can be added to the total error contribution.

Considering the reduction of the wanted component; Eq. 8.10 yields:

$$\frac{\delta V_j^H}{\delta\theta} = \gamma_j I_{cs}\left(10^{-4} B_1 \sum_{n=1}^{\infty}\left(\frac{r}{R_{ref}}\right)^{n-1}\left(-b_n n\sin\left(n(\theta+\Delta\theta)\right)+a_n n\cos\left(n(\theta+\Delta\theta)\right)\right)\right) \tag{8.27}$$

where $\theta = j\frac{2\pi}{m}$. Normalizing with respect to V_j^H as $\Delta\theta \to 0$;

$$\frac{\delta V_j^H}{V_j^H} = \delta_e\theta = n\left(\frac{\sum\limits_{n=1}^{\infty}\left(-b_n\sin(n\theta)+a_n\cos(n\theta)\right)}{\sum\limits_{n=1}^{\infty}\left(b_n\cos(n\theta)+a_n\sin(n\theta)\right)}\right)\delta\theta \tag{8.28}$$

This can be simplified by assuming that $a_n = 0$ either due to the magnet geometry (odd harmonics) or due to the probe insensitivity (even harmonics). If b above is also considered, Eq. 8.28 becomes:

$$\begin{aligned}\frac{\delta V_j^H}{V_j^H} = \delta_e\theta &= n\left(\frac{\sum\limits_{n=1}^{\infty}\left(-\sin(n\theta)\right)}{\sum\limits_{n=1}^{\infty}\left(\cos(n\theta)\right)}\right)\delta\theta + \left(\frac{V_{b2}(\sin 2((\pi/6)+\Delta\theta))}{V_{ideal}^H}+\frac{V_{b4}(\sin 4((\pi/6)+\Delta\theta))}{V_{ideal}^H}\right)\\ &= n\frac{-2(\delta\theta)^2}{\left(2-(\delta\theta)^2\right)}+\left(\frac{V_{b2}(\sin 2((\pi/6)+\Delta\theta))}{V_{ideal}^H}+\frac{V_{b4}(\sin 4((\pi/6)+\Delta\theta))}{V_{ideal}^H}\right)\\ &= -n(\delta\theta)^2+\left(\frac{V_{b2}(\sin 2((\pi/6)+\Delta\theta))}{V_{ideal}^H}+\frac{V_{b4}(\sin 4((\pi/6)+\Delta\theta))}{V_{ideal}^H}\right)\end{aligned} \tag{8.29}$$

Therefore using Eq. 8.29, the effect of the error $\Delta\theta$ of j on the Hall voltage yields:

$$V_{meas\theta}^H = V_{ideal}^H\left(1-\left(n(\delta\theta)^2\right)+\left(\frac{V_{b2}(\sin 2((\pi/6)+\Delta\theta))}{V_{ideal}^H}+\frac{V_{b4}(\sin 4((\pi/6)+\Delta\theta))}{V_{ideal}^H}\right)\right) \tag{8.30}$$

For a displacement Δz_j along the magnet axis, Eq. 8.11 becomes:

$$\frac{\delta D(t,z_j)}{\delta z} = \left(A_{pp}(t)\cdot\frac{2\pi}{L_{pp}}\cos\left(\frac{\Delta z_j}{L_{pp}}\cdot 2\pi\right)\right) \tag{8.31}$$

and normalizing with respect to V_j^H as $\Delta z_j \to 0$

$$\frac{\delta V_j^H}{V_j^H} = \delta_e z_j$$

$$= \left(\frac{A_{pp}(t)\dfrac{2\pi}{L_{pp}}\cos\left(\dfrac{\Delta z_j}{L_{pp}} \cdot 2\pi\right)}{1 + A_{pp}(t)\left(\sin\left(\dfrac{2\pi}{R}k\right) + \sin\left(\dfrac{2\pi}{R}k + \dfrac{2\pi}{L_{pp}} \cdot \Delta z_j\right)\right)} \right) \delta z$$

$$= A_{pp}(t)\frac{2\pi}{L_{pp}}\delta z_j \tag{8.32}$$

Therefore, the effect of the error Δz_j on the Hall voltage yields:

$$V_{measz}^H = V_{ideal}^H\left(1 + A_{pp}(t)\frac{2\pi}{L_{pp}}\delta z_j\right) \tag{8.33}$$

For the error due to the periodic field pattern not being bucked out totally $L_{pp} - L_{hp}$, Eq. 8.15 becomes:

$$\frac{\delta P_{Lpp-Lhp}^H}{\delta\left(L_{pp} - L_{hp}\right)} = \frac{A_{pp}(t)}{R} \cdot \frac{2\pi}{L_{pp}}\cos\left(\frac{2\pi}{L_{pp}} \cdot \left(L_{pp} - L_{hp}\right)\right) \tag{8.34}$$

and normalizing with respect to V_j^H as $\left(L_{pp} - L_{hp}\right) \rightarrow 0$

$$\frac{\delta V_{probe}^H}{V_{probe}^H} = \delta_e\left(L_{pp} - L_{hp}\right)$$

$$= \left(\frac{\dfrac{A_{pp}(t)}{R}\dfrac{2\pi}{L_{pp}}\cos\left(\dfrac{2\pi}{L_{pp}} \cdot \left(L_{pp} - L_{hp}\right)\right)}{1 + \dfrac{A_{pp}(t)}{R}\sin\left(\dfrac{2\pi}{L_{pp}} \cdot \left(L_{pp} - L_{hp}\right)\right)} \right) \delta\left(L_{pp} - L_{hp}\right)$$

$$= \frac{A_{pp}(t)}{R}\frac{2\pi}{L_{pp}}\delta\left(L_{pp} - L_{hp}\right) \tag{8.35}$$

Therefore, the effect of the error $\left(L_{pp} - L_{hp}\right)$ on the Hall voltage yields:

$$V_{meas(Lpp-Lhp)}^{probe} = V_{ideal}^{probe}\left(1 + \frac{A_{pp}(t)}{R}\frac{2\pi}{L_{pp}}\delta\left(L_{pp} - L_{hp}\right)\right) \tag{8.36}$$

where V_{ideal}^{probe} is the voltage for a ring arrangement that totally bucks out the periodic field pattern.

For Δz_k, the error due to the misalignment of the plane of the ring with respect to the ideal spacing in the period covered by the Hall probe Eq. 8.16 can be expressed as:

$$\frac{\delta P_{k\Delta z}^{H}}{\delta z_k} = A_{pp}(t)\frac{2\pi}{L_{pp}}\cos\left(\frac{2\pi}{R}k + \frac{2\pi}{L_{pp}}\Delta z_k\right) \tag{8.37}$$

and normalizing with respect to V_{probe}^{H} as $\Delta z_k \rightarrow 0$

$$\frac{\delta V_{probe}^{H}}{V_{probe}^{H}} = \delta_e z_k$$

$$= \frac{A_{pp}(t)\dfrac{2\pi}{L_{pp}}\cos\left(\dfrac{2\pi}{R}k + \dfrac{2\pi}{L_{pp}}\Delta z_k\right)}{1 + A_{pp}(t)\left(\sin\left(\dfrac{2\pi}{R}k\right) + \sin\left(\dfrac{2\pi}{R}k + \dfrac{2\pi}{L_{pp}}\Delta z_k\right)\right)}\delta z_k$$

$$= A_{pp}(t)\frac{2\pi}{L_{pp}}\delta z_k \tag{8.38}$$

Therefore, the effect of the error Δz_k of the ring on the Hall voltage yields:

$$V_{meas\Delta zk}^{probe} = V_{ideal}^{probe}\left(1 + A_{pp}(t)\frac{2\pi}{L_{pp}}\delta z_k\right) \tag{8.39}$$

Using Eq. 8.17 the rest of the errors considered can be expressed by:

$$V_{meas\gamma}^{probe} = V_{ideal}^{probe}\left(1 + \delta\gamma_j(B)\right) \tag{8.40}$$

$$V_{measIcs}^{probe} = V_{ideal}^{probe}\left(1 + \delta I_{cs}\right) \tag{8.41}$$

$$V_{measHoffset}^{probe} = V_{ideal}^{probe}\left(1 + \delta V_{offset}^{H}\right) \tag{8.42}$$

$$V_{measPXIoffset}^{probe} = V_{ideal}^{probe}\left(1 + \delta V_{offset}^{PXI}\right) \tag{8.43}$$

$$V_{measADCdriftt}^{probe} = V_{ideal}^{probe}\left(1 + \delta V_{ADCdrift}^{PXI}\right) \tag{8.44}$$

$$V_{measADCsettling}^{probe} = V_{ideal}^{probe}\left(1 + \delta V_{ADCsettling}^{PXI}\right) \tag{8.45}$$

$$V_{measnoise}^{probe} = V_{ideal}^{probe}\left(1 + \delta V_{noise}\right) \tag{8.46}$$

For the instrument the total tolerance for b$_3$ is specified to be 3 per cent whilst for b$_5$ it is specified to be 10 per cent.

The total error from the parameters considered can be expressed by:

$$V_{measgeototal} = V_{ideal}^{H}\left(1 + \sqrt{\begin{array}{l}(\delta_e\alpha)^2 + (\delta_e\beta)^2 + (\delta_e r)^2 + (\delta_e\theta)^2 + (\delta_e z_j)^2 + \left(\delta_e(L_{pp} - L_{hp})\right)^2 \\ + (\delta_e z_k)^2 + (\delta\gamma_j(B))^2 + (\delta I_{cs})^2 + (\delta V_{offset}^{H})^2 + (\delta V_{offset}^{PXI})^2 \\ + (\delta V_{ADCdrift}^{PXI})^2 + (\delta V_{ADCsetting}^{PXI})^2 + (\delta V_{noise})^2\end{array}}\right) \tag{8.47}$$

Since I_{cs} is very small (100nA rms) it can be neglected.

Eq. 8.47 can be used to calculate the requirements of the data acquisition system. Taking the manufacturing tolerances for the geometrical errors and evaluating their contribution to the total error by inserting them into Eqs 8.22, 8.23, 8.26, 8.30, 8.33, 8.36 and 8.39, the data acquisition requirements are obtained by considering the remaining error margin and by using Eqs. 8.40-8.46.

The resulting tolerances are shown in Table 8.1 and are calculated assuming that the errors are mutually independent and do not compensate for each other statistically.

In practice, the uncertainty sources do compensate each other statistically and some geometrical uncertainty sources (like $\delta\alpha$ and $\delta\beta$) are compensated in the calibration procedures. The accuracy required from the acquisition electronics is particularly high and can only be approached by using the analogue compensation system.

Table 8.1: The tolerances to remain within a total accuracy of 3 per cent for b_3 and 10 per cent for b_5.

Error Parameter	Error	b_3 tolerance	b_5 tolerance
$\delta\alpha$	pitch angle error	0.017 rad	0.017 rad
$\delta\beta$	roll angle error	0.017 rad	0.017 rad
δr	radius error	0.1 mm	0.1 mm
$\delta\theta$	Disp. in θ	0.006 rad	0.006 rad
δz_j	Hall plate disp. along magnet axis	0.1 mm	0.1 mm
$\delta\,(L_{pp}-L_{hp})$	difference between probe length and magnet cable transposition twist pitch	0.390 mm	0.521 mm
δz_k	ring disp. along magnet axis	0.1 mm	0.1 mm
δI_{cs}	Drift in supply current	100 nA	100 nA
$\delta\gamma_j(B)$	error in Hall plate sensitivity determination	0.160 μV/T max deviation	1.28 μV/T max deviation
δV^{H}_{offset}	Hall voltage due to Hall generator offset	0.05 μV	0.43 μV
δV^{PXI}_{offset}	Voltage offset of PXI ADC	0.05 μV	0.43 μV
$\delta V^{PXI}_{ADCdriftt}$	Voltage due to PXI ADC drift	0.05 μV	0.43 μV
$\delta V^{PXI}_{ADCsettling}$	Voltage due to ADC settling time	0.05 μV	0.43 μV
δV_{noise}	Voltage due to noise from the whole system	0.05 μV	0.43 μV

With the analytical description of the uncertainty sources formulated, a measurement of the individual effects may be performed to determine their values for each Hall plate. This information can then be used to compensate the systematic errors. This characterisation procedure goes beyond the scope of the thesis but a measurement proposal has been drawn up to demonstrate that it may be feasible [121].

It should be noted that the uncertainty sources due to the instrument set up were not considered in this analysis. These uncertainties most notably include the misalignment of the probe with respect to the magnet axis, which may be due to the anticryostat misalignment (in the order of 0.5 mm). These uncertainty sources are compensated by cross calibrating the instrument with the rotating coils as will be shown later.

8.5 - Analogue Compensation System

Two analogue cards for the sextupole rings and another card for the decapole rings perform the summation of the data as explained in section 8.2. This compensation system hence amplifies the signal in proportion to the harmonic of interest to obtain better resolution. The cards, designed by Masi [19] consist of the following two stages:

a. *The buffer stage:* the Hall plates are connected to zero-drift chopper-stabilized instrumentation amplifiers to have a dedicated voltage reference regulating the offset voltage. The connection is implemented in differential mode hence erasing common mode noise coming from the Hall probe itself. The amplifiers have a maximum nonlinearity of 20 ppm, a maximum offset voltage of 10 μV and a gain of about 10 at this stage.

b. *The mixer stage:* the summation of the signals is performed at this stage (3 input signals for the sextupole rings and 5 input signals for the decapole rings) using the same zero-drift chopper-stabilized instrumentation amplifiers mentioned above. The non-inverted output signal is an analogue scaled sum of the inputs and has a gain of 10. The output of this stage is then connected to the data acquisition system.

Previous experience on similar compensation cards [19] showed a critical short term output offset variation which represented one of the main uncertainty sources of the analogue compensation approach. Three countermeasures were implemented to minimize this drift:

a. The use of chopper amplifiers characterized by a very low offset, low offset drift (10nV/°C), small low-frequency noise and very high gain. Their trade off is, however, their limited bandwidth and the filtering required to remove the large ripple voltages generated by chopping. The final configuration therefore uses chopper stabilized amplifiers (AD8230) which combine the chopper amplifier with a conventional wideband amplifier that is kept in the signal path.

b. The use of resistors characterized by a high stability factor of 1 ppm/°C.

c. The use of a metallic enclosure over the circuits acting as a faraday cage to shield against electromagnetic perturbations. The enclosure is also kept at a constant temperature of 20°C by means of thermostatically controlled heaters supplied with a pulse width modulation current generator.

d. All the offset and gain settings as well as the measurement points are placed on the front end electronic rack for easy calibration.

The first order calibration of the compensation cards is carried out inside a reference resistive dipole magnet (Alstom® HB436/MCB22 - [122]) shown in Figure 8.3 which is continuously checked by an NMR teslameter (Metrolab® - PT2025 Metrolab - [123]) having an accuracy of 10^{-7} T.

Figure 8.3: The reference resistive dipole magnet - Alstom® - HB436/MCB22.

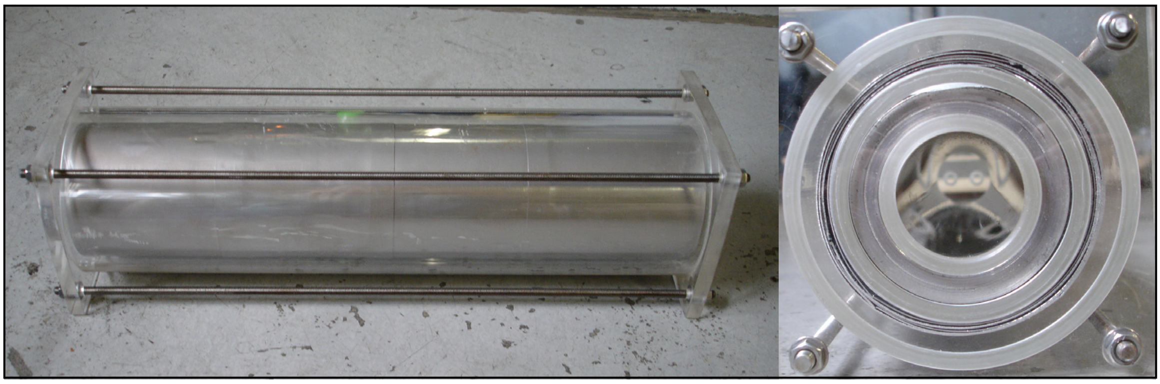

Figure 8.4: The high permeability chamber. **(left)** side view; **(right)** cross section.

The voltages on the board test points are measured using a 7½ digits integrating multimeter (Solartron Schlumberger 7151 [124]) with an estimated accuracy of ±1μV. The calibration is carried out in the following steps:

a. Hall plates offset correction: this is carried out by placing the probe into a high permeability chamber (mumetal; nickel alloy) shown in Figure 8.4. In this way, the effect of the earth's magnetic field is removed and only the intrinsic offset of the Hall plate is taken into account. The offset is removed at the buffer stage by varying the dedicated voltage reference.

b. Hall plates sensitivity and angular misalignment correction: The probe is inserted into the resistive reference magnet and a field of 0.537 T (which corresponds to the LHC magnetic field at injection conditions) is applied. It is oriented at an angle of 0° with respect to gravity by using the tilt sensor and the gain of the buffer stage is adjusted to have the expected output voltage according to the field applied. Of course, the output voltage of each plate depends on the position of the Hall plate on the ring. By keeping the instrument at 0°, the whole assembly is calibrated and errors due to angular misalignment are also compensated.

c. Dipole component compensation: Since the dipole field should be totally compensated, once the buffer stage is totally calibrated the mixer offset is adjusted to zero by keeping the probe oriented at an angle of 0° in the reference dipole field of 0.537 T. (Note that the gain at the mixer stage is kept fixed to a value of 10 for all mixer amplifiers).

Even after performing this calibration sequence, residual offsets between rings can still be detected. These are mostly due to the imperfections in the reference dipole and can be corrected by a simple but effective calibration procedure which is implemented directly in the LHC dipole during each measurement. A special calibration cycle is performed consisting of an LHC cycle with a current injection plateau of 6000 s so as to ensure that the drift due to the decay is negligible. The hall probe is then shifted by 115 mm/6 = 19.17 mm six times, parallel to the magnet axis with data being acquired at each step. The probe is aligned with respect to gravity each time using the inclinometer. The average value of all the six shifts for each ring is computed and the difference between each ring average and the first ring is hence obtained. In this way, the readings of each ring can be compared with respect to the reading of all other rings and hence the relative offset can be adjusted off-line for each measurement. The error in the shift as well as the error due to angle misalignment are ignored. Table 8.2 shows the offsets for each ring with respect to the first b_3 ring for magnet MB3370. Figure 8.5 shows the periodic field pattern obtained after a shift calibration was performed.

Table 8.2: The offset of the rings with respect to the first b_3 ring for magnet MB3370. The values have to be subtracted from the signal for the offset compensation.

Ring	Offset (V)
b_3_1	0.0000000
b_3_2	–0.0492100
b_3_3	0.1217836
b_3_4	0.1218942
b_3_5	0.1792634
b_3_6	0.1216282
b_5_1	–0.0385289
b_5_2	0.0355801

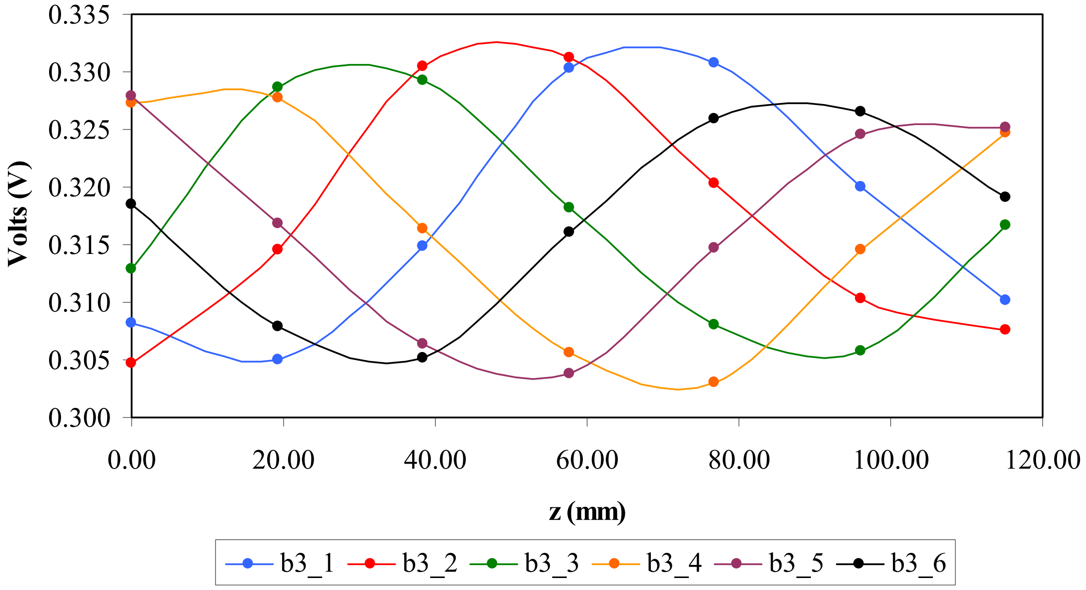

Figure 8.5: The periodic field pattern obtained after the shift calibration was performed.

8.6 - Digital Compensation and Data Acquisition System

The main limitation of the analogue compensation system is the drift in the output signal due to the offset and gain setting components. Another limitation is that the calibration of the cards only permits a first order nonlinearity compensation of the Hall plates.

These limitations can be solved by taking a digital compensation approach [97]. The idea is to acquire the voltages directly from the Hall plates using a high resolution ADC. The transfer function of each Hall plate is then applied in real-time to compensate for the Hall plate non-linearity error. This subtle yet crucial difference in the design allows a second order non-linearity compensation of the Hall plates. Of course, this approach places exceedingly high demands on the data acquisition, demands that go beyond the guaranteed resolution and stability specifications of the manufacturer. However, these demands can be approached by employing several techniques highlighted below.

The hardware used for the data acquisition system consists of a PXI real-time (RT) platform equipped with 3 data acquisition (National Instruments- NI6289 [125]) cards based on an SAR 18-bit ADC with 32 single ended multiplexed input channels (or 16 differential multiplexed input channels). In multiplexed mode, the maximum sampling frequency possible is 500 kS/s which corresponds to 15 kS/s on each channel assuring an over-sampling factor of 1500 when the signal bandwidth is 10 Hz. Since the signals that need to be acquired are at a low frequency, the inter-channel delay can be considered to be negligible. The input gain is set to a ± 200 mV input range which, according to the supplier's specifications, corresponds to a sensitivity of 3.6 μV, a random noise of 9 μV rms and an absolute accuracy of 43 μV. A calibration guaranteed for two years contributes to the system stability. Note that with the required resolution of 2 ppm to resolve b_5, the resolution to be reached by the DAQ should be of 0.2 μV. This is an order of magnitude less than the guaranteed sensitivity and random noise of the system.

Tests on the overall performance of the instrument without filtering show a random noise on the channels of around 300 μV rms. This noise is reduced to 12 μV rms as follows:

a. Using shielded twisted pair cabling connected to differential input channels.
b. Implementing screened connector blocks.
c. Employing adequate grounding techniques.
d. Installing two power supply filters and introducing a single pole 250 Hz cut-off low pass filter.

In addition to these precautions, the tilt sensor is switched off every time a measurement is performed since it is supplied with a pulse width modulated signal which introduces noise along the cable. Hence, practically all the noise of the system is reduced to the noise inherent in the DAQ. The design resolution and stability of the DAQ are improved by employing several techniques:

a. Over-sampling and decimating: this is a well known technique largely used in sigma delta modulators. After over-sampling, an average of the 1500 over-sampled points is taken to establish the frequency resolution of 10 Hz. From an implementation point of view, this is equivalent to performing a moving average. This type of filter is known to be a very poor low pass filter in the frequency domain but the best smoothing filter in the time domain which is our domain of interest.

b. Using redundant channels: as expected, during the characterization procedure, a short term drift of about 3 µV peak-to-peak is seen on the DAQ channels even when they are short circuited. For b_3, such a drift would be equivalent to 9 µV (90 ppm) and 15 µV (150 ppm) for b_5. This drift is the same for all channels of one card but differs between the cards. It can hence be deduced that this drift is inherent to the programmable gain amplifier (PGA). By simply short circuiting one of the channels to ground, removing its inherent ADC offset, smoothing it with a moving average window of 10 samples and subtracting it from the other channels, this drift is practically eliminated. The result of this procedure can be seen in Figure 8.6. The orange curve shows the drift of a channel short circuited (s/c) to ground. The black curve is the averaged drift over 10 samples and the green curve is the compensated signal.

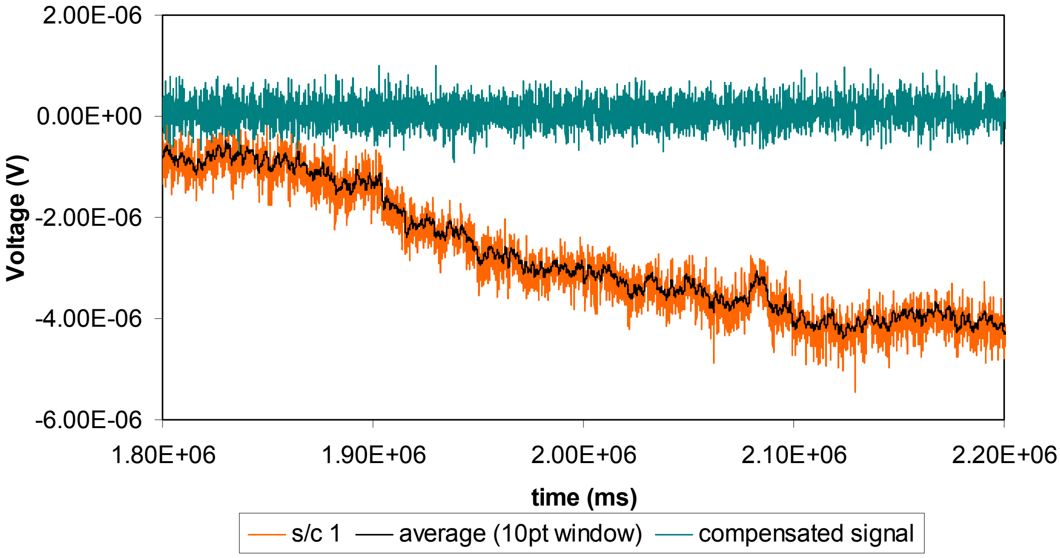

Figure 8.6: The use of a redundant channel to minimise the PGA drift.

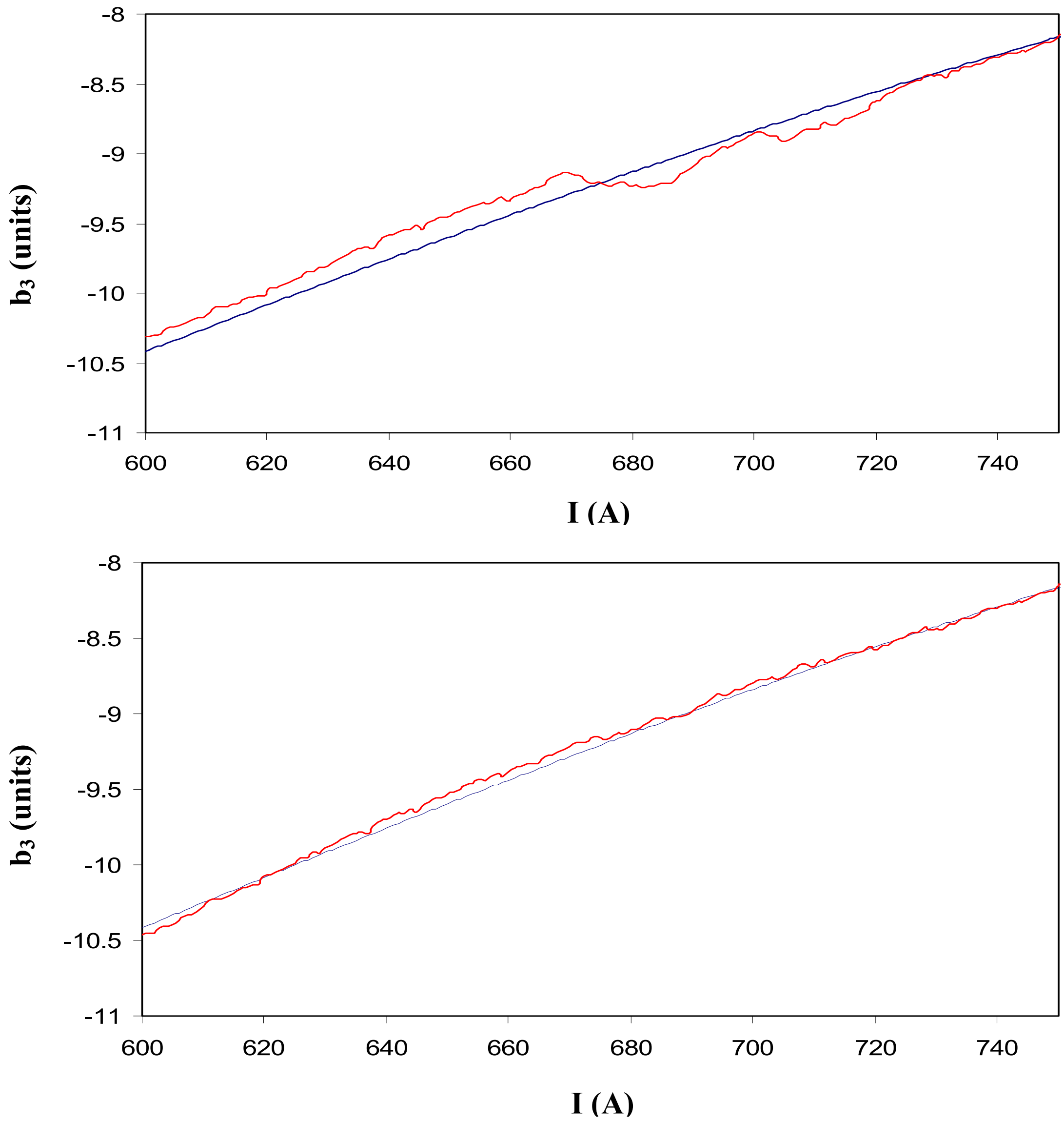

Figure 8.7: (top) Linear interpolation between measured points in the TF creates noise; **(bottom)** interpolation with a smoothing polynomial reduces the sporadic drift. The lines in red are the Hall probe measurements whilst the blue line is the interpolated rotating coil measurement.

c. Using a continuous transfer function for the Hall plates calibration: The calibration procedure of the digital system is performed using the dipole Alstom HB436/MCB22 in the same arrangement described in section 8.5. A 40-point transfer function is obtained for each Hall plate at each polarity to obtain the transfer function over the range of operation of the instrument (0.3 T to 0.8 T). The initial implementation of using a linear interpolation between calibration points of the Hall plates transfer function introduced an equivalent drift of about 10 μv every time there was a crossing between one interpolation line and the other. By using a continuous polynomial interpolation of all the calibration points, this sporadic drift is eliminated. The difference in the result between the two interpolation methods can be seen in Figure 8.7.

d. Settling error: During the characterization procedure, a catastrophic inter-channel interference of about 2000 ppm of the signal step size can be detected on the neighbouring channels. Inter-channel cross-talk was immediately dismissed since: the voltage signals have a very low frequency; twisted pair cables were used and the effect is limited to the downstream channel in the acquisition card. This effect was hence considered to be due to the settling time of the ADC. The settling time limits the acquisition frequency and the settling error measured in ppm of step size is a function of the source impedance. Since the Hall plates have a very low resistance (a few ohms) the large settling error was primarily due to the large impedance of the single pole low pass filter. Two measures were taken to reduce this effect:

   i. By choosing a low resistance at each input (around 68 Ω) and a high capacitance (around 4.7 μF) for the low pass filter, the source impedance is reduced to yield a settling error of only 30 ppm of the signal step size but still keeping the same cut-off frequency.

   ii. By grouping the channels with voltage signals of the same magnitude and placing them one after the other, large step size differences between channels can be reduced to a minimum. For example, a group consists of all the top Hall plates. The different groups can also be isolated by using redundant channels between them and shorting these channels to the first signal channel of the group. In this way all the groups are shielded from each other reducing further the risk of suffering from inter-channel interference. The optimised channel assignment to minimise the settling error is shown in Table 8.3.

e. Offset minimization: since the absolute accuracy of the system is of 43 μV, a sporadic offset of the ADC in the order of 20 μV can be measured when the DAQ is restarted. This offset is compensated after the measurement by measuring a short circuit to ground and subtracting it from each channel during the analysis procedure.

Table 8.3: The channel assignment optimised to minimise the settling error.

PXI Module 1		PXI Module 2		PXI Module 3	
PXI Channel	**Signal Name**	**PXI Channel**	**Signal Name**	**PXI Channel**	**Signal Name**
ch0	short to b3_r1_h1	**ch16**	short to b5_r1_h1	**ch32**	short to b3_r5_h1
ch1	b3_r1_h1	**ch17**	b5_r1_h1	**ch33**	b3_r5_h1
ch2	b3_r2_h1	**ch18**	b5_r2_h1	**ch34**	b3_r6_h1
ch3	b3_r3_h1	**ch19**	short to b5_r1_h2	**ch35**	short to b3_r5_h2
ch4	b3_r4_h1	**ch20**	b5_r1_h2	**ch36**	b3_r5_h2
ch5	short to b3_r1_h2	**ch21**	b5_r2_h2	**ch37**	b3_r6_h2
ch6	b3_r1_h2	**ch22**	b5_r2_h5	**ch38**	b3_r6_h3
ch7	b3_r2_h2	**ch23**	b5_r1_h5	**ch39**	b3_r5_h3
ch8	b3_r3_h2	**ch24**	short to b5_r1_h3	**ch40**	short to ground
ch9	b3_r4_h2	**ch25**	b5_r1_h3	**ch41**	s/c to magnet current
ch10	b3_r4_h3	**ch26**	b5_r2_h3	**ch42**	magnet current
ch11	b3_r3_h3	**ch27**	b5_r2_h4	**ch43**	s/c to inclinometer
ch12	b3_r2_h3	**ch28**	b5_r1_h4	**ch44**	inclinometer
ch13	b3_r1_h3	**ch29**	short to ground	**ch45**	short to ground
ch14	short to ground	**ch30**	short to ground	**ch46**	short to ground
ch15	short to ground	**ch31**	short to ground	**ch47**	short to ground

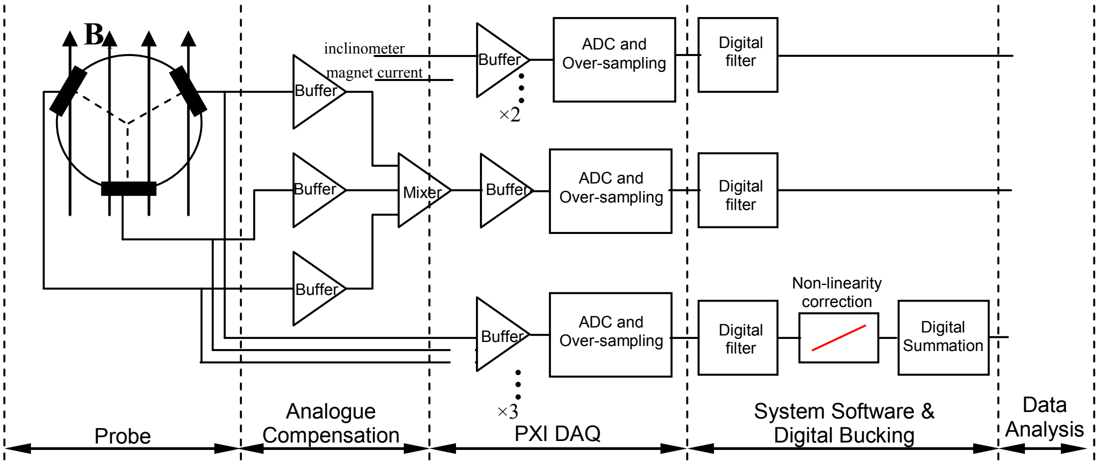

Figure 8.8: Schematic of the analogue and digital Hall plate based instrument. The above diagram is applied to every sextupole ring. The decapole rings are similar but with five Hall plates. There is only one inclinometer signal and one magnet current signal for the whole measuring system.

It should be noted that having an absolute accuracy of 46 µV represents a decisive limitation in obtaining an absolute measurement using the instrument. The instrument is hence cross-calibrated during each measurement with the rotating coils to obtain an absolute measurement. Figure 8.8 shows the schematic of the analogue and digital system of the instrument whilst Figure 8.9 shows the instrument electronics rack.

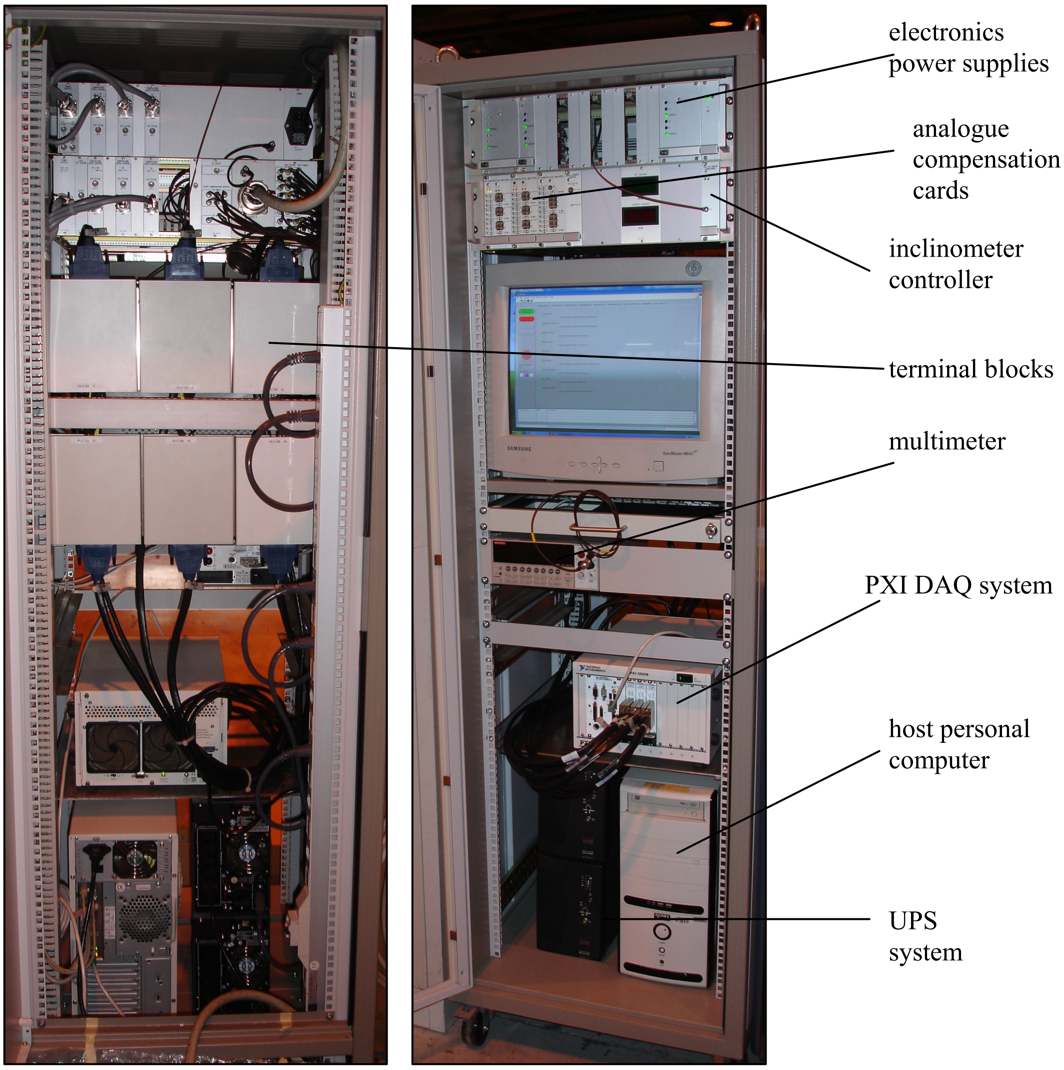

Figure 8.9: The Hall probe instrument's electronics rack **(left)** rear, **(right)** front.

8.7 - Data Analysis Procedure

The existence of residual errors in the Hall probe sensor read-out can be observed when comparing the hysteresis curves obtained from the Hall probe sensor to the ones obtained using the rotating coils. These signals include all the errors not corrected so far. In the case of the analogue compensation these errors include:

a. Non-linear sensitivity of the Hall plates (since the calibration is limited to a first order correction)

b. Hall plates and amplifier voltage offsets dependent on temperature

c. b_3 components inherently present as errors in the field of the reference magnet dipole.

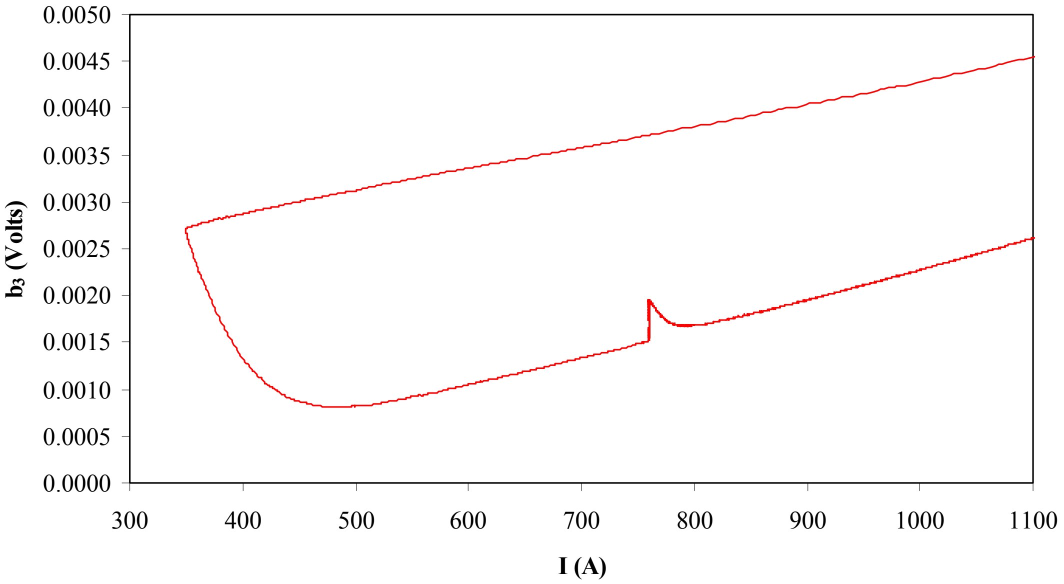

Figure 8.10: A measurement of the b_3 hysteresis curve on MB1310 before cross calibrating with the rotating coils.

In the case of the digital compensation these errors include:

a. Errors in the determination of the Hall plate transfer functions

b. The variation of the ADC offset in time.

As shown in Figure 8.10, all these residual errors result in an insufficient compensation of the main dipole field and limit the possibility of measuring the absolute value of the harmonics of interest.

A cross calibration with the rotating coils is performed to compensate for these errors. As described in [99] the Hall plate data are reduced to fit the rotating coil hysteresis curve using a second order conversion formula of the type:

$$b_n = \frac{K_n (V_n - V_{offset} - K_{bucking} B_1 - K_{non-linear} B_1^2) 10^4}{B_1} \tag{8.50}$$

where b_n is the normalized field harmonic of order n, V_n is the average voltage signal from the ring sensors, B_1 is the dipole field (obtained from the rotating coils), V_{offset} is the electronic offset from the amplifiers, K_n is the calibration factor for the voltage of the *n-th* plate sensor read-out, $K_{bucking}$ is the dipole voltage bucking ratio and $K_{non-linear}$ is a second order correction for the Hall probes non linear sensitivity as a function of the field. The parameters V_{offset}, $K_{bucking}$, $K_{non\text{-}linear}$ and K_n are obtained by an unconstrained optimization procedure that aims at minimizing the root mean square of the difference among Hall-plates reading and interpolated rotating coil results.

A LabVIEW programme (Figure 8.11) was specifically designed to approximate the solution manually and then fine tune it in an embedded MATLAB optimisation algorithm.

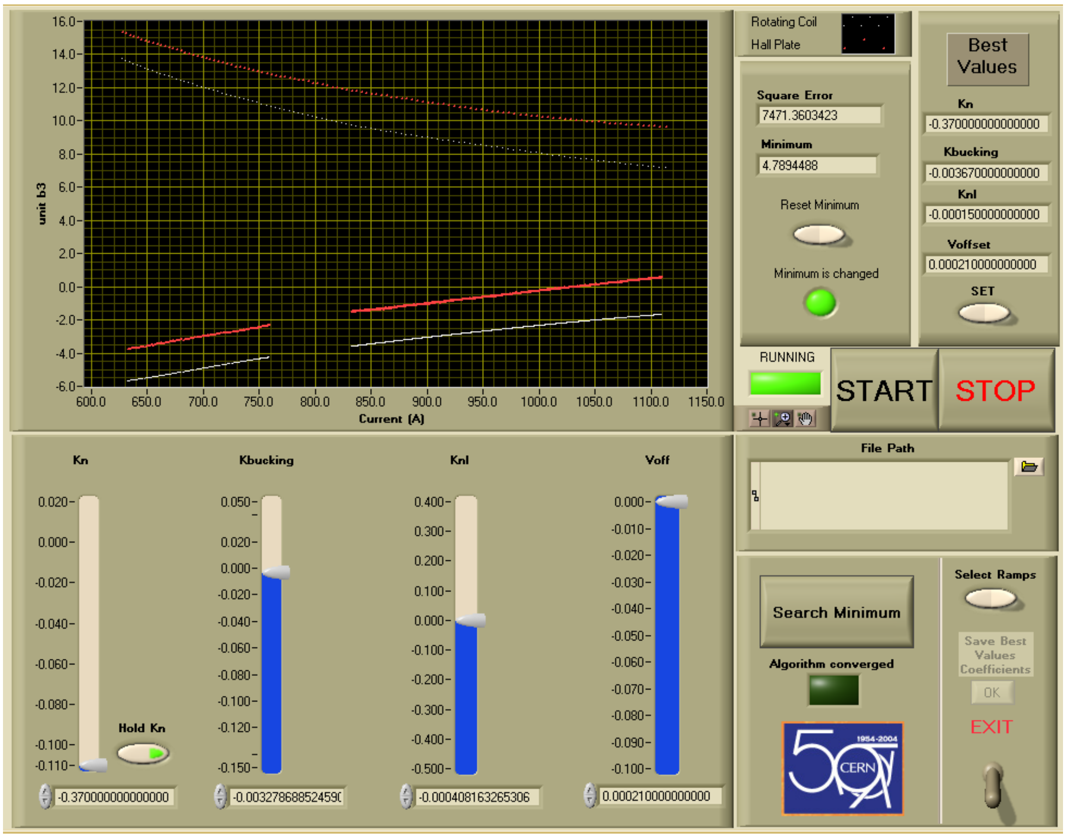

Square Error: 7471.3603423

Minimum: 4.7894488

Best Values

Kn: -0.370000000000000

Kbucking: -0.003670000000000

Knl: -0.000150000000000

Voffset: 0.000210000000000

Kn: -0.370000000000000

Kbucking: -0.00327868852459(

Knl: -0.000408163265306

Voff: 0.000210000000000

Figure 8.11: A screenshot of the LabVIEW programme used to fit the Hall probe hysteresis curve to the rotating coil hysteresis curve. (White curve is the b_3 rotating coil interpolated hysteresis curve, red curve is the b_3 Hall probe hysteresis curve).

8.8 - Results

Figures 8.12 and 8.13 show the measurement results for b_3 and b_5, respectively, after cross calibration with the rotating coils.

As expected, the analogue compensation system performs very well in terms of resolution but is relatively weak in stability. Conversely, the digital compensation system has a larger random error but is very stable over the whole measurement.

In the case of the analogue compensation the random noise is reduced to 0.09 μV (0.9 ppm) for b_3 and 0.24 μV (2.4 ppm) for b_5. However, the drift over the whole cycle is of 430 ppm for b_3 and 200 ppm for b_5 and is prohibitive when cross-calibrating with the rotating coils. Such a large drift is probably due to the gain setting components which are inherently mechanical and hence have a weaker performance when compared to the rest of the electronics.

By using noise and drift reduction techniques in the digital compensation system, the random noise is reduced to 0.22 μV (2.2 ppm) for b_3 and 0.76 μV (7.6 ppm) for b_5. The drift over the whole cycle of 6000 s was reduced to 12 ppm for b_3 and 20 ppm for b_5. Such a drift at this resolution is acceptable particularly since the cross calibration is done over 1300 s.

After comparing these two systems and testing their performance, it is apparent that the digital compensation system has the better performance. The digital compensation system was therefore used for series measurements and the analogue cards were kept as prototypes for further research and development. The measurement results were consequently used to model the snapback phenomenon as described in chapter 5, and establish the correlation between the decay amplitude and the snapback current constant as described in chapter 6.

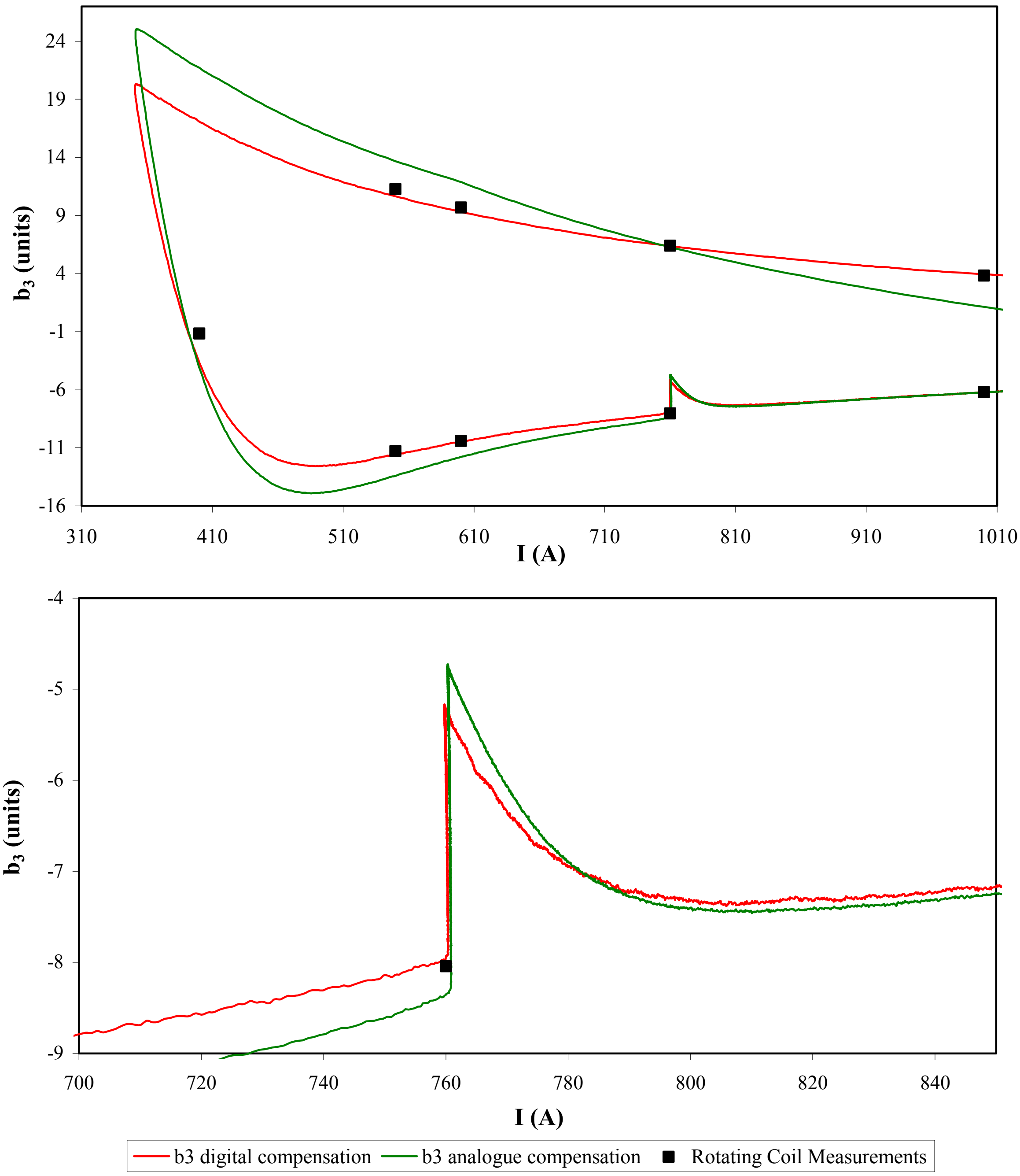

Figure 8.12: (top) The b_3 hysteresis curve measured with the Hall plate based instrument using analogue compensation and digital compensation. The black points show the measurements achieved with the rotating coils. **(bottom)** A close up of the b_3 decay and snapback.

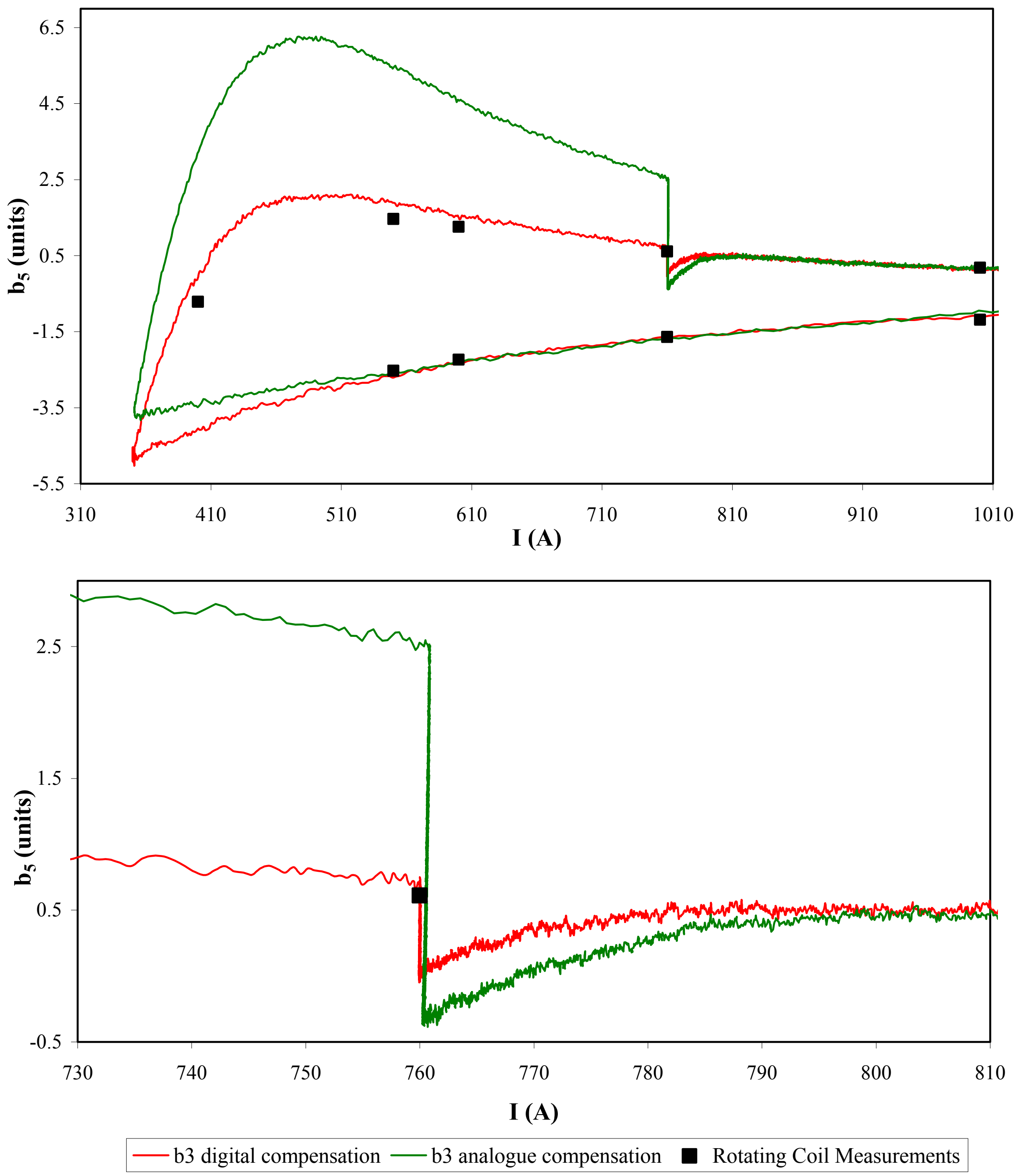

Figure 8.13: (top) The b_5 hysteresis curve measured with the Hall plate based instrument using analogue compensation and digital compensation. The black points show the measurements achieved with the rotating coils. **(bottom)** A close up of the b_5 decay and snapback.

The final step in the analysis is to isolate the snapback phenomenon from the hysteresis curve. As shown in Figure 8.14, this is done by subtracting the interpolated rotating coils data from the Hall probe data. A fit based on Eq. 5.13 is then applied to the curve of Figure 8.14 (bottom) and the parameters are used to establish the snapback correlation formulated in Eq. 6.5.

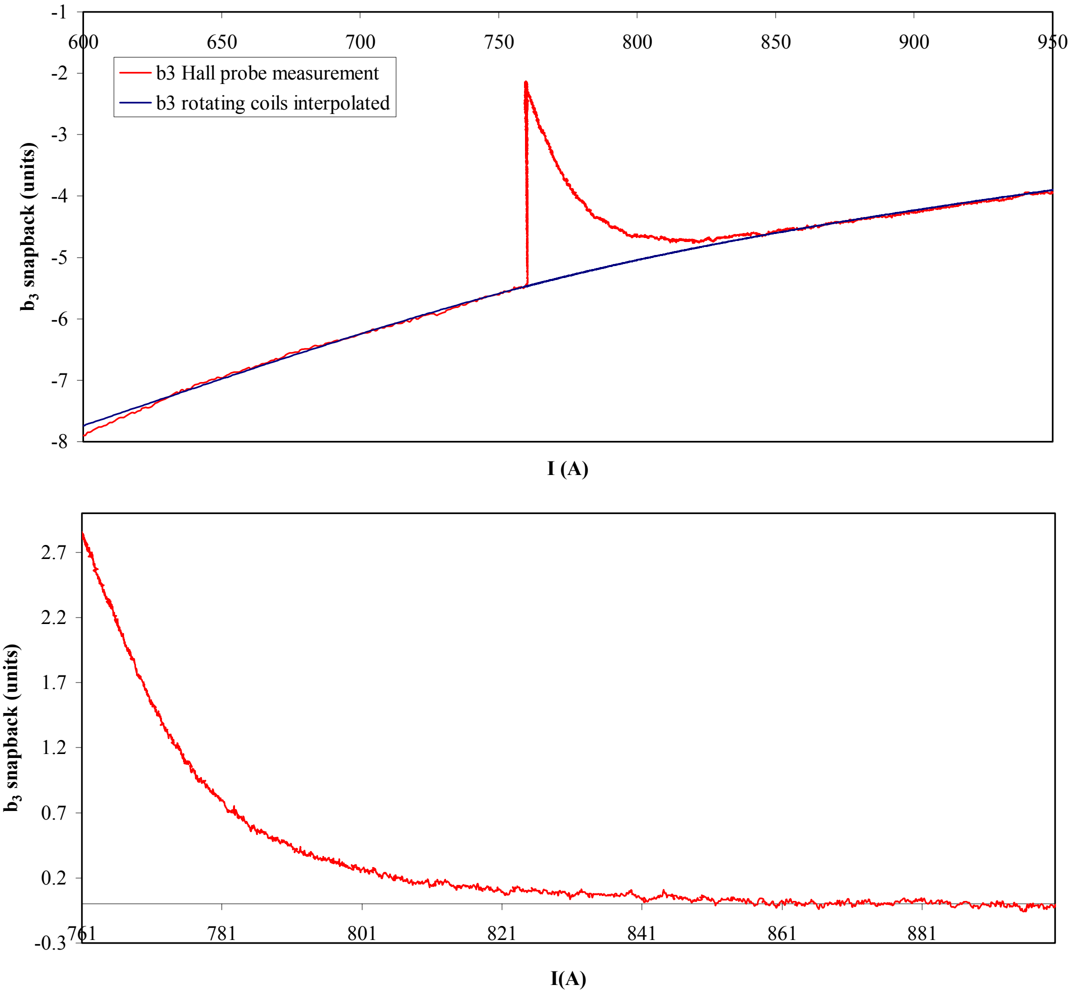

Figure 8.14: (top) The decay and snapback measured with the Hall probe and superimposed on the interpolated rotating coil measurements **(bottom)** the isolated snapback measured with the Hall probe after subtracting the interpolated rotating coil measurements.

8.9 - Conclusion

A robust instrument has been developed to measure the hysteresis behaviour at 10 Hz and hence enable the modelling of the snapback phenomenon in superconducting magnets. Its principle of operation strongly relies on the geometrical arrangement of several Hall plates to compensate for the main dipole signal and to be sensitive to the first two allowed harmonics.

An analytical description of the uncertainty sources was performed followed by a characterisation of the data acquisition system. Two compensation approaches were presented followed by the methodology used for their calibration.

The cross calibration procedure and the analysis of the data were also outlined. The resolution achieved was better than the requirement of 15 ppm. The innovative digital compensation approach was proven to work better than the analogue approach and was chosen as the platform on which to perform series measurements that were presented in chapter 5 and chapter 6.

Chapter 9

Conclusion

Welding a cryodipole held in place by a hydraulic press.

The answer to the great question of Life, the Universe and Everything is forty-two.
- Douglas Adams in "*The Hitchhiker's Guide to the Galaxy*"

Chapter 9

Conclusion

The main aim of this thesis was to establish the field model that forms the foundation of the LHC feed-forward control system. To do this a static model, a dynamic model and a set of scaling laws were developed based on magnetic measurements. The model was also shown to be robust and adaptable to several magnet types. A data acquisition system for the snapback analyser was also built to increase the reliability of the snapback scaling law.

Once the LHC is commissioned, CERN will employ this work in the machine's feed-forward system to reduce the burden on the beam based feed-back.

9.1 - Conclusion

The LHC hybrid control system will rely on feed-forward control to generate the current ramps of the main LHC superconducting magnets and to forecast their main magnetic field and harmonic variations within a residual error comparable to beam control requirements. Once the machine is within the commissioning tolerances, it will be in a state that is controllable by beam based feed-back and hence the beam diagnostics will take over to eventually reach the nominal operation precision.

This thesis dealt with the development of the field model which forms the core of the feed-forward system and which conceptually relies on the decomposition of the different components that contribute to the magnetic field behaviour. The parameters of the model were extracted from magnetic measurements at room temperature and from magnetic measurements in cryogenic conditions.

The components that are reproducible and that are solely dependent on the magnet excitation current were modeled in the static domain. These included the geometric, the d.c. magnetisation, the residual magnetisation and the saturation contribution. The maximum error for the dipoles of sector 7-8 was shown to be well within the desired modelling accuracy.

The components that are dependent both on excitation current and on time were modeled in the dynamic domain. These included the decay and snapback which are not reproducible from cycle to cycle since they are also dependent on the powering history of the magnet. The effect of the coupling currents was shown to be negligible and was therefore excluded from the model.

The dynamic field model was extended further by a set of scaling laws which allow it to be recalibrated and to be extended to a wider scope for the entire magnet population. The maximum error of the dynamic field model combined with the scaling laws for the dipoles was also shown to be well within the desired modelling accuracy.

Other issues were taken into account, such as whether the dipoles should be grouped up into families and hence whether the magnetic field model should be different for the different magnet groups. A modified version of the main dipole field decay model was presented for magnets that have 01E cables.

Other aspects such as magnet aging, the decay amplitude variation due to multiple LHC cycles and the effect of Lorentz forces after many machine cycles were also considered but their effects were shown to be small enough to be neglected by FIDEL.

The model was not only tested on the main dipole magnets but was also applied on the main quadrupoles (MQ), the insertion region wide aperture quadrupoles (MQY) and the long trim quadrupole correctors (MQTL). The error was shown to be within the desired tolerances confirming that the model was well formulated and can adapt to different magnet types.

In order to provide better measurements on which to model the snapback, a data acquisition system for the Hall plate based instrument was developed as part of this thesis. The uncertainty sources were first described analytically and the data acquisition system was then fully characterized. This new digital compensation system was shown to perform better than the preceding analogue compensation system and was therefore used to provide the data on which the b_3 snapback scaling law was based.

9.2 - Suggestions for Further Work

Further refinement of the model presented in this dissertation may be performed for the MQYs and the corrector magnets during the ramp up at very low currents where the superconducting filaments are not fully penetrated. For the corrector magnets, the crossing paths between the major hysteresis loop branches may also be modelled as a further development of FIDEL to provide their full hysteretic model.

In addition, measurements may also be organised for the MQs and the insertion magnets (including the MQMs) to establish their powering history dependence, their coupling current contributions and their decay dependence over 10000 s injection plateaus.

Furthermore, a robust software based infrastructure may be built to extract the component parameters of the dipoles in the other sectors. The model may also be applied on the other insertion region magnets (e.g. MQM) and the other corrector types.

References

The first LHC dipole magnet lowered into the tunnel.

If I have seen further it is by standing
on the shoulder of giants.
- Isaac Newton

[1] L. Evans, "The Large Hadron Collider", in *Proceedings of the 16th Biennial Particle Accelerator Conference*, pp. 40-44, Dallas, Texas, USA, May 1995.

[2] The ATLAS Experiment. [Online].
Available: http://atlas.web.cern.ch/Atlas/index.html

[3] CMS Outreach, [Online]. Available: http://cmsinfo.cern.ch/outreach/

[4] A Large Hadron Collider Beauty Experiment. [Online].
Available: http://aliceinfo.cern.ch/

[5] ALICE - A Large Ion Collider Experiment at CERN LHC. [Online].
Available: http://lhcb.web.cern.ch/lhcb/

[6] "LHC Design Report: Vol. 1 - The LHC Main Ring", CERN-2004-003, O. Brüning, P. Collier, P. Lebrun, S. Myers, R. Ostojic, J. Poole, P. Proudlock, CERN, Geneva, Switzerland, June 2004.

[7] D. Boussard, E. Chiaveri, H.P. Kindermann, R. Losito, S. Marque, V. Rodel, M. Stirbet, "The LHC Superconducting Cavities", in *Proceedings of the 18th Particle Accelerator Conference*, pp. 946-948, vol. 2, New York, USA, March 1999.

[8] "LHC Design Report: Vol. 3 - The LHC Injector Chain", CERN-2004-003, M. Benedikt, P. Collier, V. Mertens, J. Poole, K. Schindl, CERN, Geneva, Switzerland, December 2004.

[9] M. Allitt, A. Ijspeert, M. Karpinnen, J. Mazet, R. Wolf, "Status of the Production of the LHC Superconducting Corrector Magnets", *IEEE Transactions on Applied Superconductivity*, vol. 14, pp. 195-198, June 2004.

[10] S. Fartoukh and O. Brüning, “Field Quality Specification for the LHC Main Dipole Magnets”, LHC Project Report 501, CERN Geneva, Switzerland, October 2001.

[11] E. Wilson, “An Introduction to Particle Accelerators”, New York, Oxford University Press, 2001, pp. 29-31.

[12] O. Brüning, “Beam Based Nonlinear Corrections in Storage Rings: Review and Applications for LHC Commissioning”, in *Proceedings of the IEEE Particle Accelerator Conference*, pp. 429-435, Chicago, USA, June 2001.

[13] S. Fartoukh, “Criteria and Requirements from Beam Dynamics”, Field Quality Working Group, April 2004. [Online].
Available: http://fqwg.web.cern.ch/fqwg/040426/040426.html

[14] O. Brüning, “Accumulation and Ramping in the LHC”, *10th Workshop on LEP SPS Performance, Chamonix X*, pp. 198-202, Chamonix, France, January 2000.

[15] M. Lamont, R. Bailey, O. Brüning, P. Collier, R. Lauckner, R. Schmidt, “A Staged Approach to LHC Commissioning”, in *Proceedings of the European Particle Accelerator Conference*, pp. 538-540, Edinburgh, UK, June 2006.

[16] L. Bottura, “From the LEP Warm Magnets to the LHC Superconducting Magnets”, in *Proceedings of the 10th Workshop on LEP-SPS Performance, Chamonix X*, pp. 158-161, Chamonix, France, January 2000.

[17] L. Bottura, “Standard Analysis Procedures for the Field Quality Measurement of the LHC Magnets, Part II: Transfer Functions and Parameterisation”, CERN Internal Report, MTA-IN-98-027, CERN Geneva, Switzerland, June 1998.

[18] L. Bottura, T. Pieloni, S. Sanfilippo, G. Ambrosio, P. Bauer, M. Haverkamp, “A Scaling Law for Predicting Snapback in Superconducting Accelerator Magnets”, in *Proceedings of European Accelerator Conference*, Lucerne, Switzerland, pp. 1609-1611, July 2004.

[19] A. Masi, “Advanced Measurement Systems Based on Digital Processing Techniques for Superconducting LHC Magnets”, Ph.D. Thesis, Università Degli Studi Di Napoli Federico II, Napoli, November 2005.

[20] R. Jones, “Beam Measurement Capabilities for Controlling Dynamic Effects in the LHC”, in *Proceedings of the LHC Reference Magnet System Review*, CERN, Geneva, Switzerland, July 2004.

[21] A. J. Burns, “Beam Instrumentation”, in *Proceedings of the Workshop on LEP-SPS Performance*, CERN-SL-2000-007 DI, pp. 208-213, Chamonix, France, January 2000.

[22] M. Giovannozzi, “Dynamic Aperture for Single Particle Motion: Overview of Theoretical Background, Numerical Predictions and Experimental Results”, in *Proceedings of the 29th ICFA Advanced Beam Dynamics Workshop on Beam-Halo Dynamics, Diagnostics and Collimation*, pp. 26-31, Long Island, New York, USA, May 2003.

[23] T. Wijnands, M. Lamont, A. Burns, L. Bottura, L. Vos, “Requirements for Real Time Correction of Decay and Snapback in the LHC Superconducting Magnets”, in *Proceedings of the 7th European Particle Accelerator Conference*, pp. 367-369,Vienna, Austria, June 2000.

[24] M. Lamont, “Beam Based & Reference Magnet Measurements to Complement the Magnetic Measurement Programme”, in *Proceedings of the 1st LHC Project Workshop, Chamonix XIII*, pp. 232-235, Chamonix, France, January 2004.

[25] F. Pilat and J. Van Zeijts, "The RHIC Experience", in *Proceedings of the LHC Reference Magnet System Review*, CERN Geneva, Switzerland, July 2004.

[26] F. Pilat, C. G. Trahern, J. Wei, T. Satogata, S. Tepikian, "Modelling RHIC Using the Standard Machine Format Accelerator Description", in *Proceedings of the 17th Particle Accelerator Conference*, pp. 2544-2546, Vancouver, Canada, May 1997.

[27] K. Brown, J. Niederer, T. Satogata, A. Alai Tafti, N. Tsoupas, J. van Zeijts, "The RHIC Online Model Environments: Experiences and Design for AGS Modelling", in *Proceedings of the 18th Particle Accelerator Conference*, pp. 2722-2724, New York, USA, April 1999.

[28] T. Satogata, K. Brown, F. Pilat, A. Alai Tafti, S. Tepikian, J. Van Zeijts, "The RHIC/AGS Online Model Environment: Design and Overview", in *Proceedings of the 18th Particle Accelerator Conference*, pp. 2728-2730, New York, USA, April 1999.

[29] N. Malitsky, K. Brown, N.D'Imperio, J. Kewisch, A. Fedotov, A. Luccio, F. Pilat, V. Ptitsyn, T. Satogata, S. Tepikian, J. Wei, "Joining the RHIC Online and Off-line Models", in *Proceedings of the Particle Accelerator Conference*, pp. 880-882, Knoxville, Tennessee, USA, May 2005.

[30] M. Martens, "The Tevatron Experience", in *Proceedings of the LHC Reference Magnet System Review*, CERN Geneva, Switzerland, July 2004.

[31] D. E. Johnson, D. A. Herrap, "Compensation of the Time Varying Fields in the Tevatron Superconducting Magnets", in *Proceedings of the 13th IEEE Particle Accelerator Conference: Accelerator Science and Technology*, pp. 521-523, Chicago, Illinois, USA, March 1989.

[32] D. A. Herrup, M.J. Syphers, D.E. Johnson, R.P. Johnson, A. V. Tollestrup, R. W. Hanft, B. C. Brown, M. J. Lamm, M. Kuchnir, A.D. McInturff, "Time-Varying Sextupole Corrections During the Tevatron Ramp", in *Proceedings of the 13th IEEE Particle Accelerator Conference: Accelerator Science and Technology*, pp. 518-520, Chicago, Illinois, USA, March 1989.

[33] P. Schmüser, "Field Quality Issues in Superconducting Magnets", in *Proceedings of 14th IEEE Particle Accelerator Conference v1-5*, pp. 37-41, San Francisco, USA, May 1991.

[34] B. Holzer, "The HERA Experience", in *Proceedings of the LHC Reference Magnet System Review*, CERN, Geneva, July 2004.

[35] H. Brück, B. Holzer, C. Luettge, B. Pawlowski, "Correction of the Influence of Persistent Currents in the HERA Proton Ring", in *Proceedings of the 5th European Particle Accelerator Conference*, pp. 392-394, Barcelona, Spain, June 1996.

[36] B. Holzer and C. Montag, "Reproducibility and Predictability of Persistent Current Effects in the HERA Proton Storage Ring", in *Proceedings of the 7th European Particle Accelerator Conference*, pp. 2142- 2144, Vienna, Austria, June 2000.

[37] V. Shiltsev, P. Bauer, M. Martens, S. Herb, B. Holzer, S. Wolff, F. Pilat, J. Van Zeijts, "LHC Reference Magnet System; Review Summary and Recommendations", in *Proceedings of the LHC Reference Magnet System Review*, CERN, Geneva, Switzerland, July 2004.

[38] R. Bailey, F. Bordry, L. Bottura, P. Burla, P. Collier, K. Henrichsen, J. P. Koutchouk, R. Lauckner, L. Walckiers, R. Wolf, "Dynamic Effects and Their Control at the LHC", in *Proceedings of the 17th Particle Accelerator Conference*, pp. 66-68, Vancouver, Canada, May 1997.

[39] S. Amet, L. Bottura, L. Deniau, L. Walckiers, “The Multipoles Factory; an Element of the LHC Control”, in *Proceedings of the 17th International Conference on Magnet Technology*, pp. 1417-1421, Geneva, Switzerland, September 2001.

[40] H. Brück, D. Degele, P.D. Gall, G. Hase, R. Meinke, M. Stolper, F. Willeke, P. Schmüser, C. Stolzenburg, “Reference Magnets for the Superconducting HERA Proton Ring”, in *Proceedings of the International Conference on High Energy Accelerators*, pp. 614-616, Hamburg, Germany, July 1992

[41] E. Todesco, B. Bellesia, L. Bottura, A. Devred, V. Remondino, S. Pauletta, S. Sanfilippo, W. Scandale, C. Völlinger, E. Wildner, “Steering Field Quality in the Main Dipole Magnets of the Large Hadron Collider”, *IEEE Transactions on Applied Superconductivity*, vol. 14, pp. 177-180, June 2004.

[42] L. Bottura, M. Buzio, S. Fartoukh, S. Russenschuck, S. Sanfilippo, W. Scandale, F. Schmidt, E. Todesco, L. Walckiers, R. Wolf, “Field Quality of the LHC Dipole Magnets in Operating Conditions”, in *Proceedings of the 8th European Particle Accelerator Conference*, pp. 260-263, Paris, France, June 2002.

[43] S. Sanfilippo, L. Bottura, M. Calvi, V. Chohan, M. Durante, P. Hagan, P. Pugnat, N. Smirnov, P. Schnizer, N. Sammut, A. Siemko, F. Simon, A. Stafiniak, E. Todesco, T. Tortschanoff, L. Walckiers, “Axis Measurements, Field Quality and Quench Performance of the First LHC Short Straight Sections”, *IEEE Transactions on Applied Superconductivity*, vol. 15, pp. 1098-1101, June 2005.

[44] M. Allitt, M. Bagre, C. Giloux, M. Karpinnen, P. Khare, A. M. Lombardi, T. Maurya, A. Puntambekar, V. Remondino, A. Santrich-Badal, W. Venturini Delsolaro, R. Wolf, "Field Quality and Hysteresis of LHC Superconducting Corrector Magnets", in *Proceedings of the European Particle Accelerator Conference*, pp. 1600-1603, Lucerne, Switzerland, July 2004.

[45] J. Billan, L. Bottura, M. Buzio, G. D'Angelo, G. Deferene, O. Dunkel, P. Legrand, A. Rijllart, A. Siemko, P. Sievers, S. Schloss, L. Walckiers, "Twin Rotating Coils for Cold Magnetic Measurements of 15 m Long LHC Dipoles", *IEEE Transactions on Applied Superconductivity*, vol. 10, pp. 1422-1426, December 1999.

[46] N. Smirnov, L. Bottura, M. Calvi, G. Deferne, J. DiMarco, N. Sammut, S. Sanfilippo, "Focusing Strength Measurements of the Main Quadrupoles for the LHC" in *Proceedings of the Magnet Technology Conference*, pp. 18-23, Genova, Italy, September 2005.

[47] A. Arn, S. A. Arshad, C. Giloux, F. Patru, H. Reymond, R. Senis, L. Walckiers, "The Measurement Bench for the LHC Spool Corrector Magnets in Industry", *IEEE Transactions on Applied Superconductivity*, vol. 12, pp. 1684-1687, March 2002.

[48] L. Deniau, "The LHC Reference Magnet System", in *Proceedings of the 1st LHC Project Workshop, Chamonix XIII*, pp. 190-195, Chamonix, France, January 2004.

[49] S. Sanfilippo, L. Bottura, M. Buzio, M. Calvi, N. Sammut, N. Smirnov, N. C. Lasheras, E. Todesco, A. Verweij, W. Venturini, "Magnetic Measurements of MB, Arc and DS-MS Quadrupoles", in *Proceedings of the Review of the Test of Superconducting Magnets at CERN*, CERN, Geneva, February 2006.

[50] L. Bottura, “The Magnet Evaluation Board”, in *Proceedings of the 2nd LHC Project Workshop*, *Chamonix XIV*, pp. 249-254, CERN, Geneva, Switzerland, January 2005.

[51] A. Siemko, “SM18 Test Facility”, in *Proceedings of the Workshop on Test Facilities and Measurement Equipment Needed for the LHC Exploitation*, CERN, Geneva, Switzerland, April 2006.

[52] M. Calvi, E. Todesco, L. Bottura, S. Sanfilippo, A. Siemko, “Impact of the First Powering Cycles on the LHC Superconducting Dipole Geometry”, in *Proceedings of the 19th International Conference on Magnet Technology*, pp. 18-23, Genova, Italy, September 2005.

[53] M. Buzio, “FAME and Other Magnetic Measurement Equipment”, in *Proceedings of the Workshop on Test Facilities and Measurement Equipment Needed for the LHC Exploitation*, CERN, Geneva, Switzerland, April 2006.

[54] P. Arpaia, L. Bottura, P. Cimmino, D. Giloteaux, A. Masi, J. Garcia Perez, G. Spiezia, L. Walckiers, “A Fast Digital Integrator for Magnetic Field Measurements at CERN”, in *Proceedings of the Instrumentation and Measurement Technology Conference*, Sorrento, Italy, April 2006.

[55] F. Schmidt, “MAD-X a Worthy Successor for MAD8?”, in *Proceedings of the 8th International Computational Accelerator Physics Conference*, pp. 47-49, St. Petersburg, Russia, June 2004.

[56] L. Rossi, “Experience with LHC from Prototyping to Large Scale Industrial Production and Integration”, in *Proceedings of the European Particle Accelerator Conference*, pp. 118-122, Lucerne, Switzerland, July 2004.

[57] T. Tortschanoff, V. Parma, P. Rohmig, M. Peyrot, J.M. Rifflet, P. Védrine, “The Short Straight Sections for the LHC”, in *Proceedings of the 17th Particle Accelerator Conference*, pp. 3374-3376, Vancouver, Canada, May 1997.

[58] J. Billan, J.P. Gourber, G. Guignard, K.N. Henrichsen, J.M. Maugain, R. Wolf, “Magnetic Performance of the LEP Bending Magnets”, in *Proceedings of the 13th IEEE Particle Accelerator Conference*, pp. 1148-1150, Chicago, Illinois, USA, March 1989.

[59] S. Russenschuck, M. Aleksa, M. Bazan, J. Lucas, S. Ramberger, C. Völlinger, “Integrated Design of Superconducting Magnets with the CERN Field Computation Program Roxie”, in *Proceedings of the 6th International Conference on Computational Accelerator Physics*, pp. 2017-2019, Darmstadt, Germany, September 2000.

[60] K.H. Mess, P. Schmüser, S. Wolf, “Superconducting Accelerator Magnets”, Singapore, World Scientific Publishing, 1996.

[61] A.K. Jain, “Basic Theory of Magnets”, in *Proceedings of the CERN Accelerator School: Measurement and Alignment of Accelerator and Detector Magnets*, pp. 1-21, Ed. S. Turner, CERN 98-05, Anacapri, Italy, August 1998.

[62] L. Bottura, A. Devred, V. Remondino, S, Sanfilippo, W. Scandale, E. Todesco, C. Völlinger, E. Wildner, “Controlling Field Quality in Magnet Production”, in *Proceedings of the Particle Accelerator Conference*, pp. 173-175, Portland, Oregon, USA, May 2003.

[63] W.C. Elmore and M.W. Garrett, “Measurement of Two-Dimensional fields. Part 1: Theory”, *Review of Scientific Instruments*, vol. 25, pp. 480-485, May 1954.

[64] F. Rodríguez-Mateos, R. Schmidt, A. Siemko, F. Sonnemann, “Quench Process and Protection of LHC Dipole Magnets”, LHC Project Note 184, CERN, Geneva, July 1999.

[65] L. Bottura, P. Burla, R. Wolf, “LHC Main Dipole Proposed Baseline Current Ramping”, LHC Project Report 172, CERN, Geneva, Switzerland, March 1998.

[66] L. Walckiers, L. Bottura, M. Buzio, P. Schnizer, N. Smirnov, “Sensitivity and Accuracy of the Systems for the Magnetic Measurements of the LHC Magnets at CERN”, in *Proceedings of the European Particle Accelerator Conference*, pp. 2181-2183, Vienna, Austria, June 2000.

[67] N. Smirnov private communication.

[68] E. Todesco, “Report on Field Quality in the main LHC dipoles: May-June 2006”, CERN Internal Report, EDMS 753956, June 2006. [Online]. Available: http://lhc-div-mms.web.cern.ch/lhc-div-mms/MMSPAGES/MA/obs.html

[69] S. Sanfilippo, L. Bottura, M. Buzio, M. Calvi, V. Chohan, M. Coccoli, J. Garcia, N. Sammut, N. Smirnov, E. Todesco, W. Venturini, L. Walckiers, A. Verweij, “Field Quality of MB. Alignment and Field Quality of SSS”, in *Proceedings of the Test Review of Superconducting Magnets*, CERN, Geneva, Switzerland, January 2005.

[70] N. Sammut, L. Bottura, J. Micallef, “Mathematical Formulation to Predict the Harmonics of the Superconducting Large Hadron Collider”, *Physical Reviews Special Topics: Accelerators and Beams*, vol. 9, 012402, January 2006.

[71] M. Ashkin, “Flux Distribution and Hysteresis Loss in a Round Superconducting Wire for the Complete Range of Flux Penetration”, *Journal of Applied Physics*, vol. 50, pp. 7060-7066, November 1979.

[72] C. P. Bean, “Magnetization of High-Field Superconductors”, *Reviews of Modern Physics*, vol. 36, pp. 31-39, January 1964.

[73] L. Bottura, “A Practical Fit for the Critical Surface of Nb-Ti”, *IEEE Transactions on Applied Superconductivity*, vol. 10, pp. 1054-1057, March 2000.

[74] M.S. Lubell, “Empirical Scaling Formulas for Critical Current and Critical Field for Commercial Nb-Ti”, *IEEE Transactions on Magnetics*, vol. 19, pp. 754-757, May 1983.

[75] J. W. Ekin, “Strain Scaling Law for Flux Pinning in Nb-Ti, Nb_3Sn, Nb-Hf/Cu-Sn-Ga, V_3Ga and Nb_3Ge”, *IEEE Transactions on Magnetics*, vol. 17, pp. 658-661, January 1981.

[76] P. W. Anderson, “Theory of Flux Creep in Hard Superconductors”, *Physical Review Letters*, vol. 9, pp. 309-311, October 1962.

[77] A.V. Tollestrup, R. E. Peters, K. Koepke, R. H. Flora, “Coil Extension, Deformation and Compression during Excitation in Superconducting Accelerator Dipole Magnets”, *IEEE Transactions on Nuclear Science*, vol. 24, pp. 1331-1333, June 1977.

[78] B. Auchmann, “Effect of Beam Screen Effects Through Simulations”, Field Quality Working Group. [Online].
Available: http://fqwg.web.cern.ch/fqwg/050405/050405.html

[79] K. Levenberg, “A Method for the Solution of Certain Problems in Least Squares,” Quarterly of Applied Mathematics, vol. 2, pp. 164-168, 1944. As cited by *The Mathworks* [Online]. http://www.mathworks.com/

[80] D. Marquardt, "An Algorithm for Least Squares Estimation of Nonlinear Parameters”, SIAM Journal of Applied Mathematics, vol. 11, pp. 431-441, 1963. As cited by *The Mathworks.* [Online]. http://www.mathworks.com/

[81] D.A. Finley, D.A. Edwards, R.W. Hanft, R. Johnson, A. D Mc Inturff. J. Strait, “Time Dependent Chromaticity Changes in the Tevatron”, in *Proceedings of the 12th Particle Accelerator Conference*, pp. 151-153, Washington, DC, USA, March 1987.

[82] M. Kuchnir and A. V. Tollestrup, “Flux Creep in a Tevatron Cable”, *IEEE Transactions on Magnetics*, vol. 25, pp. 1647-1651, March 1989.

[83] S. Le Naour, L. Oberli, R. Wolf, P. Puzniak, A. Szewczyk, A. Wisniewski, H. Fikis, M. Foitl, H. Kirchmayr, “Magnetisation Measurements on LHC Superconducting Strands”, in *Proceedings of the Applied Superconductivity Conference*, pp. 1763-1766, Palm Springs, California, USA, September 1998.

[84] A. Verweij, “Electrodynamics of Superconducting Cables in Accelerator Magnets”, Ph.D. Thesis, University of Twente, Netherlands, September 1995.

[85] L. Krempasky and C. Schmidt, “Influence of a Longitudinal Variation of dB/dt on the Magnetic Field Distribution of Superconducting Accelerator Magnets”, *Applied Physical Letters*, vol. 66, pp. 1545-1547, March 1995.

[86] L. Krempasky and C. Schmidt, “Experimental Verification of ‘Supercurrents’ in Superconducting Cables Exposed to ac-Fields”, *Cryogenics*, vol. 39, pp. 23-33, January 1999.

[87] L. Bottura, M. Breschi, M. G. Fabbri, “Analytical Solution for the Current Distribution in Multistrand Superconducting Cables”, *Journal of Applied Physics*, vol. 92, pp. 7571-7580, December 2002.

[88] W. B. Sampson and A.K. Ghosh, "Induced Axial Oscillations in Superconducting Dipole Windings", *IEEE Transactions on Applied Superconductivity*, vol. 5, pp. 1036-1039, June 1995.

[89] H. Brück, D. Gall, J. Krzywinski, R. Meinke, H. Preiβner, M. Halemeyer, P. Schmüser, C. Stolzenburg, R. Steining, D. ter Avest, L.J.M. van de Klundert "Observation of a Periodic Pattern in the Persistent-Current Fields of the Superconducting HERA Magnets", *Cryogenics*, vol. 30, Supplement, pp. 605-609, September, 1990.

[90] R. Wolf, "The Decay of Field Integral in Superconducting Accelerator Magnets Wound with Rutherford Cables", in *Proceedings of the 15th International Conference on Magnet Technology,* pp. 20-34, Beijing, China, October 1997.

[91] G. Velev, G. Ambrosio, G. Annala, P. Bauer, R. Carcagno, J. DiMarco, H. Glass, R. Hanft, R. Kephart, M. Lamm, M. Martens, P. Sclabach, C. Sylvester, M. Tartaglia, J. Tompkins, "Measurements of Field Decay and Snapback Effect on Tevatron Dipole and Quadrupole Magnets", in *Proceedings of the Particle Accelerator Conference*, pp. 2098-3000, Knoxville, Tennessee, USA, May 2005.

[92] R.W. Hanft, B.C. Brown, D. A. Herrup, M. J. Lamm, A. D. McInturff, M.J. Syphers, "Studies of Time Dependence of Fields in Tevatron Superconducting Dipole Magnets", *IEEE Transactions on Magnetics*, vol. 25, pp. 1647-1651, March 1989.

[93] T. Schreiner, "Current Distribution Inside Rutherford-type Superconducting Cables and Impact on Performance of LHC Dipoles", Ph.D. Thesis, Vienna University of Technology, February 2002.

[94] M. Haverkamp, "Decay and Snapback in Superconducting Accelerator Magnets", Ph.D. Thesis, University of Twente, Netherlands, October 2003.

[95] M. Schneider, “Decay and Snapback Studies on the LHC Dipole Model Magnets”, Ph.D. Thesis, Institute for Experimental Physics, Vienna, Austria, November 1998.

[96] N. Sammut, L. Bottura, S. Sanfilippo, “Extended Tests at 1.9 K: Snapback Scaling Law and Powering History Effect on Snapback and Decay”, Field Quality Working Group, Dec. 2004. [Online]. Available: http://fqwg.web.cern.ch/fqwg/041214/041214.html

[97] N. Sammut, E. Benedico Mora, L. Bottura, P. Galbraith, D. Giloteaux, G. Greco, M. Haverkamp, M. Marchesotti, A. Masi, J. Micallef, T. Pieloni, N. Smirnov, A. Tikhov, “A Hall Plate Based Instrument to Measure the Snapback in the Large Hadron Collider Superconducting Dipole Magnets”, in *Proceedings of the Instrumentation and Measurement Technology Conference*, Sorrento, Italy, April 2006.

[98] M. Haverkamp, E. Benedico, L. Bottura, B. ten Haken, H. ten Kate, S. Sanfilippo, “Field Decay and Snapback Measurements Using a Fast Hall Plate Detector”, *IEEE Transactions on Applied Superconductivity*, vol.12, pp. 86-89, March 2002.

[99] T. Pieloni, S. Sanfilippo, L. Bottura, M. Haverkamp, A. Tikhov, E. Effinger, E. Benedico, N. Smirnov, “Field Decay and Snapback Measurements Using a Fast Hall Probe Sensor”, *IEEE Transactions on Applied Superconductivity*, vol. 14, pp. 1822-1825, June 2004.

[100] A. Devred and T. Ogitsu, “Influence of Eddy Currents in Superconducting Particle Accelerator Magnets Using Rutherford-type Cables”, *CERN Accelerator School*, CERN 96-03, pp. 93-122, Hamburg, Germany, May 1995.

[101] L. Bottura, private communication.

[102] G. Annala, G. Ambrosio, P. Bauer, L. Bottura, R. Carcagno, J. DiMarco, R.W. Hanft, M.J. Lamm, M. Martens, P. Sclabach, C. Sylvester, M. Tartaglia, J.C. Hopkins, G. Velev, "Measurements of Geometric, Hysteretic and Dynamic Sextupole in Tevatron Dipoles", Fermilab/TD Report TD-04-043, November 2004.

[103] G. Annala, P. Bauer, M. Martens, D. Still, G. Velev, "Tevatron Chromaticity and Tune Drift and Snapback Studies Report", Fermilab/AD/TEV Report Beams-doc-1236, Fermilab, Batavia, Illinois, USA, January 2005.

[104] J. D. Gibbons, "Nonparametric Statistics", in Handbook of Statistical Methods for Engineers and Scientists, Hauserman Ed. McGraw-Hill, 1990.

[105] G.V. Velev, "Measurements of Sextupole Decay and Snapback in Tevatron Dipole Magnets", in *Proceedings of European Accelerator Conference*, pp. 1780-1782, Lucerne, Switzerland, July 2004.

[106] P. Bauer, G. Ambrosio, G. Annala, J. DiMarco, R.W. Hanft, M.J. Lamm, M.A. Martens, P. Schlabach, D. Still, M. A. Tartaglia, J.C. Tompkins, G. Velev, "Proposals for Improvements of the Correction of Sextupole Dynamic Effects in Tevatron Dipole Magnets", in *Proceedings of European Accelerator Conference,* pp. 818-820, Lucerne, Switzerland, July 2004.

[107] B. Holzer, "Impact of Persistent Currents on Accelerator Performance", *CERN Accelerator School,* CERN 96-03, pp. 123-129, Hamburg Germany, May 1996.

[108] N. Sammut, L. Bottura, S. Sanfilippo, J. Micallef, "The Dependence of the Field Decay on the Powering History of the LHC Superconducting Dipole Magnets", in *Proceedings of the European Particle Accelerator Conference*, pp. 2622-2624, Edinburgh, UK, June 2006.

[109] L. Bottura, G. Ambrosio, P. Bauer, M. Haverkamp, T. Pieloni, S. Sanfilippo, G. Velev, “A Scaling Law for the Snapback in Superconducting Accelerator Magnets”, *IEEE Transactions on Applied Superconductivity*, vol. 15, pp. 1217-1220, June 2005.

[110] G. Velev, P. Bauer, R. Carcagno, M. Lamm, D. Orris, P. Sclabach, C. Sylvester, M. Tartaglia, J. Tompkins, “New Measurements of Sextupole Field Decay and Snapback Effect on Tevatron Dipole Magnets”, in *Proceedings of the European Particle Conference*, pp. 2640-2642, Edinburgh, UK, June 2006.

[111] B. Bellesia, L. Bottura, V. Granata, S. Le Naour, L. Oberli, S. Sanfilippo, C. Santoni, W. Scandale, N. Schwerg, E. Todesco, C. Völlinger, “Trends in Cable Magnetization and Persistent Currents During the Production of the Main Dipoles of the Large Hadron Collider”, *IEEE Transactions on Applied Superconductivity*, vol. 15, pp. 1213-16, June 2005.

[112] M. Peyrot, J.M. Rifflet, F. Simon, T. Tortschanoff, P. Vedrine, “Construction of the New Prototype of the Main Quadrupole Cold Masses for the Arc Short Straight Sections of LHC”, *IEEE Transactions on Applied Superconductivity*, vol. 10, pp. 170-173, March 2000.

[113] N. Sammut, L. Bottura, S. Sanfilippo, J. Micallef, “The Field Description Model for the LHC Quadrupole Superconducting Magnets”, in *Proceedings of the European Particle Accelerator Conference*, pp. 2619-2621, Edinburgh, UK, June 2006.

[114] R. Ostojic, “Superconducting Magnets for LHC Insertions”, *IEEE Transactions on Applied Superconductivity*, vol. 14, pp. 181-186, June 2004.

[115] F. Toral, "Design and Fabrication of a Superconducting Trim Quadrupole for the LHC", in *Proceedings of the 4th European Conference on Applied Superconductivity*, pp. 1195-1198, Sitges, Spain, September 1999.

[116] W. Venturini, A. Arn, L. Bottura, C. Giloux, R. Mompo, A. Siemko, L. Walckiers, "The Test Facility for the Short Prototypes of the LHC Superconducting Magnets", in *Proceedings of the Cryogenic Engineering Conference*, pp. 106-113, Madison, Wisconsin, USA, May 2002.

[117] W. Venturini Delsolaro, L. Bottura, Y. Chaudhari, M. Karppinen, N. Sammut, "Measurement and Modeling of Magnetic Hysteresis in the LHC Superconducting Correctors", in *Proceedings of the European Particle Accelerator Conference*, pp. 2026-2028, Edinburgh, UK, June 2006.

[118] Walter Venturini Delsolaro; private communication.

[119] L. Bottura, L. Larsson, S. Schloss, M. Schneider, N. Smirnov, M. Haverkamp, "A Fast Sextupole Probe for Snapback Measurement in the LHC Dipoles", in *Proceedings of the International Conference on Magnetic Technology*, pp. 1435-1438, Ponte Vedra Beach, USA, September 1999.

[120] Spectron Glass and Electronics Incorporated [Online].
Avaliable: http://www.spectronsensors.com/

[121] N. Sammut and N. Smirnov, "A possible characterisation procedure to determine the systematic errors of the b_3-b_5 Hall probe", CERN Internal Memorandum, March 2006.

[122] O. Dunkel, R. Beltron, J. Billan, L. Gaborit, P. Galbraith, J. Garcia Perez, D. Giloteaux, B, Girod, “Coil Manufacture, Assembly and Magnetic Calibration Facility for Warm and Cold Magnetic Measurements of LHC Superconducting Magnets at CERN”, in *Proceedings of the 14th International Magnetic Measurement Workshop*, Geneva, Switzerland , September 2005. [Online]. Available: http://immw2005.web.cern.ch/immw2005/

[123] Metrolab instruments SA. [Online].
Available: http://www.metrolab.ch/ 2025/2025_GENERAL.HTML

[124] “7151 Computing Multimeter Operating Manual”, Solartron Instruments; Schlumberger, Issue 2, April 1984.

[125] National instruments website. [Online].
Available: http://sine.ni.com/nips/cds/view/p/lang/en/nid/14121

Appendix

Model Parameters

Dipole magnet transport in the LHC tunnel.

The personal commitment of a man to his skill, the intellectual commitment and
emotional commitment, working together as one, has made the ascent of man.
- Jacob Bronowski in "*The Ascent of Man*"

In this appendix, the main parameters of the field model are recalled.

A.1 - Main Dipoles

Table 9.1 shows the main dipole parameterisation in the static domain of sector 7-8, based on the data of 130 apertures. For the dipoles, the injection current I_{inj} is 760 A, the nominal current I_{nom} is 11850 A and the critical current I_c is 15000 A. The model is valid for the whole magnet operation range which is 760 A < I < 11850 A.

Table 9.2 recalls the dipole parameterisation in the dynamic domain. The decay modeling up to 1000 s is based on 130 apertures whilst the decay modeling from 1000 s to 10000 s is based on 13 apertures. In the case of the powering history magnets, 18 apertures were measured for I_{FT}, 24 apertures were measured for t_{FT}, and 14 apertures were measured for $t_{preparation}$. 96 measurements were performed to establish the b_3 snapback correlation.

Table A.1: Parameters used for the static model of the LHC dipoles of sector 7-8. The units of the parameters are the same as shown in Table 4. 1. (Data taken from Table 4.3 and 4.4)

	TF	b_2	a_2	b_3	a_3	b_4	a_4	b_5	a_5
Δ^{wc}	0.0083	−1.370	−0.015	−0.319	−0.002	−0.025	0.015	−0.132	0.012
γ	10.1141	1.3601	0.031	2.518	−0.132	0.072	0.025	0.088	0.057
μ	−0.0055	0.154	−0.032	−7.466	0.026	−0.001	−0.008	0.929	0.003
p	0.4487	1.532	0.467	0.630	1.116	0.012	0.420	0.168	1.430
q	1.6715	0.929	1.103	0.550	1.015	1.136	1.105	0.000	0.977
h	2.000	2.000	2.000	2.000	2.000	2.000	2.000	2.000	2.000
σ^1	−0.4203	−3.241	−0.118	−0.095	−0.008	0.207	−0.002	−0.142	−0.002
I_0^1	13239	8568	11090	7224	10255	10055	11429	9213	7712
S^1	3.5519	8.088	32.181	9.760	10.453	12.985	13.965	8.150	4.446
σ^2	0.1657	20.131	-	0.347	-	-	-	-	0.026
I_0^2	9735	14107	-	11031	-	-	-	-	16672
S^2	1.7023	25.551	-	16.923	-	-	-	-	21.333
ρ	0.0037	−0.182	−0.008	0.340	−0.018	−0.011	−0.002	0.126	−0.009
r	1.3992	1.953	2.817	10.000	2.522	1.357	1.885	2.851	3.974

Table A.2: Parameters used for the dynamic field model of the dipoles of sector 7-8. (Data taken from Tables 5.2, 5.8, 6.1 and Eq 6.5.)

	units	b_1	b_3	b_5
g^{SB}	(-)	-	0.176	-
τ	(s)	227.58	189.04	284.15
d	(-)	0.978	0.660	0.660
δ	(units)	1.41	2.01	–0.34
E_0	(-)	–0.4669	1.2807	–0.7025
E_1	(-)	–1.0266	1.6991	–1.0329
τ_E	(A)	4665.0	6900.1692	5843.0
T_0	(-)	-	–0.1986	-
T_1	(-)	-	–0.0512	-
τ_T	(s)	-	494.5232	-
P_0	(-)	-	0.9172	-
P_1	(-)	-	–0.3934	-
τ_P	(s)	-	380.5939	-

Table A.3: The model parameters for 01E cables based on a sample of 65 apertures taken from the whole magnet population. (Data taken from Table 7.3)

parameter	units	b_1 (01E)
τ	(s)	54.89
d	(-)	0.98
δ	(units)	0.285
max error	(units)	0.09

Sector 7-8 mostly consists of magnets with 01B cables. For sectors that consist of 01E cables, a single exponential decay formulation is used. Based on a sample of 65 apertures taken from the whole population, the decay parameters of magnets with 01E cables are shown in Table 9.3.

A.2 - MQ

Table 9.4 shows the MQ parameterisation is the static domain for the entire magnet population based on 61 aperture measurements. For the main quadrupoles, I_{inj} is 760 A, I_{nom} is 11850 A and I_c is 15000 A. The model is valid over the whole magnet operation range which is 760 A< I< 11850 A. Table 9.5 recalls the MQ decay parameters based on 27 apertures for a decay plateau of 1000 s.

Table A.4: The static model parameters used for the MQs. (Data taken from Table 7.4)

parameter	units	TF
Δ^{wc}	(T/kA)	0.203
γ	(T/kA)	58.387
μ	(T/kA)	−0.128
p	(-)	−0.677
q	(-)	5.486
h	(-)	2.000
σ^1	(T/kA)	−0.949
I_0^1	(A)	1555
S^1	(-)	3.987
σ^2	(T/kA)	0.253
I_0^2	(A)	1211
S^2	(-)	1.152
ρ	(T/kA)	0.127
r	(-)	2.422

Table A.5: The decay parameters of the TF of the MQs. (Data taken from Table 7.5)

parameter	units	TF
τ	(s)	138.490
d	(-)	0.353
δ	(units)	−1.618

A.3 - MQY

Table 9.6 shows the static model parameters for the MQYs based on 6 aperture measurements. I_{inj} is 176 A, I_{nom} is 3610 A and I_c is 15000 A. The range of validity of the model is 150 A< I< 3610 A. Table 9.7 shows the MQY decay parameters based on 4 apertures for a decay plateau of 1000 s.

Table A.6: The static model parameters used for the MQYs. (Data taken from Table 7.6)

parameter	units	TF
Δ^{wc}	(T/kA)	–0.309
γ	(T/kA)	152.6384
μ	(T/kA)	0.6046
p	(-)	0.000
q	(-)	1.602
h	(-)	2.000
σ^1	(T/kA)	–29.79
I_0^1	(A)	5027.8
S^1	(-)	9.414
σ^2	(T/kA)	2.890
I_0^2	(A)	2776.06
S^2	(-)	1.329
ρ	(T/kA)	–0.323
r	(-)	0.795

Table A.7: The decay parameters of the TF of MQYs. (Data taken from Table 7.7)

parameter	units	TF
τ	(s)	32.873
d	(-)	0.154
δ	(units)	–4.640

A.4 - MQTL

The static field model parameters for the MQTL based on one aperture measurement are shown in Table 9.8. $I_{inj} = 1$ A, $I_{nom} = 550$ A and $I_c = 930$ A. The model is valid over the entire operation range of the magnet which is -550 A< I < 550 A.

Table A.8: The static model parameters used for the MQTL. (Data taken from Table 7.8)

parameter	units	TF
γ	(T/kA)	307.362
μ	(T/kA)	−7.041
p	(-)	0.142
q	(-)	2.000
h	(-)	2.000
σ^1	(T/kA)	333.105
I_0^1	(A)	433.118
S^1	(-)	2.571
σ^2	(T/kA)	−368.906
I_0^2	(A)	447.758
S^2	(-)	2.795
ρ	(T/kA)	3.893
r	(-)	1.096

We shall not cease from exploration
And the end of all our exploring
Will be to arrive where we started
And know the place for the first time.
Thomas Stearns Eliot in ‘*Little Gidding’*